PNNL-11525
UC-400

Laboratory Directed Research and Development Annual Report

Fiscal Year 1996

May 1997

Prepared for
the U.S. Department of Energy
under Contract DE-AC06-76RLO 1830

Pacific Northwest National Laboratory
Richland, Washington 99352

DISCLAIMER

Contents

Introduction viii

Overview and Management Process ix

Atmospheric Sciences

A Multidisciplinary Investigation of Heterogeneous Atmospheric Processes 1

Installation Application Tool for the Multimedia Environmental Pollutant Assessment System (MEPAS) 4

Biotechnology

Biodegradation of Explosives by Combining Enzymatic and Microbial Processes 9

Classification of Microorganisms by Rapid, Efficient Sampling and Mass Spectrometric Detection 10

Development of Enzymatic Bioprocesses Based on Redox Enzymes 11

Dynamics, Modeling and Redesign of Microbial Proteins 12

Enzymology of Bacterial Metal Reductase and Dehalogenase 14

Fourier Transform EPR Studies of Radiation-Induced Structural Alteration of DNA 16

Functional Characterization of Bacterial Plasmids 18

Identification, Purification and Characterization of the Reductive Dehalogenase of Desulfomonile tiedjei DCB-1 20

Microbial Genomics 21

NMR Studies of DNA Structure Associated with Chemical Adduction 23

Protein Identification in Sequenced Genomes 25

Chemical Instrumentation and Analysis

Speciation of Uranyl Aqueous and Surface Complexes by Cryogenic Spectroscopic Methods 29

Theoretical and Experimental Study of ^{195}Pt Solid NMR Shift Tensors 32

Waste Tank Vapor Characterization of Polar Organic Constituents 35

Computer and Information Science

Adaptive Life Simulator 39

Automated Lung Ventilation Diagnosis 40

Collaborative Environment Prototype for Molecular Science 42

Development of Intuitive User Interfaces 45

Human Factors Evaluation of Immersive Virtual Environments Technology 46

Information Visualization 48

Medical Imaging Three-Dimensional Reconstruction and Visualization 52

Molecular Visualization on Parallel Computers 54

Neural Network Data Processing for Sensor Applications 56

Property Prediction from Molecular Dynamics Simulation 58

Ecological Science

Coplanar PCB Congener Separation and Quantitation 63

Electronics and Sensors

A Real-Time Adaptive Intelligent System for Sensor Validation 67

Automotive Exhaust Sensor for Engine Control 69

Cylinder Design for Reduced Emission Origins 71

Improved Fiber-Optic Sensor 73

Ultrasonic Measurement of Elastic Properties of Bone 75

Health Protection and Dosimetry

Optical In Vivo Blood Characterization and Multivariate Analysis 79

PBPK-Based Breath Analysis Instrumentation 82

Real-Time Dosimetry for Therapeutic Radiation Delivery 84

Hydrological and Geologic Sciences

Development of a PC-Based Watershed Modeling and Visualization Package 87

Marine Sciences

Development of a Lagrangian Particle-Tracking Method for Quantifying Fluxes in the Near-Shore Marine Environment 91

Remote Sensing of Coastal and Marine Environments with Airborne Multisensor Pod System (AMPS) 93

Materials Science and Engineering

Advanced Energy Storage Materials 97

Coatings Characterization 99

Die Casting Materials 100

High Performance Barrier Coatings Using Polymer Multilayers 101

High Porosity Dielectric Films Through Biomimetic Processing 104
High Temperature Catalytic Materials 105
Intelligent Organic/Inorganic Composites 107
Materials Synthesis and Processing for Flat Panel Displays 109
Mesoporous Materials 111
Nanoparticle Processing 113
Nanoparticle Science 115
Ordered Mesoporous Membranes and Thin Films 117
Shape Selectivity Porous Catalysts 119
Solution Chemistry 120
Surface Modification 122
Synthesis of Model Inorganic Ion Exchange Materials 123

Molecular Science

Bonding and Structure of Organic Ligands at Oxide/Water Interfaces 127
High Resolution and Solid State NMR Studies of Proteins and DNA-Adducts 130
Identification and Structural Determination of Paramagnetic Species Using Pulsed EPR 132
NMR Studies of Altered DNA-Protein Complexes 134
Novel Synthesis of Metal Cluster/Polymer Composites 136
Numerical Solution of the Schrödinger Equation 138
The Development of a Dissociative Model for Water 139
Tumor Formation in Cells and Tissues Studied by Means of Liquid-State and Solid-State NMR 142

Process Science and Engineering

Advanced Instrumentation Real-Time Acoustic Planar Imaging of Dense Slurries - RAPIDS 147
Advanced Spot Welding of Aluminum Automotive Sheet 150
Alkane Oxidation 152
Development of Small-Scale Reformer for Hydrogen Production 154
Electroactive Materials 155
Electroconversion 157
Formation of a Contaminant Barrier by Injecting Metallic Sulphate Colloids 159

Gas Phase Corona Scaleup 162
Hydrogen-Free Processing of Metallic Sodium Mixed Waste 165
Hydrogen Separation Technology Using the CHASP Process 167
In Situ Stabilization of Mercury by Apatite 169
Ionizing Radiation Assisted Processing of Hazardous Wastes 171
Kinetics, Scale-up, and Demonstration of Uranium Bioprecipitation Technology 173
Liquid Corona Process Development and Novel Electrode Scale-Up 174
Liquid Metal Micropump 176
Membrane Separations 177
Microchannel Separations 178
Microplasma Reactor 180
Nonaqueous Based Processing 183
Plasma Engineering and Prototype Development 184
Prediction of Physical Properties of Colloidal Gels 188
Structure/Function Analysis 189
Supercritical Fluids Separations 191
Synthesis Reaction in a High Energy Corona 192
Ultra High Rate Sputter Deposition of Highly Reflective Metal Films 195
Vacuum Extruded Polymer Films 199
Vegetable Oil-Pilot Scale Test: Transport Analysis 202

Risk and Safety Analysis

Data Quality Analysis for Risk and Environmental Assessment 207
Risk-Based Hydropower Refurbishment Methodology 208

Socio-Technical Systems Analysis

An Integrated Model of Organizations and Information Technology in the 21st Century 213
Ethical, Legal and Social Issues Surrounding Microbial Biotechnologies 215

Statistics and Applied Mathematics

Environmental Statistical Sampling Design Framework Tool 219

Thermal and Energy Systems

Advanced Numerics and Visualization for Power Systems 223

Artificial Intelligence for Power System Control 225

Distributed Power System Dynamic Controller 227

Flat Residential/Commercial Light Architecture 229

Low Cost Microchannel Heat Exchanger Development 231

Microcompressor Development 233

Micro Heat Exchanger Development 235

Acronyms and Abbreviations 241

Introduction

The Department of Energy Order 413.2[a] establishes DOE's policy and guidelines regarding Laboratory Directed Research and Development (LDRD) at its multiprogram laboratories. As described in 413.2, LDRD is "research and development of a creative and innovative nature which is selected by the Laboratory Director or his or her designee, for the purpose of maintaining the scientific and technological vitality of the Laboratory and to respond to scientific and technological opportunities in conformance with the guidelines in this Order."

DOE Order 413.2 requires that each laboratory submit an annual report on its LDRD activities to the cognizant Secretarial Officer through the appropriate Operations Office Manager. The report provided in this document represents Pacific Northwest National Laboratory's LDRD report for FY 1996.

During FY 1996, 161 LDRD projects were selected for support through Pacific Northwest National Laboratory's LDRD project selection process. Total funding allocated to these projects was $13.3 million. This amount represented 3 percent of the Laboratory's operating budget, which is half of the 6 percent maximum allowed by DOE Order 413.2.

In recognition that the Laboratory must focus on a defined set of research that reflects our missions and unique assets, LDRD investments are focused on developing new and innovative approaches in research which support our "core technical capabilities." Currently, the Laboratory's core technical capabilities have been identified as

- Atmospheric Sciences
- Biotechnology
- Chemical Instrumentation and Analysis
- Computer and Information Science
- Design and Manufacturing Engineering
- Ecological Science
- Electronics and Sensors
- Health Protection and Dosimetry
- Hydrologic and Geologic Sciences
- Marine Sciences
- Materials Science and Engineering
- Molecular Science
- Nuclear Science and Engineering
- Process Science and Engineering
- Risk and Safety Analysis
- Socio-Technical Systems Analysis
- Statistics and Applied Mathematics
- Thermal and Energy Systems
- Toxicology

In this report, the individual summaries of LDRD projects are organized according to these core technical capabilities. The largest proportion of Laboratory-level LDRD funds is allocated to our capability in molecular science and the second largest allocation is in process science and engineering. A significant proportion of the Laboratory's LDRD funds were allocated to projects proposed by individual researchers or small research teams within the various technical research organizations. Funding allocated to each of these projects is typically $40K or less.

The projects described in this report represent the Laboratory's investment in its future and are vital to maintaining the ability to develop creative solutions for the scientific and technical challenges faced by DOE and the nation. In accordance with DOE guidelines, the report provides

- an overview of the Laboratory's LDRD program and the management process used for the program
- a 5-year project funding table
- project summaries for each LDRD project
- brief descriptions and funding profiles for each new project started in FY 1997 (Attachment).

(a) U.S. Department of Energy Order DOE 413.2, Laboratory Directed Research and Development, 04-09-92.

Overview and Management Process

The relevance and value of a Department of Energy (DOE) multiprogram laboratory lies in its ability to apply science and technology to national needs that fall within the missions of the DOE. The increasing complexity of these needs and the inadequacy of using conventional approaches demand that creativity and innovation underlie scientific and technological efforts so that new and novel solutions are discovered and applied. In addition, new ideas and opportunities frequently occur at a faster pace than can be anticipated or adopted in the federal budget process.

A national laboratory must establish and maintain an environment in which creativity and innovation is encouraged and supported if it is to fulfill its missions and remain viable in the long term. For these reasons, external reviews of the DOE multiprogram laboratories have consistently recommended that laboratory directors be given discretion to select research and development projects for support and to allocate a percentage of their operating budgets to provide this support.

The Laboratory Directed Research and Development (LDRD) program, in the long term, allows the Pacific Northwest National Laboratory to assist DOE in fulfilling its missions and contributes to other priority needs of the nation. Pacific Northwest National Laboratory's program supports creative endeavors in areas of strategic national importance that utilize the core technical capabilities of the Laboratory. The Laboratory seeks to continually replenish its inventory of ideas that have the potential to address major national needs. The principal goals of the LDRD program are to 1) encourage the advancement of basic science and fundamental research at the Laboratory, and 2) develop major new research and development approaches and capabilities. Specific objectives are to:

- foster an environment that encourages creativity and innovation
- fund new and novel ideas that have scientific/technical merit but that cannot be funded promptly through programmatic channels
- investigate new ideas/concepts to the proof-of-principle stage.

The LDRD program serves to enhance the morale and vitality of the Laboratory's scientific and technical staff and to recognize their importance to the future of the Laboratory. This program has a major impact on our staff by providing a mechanism to promptly pursue new ideas and concepts and to enrich the Laboratory's capabilities.

Program Benefits

Pacific Northwest National Laboratory's LDRD program has provided a number of benefits relative to the generic goals of fostering creativity and innovation within the Laboratory. The program has also provided specific benefits to the Laboratory that have allowed it to assume a major role in the development of science and technology to address significant national needs, such as the environmental restoration of DOE sites and global climate change.

When Pacific Northwest National Laboratory became an Energy Research laboratory in 1985, one of the major DOE directives was strengthening its fundamental research capabilities. A strengthened fundamental research component would establish a sound scientific basis for the Laboratory's applied research and development programs that would provide a complete capability for the integrated management of scientific and technical programs of national importance.

LDRD has been the principal vehicle by which the Laboratory has made substantial progress in improving its fundamental research base. The new capabilities developed at PNNL in molecular science, high-performance computing, biotechnology, and the environmental sciences have enhanced its ability to serve DOE missions. These new capabilities have changed and renewed the institutional vitality of the Laboratory during a time when the Hanford Site was undergoing significant changes that appeared likely to undermine this vitality.

The national goal of restoring DOE sites, the total cost of which is now estimated to exceed $100 billion, will never be accomplished in a reliable and cost-effective manner without significant contributions from science and technology. These contributions will range from developing a fundamental understanding of the effects of contaminants on molecular structure and function, to developing innovative new technologies for processing wastes. Bioremediation is an example of where advances in both fundamental science and applied engineering will be necessary if it is to be successfully implemented. Similarly, a rational and defensible approach to addressing global environmental change will not be

developed until the nature of possible changes are more fully understood and the impacts of alternative mitigating strategies are analyzed. Investments in advanced computing underlie the Laboratory's approach to these and other major scientific areas.

The LDRD program has allowed PNNL to initiate the process of bringing the capabilities of the national scientific and technical community to bear on these environmental problems. These efforts are still evolving and significant challenges remain. However, many of the Laboratory's ideas and concepts related to these areas were originally developed with LDRD funds and are now receiving programmatic support from DOE. Examples include previous LDRD-supported work in the atmospheric sciences that is now being applied through Pacific Northwest National Laboratory's participation in the Atmospheric Research Measurement (ARM) program, and studies in chemical dynamics that are now being supported by the Office of Basic Energy Sciences. Another example is PNNL's success in the Environmental Management Science Program (EMSP) where many of the Laboratory's winning proposals were based on concepts initially explored through LDRD. It is believed that current LDRD projects in process science and engineering, bioremediation, and health effects research will produce similar scientific and technical benefits as national efforts in these areas more fully emerge.

Pacific Northwest National Laboratory has traditionally made a portion of its LDRD funding available to small, interdisciplinary teams of researchers with new ideas or concepts that require only a small amount of funding (typically less than $40K) for initial testing. This practice is planned to be continued because of the significant scientific and technical benefits that have resulted.

In the current environment, the DOE laboratories are under pressure to increase their value to the nation. Important components of the Laboratory's strategy in response to this environment are to 1) increase our productivity and 2) focus on addressing major national problems that can effectively use our core technical capabilities. In this environment, the LDRD program becomes even more important as a key mechanism for achieving these goals and increasing the Laboratory's value to the nation.

In summary, LDRD has enabled Pacific Northwest National Laboratory to enhance its research vitality as a DOE multiprogram laboratory during a period of significant change. LDRD has facilitated the Laboratory's ability to make significant contributions to addressing national problems, particularly in the environmental research area which represents the primary distinctive signature of the Laboratory. It is essential that PNNL and the other DOE laboratories retain the capability provided by LDRD if their full capacity to assist DOE and the nation is to be realized.

Laboratory Directed Research and Development Management Process at Pacific Northwest National Laboratory

LDRD at Pacific Northwest National Laboratory is funded through a General and Administrative overhead account applied to all internal costs (i.e., staff labor, travel, miscellaneous expenses) charged to the Laboratory's 1830 Contract accounts funded by DOE and other federal agencies. The PNNL Director of Finance is responsible for ensuring that these funds are accumulated and accounted for in the appropriate manner. Formal proposals in an authorized format are required for each LDRD project.

Decisions regarding funding levels for the LDRD accounts are made by the Laboratory Director, with assistance from the Laboratory Strategy Council (composed of the Associate Laboratory Directors). Primary responsibility for allocations to individual LDRD projects within these accounts also rests with the Director and the Strategy Council. The Laboratory Technical Council (composed of the leaders of the core technical capabilities) and the Laboratory Business Council (composed of major DOE program managers) play key roles in developing recommendations for the Director on these allocations. The Laboratory Technical Council has primary responsibility for ensuring the technical soundness of the LDRD investments, through peer reviews conducted by both internal and external scientific reviewers. The Associate Laboratory Director for Strategic Planning has responsibility for the general oversight and conduct of PNNL's LDRD program.

All projects are reviewed for technical merit by line managers and/or scientific staff, and in some cases by external peer reviewers. Written guidance (including a formal LDRD Guide) pertaining to the criteria and guidelines for LDRD projects provided in DOE Order 413.2 is widely distributed to Laboratory staff. Adherence to these criteria is further ensured through reviews by the LDRD Office. Individual projects are usually limited to $1M in total funding and $500K in a single fiscal year. The Director of Finance is responsible for financial oversight of the LDRD program. Accountability for individual LDRD projects rests with the principal investigators conducting the projects and their cognizant line manager.

The major sequential steps of Pacific Northwest National Laboratory's LDRD process are as follows:

- Ongoing LDRD projects are reviewed for progress in achieving their intended goals and, if warranted, preliminary commitments are made to continue funding first- and second-year LDRD projects into the next fiscal year.

- Initial concepts for new LDRD investments are solicited through the Laboratory's business planning process managed by the Associate Laboratory Director for Strategic Planning.

- Based on the approval of Pacific Northwest National Laboratory's LDRD Plan by DOE, initial funding allocations for the LDRD accounts are approved by the Laboratory Director and a request for proposals is issued.

- Line and program managers solicit proposals for specific LDRD projects from research staff and select projects as candidates for funding. Each manager selecting an LDRD project must certify in writing that the project has been peer-reviewed and meets the requirements of DOE 413.2.

- All LDRD project proposals and the electronic files must be submitted to the Laboratory's LDRD Office for review for compliance with DOE requirements after the principal investigator and the cognizant manager have signed them. All documentation required to meet National Environmental Policy Act (NEPA) and other environmental, safety, and health compliance requirements for the projects must also be submitted.

- The emphasis of the proposals is on the technical objectives and approaches that will be incorporated in the project.

- The Budget and Analysis Office has established four-digit alpha codes that are used to represent the work breakdown structure (WBS) code for each of the LDRD accounts. After a project receives final approval, a project-level work breakdown structure code is assigned by the LDRD Office for each LDRD project.

Primary responsibility for ensuring adequate technical review of LDRD projects rests with line and program managers. In addition, regular peer reviews of selected activities are performed by the Laboratory Technical Council. Additional oversight of the progress of the LDRD investments is provided by the Laboratory Strategy Council. Some of the major LDRD investment areas, such as molecular science and process science and engineering, also have designated advisory councils that include external advisors in their peer reviews of the status and progress of the research. The various technical reviews constitute the most important means of ensuring that LDRD funds are used for their intended purpose.

Principal investigators and management are also required to develop input to meet all DOE LDRD reporting requirements. These requirements include the LDRD annual reports and the quantitative survey of LDRD project results. Selected principal investigators may also be asked to participate in periodic DOE LDRD program reviews, which are organized by the LDRD Office. The LDRD Office has primary responsibility for developing the annual LDRD Plan.

Atmospheric Sciences

A Multidisciplinary Investigation of Heterogeneous Atmospheric Processes

Douglas Ray (Chemical Structure and Dynamics)
Bruce C. Garrett (Theory, Modeling, and Simulation)
Yang Zhang (Atmospheric Sciences)

Project Description

This project investigated heterogeneous atmospheric chemical processes. The result of this project is an improved scientific and technological capability to study the importance of heterogeneous chemical processes in the context of global environmental change.

Technical Accomplishments

Development, Testing, and Application of a Detailed, Mixed-Phase Atmospheric Chemistry Box Model

We have made considerable progress in this task during FY 1996. The Mass Transfer with Chemistry Model (MaTChM) developed during FY 1994 and FY 1995 has been applied to a case study in Atlanta, Georgia. Our results show that the aerosol surface uptake processes have an important impact on photochemical ozone (O_3) formation under urban atmospheres. More recently, we conducted a comprehensive sensitivity analysis of overall model predictions with respect to a variety of model parameters using automatic differentiation technology. This work was a coordinated effort between PNNL's Atmospheric Sciences group and computer scientists Christian Bischof and his postdoctoral fellow Po-Ting Wu at Argonne National Laboratory. We have successfully applied the Automatic DIfferentiation of FORtran (so-call ADIFOR package co-developed by Christian Bischof) to calculate the first-order sensitivity coefficients of 58-145 chemical species concentrations with respect to 147-407 model parameters including 125 gas-phase reaction rate constants, 120 aqueous-phase kinetic reaction rate constants, 29 Henry's law constants, 29 effective Henry's law constants, 29 mass accommodation coefficients, 29 uptake coefficients, 21 dissociation equilibrium constants, 21 species initial concentrations, temperature, relative humidity, cloud water content and droplet size. The sensitivity studies were performed under typical atmospheric conditions ranging from remote to heavily-polluted atmospheres. Under each condition, we further evaluated four scenarios: clear air, air with aerosols, cloudy conditions, and clouds plus aerosols. We are in the process of analyzing the results and preparing papers for journal publication.

The most influential reactions and the most important parameters under each atmospheric conditions have been identified through the sensitivity analysis. Photochemical ozone formation is much more sensitive to the changes of reaction rate constants under polluted atmospheres (with sensitivity 5 to 20 orders of magnitude higher than that in relatively clean atmospheres). The identified most influential reactions on O_3 formation are 1) the photolytic reactions of O_3 and its precursor species; 2) the conversion of nitric oxide (NO) to nitrogen dioxide (NO_2); 3) the reactive radical reactions; 4) the oxidation of O_3 and its precursors by radical species; 5) the formation and dissociation of oxidant and acid; and 6) the aqueous oxidation of O_3, hydroperoxy radical (HO_2), and sulfur species.

One of the most interesting findings from this study is that the sensitivity coefficients of photochemical "indicators species" such as the ratio of O_3 to the difference of odd nitrogen (NO_y) and nitrogen oxides (NO_x) ($O_3/(NO_y-NO_x)$) can be used to evaluate O_3-NO_x-hydrocarbon sensitivity, as shown in Figure 1.

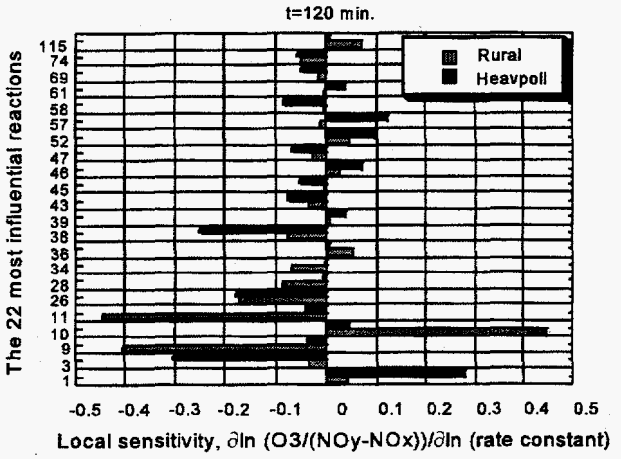

Figure 1. Sensitivity of $O_3/(NO_y-NO_x)$ with respect to gas-phase reaction rate constants under rural and heavily polluted clear air conditions. The values shown are sensitivity to the 22 most influential reactions at 120 minutes from a 2-hour simulation starting from local noon time. The reactions may have positive or negative influence on $O_3/(NO_y-NO_x)$ depending on the sign of their sensitivities ("-" indicates the ratio decreases with an increase in that reaction rate constant). Reactions 1 through 28 are O_3-NO-NO_2 reactions, and reactions 38 through 74 are hydrocarbon reactions.

The sensitivities of $O_3/(NO_y\text{-}NO_x)$ to hydrocarbon reactions under heavily polluted atmosphere are a factor of 2 to 25 greater than that under less polluted atmospheres, indicating a hydrocarbon-sensitive chemistry in heavily polluted regions. Lower sensitivity to hydrocarbon reactions and higher sensitivity to $O_3\text{-}NO\text{-}NO_2$ reactions indicates a NO_x-sensitive chemistry. Other good markers for $O_3\text{-}NO_x$-hydrocarbon sensitivity analysis are the ratio of hydrogen peroxide to nitric acid (H_2O_2/HNO_3), the ratio of formaldehyde to odd nitrogen ($HCHO/NO_y$), and the ratio of hydrogen peroxide to formaldehyde ($H_2O_2/HCHO$). These results will aid the U.S. EPA in the development of more effective O_3 abatement strategies in the O_3 non-attainment regions.

Our results also show that the presence of clouds and aerosols significantly reduces the total oxidizing capacity, with the sensitivity of O_3 lowered by 2 or larger orders of magnitude. More importantly, these heterogeneous processes alter the O_3-precursor relations through changing the reaction influential amplitudes and the signs of the sensitivities. Cloud chemistry is the dominant heterogeneous process under the remote and marine atmospheres. Aerosols are important scavengers for gaseous species and contribute to the heterogeneous perturbation to photochemistry in polluted atmospheres. The overall model predictions are not sensitive to the changes in individual species mass accommodation coefficient, but they are sensitive to changes in uptake coefficients of HNO_3, nitrous acid (HNO_2), HO_2, H_2O_2, HCHO, NO_x, peroxyacyl nitrate (PAN), dinitrogen pentoxide (N_2O_5), and O_3. These results indicate that the current O_3 abatement strategies developed based on clear air chemistry may not be effective in some regions with high cloud frequency and/or large aerosol loading. The heterogeneous chemistry associated with clouds and aerosols and their effects on photochemical O_3 formation must be taken into account in these regions.

Simulation of Molecular-Scale Processes at a Gas-Liquid Interface

Molecular dynamics simulations have been used to directly examine the structure of the water surface and the interaction of alcohol molecules with the surface and bulk liquid. One of the first steps in this task was the evaluation of interaction potentials for water. Simulations were run using a pairwise-additive interaction potential, the extended single point charge (SPC/E) model, and an interaction potential that includes many-body effects using a polarization model (POL1). The reliability of these models was assessed by comparing experimental observables (such as surface tension, structural information, etc.) against the computed results. For example, the computed values of the surface tension for the SPC/E model agrees with the experimental values to within 20% over a temperature range from 268 K to 373 K. Detailed information about the structure at the interface is also provided. For example Figure 2 shows the profile of the density as a function of the distance z normal to the liquid/vapor interface. The density of the water near the interface decreases, falling off smoothly to zero in the vapor. This is not the result of the presence of a diffuse fluid or dense vapor in the interface region, but is instead due to the tendency of the surface H_2O molecules to form transient cavities which, averaged over time and distance, give a lowered density compared to the bulk. This is depicted in a snapshot of the interface in the top of Figure 2.

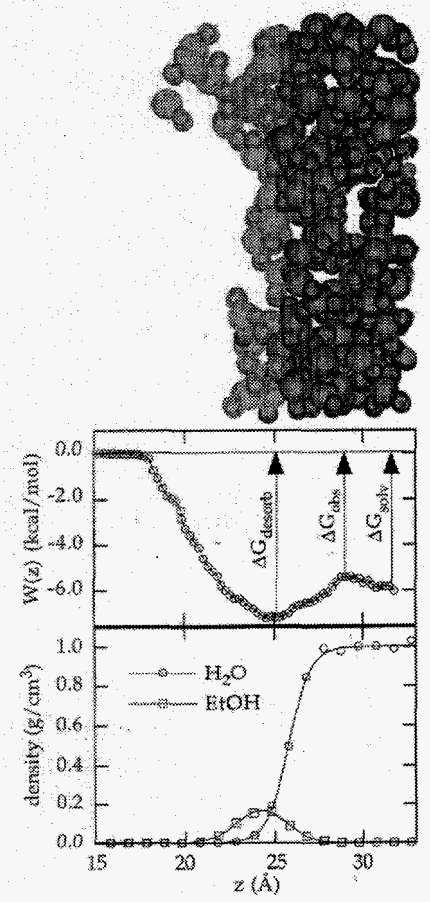

Figure 2. Top: Snapshot of the liquid/vapor interface of water. Middle: Free energy profile for the insertion of an ethanol molecule into H_2O. Bottom: Density profile of 1 ethanol and 525 H_2O molecules equilibrated at 298 K for 500 psec.

Potentials for the interaction of solute molecules, such as simple alcohols and ethylene glycol, have been developed and tested by comparing computed bulk phase properties with experimental ones. For example, interaction potentials for ethanol accurately reproduce experimental solvation energetics and structures. The mass accommodation coefficient is an indication of the probability that a molecule which strikes the surface of the liquid will be captured by the liquid before it escapes back into the gas. Davidovits, Worsnop, and coworkers

have measured the mass accommodation coefficients for a variety of small molecules in water droplets and have proposed a mechanism for the accommodation process. In this mechanism, the gas-phase molecule strikes the surface and sticks with unit probability in a weakly bound interfacial state. It is then either desorbed back into the gas phase or surmounts a dynamical barrier and becomes incorporated into the bulk liquid. One goal of this work is the development of a detailed, molecular-scale understanding of the accommodation process that will allow generalization to other molecular species, such as radicals, that may be difficult to study experimentally.

The mass accommodation process is controlled by the relative rates of desorption and incorporation into the bulk liquid. The ratio of the two rates is expressed in terms of the difference in free energies of activation, or DG_{obs}, for the accommodation and desorption processes. Davidovits, Worsnop, and coworkers have determined DG_{obs} for a variety of molecules and found it to be positive, indicating that the accommodation rate is slower than desorbtion rate. Although DG_{obs} is experimentally determined from kinetic parameters, as a first step, we approximate it from the potential of mean force (PMF) for insertion of a solute molecule from the gas phase through the surface and into bulk water. The PMF is determined from equilibrium ensemble averages of the systems energy as a function of the distance from the center of mass of the solute molecule to the liquid/vapor interface. PMFs are calculated for incorporation of a water, an ethanol, an ethylene glycol, and a pentanol molecule into water. In Figure 2, the potential of mean force W(z) for ethanol is shown as a function of the distance z normal to the liquid/vapor interface. In contrast to the experiments, the equilibrium solvation calculations predict that DG_{obs} is negative. Thus, mass accommodation is not controlled by equilibrium solvation energetics. Further studies are in progress to examine the dynamics of the process.

Uptake of Gases by Aqueous Solutions Probed by Surface Nonlinear Optical Spectroscopy

Measurement of the adsorption isotherm for dimethyl sulfoxide (DMSO) on DMSO/water solutions by surface second harmonic generation spectroscopy and determination of $\Delta G^{o}ads$ from 278K to 323K have been accomplished. DMSO was selected for these experiments because of its role in tropospheric chemistry and because accurate values for the mass accommodation coefficient and Henrys Law constant of DMSO in water over the same range of temperatures are available. Our determinations of $\Delta G^{o}ads$, in conjunction with data obtained from the literature, provides the first complete set of thermodynamic data for the mechanism proposed for the uptake of nonreactive solutes by dilute aqueous solutions.

Publications

R.S. Taylor, L.X. Dang, and B.C. Garrett. 1996. *J. Phys. Chem.* 100, 11720.

R.S. Taylor, D. Ray, and B.C. Garrett. "Understanding the mechanism for the mass accomodation of ethanol by water droplets." *Science* (submitted).

D.S. Karpovich and D. Ray. "DMSO at the liquid/vapor interface of water: Thermochemistry." (in preparation).

R.S. Taylor, G.K. Schenter, and B.C. Garrett. "Effects of non-equilibrium solvation on the mass accommodation of ethanol by H_2O." (in preparation).

R.S. Taylor, L.X. Dang, and B.C. Garrett. "The structure of alcohols at the liquid/vapor interface of water: A molecular dynamics study." (in preparation).

Y. Zhang, C.H. Bischof, R.C. Easter, and P.-T. Wu. "Sensitivity analysis of a multi-phase chemical mechanism using automatic differentiation." (in preparation).

Y. Zhang, R.D. Saylor, R.C. Easter, and W.L. Chameides. "Potential coupling of aerosols and ozone photochemistry in the urban atmosphere." (in preparation).

Installation Application Tool for the Multimedia Environmental Pollutant Assessment System (MEPAS)

Karl J. Castleton (Systems and Risk Management)

Project Description

The Multimedia Exposure Assessment Group previously received funding to compute human health risks from all contaminated sites for entire DOE installations using the Multimedia Environmental Pollutant Assessment System (MEPAS). To make this kind of assessment more effective, a tool could be added to MEPAS to eliminate the restrictions that make this work tedious and to ensure more consistent analysis of large numbers of release sites.

Technical Accomplishments

MEPAS 3.1 was developed to compute the risk from one release site to multiple receptors given a short list of constituents. This structure introduces difficulties in using MEPAS to compute the risk for an entire installation (over 1400 release sites and 200 constituents). Three limitations must be circumvented in MEPAS to enable automated installation assessments.

1. The number of contaminants per site is currently limited to 20 per model run which is resource intensive for installations that have on the order of hundreds of contaminants. Currently, when using MEPAS, this is accomplished by making multiple MEPAS runs with all data the same except the contaminants. This takes extra time and resources to ensure that the duplicate data is consistent and correct.
2. The limitation of one environmental setting in a run must also be remedied. Originally MEPAS was intended to model only one site at a time. Thus, the user must create a file for each environmental setting for each set of contaminants.
3. The restriction of MEPAS to one dimension (length, width, depth) for a release site within an environmental setting also must be expanded. This would allow the use of all the sizes of release sites on the installation while holding the rest of the data constant.

The result of this project is a tool that enables a single user to compute the risk for an installation using MEPAS. The user is unconstrained in the number of sites, number of contaminants, or dimension of sites. This eliminates the tedious and error prone work of prior methods. The tool created is intuitive in its approach to configuring the MEPAS models for the computations the users need to perform.

Figure 1 is a diagram of an example model run using the interface constructed for the Installation Application Tool for MEPAS. It shows the flow of contamination from a hypothetical tank on the Hanford Site to Richland, Kennewick, and Pasco via the Columbia and Yakima rivers, air, and aquifer under the Hanford Site. It also shows the risk to the Native American and adult.

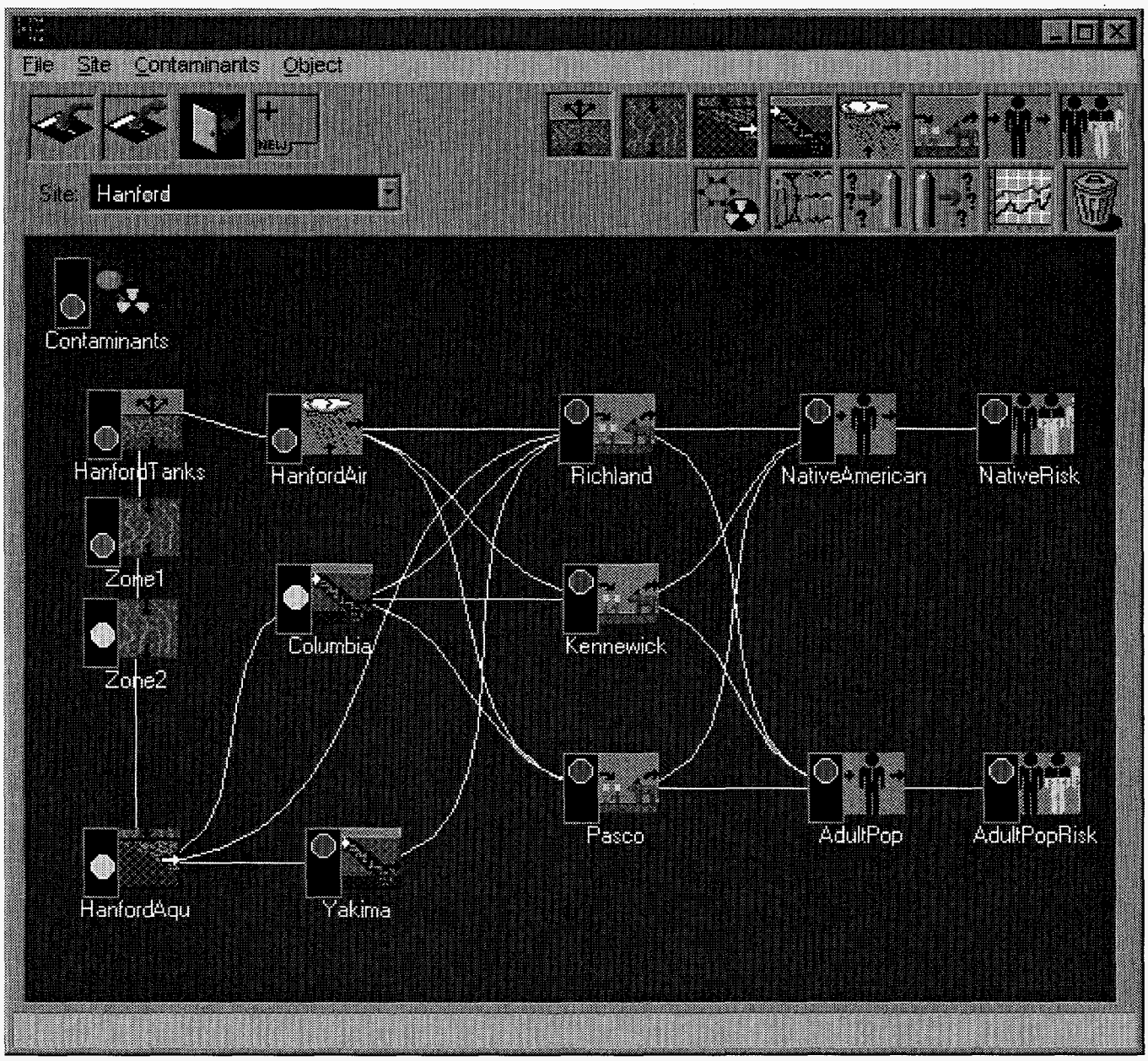

Figure 1. Diagram of an example model run using the interface for MEPAS.

Biotechnology

Biodegradation of Explosives by Combining Enzymatic and Microbial Processes

Rodney S. Skeen (Bioprocessing)
James A. Campbell (Process Technologies)

Project Description

More than 25 explosive contaminated sites of the DoD and DOE need to be remediated and ongoing military operations lead to the production of explosive contaminated waste streams on a continuous basis. However, there is currently no cost-effective technology to degrade explosives in soil and water. Bioremediation has a potential to remediate these sites, however, current microbial processes are limited by technical problems such as the toxicity of explosives to microorganisms, slow transformation rates, and incomplete mineralization. The incomplete mineralization has been attributed to formation of polymeric products of TNT. The goal of this project is to overcome these limitations by enhancing microbial processes using redox enzymes to pretreat explosives before microbial degradation. A simplified reaction scheme for the proposed process is shown below:

Step 1 - Enzymatic:

Redox Enzymes
Explosives + Reductant ----------> Reduced Explosives + Oxidized Reductant

Step 2- Microbial:

Aerobic Microbial Processes
Reduced Explosives ----------> $CO_2 + H_2O + NO_2^-$

or

Anaerobic Microbial Processes
Reduced Explosives----------> $CH_4 + CO_2 + H_2O + NH_4^+ + N_2$

To achieve this goal, proof-of-concept tests were conducted to identify the transformation products of trinitrotoluene (TNT) after enzymatic treatment and identify degradation products after aerobic or anaerobic biotreatment of the transformation products.

Technical Accomplishments

Transformation of explosives by ferredoxin reductase from spinach was tested. It was found that ferredoxin NADP reductase enzyme (FNR) from spinach could reduce 2,4,6-trinitrotoluene using NADPH as reductant. It was also found that NADPH could be recycled using an inexpensive reductant such as ethanol coupled with ethanol dehydrogenase. Results suggest that treatment time for 1 L of waste stream containing 440 μM (100 ppm) of TNT could be as low as 4 seconds for an enzymatic reactor containing 1 g of FNR. This is a significant improvement over traditional microbial processes which would require days, weeks, or months to degrade a similar amount of waste.

Separation and identification methods were also developed for the metabolites from enzymatic transformation of TNT. A membrane separation technology was employed to separate the enzyme from the reaction mixture. Particle beam liquid chromatography (LC)/mass spectrometry (MS) was used to identify degradation products. Particle beam LC/MS is a technique that yields classical, library searchable electron impact spectra for compounds that are too thermally labile or nonvolatile to be analyzed by gas chromatography/mass spectrometry.

Particle beam LC/MS was performed using an HP 5988A mass spectrometer. Particle beam spectra showed ions at m/z 60, 90, 122, 135, 152, and 164. Ions at m/z 90 were also evident in the sample of the blank which included enzyme, NADPH, buffer, and no TNT. The possible identification of the ion at m/z 152 may be 2-amino-6-nitrotoluene. Another possible identification of the degradation product at m/z 164 may be 2-amino-4-nitrobenzoic acid (MW 182). The ions were also evident in the direct insertion probe/high resolution mass spectrometry studies of concentrated samples.

In the mass spectra, there was a lack of intensity for m/z 77 which is indicative of aromatic degradation products. This may indicate the possibility of ring-opening reactions. In addition, preliminary results on ion chromatography analysis indicate the removal of one or more nitrite groups from TNT.

Classification of Microorganisms by Rapid, Efficient Sampling and Mass Spectrometric Detection

Karen L. Wahl (Materials and Chemical Sciences)

Project Description

The objective of this project was to develop and improve sample preparation and sampling techniques for the rapid analysis of microorganisms such as bacteria using matrix-assisted laser desorption/ionization mass spectrometry (MALDI-MS) for detection.

Technical Accomplishments

Rapid detection and classification of microorganisms is important for public health, food processing, biotechnology, biological warfare, and other areas. Most analytical methods developed for detection required significant sample handling and preparation time, or exhibited indirect evidence of the presence of specific microorganisms. Recent advances in analytical instrumentation, such as MALDI-MS, have made it possible to rapidly and efficiently analyze biological components such as proteins, peptides, oligonucleotides, and phospholipids intact. MALDI-MS was chosen for detection of the microorganisms for this project due to its rapid analysis time (less than 10 minutes), minimal sample requirement (microliters), and for providing molecular weight information of biological components.

Thirteen bacterial samples were obtained from both gram-positive and gram-negative bacterial strains for analysis and comparison. Separation of the whole bacterial cells from the soy broth growing media was required prior to mass spectral analysis using simple washing techniques. Unique ions from bacterial cell components were obtained by MALDI-MS analysis directly from the whole cell samples without further sample preparation. Representative positive ion MALDI spectra of two bacterial samples are shown in Figure 1. Distinct ions are observed for different types of bacteria providing fingerprints for unknown comparison. A preliminary blind unknown test of sample preparation and MALDI analysis of the 13 samples showed promising results based on comparison with the known MALDI spectra. These results show the potential of this rapid analytical technique for screening for the presence of microorganisms such as bacteria.

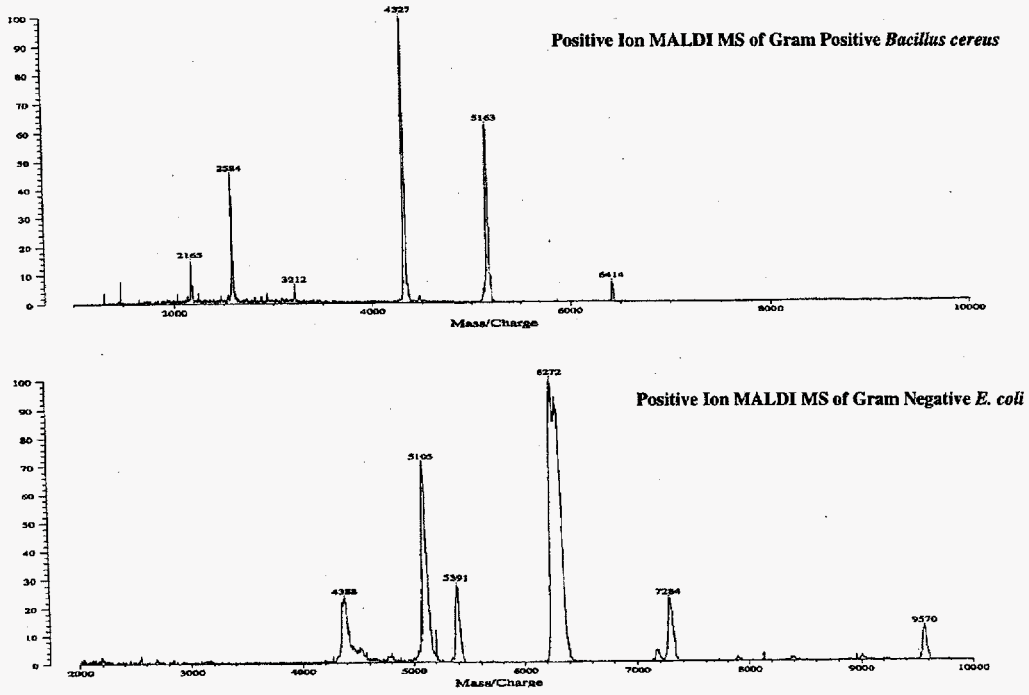

Figure 1. MALDI mass spectrometry of whole cell bacteria.

Development of Enzymatic Bioprocesses Based on Redox Enzymes

Michael Huesemann, Manish Shah (Bioprocessing)
Rick Ornstein, Karole Miaskiewics, Ya-Jun Zheng (Theory, Modeling, and Simulation)

Project Description

The goal of this research was to develop an enzymatic process for the production of high value nitroaromatic intermediates such as 4-aminophenol, 4-aminobenzoic acid, 2-aminophenol, and others. Proof-of-principle experiments were conducted to evaluate the technical and economic feasibility of the proposed enzymatic process.

The objectives were achieved by following a three-step approach:

1. Potential redox enzymes from bacteria, fungi, plants, and algae were screened for their ability to reduce nitrobenzene, nitrophenols, and nitrobenzoic acid.

2. The selected enzymes were evaluated in terms of their stability, substrate specificity, and activity.

3. Enzyme functions were improved using computer simulation tools.

Technical Accomplishments

A series of enzymes were screened for their ability to reduce nitroaromatic compounds. Among all screened enzymes, it was found that ferredoxin-NADPH-reductase (FNR) showed the highest activity. Subsequent experiments with FNR indicated that the enzyme is only active under unaerobic conditions; a complex co-factor recycling system involving ferredoxin, NADPH, alcohol dehydrogenase, and alcohol is necessary to provide reducing power to drive the enzymatic reaction (see Figure 1 below); and nitrobenzene and trinitrotoluene (TNT) are enzymatically converted by FNR while the conversion of nitrophenol and nitrobenzoic acid could not be conclusively determined due to analytical interferences. Attempts to identify the exact nature of the enzymatic conversion products (i.e., phenylhydroxylamine and 4-amino-phenol [see the figure]) were also inconclusive due to analytical problems.

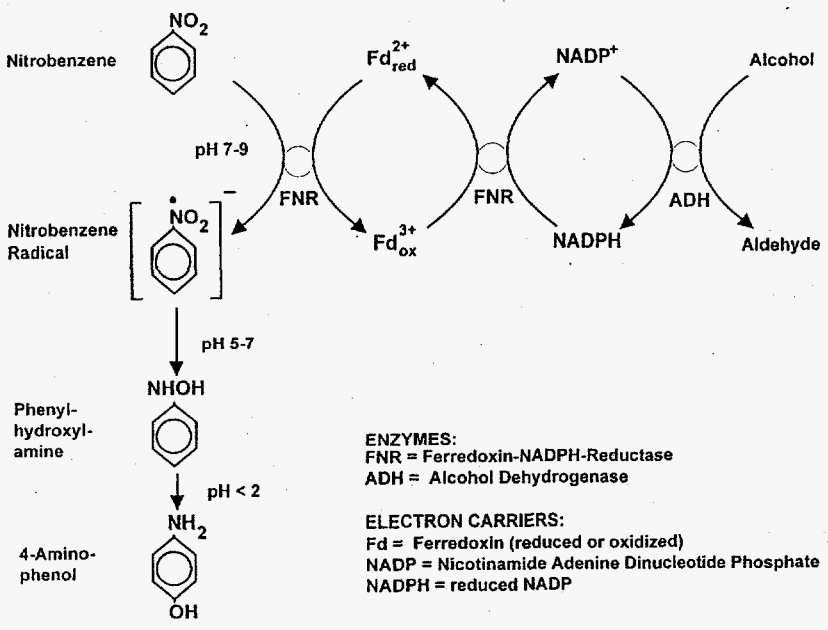

Figure 1. Proposed enzymatic reaction mechanism for the reduction of nitrobenzene to 4-amino-phenol by ferredoxin-NADPH-reductase.

Dynamics, Modeling and Redesign of Microbial Proteins

Rick L. Ornstein (Theory, Modeling, and Simulation)

Project Description

The objective of this project is to compare the underlying structure-function-dynamics relationships of bacterial proteins/enzymes under biologically moderate physiological conditions and under extreme conditions, such as in aqueous versus nonaqueous solvents. Nonaqueous enzymology is of great importance both from the mechanistic point of view and from the practical application point of view. Developing enzymes that are functional in highly concentrated halocarbon solutions, such as carbon tetrachloride, may prove useful in the development of new strategies for environmental remediation and monitoring of pollutant plumes, as well in developing "green" processes. Doing so will require gaining an understanding of the underlying structural and dynamic effects to enzymes induced by such solvents. State-of-the-art computational molecular dynamics simulations, starting with an experimental aqueous three-dimensional protein structure, allows one to directly compare structure-function-dynamics relationships of a protein in solvents for which experimental structural data is not available.

Technical Accomplishments

Recent studies by Klibanov and co-workers have demonstrated that subtilisin (and other enzymes) maintains considerable activity in certain nonaqueous solvents. Klibanov, Ringe, and co-workers have recently determined the x-ray crystal structure of subtilisin in water and in water with acetonitrile. In FY 1996, we completed the analysis and reporting of molecular dynamics simulations on this bacterial enzyme in four different solvent systems: water, water plus acetonitrile, water plus carbon tetrachloride, and water plus dimethyl sulfoxide (DMSO). We also completed a detailed quantum mechanical assessment of the effects of different solvents on protein salt-bridge formation and began some additional related studies.

Last year's report focused on the technical results for the simulation in carbon tetrachloride. This year's report focuses on the technical results for the DMSO simulation and briefly compares it to the simulations in the other solvents. DMSO is a dipolar, aprotic solvent with a dielectric constant of 46.45. DMSO has been widelyz used as an alternative solvent to water, due to the high solubility of peptides and proteins in it. It can compete with protein hydrogen bond acceptors for hydrogen bond donors. For the simulation in DMSO, the protein, together with crystal waters, was immersed in a box containing 1822 DMSO molecules.

The molecular dynamics simulation was carried out for 745 ps using the AMBER 4.0 program and force field. Although the overall structure of subtilisin is stable throughout the simulation, some structural perturbations are observed. The five N-terminal residues of the protein migrates away from the rest of the protein; whether this movement is the start of partial unfolding in DMSO is unclear. The simulation has also shown that DMSO is capable of stripping away waters from the protein surface and this ability seems to be related to the hydrophilicity of the solvent. We saw more waters that left the protein surface in DMSO than in acetonitrile, while in a hydrophobic solvent such as CCl_4, no water left the protein surface during the simulation. This is in agreement with experimental observation.

There are three metal ions in the system. During the molecular dynamics simulation, one of the metal ions got sequestered by solvent and started to move into solution and another one has one DMSO coordinated to it. The ability of polar solvent to sequester metal ions seems to be supported by the observation that when a subtilisin crystal grown from aqueous solution was washed using acetonitrile, two metal ions were lost. The formation of a metal ion-solvent complex is very interesting, which provides a plausible explanation to previous reports that salts (or counter ions) could have profound effects on protein stability and activity in organic solvents. The presence of these salt ions will prevent direct contacts between organic solvents and protein by either retaining more water molecules during lyophilization or by coordinating to solvent molecules to form complexes.

The calculated total number of intra-protein hydrogen bonds behaves differently in DMSO compared with that in water. The behavior in DMSO is similar to that in other organic solvents. It seems to be a general trend that there are more intra-protein hydrogen bonds in a protein in nonaqueous solution compared to in aqueous solution. The increase in total number of intra-protein hydrogen bonds is likely to be partially responsible for the increased thermostability of proteins in nonaqueous solutions.

Quantum mechanics calculations were performed to examine the strength of hydrogen bonding interactions

between DMSO and a protein amide hydrogen and between DMSO and water. Quantum mechanics calculations predict that the hydrogen bonding between DMSO and water is stronger than that between two water molecules, which is in agreement with experiment. The calculations also indicate that hydrogen bonding between DMSO and an amide hydrogen is stronger than between a carbonyl oxygen and an amide hydrogen. Taken together, our studies provide a good explanation as to why DMSO is a protein-dissolving solvent and is capable of causing partial unfolding or denaturation of proteins.

From our simulation, we have also identified 18 DMSO binding sites (Table 1). Most of the "localized" DMSO molecules are hydrogen-bonded to an amide hydrogen of an amino acid residue. One of these 18 DMSO molecules is coordinated to a metal ion; the rest of these DMSO molecules do not appear to form any specific interactions. These predicted DMSO binding sites could be examined by x-ray crystallography or nuclear magnetic resonance techniques. Previously, it has been suggested that organic solvents may be used to map an interaction surface and to identify possible lead compounds for drug design. This idea has been confirmed by a recent success in designing a new elastase inhibitor. Molecular dynamics simulations could also play an important role here, especially when obtaining experimental molecular structures is difficult.

Table 1. Environments of 18 "Localized" DMSO Molecules

No.	RMS Fluctuation of Amino Acid Environment O of DMSO (Å)	
1	1.219	H-bonded to Arg 186
2	1.274	H-bonded to amide hydrogen of Phe 261
3	1.464	H-bonded to amide hydrogen of Ser 130
4	1.480	H-bonded to amide hydrogen of Gly 23
5	1.511	Asn 158
6	1.516	Coordinated to Ca2+ ion
7	1.559	Asn 62, Gly 61, Ser 98, Ser 99
8	1.586	H-bonded to Phe 189
9	1.607	H-bonded to HN of Ala 243
10	1.609	H-bonded to HN of Asn 240
11	1.709	H-bonded to HN of Gly 154
12	1.764	Arg 145, Gly 146, Val 147, and Thr 115
13	1.807	H-bonded to HN of Asp 155
14	1.824	Ala 194, Lys 265, Phe 261
15	1.849	H-bonded to HN of Ala 134
16	1.909	Thr 208, Tyr 209, His 39, Asn 212
17	1.915	H-bonded to HN of Tyr 6 most of the time
18	1.995	H-bonded to HN2 of Asn 62

Publications and Presentations

Y.-J. Zheng and R.L. Ornstein. 1996. "Molecular dynamics of subtilisin Carlsberg in aqueous and nonaqueous solutions." *Biopolymers* 38, 791-799.

Y.-J. Zheng and R.L. Ornstein. 1996. "A molecular dynamics study of the effect of carbon tetrachloride on enzyme structure and dynamics: subtilisin." *Prot. Eng.* 9 485-492.

Y.-J. Zheng and R.L. Ornstein. 1996. "A molecular dynamics and quantum mechanics analysis of the effect of DMSO on enzyme structure and dynamics: subtilisin." *J. Am. Chem. Soc.* 118, 4175-4180.

R.L. Ornstein and Y.-J. Zheng. "Impact of carbon tetrachloride and other solvents on enzyme intramolecular hydrogen bonding: subtilisin." In *Biomacromolecules: From 3-D Structure to Applications,* R.L. Ornstein, Ed., Battelle Press, Columbus, Ohio (in press).

Y.-J. Zheng and R.L. Ornstein. 1996. "A theoretical study of the structure of flavin in different oxidation and protonation states." *J. Am. Chem. Soc.* 118, 9402-9408.

Y.-J. Zheng and R.L. Ornstein. 1996. "An explanation of the single-turnover experiment of 4-chlorobenzoyl CoA dehalogenase." *Prot. Eng.* 9, 721-723.

Y.-J. Zheng and R.L. Ornstein. "What happens to salt-bridges in nonaqueous environments: Insights from quantum mechanics calculations." *J. Am. Chem. Soc.* 18 (in press).

R.L. Ornstein. 1995. "The effect of solvent on protein structure and dynamics in nonaqueous environments." 34th Hanford Symposium on Health and the Environment: Biomacromolecules: From 3-D Structure to Applications, Pasco, Washington, October 26.

R.L. Ornstein. 1996. "Protein salt-bridges in nonaqueous environments: Insights from quantum mechanics calculations." 51st Northwest Regional Meeting of the American Chemical Society, Corvallis, Oregon, June 19-22.

R.L. Ornstein. 1996. "The role of "weak" hydrogen bonds in proteins." Gordon Conference: Biocatalysis, Kimball Union Academy, New Hampshire, July 7-12.

Enzymology of Bacterial Metal Reductase and Dehalogenase

Yuri A. Gorby, Luying Xun (Environmental Microbiology)

Project Description

The objective of this project was to purify and characterize the enzyme responsible for reduction of multivalent metals in the dissimilatory metal reducing bacterium *Shewanella alga*, strain BrY. This enzyme catalyzes the reduction of metals such as iron, manganese, cobalt, uranium, and chromium. This activity is important for directing the fate and transport of these multivalent radionuclides and heavy metals in natural and contaminated surface and groundwater. Understanding the mechanisms by which this important enzyme functions is vital for predicting the fate of these metals in the environment and for exploiting metal reducing bacteria in engineered bioreactor systems designed to remove heavy metals and radionuclides from aqueous waste streams.

Technical Accomplishments

In FY 1995, a protein complex that expressed metal reductase activity was purified from strain BrY. The complex contained a hydrogenase, menaquinone, and a c-type cytochrome. Circumstantial evidence suggested that the 37 kDa cytochrome c serves as the terminal reductase. This cytochrome was analyzed by a variety of techniques as part of the active protein complex.

Oxidized and reduced absorption spectra of the c-type cytochrome in BrY were similar to c-type cytochromes found in a wide variety of microorganisms that are unable to reduce metals (Figure 1). However the midpoint potential of this cytochrome (-205 mV) was much lower than other c-type hemes (Figure 1 inset).

With this midpoint potential, it is thermodynamically impossible for BrY to reduce any multivalent electron acceptor with a midpoint potential below about -200 mV. We previously determined that BrY can reduce a wide range of metals with midpoint potentials above, but not below, -200 mV.

We further investigated the cytochrome c by electron paramagnetic resonance spectroscopy to gain a better understanding of the structure of this enzyme (data not shown for brevity). Differences in the relative

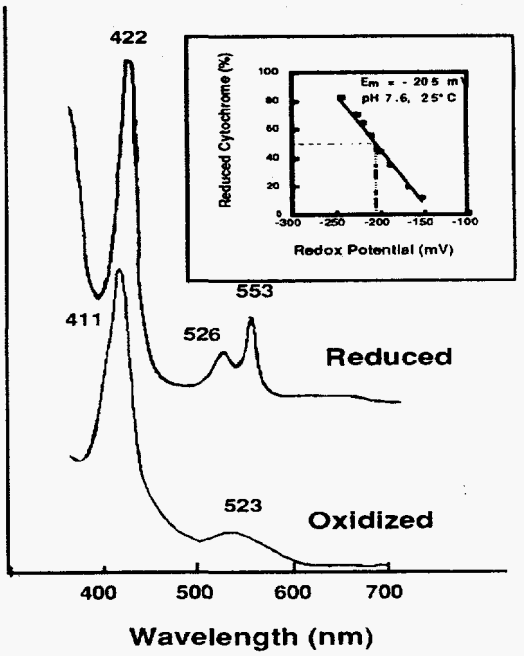

Figure 1. Visible absorption spectra of oxidized and reduced cytochrome c from BrY. Inset indicates the midpoint potential of this cytochrome c.

intensities of the resonance peaks indicate that many components of the protein complex contributed to the electron paramagnetic resonance signal.

To determine which peaks represent the c-type heme, electron paramagnetic resonance spectra were generated at redox conditions that spanned from above the midpoint potential to below the midpoint potential of the cytochrome. The results demonstrated that this cytochrome is similar to the imidazole complex of heme octapeptide in mammalian cytochrome c. However, further analyses and characterization was problematic in the presence of other components within the protein complex. Research in FY 1996 was therefore focused on isolating the 37 kDa cytochrome from other cellular components.

We first determined that the 37 kDa c-type cytochrome was associated with the cellular membrane (Figure 2).

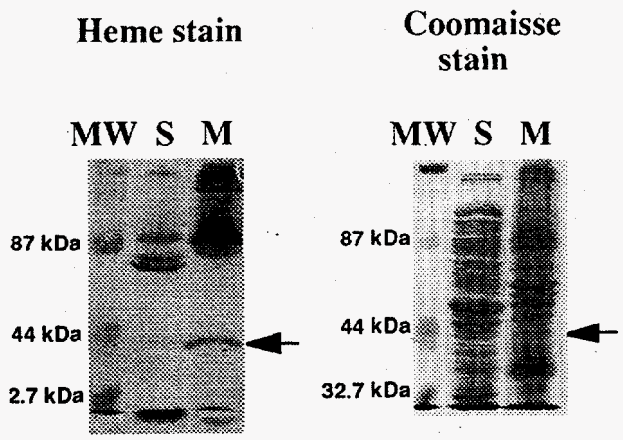

Figure 2. Coomaisse stained and heme-specific stained SDS-polyacrylamide gels of the soluble and membrane separated fractions from *Shewanella alga*. The arrows indicate the 37.5 kDa c-type cytochrome. MW=Kaleidoscope molecular weight markers. S=Soluble fraction. M=Membrane fraction.

We then developed a purification scheme that yielded sufficient quantities of the 37 kDa protein (Figure 3) for amino acid sequence determination.

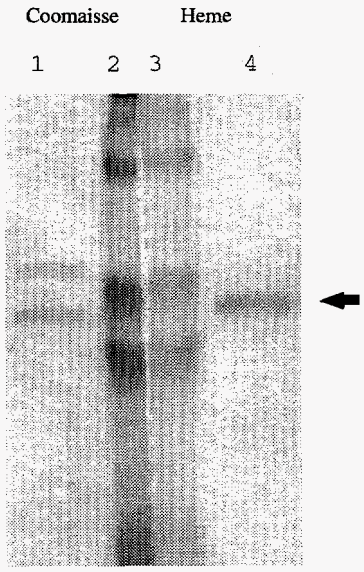

Figure 3. SDS-PAGE of protein sample following anion exchange chromatography. Lanes 1 and 2 were coomaisse stained, Lanes 3 and 4 were heme stained. Lanes 2 and 3 are Kaleidoscope molecular weight markers (Biorad). The arrow indicates the 37.5 kDa c-type cytochrome.

Results obtained from research conducted in FY 1995 was important for determining which cellular component was involved in the reduction of multivalent metals by bacteria. Determining the midpoint potential of the active redox center of the heme defines not only the limit of metals that can be reduced, but also provides a sensitive tool for selectively controlling the valence of the iron center. Results obtained in FY 1996 are important for obtaining the reductase protein in quantities needed for determining the amino acid sequence that will be used to develop a probe for identifying the genes that encode for the metal reductase enzyme. Through increasing our understanding of the genetic and molecular processes involved in enzymatic reduction of metal comes the ability to exploit this activity to its fullest potential as a remediation tool.

Publication

F. Caccavo, Jr., Y.A. Gorby, and M.J. McKinerney. "Purification of the metal reductase complex in the dissimilatory metal-reducing bacterium Shewanella alga, strain BrY." *Applied Environmental Microbiology* (submitted).

Fourier Transform EPR Studies of Radiation-Induced Structural Alteration of DNA

Michael K. Bowman (Macromolecular Structure and Dynamics)

Project Description

This project involves understanding the altered forms of DNA and the enzymes that deal with damaged DNA. The focus is on nucleotide excision repair and the enzymes involved in this type of repair of damaged DNA.

Damage to DNA can lead to permanent changes in the genome. Cells, however, have a very efficient mechanism for the recognition and repair of damage to DNA. This highly evolved mechanism for the repair of DNA is sometimes defeated by damage. We seek to understand the way that damage is recognized by the xeroderma pigmentosum A complementing (XPAC) and replication protein A proteins and the ways in which damage may escape recognition. We are particularly interested in the nucleotide excision repair process in the context of DNA in chromatin because the DNA in human cells is packaged around histone proteins to form chromatin.

DNA is constantly associated with either structural or functional proteins. The proteins not only process the DNA, they also package it into a compact form that fits inside the cell. This packaged DNA and its associated proteins are immense and many of the conventional methods for determining macromolecular structure such as nuclear magnetic resonance and x-ray diffraction are of limited utility. We are developing methods to investigate these large structures through the application of Fourier transform electron paramagnetic resonance.

Technical Accomplishments

We are currently focusing on chromatin structure and its influence on nucleotide excision repair. We have explored the utility of using spin labels attached to the histones as a way of probing both the dynamics and the structure of chromatin. Figure 1 shows electron paramagnetic resonance spectra of histone H3 with an attached iodoacetamide spin label. The three lines arise from hyperfine splittings from the nitrogen in the spin label. Differences in the intensities and the widths of these three lines indicate the mobility and the anisotropy of the mobility of the spin label. This spectrum shows a slightly motionally hindered spin label and a strongly immobilized spin label in solution.

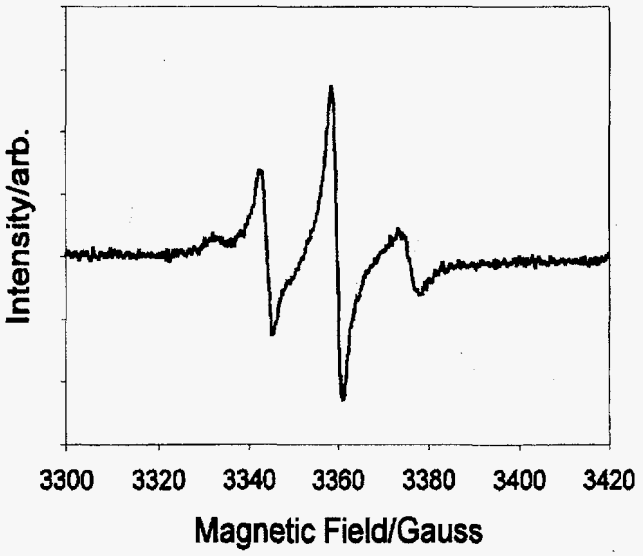

Figure 1. The EPR spectrum of a solution of histone H3 spin labeled with an iodoacetamide spin label at the unique cysteineresidue. The distinct shoulder at the left-hand side of the spectrum is indicative of a highly immobilized fraction due to the well-known tendency of the histone to aggregate.

The immobilization is caused by the formation of aggregates of H3 and was verified by small angle neutron scattering measurements made by Dr. Trewhella of LANL. When the sample is heated or when denaturing agents such as urea are added, the protein structure of H3 is destroyed and the spin label becomes more mobile.

That increased mobility produces sharper lines in the electron paramagnetic resonance spectrum and a decrease in the spin relaxation rates for the electron spin. If the line shape of the spectrum is tracked as a function of the sample temperature, the temperature response of the histone structure is revealed. This histone is quite stable and retains its structure until quite high temperatures near the boiling point of water as shown in Figure 2. Similar spectra have been obtained for spin labels attached to a recombinant histone H3 expressed in bacterial cells. This makes it possible to carry out site-directed spin labeling of H3 as well as larger complexes incorporating H3.

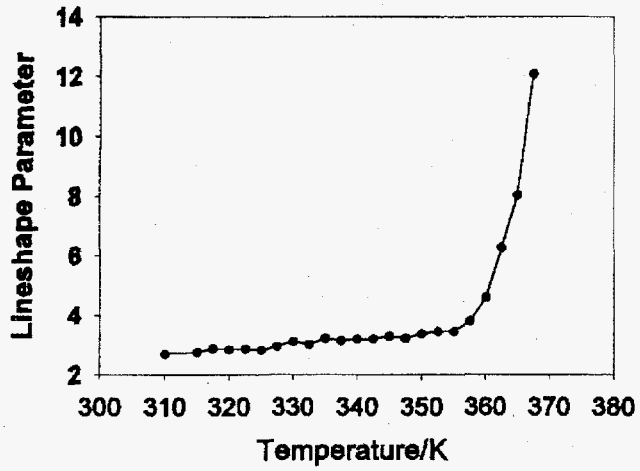

Figure 2. A line shape parameter in arbitrary units from the EPR spectrum of spin labeled histone H3. The parameter and the spin label mobility increase slowly with temperature from 310K or 37°C to nearly 85°C. At that point, the mobility of the spin lavel sharply increases. This behavior is indicative of a stable protein structure up to a temperature of about 85°C, followed by rapid loss of structure.

To this end, other researchers at PNNL have reconstituted nucleosomes, the basic unit of chromatin, using spin-labeled histone H3 with DNA from the Xenopus 2S ribosmal gene. These reconstituted nucleosomes are stable and in sufficient yields to make possible a study of nucleosome structure and dynamics and to probe complexes with XPAC and replication protein A by electron paramagnetic resonance. This will be carried out as follow-on work under the recently funded project on nucleotide excision repair.

Functional Characterization of Bacterial Plasmids

James K. Fredrickson, Margaret F. Romine (Environmental Microbiology)

Project Description

The objective of this project was to study biodegradative activity in several species of *Sphingomonas* that had been isolated from the deep subsurface. Several years ago, we demonstrated that a subsurface isolate, designated F199, possessed the unusual capability to degrade a wide variety of both single and multiple ring aromatic compounds and that it contained two large plasmids. Because genes encoding biodegradative functions are often found on plasmids, we postulated that the F199 biodegradative genes might be found on one or both of the plasmids resident in this strain. Research performed over the last 3 years has demonstrated that many of the biodegradative genes are encoded on the smaller of these two plasmids, designated pNL1, and that there is sequence homology between the pNL1-encoded biodegradative genes with sequences on plasmids in four other subsurface *Sphingomonas* strains and with the chromosome in *Sphingomonas yanoikuyae* B1 and *Sphingomonas paucimobilis* Q1, both isolated from river samples by other investigators.

Technical Accomplishments

This ability to degrade such a large variety of aromatics appears to be unique to the genus *Sphingomonas*. Results from FY 1994 and FY 1995 demonstrated that in addition to strain F199, there are at least four additional *Sphingomonas* sp. in the subsurface culture collection that are capable of degrading single and multiple ring aromatics and that also contain multiple large plasmids. The phylogenetic identification of these five subsurface isolates as *Sphingomonas* sp. and a description of their biodegradative capability was published in 1995 (Fredrickson et al.). During this fiscal year, in collaboration with Dr. David Balkwill at Florida State University, we completed an extensive taxonomic study of this group of bacteria, naming three new bacterial species (Balkwill et al., in press). Strains F199, B0522, and B0695 were classified as *S. aromaticivorans*, strain B0478 as *S. subterrae*, and strain B0712 as *S. stygialis*.

The localization of the biodegradative functions to pNL1 was first demonstrated by noting that subclones of pNL1 gave *Escherichia coli* the ability to degrade catechol, a common intermediate in the degradation of aromatic compounds. This activity was found in two regions of the plasmid (Stillwell et al. 1995). The substrate specificity of these catechol dioxygenases suggested that one of the enzymes has greater specificity for multiple ring intermediates from the naphthalene and biphenyl pathways and the other for the single ring aromatic catechol. Both enzymes would be required for degradation of multiple ring aromatics. The possibility these enzymes are also used for degradation of single ring aromatics is suggested by results from the microbial genomics effort and by Dr. Gerben Zylstra on a similar system in *S. yanoikuyae* B1.

Work in collaboration with Dr. Zylstra at Rutgers University demonstrated that there is considerable DNA homology among the chromosome-encoded *m*-xylene/ biphenyl degradative genes from *S. yanoikuyae* B1 and *S. paucimobilis* Q1 and plasmid-encoded genes from strain F199 and the four other *Sphingomonas* subsurface isolates. Two of the plasmids in strain B0695 possessed homologous sequences, suggesting a possible gene duplication between the plasmids. Comparison of the sequences from the ring cleavage dioxygenases in F199, B1, and Q1 to other dioxygenases indicate that these enzymes fall into a unique group that includes one additional sequence from another *Sphingomonas* strain HV3.

Transposon-mediated mutagenesis of strains F199 and B1 has proven to be very difficult due to the poor frequency of transposon insertion. We have isolated approximately 400 mutants and determined that one of these contains a transposon insertion on the plasmid. The insertion resulted in knocking out the ability to degrade the multiple ring aromatics, dibenzothiophene, fluorene, and naphthalene past the ring cleavage step. Its inability to convert indole to indigo suggests that the mutation affects the first enzyme in the pathway, a ring dioxygenase. The finding that degradation of all of the compounds was inactivated by a single mutation suggests that a single pathway is responsible for degradation of all these compounds, a portion of the pathway is shared for degradation, and/or that the genes are encoded on a single operon. Using this mutation as a selective marker, we were able to transfer the plasmid into another *Sphingomonas* host, demonstrating that pNL1 is a self-conjugative plasmid.

Proteins that regulate expression of benzoate genes are known to effect expression of toluene degradative pathways in hosts that possess both pathways. In some

such strains, repeated transfer through benzoate results in loss of the toluene degradative genes. We tried the repeated passage in media with benzoate as the sole carbon source in hopes of losing the plasmid which encodes the toluene degradative enzymes. We instead generated variants that very rapidly mediate ring cleavage of catechol, fluorene, dibenzothiophene, and biphenyl and convert indole to indigo. The fact that not all the colonies appearing on agar plates after growth on benzoate appear deep blue after exposure to indole suggests that the effect is not merely due to induction of the appropriate biodegradative enzymes. Growth of the variants in benzoate or lactate containing media results in a low rate of reversion to the wild type phenotype.

In summary, we have demonstrated that several aromatic biodegradative functions reside on a 180 kb plasmid, designated pNL1, from *S. aromaticivorans* F199 including those responsible for degradation of toluene, xylene, dibenzothiophene, fluorene, and biphenyl. Based on DNA homology studies, we found that similar genes are on megaplasmids in four subsurface *Sphingomonas* strains as well as on the chromosome of *Sphingomonas* strains B1 and Q1. These genes are part of a previously undescribed pathway for degradation of aromatics that is only distantly related to other similar functioning pathways and appears to be unique to the *Sphingomonas* genus. The localization of these genes on the chromosome in the surface isolates versus on the plasmid in the subsurface isolates, which are postulated to have been isolated from surface environmental conditions for hundreds and possibly thousands of years, poses interesting questions about the evolution of these pathways, the significance of their frequency in this genus, and about the selective pressures in the subsurface for maintenance of these genes in an environment not contaminated with these aromatic compounds.

References

J.K. Fredrickson, D.L. Balkwill, G.R. Drake, M.F. Romine, D.B. Ringelberg, and D.C. White. 1995. "Aromatic-degrading *Sphingomonas* isolates from the deep subsurface." *Appl. and Environ. Microbiol.* 61:1917-1922.

L.C. Stillwell, S.J. Thurston, R.P. Schneider, M.F. Romine, J.K. Fredrickson, and J.D. Saffer. 1995. "Physical mapping and characterization of a catabolic plasmid from the deep-subsurface bacterium *Sphingomonas* sp. strain F199." *J. Bacteriol.* 7:4537-4539.

Publications and Presentations

M.F. Romine, L.C. Stillwell, C.M. Spadoni, J.K. Fredrickson, and J.D. Saffer. "Functional and sequence analysis of a 9 kb region from a *Sphingomonas* megaplasmid." (in preparation).

D.L. Balkwill, G.R. Drake, R.H. Reeves, J.K. Fredrickson, D.C. White, D.B. Ringelberg, D.P. Chandler, M.F. Romine, D.W. Kennedy, and C.M. Spadoni. "Taxonomic study of aromatic-degrading bacteria from deep terrestrial subsurface sediments and description of *Sphingomonas aromaticivorans* Sp. Nov., *Sphingomonas subterrae*, Sp. Nov., and *Sphingomonas stygialis* Sp. Nov." *Internatl. J. Syst. Bacteriol.* (in press).

E. Kim, P.J. Aversano, M.F. Romine, R.P. Schneider, and G.J. Zylstra. 1996. "Homology between genes for aromatic hydrocarbon degradation in surface and deep-subsurface *Sphingomonas* strains." *Appl. and Environ. Microbiol.* 62:1467-1470.

M. Romine, J. Fredrickson, L. Stillwell, K-K. Wong, and J. Saffer. 1996. "Characterization of a 180 kb catabolic plasmid in subsurface isolate *Sphingomonas* sp. strain F199." American Society for Microbiology Meeting, New Orleans, Louisiana, May 20-23.

Identification, Purification and Characterization of the Reductive Dehalogenase of Desulfomonile tiedjei DCB-1

Luying Xun (Environmental Microbiology and Washington State University)
Shuisong Ni (Environmental Microbiology)

Project Description

Reductive dehalogenation is one of the promising anaerobic bioremediation techniques in the removal of halogenated compounds from the environment. The key enzyme involved in this process is the reductive dehalogenase. *Desulfomonile tiedjei* is the best characterized anaerobic bacterium in pure culture capable of reductive dehalogenation of halogenated aromatic compounds. The dehalogenase system in this organism is believed to be linked to its energy metabolism.

The overall objectives of this project are to identify, purify, and characterize the reductive dehalogenase system of *Desulfomonile tiedjei* DCB-1 and to clone and sequence the corresponding genes. The knowledge gained from this study will enable us to develop a model system for reductive dehalogenation by anaerobic microorganisms and will facilitate designing effective bioremediation methods for halocarbon removal.

Technical Accomplishments

We have purified the dehalogenase by a combination of several column chromatographic techniques from the solubilized membrane fraction. The enzyme consisted of two subunits with a molecular weight of about 64,000 and 37,000. The N-terminal amino acid sequence of the small subunit was used to design degenerate nucleotide primers for polymerase chain reaction. The polymerase chain reaction products were cloned into a TA vector for DNA sequencing. One of those clones showed DNA sequences that completely matched those of the N-terminal region of the 37,000 daltons. Based on its DNA sequences, a 30-bp end-labeled nucleotide (nonradioactive label) was synthesized to screen the genomic libraries.

Two genomic libraries were constructed by using standard procedures. For a partial library, a 2-kb Hind III fragment was ligated with Hind III-digested pBluescript DNA. The ligated DNA was used to transformed DH5a competent cells. For a complete genomic library, pLAFR3 cosmid vector was used. To prepare the DNA inserts for cosmid library, total DCB-1 DNA was partially digested by BamH I and large (above 20 kb) DNA fragments were purified by a linear sucrose gradient (10% to 40%). Construction of both libraries was successful.

Several clones have been identified through either colony hybridization or Southern blotting, but so far a positive clone has not been identified by sequence analysis that contains the exact match with the N-terminal sequence of the small subunit. One possibility is that the probe is not specific. Another hurdle is the use of chemiluminescent probes instead of radioactive probes since our lab is not set up for this kind of radioactive work. If the probe is not specific, it will be hard to proceed any further. If the chemiluminescent probe is the problem, cloning the gene is still possible.

In addition to cloning the dehalogenase genes, we also attempted to study other components of the electron transport chain involved in reductive dehalogenation by DCB-1. Through collaboration with Dr. Mohn at University of British Columbia, Vancouver, Canada, we successfully purified a c-type cytochrome. This heme protein was only induced under dehalogenating conditions, but its exact function is still unknown. It might serve as an electron carrier for the reductive dehalogenation.

In summary, we have successfully purified the first reductive dehalogenase linked with energy metabolism. Our work demonstrates that the reductive dehalogenase can be reduced by artificial electron donors and then it can transfer the electrons and dehalogenate. In addition, we also purified a c-type cytochrome that is likely involved in transferring electrons from carbon metabolites to the dehalogenase. Our effort in the cloning of the corresponding genes has not succeeded, yet.

Publication and Presentation

T.-M. Louie, S. Ni, L. Xun, and W.W. Mohn. 1996. "Purification and partial characterization of two type c cytochromes potentially involved in reductive dechlorination by *Desulfomonile tiedjei*." *In Abstracts* of the 96th General Meeting of the American Society for Microbiology, Washington, D.C.

Microbial Genomics

Jeffrey D. Saffer (Molecular Biosciences)

Project Description

The use of microbes in biotechnology is rapidly increasing. These diverse organisms represent the majority of organisms in the world and provide a limitless resource of genetic coding information. To exploit microorganisms fully, considerable information about their function and genetic coding capacity needs to be learned. This project uses genomic studies to provide a genetic basis for bioremediation and other biotechnological applications.

Research has focused on the subsurface *Sphingomonas* species F199, which has capability for aromatic hydrocarbon degradation. The majority of the genes responsible for this activity have been identified using genomic approaches and have been found to be localized on a 180-kilobase pair (Kb) megaplasmid. The complete DNA sequence of this megaplasmid is being determined and has revealed important information regarding the nature of the genes responsible for aromatic degradation.

Technical Accomplishments

Most enzymatic activities of use in bioremediation are plasmid-borne. In addition, biodegradative genes on plasmids are usually organized into polycistronic units; this organization facilitates identification of other genes in the pathway of interest. Therefore, these studies focus on plasmids within bacteria of interest. Through physical mapping and sequencing, progress can be made in fundamental areas such as plasmid genetics, gene organization, element mobilization, and plasmid transfer.

PNNL scientists have isolated a *Pseudomonas*-like bacterium from the deep (400 m) subsurface [*Appl Env Microbiol* 57:796, 1991]. This bacterium, F199, is uniquely able to biodegrade an array of aromatic hydrocarbons including toluene and naphthalene. Furthermore, F199 can function under microaerophilic conditions making it especially suitable for bioremediation.

We have determined that F199 contains three genetic elements of 2 Mb, 480 Kb, and 180 Kb. Previously, we generated a physical map of the plasmid to serve as a basis for comparative studies as well as for gene localization. We are nearing completion of deriving the nucleotide sequence of the 180 Kb plasmid, pNL1. We used a random sequencing approach using multiple libraries. These libraries included random, PCR-derived clones, a cosmid library whose ends were sequenced, and subclones of various restriction fragments. Over 1200 sequencing reactions were performed, generating almost complete coverage. Gap closure, being completed, uses PCR primers derived from the ends of contigs and larger clones as templates. Putative functions for several genes encoded on the plasmid have been identified by BLAST analysis (examples shown in Figure 1).

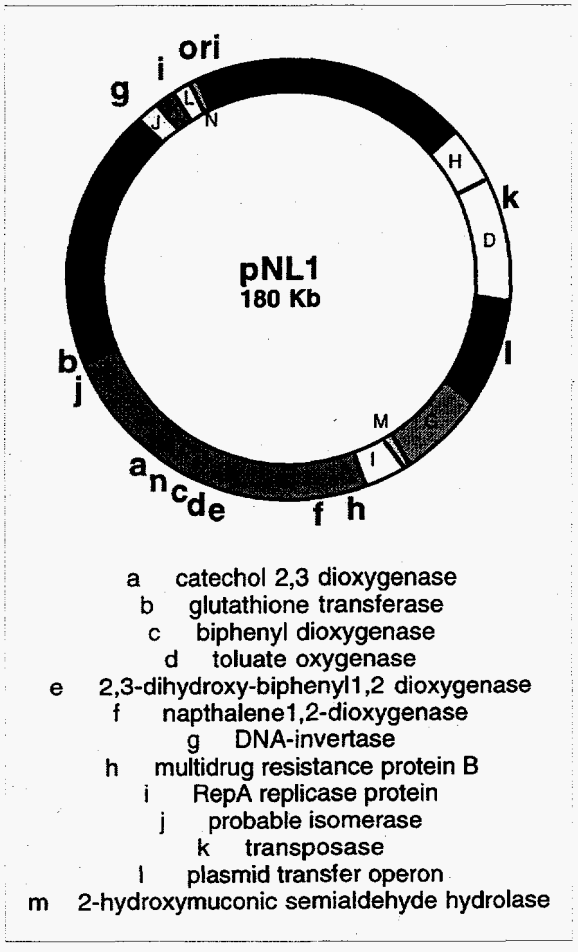

Figure 1. Representative genes found on the F199 pNL1 megaplasmid are shown localized on the physical map.

The genome structure of five other subsurface *Sphingomonas* strains as well as two typed strains, *S. capsulata* and *S. paucimobilis*, were previously determined. Now from the DNA sequence data, we have been able to determine the origin of replication. Using primers derived from this region, which serve as the

backbone of the plasmid, we have shown that two other subsurface strains isolated 25 miles distant, contain the same plasmid as F199 (Figure 2).

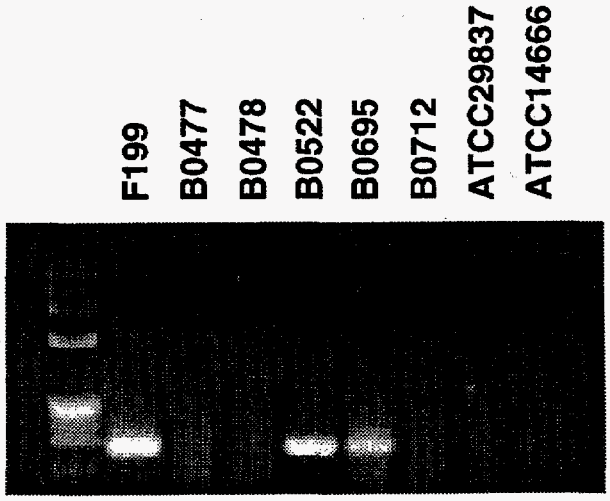

Figure 2. The replication origin of 180 Kb plasmids found in two other subsurface *Sphingomonas* strains is identical to that on pNL1. PCR primers derived from the pNL1 origin of replication were used for amplification of similar regions in related subsurface strains. The positive amplification in strains B0512 and B0695 indicates that these strains contain similar plasmids.

NMR Studies of DNA Structure Associated with Chemical Adduction

Michael A. Kennedy (Macromolecular Structure and Dynamics)

Project Description

This goal of this project was to establish the structural perturbation to DNA caused by ultraviolet damage. The three-dimensional structure of a DNA oligonucleotide containing a cis-syn cyclobutane thymine dimer was determined by nuclear magnetic resonance and restrained molecular dynamics.

Technical Accomplishments

The structure of [d(GCACGAAT=TAAG): d(CTTAATTCGTGC)] was determined using nuclear magnetic resonance data collected at 750 MHz. The structure was determined at 5°C, a temperature at which all exchangeable imino resonances, including those of T8 and T9, were observable (Figure 1). The structure was pursued at this temperature to ensure that a duplex molecule was investigated. Consequently, the structure should indicate the extent of structural perturbation in a stable duplex form. However, at higher temperatures such as 25°C (Figure 1), many of the imino resonances, including those of the thymines that form the cyclobutane dimer are unobservable, the base pair lifetime at the dimer site may be very short, raising the possibility that base "flip out" may be an important feature for damage recognition. Base pair lifetimes will be measured as a function of temperature to address this question.

The structural model generated from the nuclear magnetic resonance data is shown in Figure 2. Overall, no significant perturbation of the structure is observed and the deformations of structure are largely localized nearby the dimer site. Our current model indicates an irregularity in the phosphodiester backbone which is visibly apparent in Figure 2. Since these calculations were performed in vacuo and with reduced partial charges on phosphate oxygen atoms to mimic the presence of sodium counter ions, we are repeating our calculations in a solvated system including sodium counter ions to investigate the significance of solvation for stabilizing the DNA backbone, which is largely unconstrained by our nuclear magnetic resonance measurements.

From the nuclear magnetic resonance data, several unambiguous observations can be made which are reflected in the current model of the structure. Several

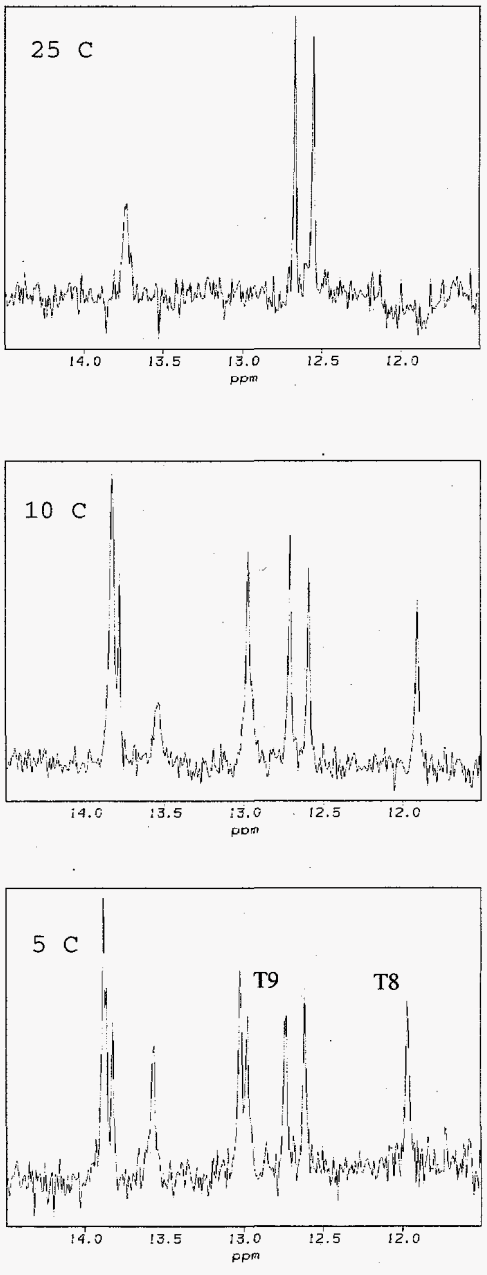

Figure 1. Imino spectra collected at 25°C (top), 10°C (middle), and 5°C (bottom) at 750 MHz.

extreme chemical shifts of both proton resonances and phosphorous resonances are observed. The extreme proton chemical shifts reflect unusual base-stacking patterns, all of which when carefully examined in the

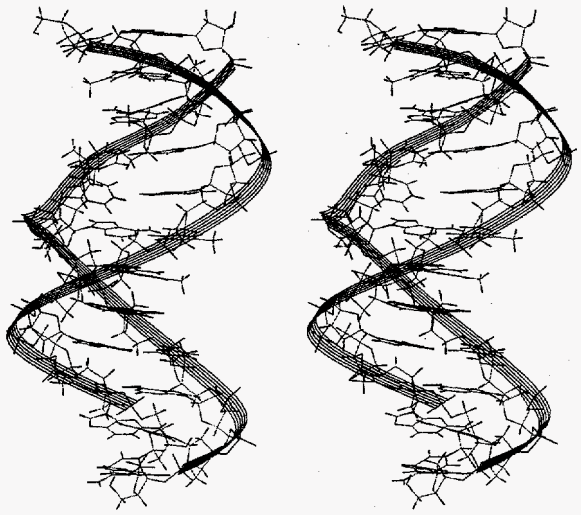

Figure 2. Wall-eyed stereo view of the cis-syn dimer cyclobutane dimer containing DNA oligo. The structure is rotated so that the dimer is viewed looking into the minor groove.

structural model are consistent in explaining the chemical shift observations in terms of ring current effects and base stacking geometries. The phosphorous chemical shift for the phosphorous atom between T9 and A10 is deshielded by ~ 2 ppm compared to all other phosphorous resonances. This resonance also has the largest $^3J_{H-P}$ coupling constant of all phosphorous atoms in the sequence. A modified Karplus relationship correlates phosphorous coupling constants with the DNA backbone dihedral angles ϵ ($C_{4'}$-$C_{3'}$-O_3-P) and ζ ($C_{3'}$-O_3-P-O_5). The ϵ and ζ angles are trans (-180°) , gauche$^-$ (-60°) in B_I backbone, the canonical values found in B-type DNA whereas ϵ and ζ angles are gauche$^-$ (-60°), trans (-180°) in B_{II} backbone. An emperical correlation has been recognized relating phosphorous chemical shift, values of ϵ and ζ , and $^3J_{H-P}$. The relationship shows that deshielded values of phosphorous chemical shifts and large coupling constants correlate with a B_{II} DNA backbone. As shown in Figure 3, this structure clearly contains a B_{II} type DNA backbone in the

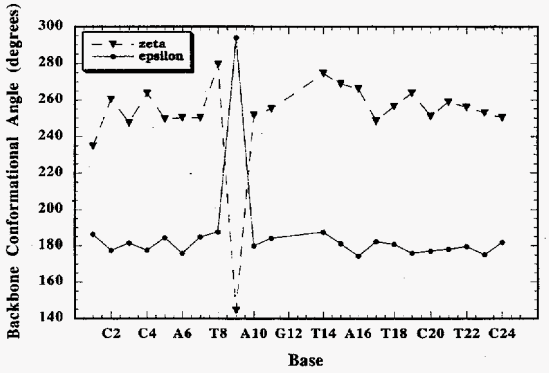

Figure 3. Plot of the ϵ and ζ angles as a function of the base position in the sequence.

transition from the T9 to A10 step. The phosphorous resonance diagnostic of B_{II} DNA backbone has been observed in all sequences investigated so far that contain the cis-syn-cyclobutane thymine dimer. However, all sequence contexts have not yet been investigated. These structure investigations are being prepared for publication.

Publications and Presentations

K. McAteer, Y. Jing , J. Kao , J.-S. Taylor, and M.A. Kennedy. "A 750 MHz NMR determination of the structure of a DNA dodecamer duplex containing a *cis-syn* cyclobutane thymine dimer." (in preparation).

K. McAteer, P.D. Ellis, and M.A. Kennedy. 1995. "The Effects of Sequence Context on Base Dynamics at TpA Steps in DNA Studied By NMR." *Nucleic Acids Res.*, 23, 3962-3966.

J.M. Lingbeck, M.G. Kubinec, J. Miller, B.R. Reid, G. P. Drobny, and M.A. Kennedy. 1996. "The effect of adenine methylation on the structure and base dynamics ot TpA steps in DNA: NMR structure determination of [d(CGAGGTTTAAACCTCG)$_2$]: and its methylated derivative at 750 MHz." *Biochemistry*, 35, 719-734.

M.A. Kennedy, M.G. Kubinec, J.M. Lingbeck, K. McAteer, B.D. Thrall, and P.D. Ellis. "750 MHz NMR studies of chemically modified DNA structure/dynamics: Sequence context effects and protein recognition." *Bulletin of Magnetic Resonance* (in press).

M.A. Kennedy, M.G. Kubinec, J.M. Lingbeck, K. McAteer, B.D. Thrall, and P.D. Ellis. "Sequence context effects on DNA structure and dynamics." *Proceedings of the 34th Hanford Symposium on Health and Environment* (in press).

K. McAteer, J. Kao, J. Taylor, M.A. Kennedy. 1996. "750 MHz NMR study of the structure of a dodecamer DNA duplex containing a cis-syn thymine dimer." The 37th Experimental NMR Conference, Asilomar, California, March 17-22.

K. McAteer, J. Kao, J. Taylor, M.A. Kennedy. 1996. "750 MHz NMR study of the structure of a dodecamer DNA duplex containing a cis-syn thymine dimer." The 212th ACS National Meeting, Orlando, Florida, March 17-22.

Protein Identification in Sequenced Genomes

Margaret F. Romine (Environmental Microbiology)
Steven A. Hofstadler (Macromolecular Structure and Dynamics)

Project Description

The objective of this research was to develop the capability to generate protein maps from bacterial cells by two-dimensional polyacrylamide gel electrophoresis and to use mass spectrometry "fingerprinting" techniques to characterize proteins that have been directly extracted from the polyacrylamide. The protein map is a display of the proteins that are expressed by an organism under specific growth conditions. By analyzing changes in the protein display when the growth conditions are changed or when the organism is mutated, this technique can be used to identify proteins associated with functions that are only required under specific growth conditions.

The identification of the uniquely expressed proteins can be accomplished by extraction of the protein from the gel, digestion with sequence specific proteases, sizing of the proteolytic fragments by mass spectrometry, and subsequent sequencing. The sequencing step can be omitted when information from entire genomic sequences from organisms is used to identify genes capable of producing the identified proteolytic fragments. Within the last 2 years, the sequence of three bacterial genomes and of the yeast genome have been released to the public, with many others being near completion. This revolution in science will make it possible to use proteolytic fragment sizing for rapid identification of expressed proteins.

This technique provides an excellent mechanism to begin understanding, at the genetic level, the complexities involved in the response of an organism to environmental change. Gene sequencing alone can only predict gene function by searching for similarities to sequences from well-characterized metabolic pathways. For the *Methanococcus jannaschii* genome, only 40% of the predicted genes could be identified by this approach. Using combined two-dimensional PAGE/mass spectrometric analysis to study bacteria that have mutations that effect their ability to grow in specific conditions, we can begin to predict the function of additional genes.

Technical Accomplishments

We focused on getting all the appropriate equipment in place, acquiring and learning to use software for analysis of data, and running some test samples to determine the limitations in parts of the technique. For the two-dimensional electrophoresis, we acquired equipment that allows us to run and prepare 20 first-dimension and 10 second-dimension gels in tandem. Ability to run and prepare the samples in tandem is essential because it reduces the variability that occurs when samples are run at different times. We tested a number of techniques for release of cellular protein. The target microbe for this work was *Sphingomonas aromaticivorans* F199, a producer of a considerable quantity of polysaccharide material which interferes with cell lysis. We found that we could improve lysis via sonication by addition of glass beads and use of a large sonication horn. Lysis with a French Press was far superior to sonication, but more labor and time intensive. We succeeded in running a suite of different samples on 20 polyacrylamide gels.

A variety of different methods for protein detection are possible. We tested two relatively new protein stains developed by Molecular Probes Inc. for their suitability in staining the second-dimension gel. These stains, sypro orange and sypro red, can be detected by fluorescent imaging and are reported to have sensitivity comparable to silver staining techniques. Their use also cuts down on waste generation and staining time. In our hands, however, we observed much lower detection levels, similar to those observed with Coomassie Blue. This observation may have been due to the use of duracryl rather than standard acrylamide. The size of our gels required the use of large quantities of stain, making the use of these stains cost prohibitive. We therefore, decided to stick with silver staining for future detection of expressed proteins.

Fourier transform ion cyclotron resonance mass spectrometry studies were performed using both intact model proteins and model peptides derived from selective solution-phase proteolysis of model proteins. Studies were performed to evaluate the efficacy of sustained off-resonance irradiation collisional activated dissociation of peptides in the FTICR trapped ion cell and to determine the number of tandem mass spectrometry steps needed to facilitate unambiguous protein identification using standard protein data base searching algorithms. The need for ultrahigh mass resolution and high precision mass measurements was evaluated from the perspective of searching genomic data bases.

Figure 1a shows an ESI-FTICR mass spectrum of a model histone protein (provided by C.G. Edmonds, PNNL) which exhibits a charge state envelope common

to ESI-MS; each labeled peak corresponds to a different charge state of the same molecular ion. The inset of the $(M+15H+)^{15+}$ species demonstrates the ability of the FTICR to resolve the ^{13}C isotopic envelope and thus determine charge state (and mass) from a single charge state of a multiply charged species. This capability is particularly important for tandem mass spectrometry experiments in which a charge state envelope is not produced. As shown in Figure 1b, solution phase V8 proteolytic digestion of the protein yields a number of proteolytic peptides. The composition of the peptide pool and the mass of the intact molecule is unique to the analyte and enables protein identification from protein data bases (i.e., peptide mapping). Once a putative protein identification is made, tandem mass spectrometry can be performed on a selected peptide to confirm partial amino acid sequence. As shown in Figure 1c, amino acid sequences are derived by the mass difference of fragment ions, thus the mass differences labeled in the figure correspond to an amino acid sequence of leucine-alanine-lysine. When these methods are applied to a protein which is not in a given protein data base (as would be the case for previously unidentified proteins), or applied to a genome for which little is known, the amino acid sequence generated by tandem mass spectrometry methods can be linked to DNA sequence data (if available) to identify the gene responsible for the protein of interest. If DNA sequence is not available, the translated amino acid sequence can be used to design PCR primers to amplify relevant regions of the genomic DNA.

Using the techniques described above, the model protein (histone H2B extracted from chicken erythrocytes) was correctly identified from protein data bases containing over 100,000 protein entries from numerous species. Despite the large number of proteins listed in the data bases, the unique combination of intact molecular weight and proteolytic fragment masses allowed correct protein identification. Interestingly, correct protein identification was obtained even when mass measurements of (intentionally) modest accuracy were employed. Thus, while the FTICR platform can routinely provide low part per million mass measurement error and ultrahigh mass resolution, in many cases other mass analyzers such as the quadrupole ion trap, appear to be well suited for peptide mapping and peptide fingerprinting applications. Future studies will employ both quadrupole ion trap and FTICR methodologies.

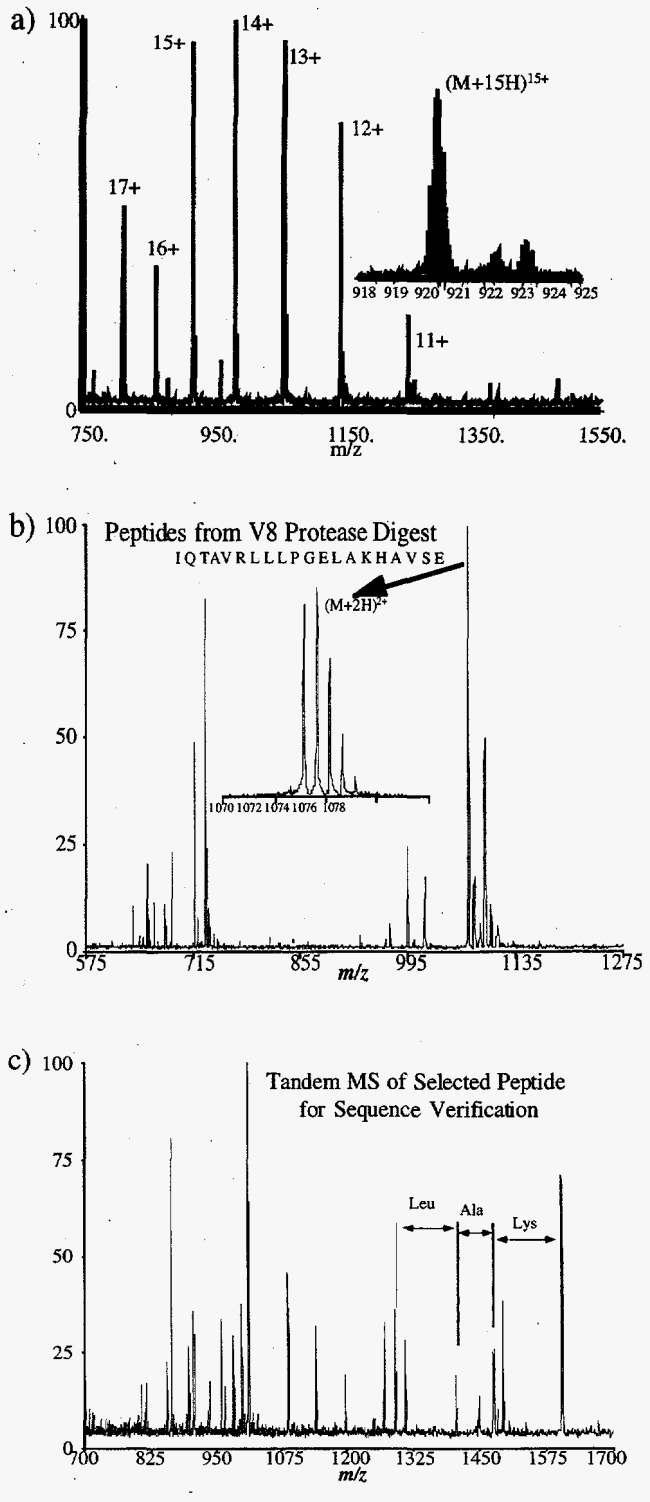

Figure 1. a) Relative abundance (%); b) peptides from V8 protease digest; c) tandem MS of selected peptide for sequence verification.

Chemical Instrumentation and Analysis

Speciation of Uranyl Aqueous and Surface Complexes by Cryogenic Spectroscopic Methods

Charles C. Ainsworth, Linfeng Rao (Earth Systems)
Donald M. Friedrich (Environmental Dynamics and Simulation)

Project Description

The objective of this project was to develop cryogenic techniques for improving the resolution of optical spectra of actinide complexes in aqueous and mineral suspension phases. Improved spectroscopic resolution provides greater detail in the speciation of the actinide complexes both in solution and at aqueous/mineral interfaces. The results obtained for aqueous speciation serves as the baseline for the interpretation of surface speciation, and help understand the interrelationship between solution and surface species as well.

The goals of this project were to: 1) determine speciation of uranyl complexes in aqueous-phase and on aqueous/clay interfaces, and 2) elucidate structural detail about the complexes and their binding sites. In support of these goals, research was focused toward the following near-term objectives: 1) to produce hyperquenched cryogenic films of uranyl complexes in aqueous solution and clay suspensions; 2) to measure excitation and fluorescence spectra at high resolution by laser excitation methods, including laser-induced fluorescence line-narrowing and hole-burning spectroscopy; and 3) to analyze the vibronic structure of the spectra in terms of structures determined for model uranyl complex systems (e.g., uranyl on alumina, silica, etc.). This research draws upon knowledge, technology, and instrumentation recently developed in the EMSL (amorphous water ice films, electrospray technique, and laser-induced sorbate fluorescence) in order to exploit the well-known effect of cryogenic line-narrowing spectroscopy for the purpose of obtaining improved resolution of sorbate structural data. This is a new technical approach to the problem of surface complex speciation.

Technical Accomplishments

Sample Preparation Protocols Established

Diluted ($\leq 10^{-4}$ M) solutions of perchlorate salt of depleted $UO_2 2+_{(aq)}$ were prepared. For spectroscopic study of room temperature solutions, small volumes of the solutions (typically < 10 mL) were transferred to optical sample cells (quartz cuvets) and sealed. The cuvets were transported to another building at another laboratory in a sealed plastic container. For preparation and study of the cryogenic films, syringes (≤ 100 mL volume) were filled with 10 to 20 mL of samples. The syringes were double-wrapped in plastic and contained in a carrier/holder during movement. In the spectroscopy lab, the syringe was mounted in a syringe pump and the solution pumped through an aerosol generator. Aerosols were sprayed directly onto a copper cold plate (maintained at < 100K by flowing cryogen) in the vacuum cryostat, forming an ice-like film of the solution. The unused portion of the sample was resealed into the original syringe carrier/holder. After spectroscopic measurements were made on the frozen film of uranyl solution, the cold-plate was removed from the cryostat. The cold-plate and exposed surfaces of the cryostat were rinsed thoroughly with deionized water and the rinseate collected. The rinseate is taken together with the remaining unused sample in the syringe for further analysis.

Room Temperature Spectra Demonstrated

The optical absorbance of aqueous uranyl is very weak. To achieve laser-induced fluorescence line-narrowing measurements in cryogenic films, it was necessary to tune a narrow-line excitation laser into the longer wavelength vibronic bands of the visible spectrum (486 nm). At room temperature the molar extinction coefficient of $UO_2 2+_{(aq)}$ is very small ($\varepsilon < 0.4$ $\underline{M}^{-1}cm^{-1}$) at 486 nm.

Nevertheless, uranyl fluorescence was readily detectable. To demonstrate this, Figure 1 shows that uranyl prepared under the conditions described above ($\leq 10^{-4}$ M) was detectable at room temperature using low intensity xenon lamp excitation (< 1 mW) in the near ultraviolet (313.5 nm, $\varepsilon \sim 40$ $\underline{M}^{-1}cm^{-1}$). This means that excitation in the 486 nm region will yield fluorescence spectra of the same intensity using dye laser excitation power on the order of 100 mW, which is easily achievable with our existing high-resolution ring dye laser.

Aerosol Generators Designed, Constructed, and Interfaced to a Vacuum Cryostat

Two methods for deposition of cryogenic films were designed and constructed. The first method seeks to preserve the ambient temperature distribution of uranyl

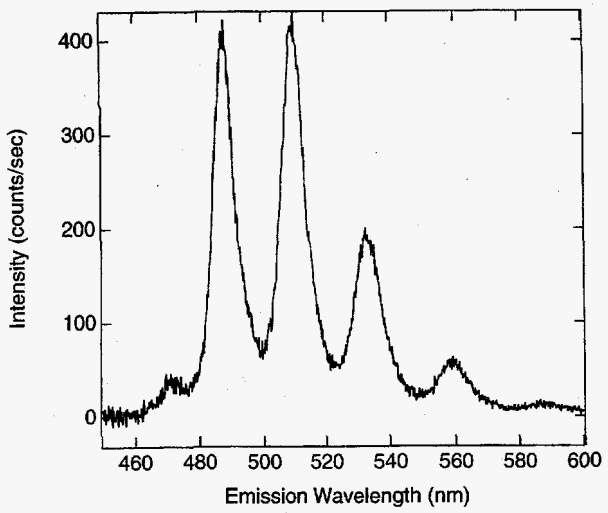

Figure 1. Fluorescence of $UO_2 2+_{(aq)}$ (10^{-4} M) in 0.1 M $HClO_4$ excited by xenon lamp/double monochromator source (~ 10^{-3} W) at 313.5 nm.

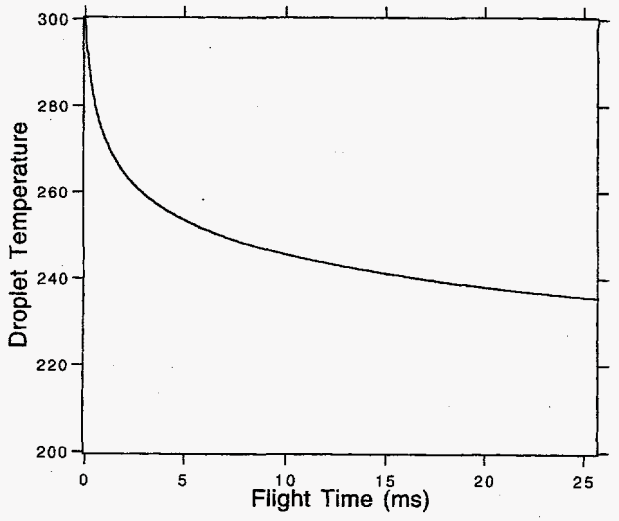

Figure 2. Cooling curve for 200 micron diameter aerosol droplets based on simple evaporation with temperature dependent vapor pressure. The final temperature range (230 - 240K) and mass loss (10%) are the same for a wide range of droplet sizes (20 - 200 micron). The cooling time scales with droplet diameter: 15 ms for 200 micron, 1.5 ms for 20 micron.

species prior to hyperquenching at the cryostat cold plate. A piezoelectric-driven vibrating orifice aerosol generator (VOAG) creates a stream of 200 micron diameter aerosol droplets in a differentially pumped antechamber. The uniform size droplets were drawn through a skimmer and deposited on the cold plate in the cryostat. This somewhat complex configuration has the distinct advantage of creating the aerosol droplets at ambient temperature. However, because the aerosols are produced external to the cryostat, the flight path and transition to high vacuum are relatively long in this method (several tens of centimeters). Modeling of the rate of droplet cooling by evaporation indicated that the temperature of an aerosol droplet decreases approximately 60K by evaporation of roughly 10% of its mass. After cooling to this point, the evaporation rate is sufficiently reduced that little additional change in temperature or mass occurs. This is valid over a wide range of aerosol sizes from tens to hundreds of microns diameter. The larger particles require longer to cool: approximately 15 ms for the 200 micron aerosols produced in the current version of our generator, but only 1.5 ms for 20 micron droplets.

Prior literature indicates that deposition of such aerosols on cryogenic plates (< 100K) will produce amorphous water films. These earlier papers emphasized the much more rapid cooling of droplets at the cryogenic surface (10^6 - 10^7K/s). However, it is now clear from simple consideration of evaporative cooling that the aerosol particles are already substantially supercooled to a relatively constant 230 to 240K during the flight from generator to cold plate (Figure 2). While production of amorphous films is not a goal or requirement of this project (LIF line-narrowing will work well in amorphous or polycrystalline cryogenic films), nevertheless it will be interesting to see how cooling rate, flight-time, and droplet size affect the phase of the deposited film. It will be especially interesting to determine the effect of clay colloidal particles on the final phase of the hyperquenched films. This VOAG system was constructed, interfaced, and tested on our cryostat in the funding period using aqueous samples of a nonradioactive fluorophore (salicylate).

The second method of hyperquenching uses a high voltage thermospray to produce a fine spray (1 to 10 micron) of aerosols directly into the high vacuum chamber of the cryostat. The flight path of the aerosols can be quite short (on the order of centimeter), minimizing effects of evaporation and prior cooling. This method has been developed in the literature extensively for the express purpose of producing amorphous water ice films. The method has the distinct advantage of technical simplicity. A hypodermic needle (100 micron inside diameter) is connected in a low-voltage high-current circuit and resistively heated to prevent the tip from freezing. Typical outlet temperatures are 100°C to 180°C. The needle is charged to a high voltage (typically 5 kV) relative to the cold plate. There are some serious problems with this method for speciation studies, however. First, the high temperature of the solution in the delivery needle means that the deposited aerosols will contain a high temperature distribution of species, not a distribution representative of ambient temperature, which is of most interest for environmental speciation. Some tank waste media do exist at higher temperatures, and the thermospray method may be appropriate for model speciation studies at such elevated temperatures.

Second, the speciation studies always require a relatively high ionic strength (typically > 0.01 N). It is well known that it is difficult to generate an aerosol spray by thermo/electrospray methods using solutions of such high ionic strengths. Finally, the high voltage, in conjunction with the high ionic strength solutions, poses a safety hazard. We have designed and constructed a thermospray generator and interface for our cryostat. However, we have not yet tested thermospray deposition in this project.

High Resolution CW Dye Laser Configured for Blue (460 to 500 nm) Excitation

LIF line-narrowing requires the use of a narrow-line-width dye laser that can be tuned to vibronic bands near or at the electronic origin of the absorption band of the fluorescing electronic state. For uranyl, this requires a tunable laser in the 460 to 500 nm region. Our existing narrow-line-width dye laser (Coherent 899-29) was previously configured for longer wavelengths and had not been operated in the blue. In this project, the dye laser was configured with new optics and interferometer to operate in the required blue range.

Theoretical and Experimental Study of ^{195}Pt Solid NMR Shift Tensors

James A. Franz (Materials and Chemical Sciences)
David A. Dixon (Theory, Modeling, and Simulation)
Paul D. Ellis (Macromolecular Structure and Dynamics)

Project Description

The uses of platinum range from automotive catalysis to cancer therapy. The spin-1/2 ^{195}Pt nucleus has been widely exploited in solution nuclear magnetic resonance studies of inorganic and organometallic structures. In spite of its great importance in catalysis and health applications, little work to characterize the ^{195}Pt nucleus by nuclear magnetic resonance in the solid state has been carried out. This is primarily due to the very large chemical shift tensor components of the ^{195}Pt nucleus in organic and inorganic complexes, which lead to very broad static solid nuclear magnetic resonance spectra, in typical cases several thousand parts per million (10^5 Hz at 2.3 tesla) in width, compared to liquid line widths of about < 100 Hz. The availability of chemical shift tensor components from the solid-state nuclear magnetic resonance provides much more information on the electronic environment of the platinum nucleus than the average isotropic chemical shift available from solution nuclear magnetic resonance spectra of the of platinum compounds, particularly if the experimental shift tensor components can be oriented to the molecular geometry structure available from crystallography.

In recent years, the Gauge-Invariant-Atomic Orbital (GIAO) method (Ditchfield 1974; Wolinski et al. 1990) has been developed for prediction of nuclear magnetic resonance chemical shifts and implemented in ab initio electronic structure programs such as Gaussian-94, TX95, and the ACES2 (Gauss 1992) electronic structure codes. The latter two programs implement post-SCF methods for certain systems (second order Moeller-Ploesset perturbation theory, MBPT[2]) in GIAO calculations. Versions of these codes (TX95, ACES2, G94) have been installed in a computational facility at PNNL. ACES2 has also been installed in collaboration with the Quantum Theory Project, University of Florida, Gainesville.

The objective of this project is to develop an experimental overview of the range of ^{195}Pt nuclear magnetic resonance chemical shift tensor components and anisotropies for a representative selection of inorganic and organometallic platinum structures, and to assess existing theoretical tools for extending theoretical chemical shift predictions to many-electron atoms.

Technical Accomplishments

Synthesis of Platinum Complexes

The following five compounds were synthesized or obtained from commercial sources. 1) *Cyclooctadienyl Platinum Dichloride* was commercially available. 2) *Cyclooctadienyldimethyl Platinum* was prepared by treatment of *Cyclooctadienyl Platinum Dichloride* with methylmagnesium bromide, (a single-crystal x-ray structure of this compound was obtained, providing atomic coordinates for GIAO calculations). 3) *Norbornadienedimethylplatinum* proved to be less thermally stable than *Cyclooctadienyldimethyl Platinum*, but could be used to obtain spectra if done quickly and at low temperature. 4) *Diaminodimethylplatinum* $(CH_3)_2Pt(NH_3)_2$ was prepared according to literature methods by treatment of *Norbornadienedimethylplatinum* with ammonia. However, the material proved to be thermally unstable and rapidly emitted ammonia to yield a mixture of unusable materials. 5) *1,2-diperfluoroethylphosphinoethane dimethylplatinum* was provided by Dr. Dean F. Roddick of the University of Wyoming. *1,2-di-perfluoroethylphosphinoethane* = $(C_2F_5)_2PCH_2CH_2P(C_2F_5)_2$.

Acquisition of ^{195}Pt Solid-State Nuclear Magnetic Resonance Spectra

^{195}Pt nuclear magnetic resonance spectra were determined at 21 MHz using an Otsuka-Chemagnetics CMX-100 spectrometer, and a Doty, Scientific 7-mm supersonic triple resonance H-F-X probe. Samples were spun at 10 kHz and at a second spin rate to identify the isotropic peak, and Bloch decay (single pulse excitation) spectra were acquired using a 2-μs observe pulse (45°) and 56 kHz field strength proton decoupling. For fluorine-containing structures, i.e., *1,2-di-perfluoroethylphosphinoethane dimethylplatinum*, a second 55 kHz ^{19}F decoupling field was used to obtain $Pt\{^{19}F,^{1}H\}$ SPE spectra. Abundant acoustic ringing was experienced. This was remediated by right-shifting the FIDs corresponding to the receiver and acquisition delays, and calculating the front 5 to 10 data points of the FID using back projection. The line widths of the platinum lines were about 100 Hz. Representative spectra are depicted in Figures 1, 2, and 3.

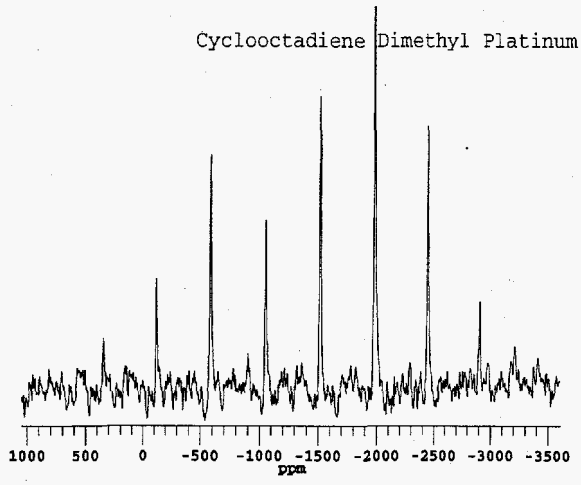

Figure 1. 10-kHz MAS SPE $^{195}Pt\{^{1}H\}$ spectrum of cyclooctadienedimethyl platinum.

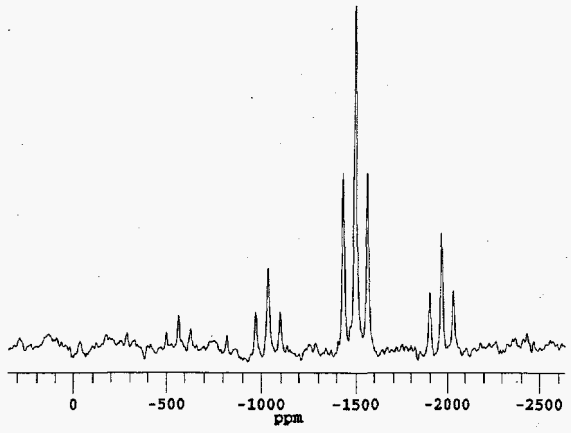

Figure 2. 10-kHz MAS SPE $^{195}Pt\{^{1}H,^{19}F\}$ spectrum of 1,2-di-perfluoroethylphosphinoethane dimethyl platinum. Note triplets due to $J(^{195}Pt\text{-}^{31}P)$.

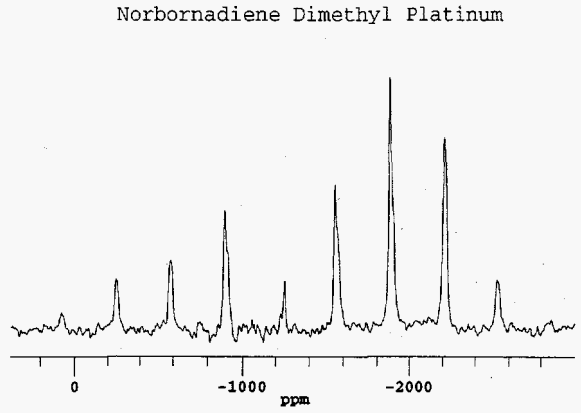

Figure 3. $^{195}Pt\{^{1}H\}$ SPE Spectrum, 7 kHz MAS, of norbornadienedimethyl platinum.

Determination of Chemical Shift Tensor Components from MAS Spectra

The spinning sideband intensities of the SPE spectra were modeled using a simplex program that optimizes principal tensor components and numerically generates the free induction decay and MAS spectrum with optimal fit to the experimental MAS spectrum.

Acquisition of Large Platinum Complex Crystals for Goniometer Spectra

The experimental effort detailed above yields principal components of the chemical shift tensor, but it does not provide the orientation of the nuclear magnetic resonance tensor in the molecular framework. To obtain the angles between the nuclear magnetic resonance tensor and the crystal principal axis, non-spinning single frequency spectra must be obtained. This requires a rather large crystal. Unfortunately, repeated attempts to produce large crystals of *Cyclooctadienyldimethyl platinum* failed. This led to the preparation of *Diaminodimethylplatinum*, which was thought to give large crystals. Unfortunately, *Diaminodimethylplatinum* proved to be quite thermally unstable, a fact not reported in the literature account of its preparation. Thus, this aspect of the study did not progress to the point of obtaining goniometer spectra.

Development of Basis Sets for ab initio GIAO Calculations

Two Huzinaga-type basis sets were constructed for use in GIAO calculations, one having functions on platinum and a second basis set having g functions on platinum. The basis functions were further adapted for use in Gaussian94, TX95, and ACES2 programs.

Evaluation of ACES2, Gaussian94, and TX95 Codes

Calculations were attempted for cyclooctadienyldimethyl platinum, since a single crystal x-ray structure was available. This is an extremely large molecule with no symmetry in the crystal. The basis set for this molecule using g functions on platinum has 268 primitive functions, making this a formidable geometry optimization, although a single-point calculation should be feasible. A single-point GIAO calculation was successfully completed at the SCF level using TX95, but attempts to carry out this calculation using Gaussian and ACES2 codes failed, in the latter case because of size limits in several subprograms. Further work was carried out to obtain SCF and MBPT[2] GIAO calculations with the ACES2 code with smaller representative structures. Successful SCF calculations were performed for the $H_2Pt(NH_3)_2$ system. Work will continue with alternate funding sources to obtain calculated tensor components at the post-SCF MBPT[2] level of theory for comparison with a variety of experimental determinations

and for the model $(CH_2=CH_2)_2Pt(CH_3)_2$. Chemical shift tensor components at the SCF level were about twice the magnitude of the experimental values for norbornadiene dimethyl platinum. These are shown as an entry in Table 1 for $codPt(CH_3)_2$.

Table 1. Experimental Tensor Components, Anisotropy, and Asymmetry

Compound	S_{33}	S_{22}	S_{11}	$\Delta\delta$	η
Norbornadiene dimethyl Pt	1476.4	-514.9	-963.5	2214.6	0.3
Cyclooctadiene dimethyl Pt	1885.1	-445.4	-1439.7	2827.6	0.527
$codPt(CH_3)_2$(calc)[a]	4708.9	4562.6	2581.3	1136.9	2.64
Compound 5	790.0	-1.06	-788.98	1185.05	0.997

(a) SCF with midi-2-p2d2f2g2 basis set, TX95

Goals to install and test GIAO code were met, model structures were prepared, and initial evaluation of the GIAO method was accomplished. Work will continue to test the MBPT[2] level of theory for representative model and experimental structures.

References

R. Ditchfield. 1974 *Mol. Phys. 27*, 789.

J. Gauss. 1992. *Chem. Phys. Lett. 191*, 614.

K. Wolinski, J.F. Hinton, and P. Pulay. 1990. *J. Am. Chem. Soc. 112*, 8251.

Waste Tank Vapor Characterization of Polar Organic Constituents

George S. Klinger (Analytical Chemistry and Spent Fuel Behavior)
Karen L. Wahl (Process Chemistry)

Project Description

The objective of this project was to investigate a method of sampling and detecting polar organics in air which are difficult to sample and measure by other means. Solvent trapping using a thin film of solvent to capture and stabilize the organic species of interest was investigated.

Introduction

Identification and measurement of polar constituents of waste tank headspace are important in that they can provide information about both safety and characterization of the tank waste at minimal expense. Some organic acids have been identified in the analysis of both SUMMA canister samples and thermal desorption of adsorbent traps using gas chromatography/ mass spectrometry (GC/MS), but quantitation of these is dubious.

A U.S. EPA-sponsored survey (Mukund et al. 1995) on the status of ambient measurement methods for hazardous air pollutants indicates that while many methods are applicable to the majority of the 189 hazardous air pollutants identified in Title III of the Clean Air Act Amendments, it lists only limited "potential" methods for some of the polar molecules, or no method at all. N-nitroso-N-methyl urea is an example of a hazardous air pollutant compound for which no valid EPA method exists. This compound is an important Hanford waste tank compound, in that it is a likely cause of the positive methyl isocyanate result reported for the U-106 tank by ORNL. It is not currently understood whether methyl isocyanate is present in the waste tank headspace, or is a decomposition product of a nitrosoamine (or related compound) formed by thermal desorption of the adsorbent trap. This compound should be amenable to thin film liquid trapping and electrospray ionization mass spectrometry (ESI-MS) methodology. ESI-MS has been demonstrated as a powerful tool for the analysis of polar molecules such as organic acids, amines, and multifunctional molecules (Campbell et al. 1994).

Technical Accomplishments

A thin film liquid trap was developed. The device consists of a Kynar™ band that spins rapidly to wipe a thin solvent film along the inner wall of a column. Solvent is added at the top of the column using a syringe pump. The solvent is forced downward so that it is countercurrent to the gas flow that is being sampled.

A small quantity of the solvent is replenished continuously by the syringe pump to offset evaporative loss.

The device allows high gas sampling flow rates, up to several liters per minute, depending on the configuration of the Kynar band. The thin film spinning band trap is shown in Figure 1.

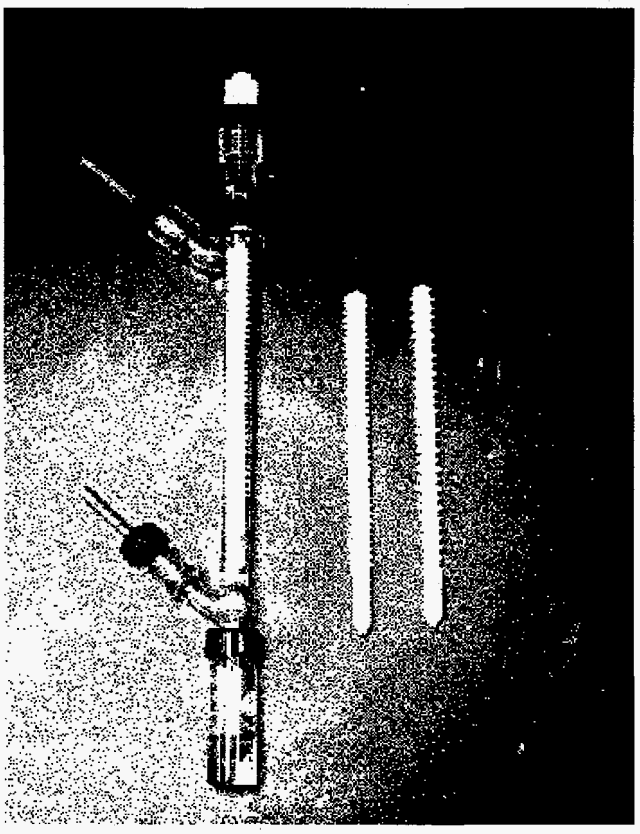

Figure 1. Thin film trap with spinning band.

Three different bands were constructed from Kynar stock. Kynar (polyvinylidine fluoride) was chosen because it is resistant (does not swell) to all the solvents used for the trapping experiments. Additionally, it is

harder and denser than Teflon™, making it much easier to machine. The bands were fabricated with different pitches and radius threads, and were of a double lead design. Two small neodymium-iron-boron magnets were used in each band in conjunction with a magnetic stirrer to spin the bands. The clearance between the bands and the walls of the glass column were only slightly larger at the nominal specification (a few thousandths of an inch) for the Pyrex™ tubing wall variation used to make the columns. Some difficulties with binding, i.e., getting the bands to start spinning were encountered, but the addition of a small Teflon o-ring, on which the band rested, solved that problem to a large extent. The band with the finest pitch was found to be too easily lifted by the gas flow at rates greater than 200 cc/minute. Most of the experiments were conducted using the other two bands, which proved satisfactory for flow rates up to 5 L/minute.

A 5 mL conical vial was used to collect the solvent containing the trapped analytes. Figures 2 and 3 show chromatograms comparing the performance of the thin film trap to a solvent-filled impinger for several volatile organic compounds using methanol as the trapping solvent. The impinger required a minimum volume of 4 mL of methanol to overcome evaporative loss during sampling. The volume of methanol in the thin film trap was maintained at approximately 1 mL during the course of sampling. The later eluting (less volatile) components appear more effectively trapped in the new method (Figure 3) than with the current method (Figure 2).

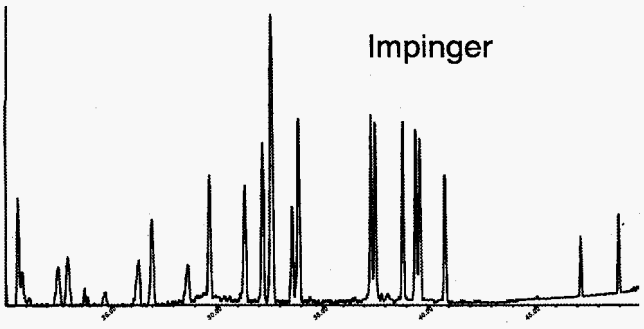

Figure 2. The impinger required a minimum volume of 4 mL of methanol to overcome evaporative loss during sampling.

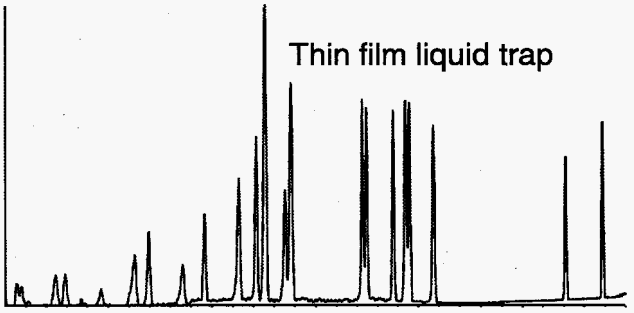

Figure 3. The volume of methanol in the thin film trap was maintained at approximately 1 mL during the course of sampling.

During the course of FY 1996 we also investigated several waste tank gas samples using direct infusion ESI-MS. The samples used were archived SUMMA canister samples of four different single-shell waste tanks. Trapping was done using an early prototype device. While the data were not extensively analyzed, these scouting experiments provided an idea of the levels of polar and ionic organic compounds that could be expected.

Additionally, some experiments with tributylphosphate were conducted. Tributylphosphate is a compound that could not be recovered from SUMMA canisters using the EPA TO-14 methodology. Preliminary results of those experiments using the thin film liquid trap were very promising and applicable to other organics that are too polar or labile to be detected using adsorbent trapping and thermal desorption GC/MS methodology. In conclusion, this new method appears quite promising, and further efforts are warranted.

References

R. Mukund, T.J. Kelly, S.M. Gordon, M.J. Hays, and W.A. McClenny. 1995. "Status of ambient measurement methods for hazardous air pollutants." *Environ. Sci Technol.* Vol. 28, No. 4, 183A-187A

J.A. Campbell et al. 1994. *Flammable Gas Safety Program Analytical Methods Development*, FY 1993 Progress Report, PNL-9062, Pacific Northwest Laboratory, Richland, Washington.

Computer and Information Science

Adaptive Life Simulator

Lars J. Kangas (Information Technology)

Project Description

This project developed a software algorithm to demonstrate a cardiovascular modeling and diagnostic tool. The software will be used to evaluate individuals in graded exercise tests. The work in FY 1995 developed the tools to model physiological data collected during graded exercise tests. The work in FY 1996 added the model-based diagnostic capability that completed the first demonstration prototype.

This research is unique in that it demonstrates a model-based diagnostic system which learns empirically the physiological graded exercise test data from individuals. Any deviations in one individual's physiological data compared to the modeled data is subsequently used for diagnosis.

Technical Accomplishments

The first prototype has been demonstrated that correctly diagnoses several medical conditions (obstructive and restrictive lung disease, hypertension, unfitness). These conditions are currently discernible by a physician from the data collected in graded exercise test evaluations. This research automated the diagnostic process. It is also expected that the developed diagnostic system will have a higher sensitivity and specificity than physicians.

Although the software algorithms and research are completed for a first prototype, this work will continue with the addition of more patient data as it becomes available. The FY 1996 prototype was completed with 66 graded exercise test data sets included in the development. This relatively small number of patient data sets is not sufficient to conclusively measure the performance of the diagnostic system. The preliminary results demonstrated to date will be revised when more patient data is added into the system.

Presentations

L.J. Kangas, P.E. Keller, P.A. Allen, and R.S. Wright. 1995. "Artificial neural networks to model and diagnose cardiovascular systems." Presented at Northcon '95, Portland, Oregon, October 10-12.

L.J. Kangas, P.E. Keller, P.A. Allen, and R.S. Wright. 1996. "Computer aided cardiovascular diagnostics." Presented at the World Congress on Neural Networks '96, San Diego, California, September 15-18.

Automated Lung Ventilation Diagnosis

Paul E. Keller, Lars J. Kangas, Charles R. Batishko (Information Technologies)

Project Description

The objective of this project was to explore the feasibility of improving a diagnostic procedure presently used to detect lung ventilation and lung perfusion abnormalities such as pneumonia and pulmonary emboli through automation. This objective was accomplished by developing several image processing routines and by analyzing several sets of patient image data. A complete software diagnostic system would integrate the various image processing routines developed and used in this project with an "intelligent" information processing system, such as an artificial neural network or fuzzy logic expert system, to implement the decision process.

Technical Accomplishments

When a patient is suspected of having a respiratory problem, he or she is subjected to a lung ventilation (V) scan and a lung perfusion (Q) scan. This procedure, known as a V/Q scan, uses nuclear scintigraphic images of the air flow and blood flow of the lungs. The physician looks at two things: the amount and distribution patterns of blood in the lungs (perfusion), and the amount and distribution of air throughout the lungs (ventilation). The physician identifies regions of the lungs that are not receiving the normal amounts of air, blood, or both, as these indicate an abnormal lung condition. This involves the patient inhaling a radioactive gas (xenon) or an aerosol that is laced with a fine radioactive dust or radioactive smoke (usually technetium-99). Images of the lungs are then taken at several different angles around the long axis of the patient with a gamma camera (i.e., gamma-ray imaging system). The images are then examined, and perfusion defects are seen as cold spots (low intensity regions) on the images. The patient is then subjected to a lung perfusion scan. The patient is injected with a radioisotope dye (technetium-99 tagged blood albumin) that attaches itself to the blood cells and is then carried through the lungs. Imaging of the lungs is repeated.

Patterns within each type of image, as well as the differences between the two image types provide useful diagnostic information concerning lung function. The diagnosis is made by viewing each lung perfusion image with its lung ventilation image counterpart as a stereo pair. There are generally four to eight pairs of images per patient representing views from different angles.

A key part of this process is the correlation of data from the same regions of the lungs under the two recording conditions. If the abnormalities of both studies have similar locations, this is indicative of diseases such as pneumonia. However, if the location of a perfusion abnormality has normal ventilation, this is indicative of pulmonary emboli. Other lung diseases such as sarcoidosis, fibrosing mediastinitis, Swyer-James syndrome, and pleural effusion can also potentially be diagnosed with a V/Q scan.

Our concept for automated lung scan diagnosis was originally devised at a meeting between PNNL and Sacred Heart Medical Center (SHMC) in Spokane, Washington. Throughout this project, Dr. Edwin Holmes director of nuclear medicine at SHMC, provided both domain knowledge and image data from 75 patients. Dr. Mahoney, director of nuclear medicine at Kadlec Medical Center in Richland, Washington, provided additional advice and domain knowledge.

The software prototype developed in this project was composed of a series of image-processing routines coupled to a decision-making routine which makes a diagnosis by examining the processed images. Several processes were developed or used as separate algorithms. These processes included data conversion, image normalization, image centering, image stretching, template table generation, contour plotting, image registration, and segment analysis. We implemented several of these algorithms in our software while others were used in existing commercial software. Some steps, such as image centering, were done manually. Integration of these components was not accomplished.

The preparation of images for analysis includes registration of the lung images to lung templates. These templates are common for all patients and are defined for several views (eight in the current prototype). A template provides both an outline of the ideal lung and boundaries for each segment in the lung. Registration of the raw image to the template is performed by generating a contour plot of the raw image and then stretching this image so that a specified contour fits the outline of the template. Given the variability in the images, this proved to be a difficult task. We implemented a contour plotting algorithm based on Freeman chain encoding for use in automated image registration.

Pulmonary emboli (the major problem diagnosed with a V/Q scan) affect either complete lung segments or partial lung segments. When partial segments are affected, the problem manifests itself at the lung periphery and moves inward. In order to compare one segment to other segments in a consistent approach, we developed a table which gives the attitude of each segment in each view relative to the peripheral edge of the segment and included this table in the software used to normalize image intensity. This routine redistributes intensity so that intensities are average at equidistances from the periphery.

Each defined segment of the lung is visible in several views. In analyzing a specific segment, one expects to combine the analysis of that segment from several views. Since certain views are better than others for analyzing specific segments, a table was developed to rank the diagnostic value of each segment in each view. These ranking values should be used to weigh the diagnostic information from each segment in each view when combining that information to the "whole" diagnosis for that segment.

An algorithm was developed that automatically develops tables representing segment boundaries for all templates (eight for our prototype). These tables provide the segment boundaries of registered images required for the automated analysis of the lungs.

We were able to test these routines on images from 75 patients. SHMC provided diagnoses for these patients. In addition, two premedical undergraduate students were trained to read V/Q scans. Their diagnosis generally followed that of the physicians. The students' work helped validate the physician's diagnoses and helped us understand what was involved in making a diagnosis.

Figure 1 shows both the ventilation and perfusion images of a patient diagnosed with a high probability of a pulmonary embolism in the anterior basilar segment of the left lower lobe. Figure 2 shows a template of the segments of the lungs as seen from the anterior view.

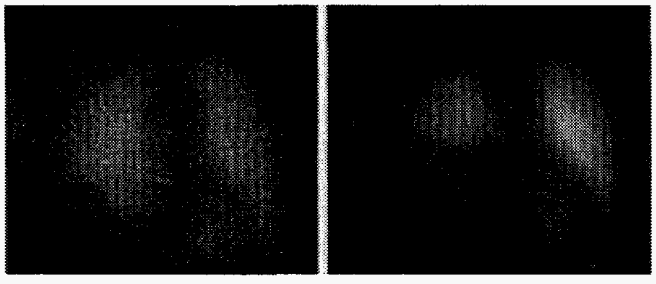

Figure 1. Lung ventilation image (left) and lung perfusion image (right) as seen from anterior view.

Figure 2. Template of lung segments as seen from anterior view.

Figure 3 shows a diagnostic map of the lungs generated by the techniques developed in this project. The medium grey areas show good ventilation the darkest areas show good perfusion, and the lightest areas show both good ventilation and good perfusion. This diagnostic map shows that while there is good ventilation in the anterior basilar segment of the left lower lobe, there is poor perfusion. Also, since the entire segment is affected, there is a high probability of pulmonary embolism. This confirms the physician's diagnosis. At this point, a physician can examine this diagnostic map and make a diagnosis. With additional work, a system could be developed to examine this diagnostic map and automatically produce the probability of a given disease.

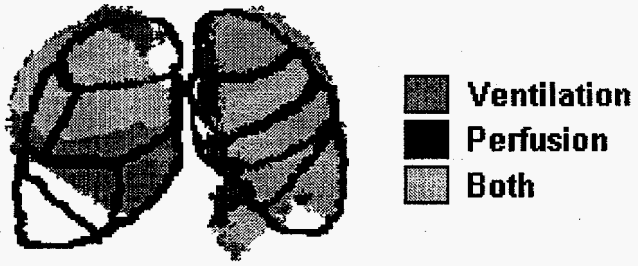

Figure 3. Diagnostic map showing ventilation (air flow) and blood flow (perfusion) in the lungs.

Results

While a complete prototype system was not finished in this effort, prototype software components of a system were developed and tested. Initial results show that an automated or semiautomated approach to the diagnosis of V/Q lung scans is feasible. Dr. Holmes, the physician collaborating on this project, was significantly impressed by the results achieved to feel that there is a potential for this approach. A complete prototype could be constructed by integrating the existing software algorithms developed and implemented in this project with the algorithms used in commercial software while also automating the manual steps. The diagnostic decision-making routine would still need to be developed. For this, a significantly larger data set (200 to 400 patients) would need to be collected. In addition, methods for combining the multiple patient views would need to be implemented.

Collaborative Environment Prototype for Molecular Science

James D. Myers (Computing and Information Sciences)

Project Description

At Pacific Northwest National Laboratory, we are developing the hardware and software infrastructure to acquire, archive, retrieve, analyze, and visualize scientific data. We are developing a collaboratory prototype environment for molecular research as the means to share data and its processing with external collaborators and enable more effective science to be carried out. We will work with researchers in nuclear magnetic resonance spectroscopy and molecular beam reaction dynamics to identify their needs and design the collaboratory environment to support them.

The advancement of the state of the art in science and engineering requires collaboration. Geographically disperse collaborations require new social and technological innovations. Networking and computer technologies have advanced to the point that computer-facilitated collaboration between remote scientists is practical and is being realized.

Technical Accomplishments

CY 1994 saw the completion of an initial prototype, development of a cross-platform screen sharing tool, deployment of the environment and several tools to internal and external groups, and the design and partial implementation of second generation of more World Wide Web (WWW)-centric tools based on user feedback. In addition, the project took the lead in developing a capability for low-cost desktop video conferencing. In FY 1995, the project completed the second generation WWW-based tools for several platforms, including an electronic notebook prototype, and began deployment of these tools.

The latest CORE software provides many of its capabilities by augmenting the WWW. To start or join a collaborative session, staff simply click the appropriate buttons on the WWW page, and all required software is launched on their computer. Hidden from the user's view are a central session manager and a desktop executive that coordinate communications between participants and configure the various components. The user can select from audio/video connections, whiteboards, chat boxes, synchronized WWW browsers, and shared application windows. Some of the components, such as the audio/video tool, have been developed elsewhere and are integrated into the CORE. Others, including the WebTour tool allowing a researcher to lead others on a tour of the WWW, and the shared application viewing tool have been developed by EMSL for the CORE.

Customized remote instrument control programs can also be launched through the CORE allowing users to run remote experiments or monitor remote tests.

Another CORE technology allows browsing of data through an electronic notebook. Researchers can browse through experiment parameters, graphs of data, and notes. A single click delivers a full dataset across the Internet and into the appropriate analysis or modeling software. Remote collaborators can analyze data and then enter text, images, graphs, data files, audio clips, etc., back into the shared notebook. Access can be restricted using standard WWW protocols.

Integration with the Research Process

As part of the Collaboratory, we studied the sociology of collaboration. Information on group styles, communication modes, and the capabilities of current tools has suggested strategies for tool development, as well as for organizational adoption of electronic collaborative technology. Based on interviews with PNNL researchers and their colleagues, we have identified a variety of research related tasks (training, data acquisition, consultation, analysis, paper writing, etc.) and a variety of collaboration types (peer-to-peer, mentor-student, interdisciplinary, and producer-consumer). The communications needs of each task/type were categorized in terms of type of data (text, files, voice, etc.), synchronicity (e.g., a conference versus email), interactivity (e.g., a lecture versus discussion), and work transitions (e.g., starting a conference to answer questions while looking at a notebook entry), they involved. This information was then used to guide development of CORE and our strategies for moving CORE into active use. An underlying philosophy of CORE is to provide access to both scientific assets (instruments, data, software) and generic communications tools (chat, video conferencing) in a seamless manner.

CORE Tools

The central user interface of CORE is the WWW page, allowing users to start or join sessions. Once the user makes a selection, all requested tools are launched on their desktop and all communications are started. The user does not see any addresses, machine names, port numbers, or other confusing technical details. The software hides them and manages everything automatically. CORE also shuts down all tools at the end of the session.

CORE offers a simple chat capability that allows multiple participants to send text messages to each other. Chat messages can be logged to a file for later perusal. CORE also provides a "paging" facility that allows remote users to catch their colleagues attentions with an audio beep.

Another tool in CORE is the WebTour. This tool synchronizes participants' WWW browsers and allows users to walk others through a series of WWW sites. WebTour can be configured to allow only lectures, where one person controls all browsers, or to allow discussions, where control is passed automatically between users.

Video conferencing in CORE is provided by CU-SeeMe, a video conferencing application for the Mac and PC (from Cornell University), and the UNIX based Multicast Backbone (MBONE) tools. The Collaboratory project has funded tests to provide external video conferencing across the firewall and supports a pilot system, started in August 1995, to provide CU-SeeMe capabilities internally and, via a Reflector Bridge, between researchers and their external collaborators. This facility was upgraded in September 1996 to provide color video. Connection to UNIX Multicast tools can also be provided, allowing true cross-platform video conferencing between Mac, PC, and UNIX workstations. Security and administrative plans have been developed to minimize the impact of video traffic on other network communications.

The EMSL TeleViewer gives CORE real-time application sharing capabilities. The TeleViewer captures a rectangle or window from the user's computer display, or the entire display, and repetitively sends it to all viewers. The TeleViewer uses loss-less compression and individual data streams to provide each viewer with the best performance their machine and network connection are capable of. The TeleViewer can be used for monitoring data acquisition by sharing the instrument control software window(s), or for data analysis and modeling, or for simple writing or graphing plots by sharing the window of a commercial word processor or scientific graphing program. The TeleViewer has received programmatic funding and will be enhanced to provide the ability to annotate and draw on the live image.

The project gained considerable experience with electronic notebooks through the use of the Virtual Notebook System (VNS). Experimentalists and theorists in three different groups at the University of Utah and PNNL have been connected over the Internet and can now make use of the VNS scientific notebook system to exchange and store text, graphics, and other information on UNIX, PC, and Macintosh computer platforms. The theorists on the project at PNNL can store images of molecular structures and diagrams of vibrational motions they have calculated to be used by the experimentalists at the University of Utah in their modeling efforts of collisionally induced dissociation reactions. We have worked closely with this group to learn the strengths and weaknesses of the notebook system. We worked closely with the VNS developer to improve the product, participating in two revision beta tests and testing a gateway tool that allows browsing the notebook from the WWW, but they have since abandoned the product.

We then began development of our own WWW-based notebook system. The current version of this system can integrate with data acquisition software and provide an automatic mechanism for loading data and metadata into the notebook. Information is organized into notebooks, chapters, and pages. Each page contains a collection of experimental data, images, text, tables, etc., organized into a series of threaded notes. The notebook can easily be extended to support new data types. Currently, the notebook shows mass spectroscopy data using a table listing the sample, voltages, and other experimental conditions, followed by a JAVA x,y graph of the data that allows researchers to zoom in on specific mass peaks and read x,y coordinates of individual data points. Other scientific data types will be supported through additional modules. The notebook also provides a simple login and security mechanism and allows viewers to respond to comments and data either in the notebook or via email. This work has also received programmatic funding and several user interface enhancements are planned over the next year.

Together, these capabilities provide an initial collaboration environment to researchers that allows them to work on a variety of tasks with external colleagues. Future work will both enhance this basic environment, and develop discipline/project specific tools for displaying and manipulating instrument controls, data, and analysis/simulation/modeling results.

Publications and Presentations

R.T. Kouzes, J.D. Myers, and W.A. Wulf. 1996. "Collaboratories: Doing science on the Internet." *IEEE Computer*, Vol. 29, Number 8, August, pp 40-46.

P.E. Keller and J.D. Myers. 1996. "The EMSL TeleViewer: A Collaborative Shared Computer Display" IEEE Fifth Workshop on Enabling Technologies: Infrastructure for Collaborative Enterprises, Stanford University, California, June.

J.D. Myers, J.M. Price, D.A. Payne, P.E. Keller, R.A. Bair, and T.H. Dunning. 1996. "An Environmental Molecular Sciences Collaboratory." Whitepaper, Pacific Northwest National Laboratory, Richland, Washington.

R.T. Kouzes. 1995. "The Collaboratory - Creating R&D laboratories without walls." Chapter in *Electronic Laboratory Notebooks and Collaborative Computing in R&D: Social, Legal, Regulatory, and Technology Issues*, (Eds.) R. Lysakowski and S. Schmidt, December.

J.D. Myers. 1996. "Down the hall while across the country: Remote collaboration via the Internet." EMSL Seminar Series, Richland, Washington, September 11.

J.D. Myers and S. Sachs. 1996. "Collaborative astronomy in the classroom: Internet collaboration tools." First Global Hands-On-Universe Conference, Stockholm, Sweden, July 29 - August 2.

J.D. Myers, C. Fox-Dobbs, J. Laird, D. Le, D. Reich, and T. Curtz. 1996. "Electronic laboratory notebooks for collaborative research." IEEE Fifth Workshop on Enabling Technologies: Infrastructure for Collaborative Enterprises, Stanford University, California, June.

P.E. Keller and J.D. Myers. 1996. "The EMSL TeleViewer: A collaborative shared computer display." IEEE Fifth Workshops on Enabling Technologies: Infrastructure for Collaborative Enterprises, Stanford University, California, June.

D.A. Payne and J.D. Myers. 1996. "The EMSL Collaborative Research Environment (CORE) - Collaboration via the World Wide Web." IEEE Fifth Workshops on Enabling Technologies: Infrastructure for Collaborative Enterprises, Stanford University, California, June.

J.D. Myers, K.R. Swanson, and R.E. Leber. 1996. "Collaborative astronomy in the classroom." U.S. Department of Education Linking for Learning: America's Technology Challenge and Beyond Region X Technology Conference, Kent, Washington, May 28.

D.A. Payne and J.D. Myers. 1996. "The EMSL Collaborative Research Environment (CORE) - Environmental collaborations via the World Wide Web." First Annual Environment on The Net Conference, Seattle, Washington, May 9-10.

P.E. Keller and J.D. Myers. 1996. "The EMSL TeleViewer: A collaborative shared computer display," First Annual Environment on The Net Conference, Seattle, Washington, May 9-10.

J.D. Myers. 1996. "Down the hall while across the country: Remote collaboration via the Internet." Emory University, invited Math and Computer Science Department Seminar, Atlanta, Georgia, April 1.

J.D. Myers. 1996. "Down the hall while across the country: Remote collaboration via the Internet." and "On-line instruments, on-line data." Collaboratory Technological Approaches for Geographical Information, Molecular Modeling, and Education Practices Workshop, West Virginia University, Morgantown, Virginia, March 29-30.

J.D. Myers. 1996. "Down the hall while across the country: Remote collaboration via the Internet." Clark Atlanta University, Invited Chemistry Department Seminar, Atlanta, Georgia, March 25.

Development of Intuitive User Interfaces

James A. Wise (Information Technologies)

Project Description

The objective of this project was to investigate the application of auditory displays to scientific visualization and analysis software. An example is the SPIRE system, which provides tools for analysis and exploration of very large text data bases in a spatial (visual) paradigm. Auditory display makes data audible, which is intrinsically difficult to visualize. Using the SPIRE system as a test bed, researchers at PNNL are creating experimental, audio-enhanced interfaces which take advantage of known strengths of both the visual and auditory perceptual systems, increasing the user's ability to glean meaning from massive amounts of information. The research led to development of a schema that organizes the auditory display into layers so that multiple sonification methods can be used without sacrificing intuitiveness and usability.

Technical Accomplishments

Even with careful interface design, SPIRE is a complex system with many interface elements. The amount of information that an analyst might need is sometimes greater than the visual interface can handle without sacrificing intuitiveness and simplicity. Graphical tactics such as iconifying, windowing, and magnifying expand the interface beyond the physical screen, but increase both the number of actions the user must learn in order to uncover information and the amount of attention the user must divert from analysis to interface management.

Auditory display has the potential to complement visual user interfaces by taking advantage of our auditory perceptual system's natural strengths—parallel listening, high temporal resolution, high dimensionality, etc. Sonification, the process of mapping source data onto audio parameters, has been successfully applied to many kinds of information. An early experimental prototype showed the potential of applying auditory display principles to the SPIRE Galaxies visualization. The prototype interface demonstrated flexible sonification, allowing the user to control how sound parameters mapped to different document characteristics. In this early prototype, the user moved a circular "microphone" across the SPIRE Galaxies visualization to hear whatever fell within its boundaries. When the microphone passed over a document, the user literally heard the sound of that document's characteristics, as expressed by variations in the pitch, volume, timbre, and duration of a note. This representation is not only much faster than reading a chart or list, but allows direct comparison of several documents at the same time, and can be more intuitive to an analyst. This early prototype served as an informal user-testing platform, and was demonstrated at the 1996 AIPA Conference.

Experience with the early prototype and further research demonstrated that although many sonification methods exist, no single approach was sufficient to meet SPIRE's diverse display needs. The application of auditory display to SPIRE required that we develop a unified plan for integrating multiple sonification methods into one seamless, aesthetic auditory environment. The next phase of research was based upon the concept of an auditory display schema, a unified plan for organizing data-to-sound mappings at all levels of the interface. To construct the schema, SPIRE information was categorized into three layers: system, objects, and domain attributes. Each layer was assigned a unique kind of sound (from a user's standpoint), corresponding to a set of sonification methods. For example, the objects layer represents information about the media type and size of each document. It does this by making sounds associated with a physical document. In contrast, the domain attributes layer represents individual themes by using orchestra instruments with their volume modulated according to the strength of the theme. All three layers generate sounds in parallel. However, because each layer is distinguished by its characteristic qualities (e.g., object sounds versus musical sounds), the layers act in concert to distinguish different kinds of information.

To illustrate how this works, we developed loudSPIRE, a prototype interface based on the auditory display schema. The construction of initial paper prototypes and audio mock-ups (by hand-playing data into an analog four-track recorder) enabled us to consider aesthetic and usability issues well before implementation. loudSPIRE was built on a Macintosh using a MIDI synthesizer as a sound generator. Preliminary feedback (from hands-on conference demonstrations and brown bag seminars) indicates that multiple sonification methods, organized by an auditory display schema, provide a promising complement to the SPIRE visual interface. Our experience with this schema and the loudSPIRE prototype directs future research toward the semantics associated with kinds of sounds, interdependencies between layers, and considerations of multi-layer listening.

Our work and results are documented in a PNNL technical brief, a WWW page, a videocassette, and the proceedings of two conferences.

Human Factors Evaluation of Immersive Virtual Environments Technology

Richard A. May (Information Technologies)
John S. Risch (Remote Sensing)

Project Description

In FY 1995, this project evaluated the value-added of immersive technology to scientific research and to develop guidelines for creating effective immersive interfaces. The two applications selected for study were a stratigraphic editor and an earth visualization system.

While the use of Non-Uniform Rational B-Splines (NURBS) as the underlying structure for the stratigraphic editor in FY 1995 proved ineffective, the concept of an immersive surface editor showed great promise. In FY 1996, we continued development on the surface editor. The goal was to 1) reexamine the mathematical models used to better represent the forces acting upon the surface; and 2) widen the scope of the surface editor to make it applicable not only for stratigraphic editing but other scientific disciplines such as fluid dynamics, molecular forces, and medical data analysis.

Technical Accomplishments

There were several potential successors to the indirect manipulation of NURBS previously used to represent the surface. The first was to expand on the basic NURBS interface. Traditional NURBS interaction is done via control points. These points affect the NURBS equations and the surface, however, but this indirect method of manipulating the surface makes it difficult to have fine control of the surface shape. NURBS also creates highly dynamic polygonal mesh densities. When a sharp bend is created in the surface, it is not uncommon to have the resulting polygonal mesh density increase by an order of magnitude. This is unacceptable for an Immersive Virtual Environment (IVE) where frame rates must remain constant. At a minimum, two improvements were required over the NURBS model: 1) to provide direct surface manipulation, and 2) constrain the resulting polygonal mesh generated for visual display.

Current papers on NURBS modifications address just these problems. Examination of these papers showed that even with these improvements NURBS were still too constrained and generated too much overhead to be effective. Other surface equations were examined but none were found to meet our requirements.

Our next (and final) approach was to develop our own underlying structure for each node of the polygonal mesh used to represent the surface. Under this model, manipulations to the underlying structure could directly affect the visual representation. This would eliminate the need for regeneration of the polygonal mesh at each frame and had the potential to provide the flexibility we needed for a generic surface editor. The model we selected to develop is a simple but extensible spring design. An underlying data structure is used to represent each node and the links between nodes.

Figure 1 shows a node, N0, and the links (L1, L2, L3, L4) connecting it to the four neighbors (N1, N2, N3, N4).

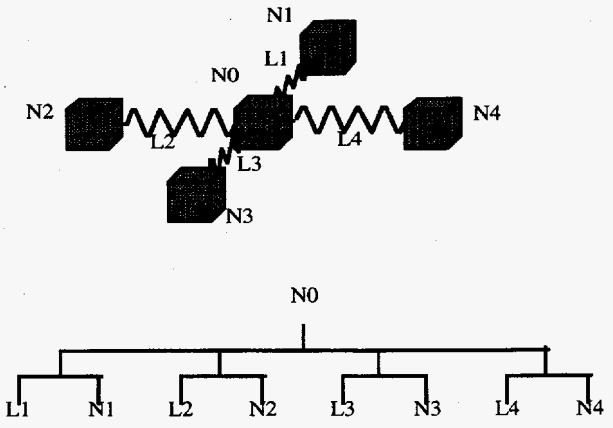

Figure 1. Model used to represent a node (N0) and the four neighbors.

Dampening coefficients, weighting factors, equilibrium constants, and other factors can all be set to define the type of surface response required in a particular application. This collection of nodes becomes a type of particle plane where moving one node affects the nodes around it in a chain reaction. The computations required at each node are simple Newtonian physics. Beyond the nodes and springs, the surface model also utilizes a modified hash table to efficiently locate the first node of contact between the surface and an external force like the tools discussed below.

The model is designed to allow interaction with the surface by using tools of various shapes and pressing them into the surface. This allows the user to mold, fold, and shape the surface as desired. While the surface is represented by a particle plane, the tool is simply the mathematical equation that represents the particular shape. The tools are rigid bodies and thus not deformed by collision with the surface. This means the equations for the tools remain constant and add no overhead to the process. Rather than performing polygon-to-polygon collision detection, the surface nodes can be tested against the mathematical "shape" of the tool. This results in a collision detection test on the order of O(n) rather than $O(n^2)$.

Currently only a simple surface and tool have been created and tested but the model meets our requirements for use in an immersive virtual environment. Direct manipulation provides finer and more flexible control over the surface shape than could be previously achieved. Overhead is not constant but the amount of frame-to-frame variation has been significantly reduced.

Information Visualization

James J. Thomas, Shawn Bohn, Marc Pottier, Kelly Pennock, Vernon L. Crow, Elena Overton, Chance R. Younkin (Information Technologies)

Project Description

Technology today requires a tedious manual process for the development and capture of a data integration scheme that is domain specific. This process identifies what can be linked by manually specifying the semantic relationship. Automation of this process has not been addressed. To be more widely used, automated methods for discovering, building, and maintaining these relationships must be developed. Additional research is the optimal method for computer representation. Storage of these rules is also required.

This project had several goals:

1. Develop a signal representation for structured documents. The methodology was built upon the research from the Text Understanding task under the initiative that produced the System for Information Discovery (SID) prototype.

2. Develop an alternative approach to navigating and exploring World Wide Web pages. Through the use of harvesting engines (such as Query_Lycos to query Lycos and LinkGoat to query Yahoo or specific http sites), visualization algorithms, web server, and JAVA visualization technologies, WebTheme was designed to provide an interactive and visual approach to searching for information on the web.

3. Define and develop principles of abstract cartography. In order to achieve this goal, it was necessary to select an application for focused development. The domain of text visualization was selected because of the availability of internally developed software tools, the requisite of spatialized information, and the ready outlet for technology.

4. Learn what kind of interactive visualization can be run effectively over Internet and determine the balance and distribution of visual analysis and computing—high-performance distributed computing via standard Internet.

5. Produce a flexible architecture for information visualizations.

Technical Accomplishments

Signal Generation from Structured Text

We developed two methods and used domain experts to determine which method worked best. Our approach was simplified by not including numerical data and minimizing the amount of categorical data used. We used SID as the basis for comparisons against our two methods. The first and second methods build from technology developed from SID. In our first method we approach defining a vector that characterizes a document similar to SID. However, our approach defined an array of vectors for each document based on the individual fields processed in the document. We then combined each vector for each document creating an agglomerate vector that represents the document as a whole. Dimensions that have common terms are combined and are appropriately weighted to reflect a topic from multiple fields. This agglomerate vector becomes our signal representation of the document.

The second approach used a graph theory approach to combining the array of vectors. The process was very similar to the first one in that each field is processed independently and array of vectors was developed for each document. However, an additional step was performed by creating a context graph of fields from the document form. The intent of this procedure was to capture the context of field relationships. It is expected that certain fields cannot stand alone and need context from other fields to provide an understanding about their topical matter. The graph structure captures this information and provided a framework for accentuating topical material in certain fields without losing context.

Categorical data was considered and used in the vector construction. It was necessary to include this data type because this type of data commonly exists in structured documents. Numerical data is also a common data type but was ignored for this data analysis. It will need to be examined and incorporated to better characterize documents in the future.

To validate our process, we selected documents from DOE's Occurrence Reporting and Processing System

(ORPS). Part of our initial background research was to define a test set where domain experts were available to validate our results. Additionally, the test set had to have a large enough breadth of subject matter to be expanded in further studies. The ORPS program office provided us with approximately 2000 reports from across the DOE complex from which we could choose. One hundred reports were chosen to expedite the processing and analysis of the data.

In order to validate our methodology, projections of the high-dimensional document space were constructed and these results were evaluated by the local DOE-RL ORPS program. We used two approaches in spatializing the document space. For the validation session with the domain expert the clustering spatialization approach was only available based on time constraints. The multidimensional scaling (MDS) technique was also used to provide an alternate view.

Through processing and studying the data the following conclusions were made:

- A larger sample size, at least 500 documents is needed to validate the method. This was determined after conferencing with the domain experts and examining the vocabulary sizes for the data used.

- The MDS approach appears to provide a better understanding of the information space than the clustering approach. A major reason for this is the small number of documents. It has been shown empirically that the MDS approach tends to produce better display for a smaller number of documents.

- SPIRE will need to be modified to handle fielded data. As vectors are agglomerated from the different fields their topical dimensions in one field may be noise in another. The software will need to compensate by recognizing terms are associated not with just a document but a field. This will directly improve Themescape and queries.

With respect to our methodology:

- This approach provided a good initial start to understanding the difficulty in processing, user perception, and interaction with fielded data.

- The methodology could be greatly improved by directly accessing the association matrix that SID produces for each field. This will allow for greater correlation among the cross terms that exist from other fields when agglomeration occurs.

- Field data provides an explicit method for weighting fields to provide a greater focus. Our method use that information to insure context for other fields are not lost but accentuate if their is a field cross-over topic.

The domain experts provided some major comments for directions:

- When examining the galaxy space the document characterization needs to convey a focus or allow the user to define the focus. Some parties/users are only interested in certain fields and are interested in how related to other content in the field. The expectation is that the domain expert should recognize the focus and it should "jump" out at him/her.

- Trending is major focus in recognizing structure or patterns rather than a static picture.

WebTheme

WebTheme was developed to create an alternate approach to navigating and exploring world wide web pages. Through the use of harvesting engines, visualization algorithms, web server and JAVA visualization technologies, WebTheme was designed to provide an interactive and visual approach to searching for information on the web.

The general approach used in WebTheme is to harvest descriptions of web pages (whether these be automatically generated abstracts, or full text pages), process their contents through the SID (System for Information Discovery) text engine, and visualize the resulting themes and topics as both a Galaxies and Themescape visualization.

The WebTheme visualizations allow a user to rapidly and interactively evaluate the contents of thousands of web pages in a single visual image. Themes and topics found within the web pages are automatically identified and labeled, allowing users to identify regions of interest and focus their retrieval and analysis tasks on information which is relevant to their task.

To be an effective alternative to browsing and retrieving information on the web, WebTheme was designed to be a cross-platform solution. The most effective way of doing this was to leverage off existing applications such as Netscape to provide the vehicle for interacting with the server and delivering the visualizations to the users desktop. With incorporation of JAVA into the Netscape browser, applets or small applications allowed us to explore the possibility of setting up a WebTheme server capable of servicing visualization and query requests and shift the processing responsibility for interacting with visualizations to the users desktop machine.

The resulting architecture is a distributed visualization engine capable of handling harvesting and visualization

requests from many different users regardless of their physical location or platform type.

Information Maps

As previously mentioned, our first effort was to define the elements or components of abstract cartography in order to define the boundaries of research in this new field. We have identified five major sections of research within the field that are of most immediate interest for the purposes of advanced information visualization: map semeiotics, map themes, map presentation, map transforms, and discrete space characterizations.

Several prototype algorithms and displays that illustrate some applications of abstract cartography specifically with regards to the SPIRE information visualization system were developed and are summarized as follows.

1. Map Symbols

The table below contains a set of map symbols for the SPIRE system, along with characteristic examples of their instantiation. Each of these symbols can be defined automatically by the system with existing knowledge already contained within current data structures.

Symbol	Definition	Physical Ex.	SPIRE Ex.
landmark	location of significance	historical site	document of interest
node	object with unique identify	city	cluster centroid
path	established course of travel	highway	n space path, user path of exploration
district	area with one or more common characteristics	state, county	area of similar content
barrier	object restricting access or movement	highway detour	area of non-interest within the information space
description	definition of map symbols	label as in city or state name	peak label

*scale dependent

In Figure 1, story boarded examples of an information space containing some of the predefined symbols is provided.

2. Map Themes

Our efforts have produced an incomplete set of abstract cartography themes relevant to the domain of text visualization. In brief, the process of creating a generalized document description visualization is illustrated in Figure 2. It involves projecting documents from an n-space vector to two space, and then characterizing each document according to one of several possible functions (themes). After computing the value for each theme as a function of the document, the individual document values, initially

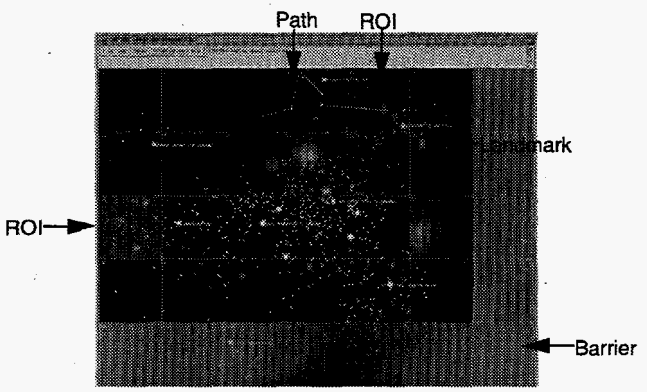

Figure 1. Map Symbols

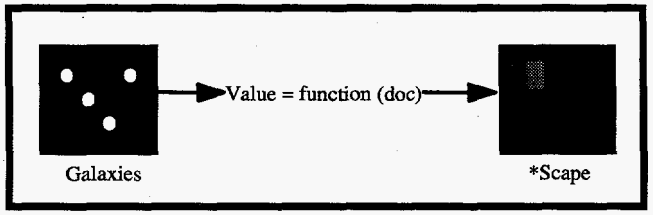

Figure 2. *Scape Construction

residing as a scalar value with 2D coordinates, are smoothed by an exponential hat function to produce a three dimensional visualization of the theme.

Examples of some of the themes defined are found in the table below:

*Scape	Content	f Arguments
ThemeScape	frequency of selected key terms	key terms
QueryScape	proximity to selected query	distance measure between document and query
TimeScape	recentness of document	document time stamp
ErrorScape	magnitude of placement error (possible difference between nearest neighbors in n space and 2 space)	doc ID
LengthScape	length of document	document size

Several of these different Scape algorithms have been implemented. Files are available for viewing in .gif format.

3. Map Resolution

As with theme algorithms, prototype variable resolution algorithms were developed to experiment with a variable resolution display. These algorithms were developed primarily to address the issue of scaling to large datasets, but can also be used to support variable resolution displays, activity monitoring in low resolution, spatial filtering, and even some of the dynamics of cellular automata

described previously. The algorithms were applied to existing data sets in order to determine effectiveness.

In this project, each of the areas selected for prototype development showed promise for more effectively conveying information in complex information spaces. We believe that each of the areas identified within this report could benefit significantly from further research and development; but further, we also believe that current text visualization efforts could benefit immediately from the inclusion of several elements of functionality discussed in this report.

Remote and Dynamic SPIRE Web Visual Analysis

The first step was to implement a simple yet functional version of the "Galaxy" visualization as a JAVA applet. This was used to visualize several typical SPIRE-generated data sets from within Netscape 2.0 browsers running on Solaris and Windows-95 platforms, and immediately validated the concept. Then, the much more complex Themescape™ visualization was refined for client/server application and ported to JAVA. Again, tests on several typical SPIRE data sets yielded very encouraging results.

In late March 1996, these applets were demonstrated live at a session at the AIPA96 Conference for the U.S. Intelligence Community. The favorable response was overwhelming. Following the conference, this effort was merged with the LDRD research effort that led to the development of WebTheme™.

The initial research and subsequent WebTheme™ integration effort taught us a good deal about where to build the boundary between the client and the server in order to attain acceptable performance. The kind of client/server architecture effected by a JAVA applet, with its downloaded virtual machine code and necessary security firewalls, does not always yield to traditional techniques for performance optimization. The primary techniques, of course, are to put computation on the server side and interaction on the client side, and to minimize network traffic. The "trick" is to architect the software such that this division is realized without sacrificing other desirable traits, such as functionality and good programming practices. While we gained considerable insight, we still have much to learn in this area.

Flexible Architecture for Information Visualizations

Our goal in this task was to define the requirements of a flexible architecture for information visualization. We, therefore, set out to define the major needs of information visualization, from a data oriented point of view. The main goal of information visualization applications is to provide information about data in a visual, easy to understand, and easy to manipulate, manner. Due to this, there are three major areas of data modeling/management that need to occur. The first is the management of the data itself.

In large-scale applications this may be terrabytes of data to be processed. Since our example of information visualization is SPIRE and SPIRE uses textual data in the form of documents - this is where we focused research - how to manage terrabytes of documents. The general conclusion so far is that a client server model would be needed since even today's machines don't have the capability of storing that much data. And it would be redundant if two analysts were processing the same data on two different machines.

The second big data modeling/management issue is the information gleaned from the data. We need to model that information in such a way that it can be visualized. Also, the data model needs to be flexible enough to be visualized in many different ways, and queried, and archived etc. A relational data base would not be able to handle the complexity of the visualizations and the underlying data structure. That brought the conclusion that an OODB would be necessary. Research on large OORDBs shows that they would probably be two slow and have the same problems of an RDB since they still store things relationally.

The third data management question is how to tie everything together. How does an information visualization application keep track of the data put into it, the data it uses for processing, the data the user enters (i.e., changeable parameters) and finally the visualizations and other output data. Again, the answer seems to be a client/server OODB as the basic building block of the information visualization application.

For flexibility the information visualization application has to be able to grow or shrink as to the clients needs. It also needs to facilitate and not hinder ongoing and new research. An architecture that modularizes the processing from the data management from the GUI/Viz is a model that will allow for maximum flexibility. The place to start in a model such as this is an underlying data model and a system to manage that model.

Medical Imaging Three-Dimensional Reconstruction and Visualization

Richard A. May (Information Technologies)
Randy W. Heiland (Computer and Information Sciences)

Project Description

The use of immersive virtual environment (IVE) interfaces for medical applications has the potential to reduce the cost of health care. Part of the cost associated with health care today stems from the need for a medical professional to rigorously analyze images from patient data in order to make important decisions that will determine future treatment. Traditionally, the medical professional interacts with three-dimensional data on a two-dimensional computer screen via dial and mouse movements. An immersive virtual environment could provide a more natural and intuitive interface to the data, thereby reducing the amount of time involved in the analysis.

This project focused on volumetric data and the development of superior interactions and interfaces. The goals were 1) develop a volumetric data analysis capability, 2) build on our scientific visualization research, and 3) create more intuitive interfaces for volumetric data analysis.

Technical Accomplishments

To facilitate project development, two prototype volume rendering applications were developed; VRend and VRend-I. VRend is a nonimmersive prototype—it uses traditional technologies for display and interaction. Vrend-I is an immersive version that provides the same basic volumetric analysis functionality.

The creation of two independent applications was very important for project development. VRend provided a software environment in which we could develop innovative volumetric tools and techniques that could then be incorporated into VRend-I. This left us free to focus on development of immersive interface functionality within VRend-I. Additionally, VRend does not require the hardware of an immersive virtual environment, allowing the software tools to be developed on a personal workstation, thereby freeing up the hardware and its associated high-demand computer for strictly immersive virtual environment software development. Second, the VRend application served as a standalone demonstration which could be used as backup when the immersive virtual environment hardware was otherwise utilized or could be taken "on the road" since it did not require that hardware. Third, it provided us an opportunity to broaden our expertise in the defacto standard graphics language OpenGL as well as user-interface development languages. Currently, both VRend and VRend-I applications run on a Silicon Graphics UNIX workstation with VRend-I requiring a run-time license for the virtual environment simulation engine. With minor modifications, both can be made to run on most personal computers or workstations that support the OpenGL graphics language.

The prototypes import 8-bit, rectilinear, scaler volumetric data. There is no requirement that the data be of a medical nature. Volumetric analysis tools have been created to generate rendered images that reveal various structures within the data; interactively rotate, zoom, and scale the volume; interactively reclassify the data (control what structures are highlighted by interactively changing ramps that assign "weights" to ranges of values in the data); interactively select and visualize orthogonal and arbitrary slices of the volume; erase user-defined sections; and apply three-dimensional filters.

The creation of the immersive interface for VRend-I focused on 1) providing a superior data management system for volumetric and image data sets, and 2) design for use of the software at the point of care for the patient. Designing for use by medical professionals while data is being collected meant the immersive technologies utilized had to be nonintrusive. Interaction with VRend-I is accomplished with either a Spaceball (a 6 degree-of-freedom input device) or the Pivot tracker (a 3 degree-of-freedom input device). The environment can be displayed on either a traditional flat screen or through the immersive Desktop Boom system. All of these devices are non-encumbering and allow the user to move in and out the immersive environment at will.

The basic design concept for the immersive virtual environment is shown in Figure 1. The user is placed in the center of a sphere and information is portrayed on the inside surface of the sphere. The spherical work space provides several advantages over the simple desktop metaphor. All information (volumetric data, image slices, graphs, etc.) is always directed at the user thus, providing the maximum visible surface area. The user can zoom in/out and pan around the environment,

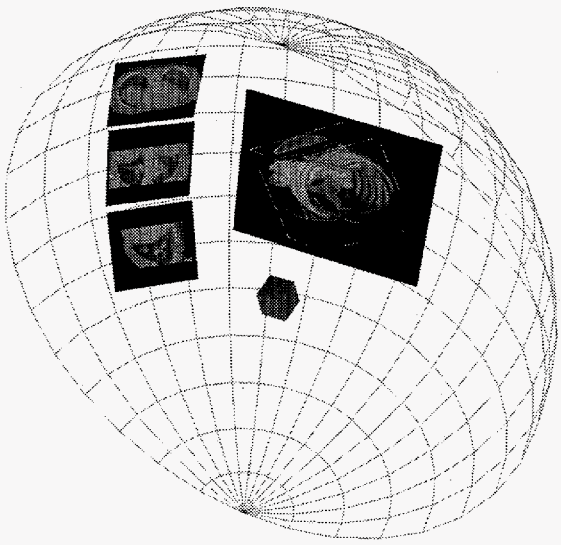

Figure 1. IVE design. The cube in the exact middle defines the user viewpoint. The larger image is the typical location of the volumetric data set. The three smaller images would be typical placement for slices.

control the size of the sphere, and change the relative displayed resolution of the data. Combined, these allow for the work space to be resized depending on the quantity of information displayed. There is no limitation on the amount of information displayed due to screen real estate or image resolutions. Similar to the physical work environment, VRend-I allows the user to organize data spatially. Information can be grouped and placed in locations selected by the user. An example would be for old data to be placed in the upper left, new data just below center, and current data being worked on in the center and to the right. In essence, the data can be organized in any fashion preferred by the individual.

Current immersive functionality incorporated into the immersive virtual environment includes a three-dimensional cursor to allow the user to browse through volumetric data, selection of three-dimensional subvolumes of a volumetric data set, grabbing of orthogonal slices from a volumetric data set, and selection and moving of slices on the sphere surface. The existing functionality is only a sample of the potential. Techniques could be developed for grouping of slices to minimize space and help organize data. Annotation of data by text, voice, and drawing both statically and temporally would allow users to pass information between each other and between sessions.

Initial user response has been positive. This work represents a major shift in how medical professionals will interact with and organize electronic image data. Because of difficulties in the development of the immersive virtual environment, a stable version was just completed at the end of the project. This has limited the amount of user input to date.

Molecular Visualization on Parallel Computers

Randy W. Heiland (Computer and Information Sciences)

Project Description

The objective of this project was to develop parallel visualization software, i.e., software that would run concurrently on multiple processors, for the display of various three-dimensional molecular datasets. The primary goal during FY 1996 was to develop a parallel software application that would compute and display molecular orbitals of a chemical system.

Technical Accomplishments

Molecular science generates many three-dimensional datasets—either from computer simulations or from measured experimental data. A scientist often wants to display such data in graphical form for a variety of reasons. For example, given a three-dimensional temperature field of a waste tank, one might want to see the relative location of "hot spots"; or, for a computer simulation, one might want to visually verify that an iterative calculation of a particular three-dimensional scalar field is progressing normally. Ideally, we would like such visualizations to be computed fast enough so that interactive viewing is possible. This is the goal of parallel rendering when dealing with very large datasets.

There are two classes of rendering algorithms associated with three-dimensional scalar data: surface-rendering and volume-rendering. A common example of a surface-rendering algorithm is one that displays an isosurface, i.e., a surface of constant value, within the three-dimensional data. This technique generates (potentially) hundreds of thousands of polygonal facets that need to be rendered as two-dimensional pixels onto the computer screen. A parallel algorithm using the EMSL-developed Global Arrays toolkit was implemented in FY 1994 to display such a polygonal dataset.

A focus of the project in FY 1995 was on volume-rendering. A volume-renderer, unlike a surface-renderer, attempts to display the entire three-dimensional field. Another focus of the project in FY 1996 was to develop parallel software that could compute and display molecular orbitals (MOs) of a chemical system. Molecular orbitals are used to approximate the wave function of a molecule and offer some insight into the bonding possibilities within a chemical system. For this project, we deal only with molecular orbitals that are linear combinations of atomic orbitals (LCAO MOs). Furthermore, we compute only Cartesian MOs, i.e, molecular orbitals defined over a three-dimensional rectilinear grid.

After a substantial amount of experimentation with the various parallel software development tools at our disposal, including TCGMSG, Message-Passing Interface, and various shared-memory programming utilities (Global Arrays, etc.), a decision was made to use the native "share group process," sproc, utility available on the Silicon Graphics multiprocessor Onyx workstation. This decision was based on the best performance we received with a minimal programming effort. To compute the molecular orbital field over a three-dimensional rectilinear grid, we simply perform a slab decomposition of the domain along one axis, sending one slab to each processor. No load balancing problem exists since we compute a molecular orbital value at each grid point and each point evaluation depends on the entire set of atoms (and associated basis functions) in the chemical system. After computing the molecular orbital field, each processor then uses the Silicon Graphics Molecular Inventor graphics library to display color-coded isosurfaces of the positive and negative lobes of the molecular orbital. A load balancing problem will likely exist at this stage since an isosurface will not typically be homogeneous throughout the entire three-dimensional domain. To control the various calculation and visualization parameters, a rudimentary graphical user interface is also part of the application. This application can be run remotely on a multiprocessor Silicon Graphics with the Molecular Inventor library if the client workstation has the OpenGL graphics library. In Figures 1, 2, and 3, we show an example.

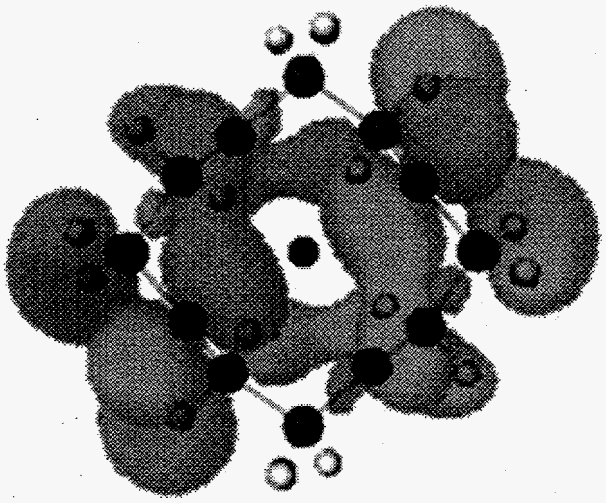

Figure 1. Highest occupied molecular orbital for a crown ether molecule (K + :12C4) shown as partially transparent isosurfaces. The grayscale image unfortunately loses the color-coding of the positive and negative lobes of the MO. (MO coefficient data provided courtesy of Dr. David Feller running Gaussian94™.)

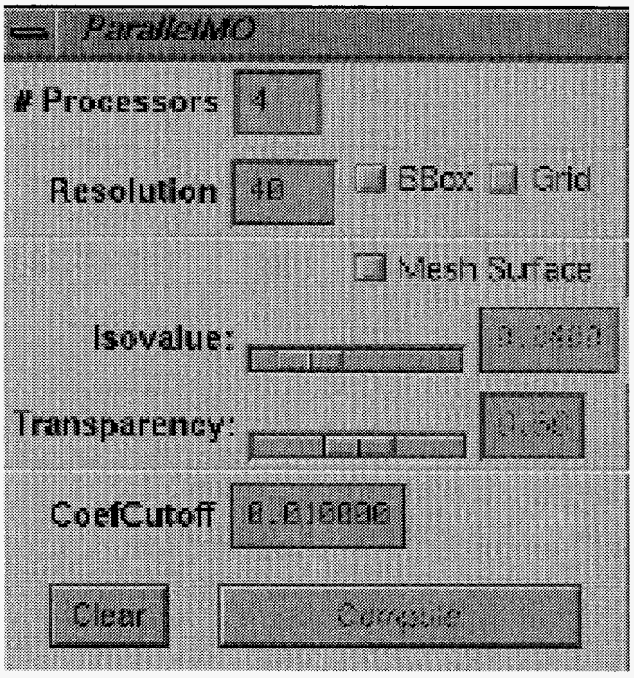

Figure 2. The graphical user-interface.

Figure 3. Computation and display times using 1, 2, 3, or 4 processors.

Publications and Presentations

R.W. Heiland. 1996. DOE Computer Graphics Forum, May 7.

R.J. Littlefield, R.W. Heiland, and C. Macedonia. 1996. "Virtual reality volumetric display techniques for 3-D medical ultrasound." Medicine Meets Virtual Reality Conference IV, San Diego, January 17-20. (This paper, which was published on the World Wide Web, demonstrates the use of volume rendering for three-dimensional medical datasets. This work was a direct outgrowth of this LDRD project.)

Neural Network Data Processing for Sensor Applications

Paul E. Keller (Computing and Information Sciences)

Project Description

The objective of this project was to develop and demonstrate the potential data processing capabilities of artificial neural networks in sensing applications. This effort concentrated on the problem of identifying unknown objects (e.g., contaminants) in the environment from their sensor signatures. This work involved the development of neural network techniques for automated sensing applications and an evaluation of whether the neural network approach is beneficial to these applications. In FY 1996, neural network techniques were applied to the analysis of spectroscopic data. Due to funding priorities during FY 1996, this project was cut short prematurely with only half of its objectives completed.

Technical Accomplishments

An artificial neural network (ANN) is a computing architecture derived from a rudimentary understanding of the brain. It is basically an information processing paradigm composed of a large number of highly interconnected processing elements (neurons) working in unison to solve specific problems, and it can be implemented in either hardware or software. Artificial neural networks are generally used for pattern recognition, prediction, decision making, and modeling.

Unlike more traditional analysis techniques (including chemometric methods), artificial neural network techniques lend themselves to situations requiring automation or real-time data processing. Once an artificial neural network is trained for an analyte recognition task, operation consists of propagating the data through the network without human intervention. Since this is simply a series of vector-matrix multiplications, unknown analytes can be rapidly identified in the field. However, artificial neural network techniques tend to give qualitative results and thus are not applicable to situations requiring precise measurements.

During FY 1994, we designed and built a prototype electronic nose from an array of 10 tin-oxide sensors, data acquisition system, computer, and artificial neural network software. During FY 1995, we concentrated on the development of artificial neural network techniques for analyzing chemical sensor data.

During FY 1996, we concentrated on developing neural network techniques for analyzing spectroscopic data. Spectroscopic data differs from other forms of sensor data in the number of points in a data vector (i.e., resolvable chartificial neural networkels in the spectrum). Much of the FY 1996 effort in this project was centered on exploring methods for extracting the pertinent information from the spectra before applying a classification technique. We assumed that most of the important information in a spectrum used for classification was limited to a small proportion of the spectrum's resolvable elements (i.e., chartificial neural networkels, resolvable wavelengths, resolvable masses, etc.). We examined and developed several artificial neural network-based methods for preprocessing the spectroscopic data. For testing, we received a set of 5400 mid-range infrared spectra of stellar atmospheres from NASA, a set of 2000 time-of-flight mass spectra data of air pollutant aerosols from Kim Prather, a collaborator at the University of California at Riverside, and a set of 6400 mass spectra of common compounds from NIST.

One of the techniques we explored was the artificial neural network equivalent to nonlinear principal component analysis. In this technique, an artificial neural network with a input layer, mapping layer, bottleneck layer, remapping layer, and output layer is trained with back propagation to autoassociate each spectrum (i.e., reconstruct the input spectrum) in a set of spectra. An acceptable reconstruction error is chosen. The number of nodes in the mapping layer is varied, and the artificial neural network retrained. When an acceptable reconstruction error is found, the artificial neural network from the input layer to the bottleneck layer represents a feature extractor with each node in the bottleneck layer representing a unique feature of the input spectrum. This technique can be used as either an unsupervised classifier for clustering unlabeled spectra or as a feature extractor for a supervised (i.e., known classes) classification system.

Another approach tried was an implementation of the Kohonen self-organizing map. A self-organizing map is a type of unsupervised artificial neural network. In this approach, similar spectra are clustered together. Our results were mixed. In some cases, spectra of similar compounds were clearly clustered together, while in

other cases the reason for clustering was unclear. Due to a funding recision, we were unable to optimize this approach.

We implemented a sensitivity analysis method to reduce the number of inputs to our artificial neural network classifier. This technique selected the more sensitive inputs by thresholding the largest weight going out from each artificial neural network input processing element. In this experiment, we used an autoassociative artificial neural network which was trained to reproduce at the output the spectrum presented at the input. The spectra were forced through a hidden layer with reduced numbers of hidden nodes. This in turn caused the weights from the input layer to adjust so that only the most relevant information was used through selective use of the spectrum. Weights from input nodes corresponding to relevant inputs tend to increase and irrelevant channel weights tend to decrease.

We began formulating a novel method for spectrum classification which involved an artificial neural network spectrum classifier coupled with a spectrum simulator for use in identifying concentrations of component compounds in a sample. In this approach, the classifier would make an initial estimate of the composition. This estimate would be used to control a spectrum simulator which would generate the ideal spectrum for the estimated combination of compounds. This spectrum would be compared to the actual spectrum, and the comparison would be fed into the classifier for adaptive tuning. Again, due to the funding recision, we were unable to complete the development of this technique.

In FY 1996, the research from this project resulted in three presentations and the publication of a book on the applications of neural networks in environment, energy, and health.

As part of our effort to develop collaborative efforts with the outside world, we continued to maintain a World Wide Web server on the field of artificial neural networks.

Publications and Presentations

P.E. Keller, S. Hashem, L.J. Kangas, and R.T. Kouzes, Eds. 1996. *Applications of neural networks in environment, energy, and health*, World Scientific Publishing Company, Singapore.

P.E. Keller, L.H. Liden, L.J. Kangas, S. Hashem, and R.T. Kouzes. 1995. "Electronic noses and their applications." IEEE Technical Applications Conference, Portland, Oregon, October 12.

J. Griffin. 1996. "Electronic noses." The 82nd artificial neural networkual Northwest Food Processors Convention and Exposition, Portland, Oregon, January 21-23.

P.E. Keller, L.H. Liden, L.J. Kangas, S. Hashem, and R.T. Kouzes. 1996. "Electronic noses and their applications." World Congress on Neural Networks, San Diego, California, September 15-18.

Property Prediction from Molecular Dynamics Simulation

Bruce J. Palmer (Theory, Modeling, and Simulation)

Project Description

This research was aimed at extending the ability to accurately calculate bulk thermodynamic and transport properties of molecular fluids and solids using molecular dynamics simulations. The work was divided into two major tasks. The first focused on calculating a comprehensive set of bulk thermodynamic and transport properties for simple molecular liquids. The constant pressure heat capacity, viscosity, and thermal diffusivity were calculated for molecular models of water and carbon dioxide at several points along the liquid-vapor coexistence curve. The second major task was to extend a molecular dynamics technique developed for calculating the liquid-vapor coexistence curve for simple atomic liquids to molecular liquids. This was used to calculate the liquid-vapor coexistence of carbon dioxide.

Technical Accomplishments

A series of simulations were performed using the extended simple point charge (SPC/E) model of water and the Murthy-Singer-McDonald model of carbon dioxide. These simulations were focused at obtaining standard bulk properties of molecular liquids. To speed up the calculations, a rather drastic truncation of the long-ranged Coulomb interactions was used, but reasonably quantitative results when compared to experiments were still obtained for many properties. Constant energy simulations were used to obtain the shear viscosity, thermal diffusivity, and constant volume heat capacity, while simulations at constant temperature and pressure were used to obtain the constant pressure heat capacity. The results of shear viscosity and thermal diffusivity calculations on SPC/E water are summarized in Table 1. The SPC/E model does a good job of modeling the transport behavior of water at higher temperatures, but gives poorer agreement at lower temperatures. However, all computed values are within 50% of the experimental numbers, and most of the computed values are considerably better than that.

Table 1. Calculated and experimental values of the shear viscosity, ν, and thermal diffusivity, D_T, for water as a function of temperature.

Temp. (Kelvin)	Calculated ν (cP)	Experimental ν (cP)	Calculated D_T ($10^3 \times cm^2/s$)	Experimental D_T ($10^3 \times cm^2/s$)
298	0.581 ± 0.012	0.983	1.72 ± 0.13	1.45
373	0.286 ± 0.005	0.279	2.14 ± 0.19	1.69
473	0.138 ± 0.015	0.134	1.57 ± 0.18	1.69
573	0.096 ± 0.003	0.090	1.31 ± 0.16	1.29

A significant amount of effort was also focused on developing methods for determining the phase diagram of simple molecular liquids using an extension of a molecular dynamics version of the Gibbs ensemble algorithm originally worked out for simple atomic liquids. The Murthy-Singer-McDonald model of carbon dioxide was used as the original test case for this method, although some preliminary studies using the SPC/E water model have also been performed. As an independent check on the accuracy of the results, a separate set of simulations using 1000 molecules of carbon dioxide in a rectangular box were also performed. The dimensions of the box where chosen to be large enough so that both the liquid and vapor phases would form. A density profile for the 1000-molecule simulation of carbon dioxide at 210K is shown in Figure 1. Also included in the figure are four values of the vapor phase density calculated using the Gibbs molecular dynamics algorithm. The four separate values of the vapor density are calculated using different parameters in the coupling potential. The vapor densities should, in principle, be independent of these parameters, so the spread in values is an indication of numerical instabilities in the algorithm. However, at

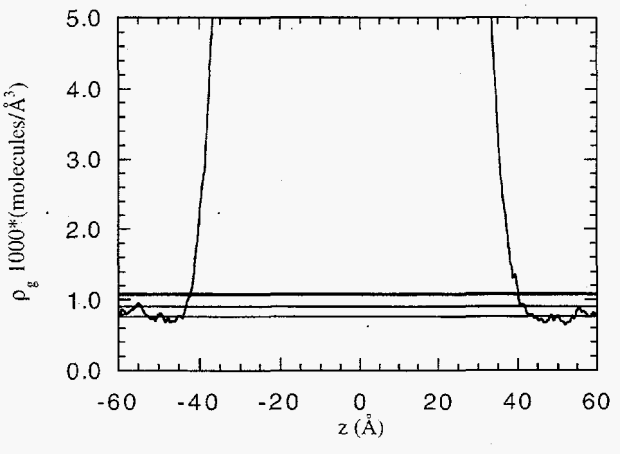

Figure 1. Density profile for 1000 molecules of MSM CO_2 in a $32 \times 32 \times 120$ Å box. Also included are four values of the vapor density calculated using Gibbs ensemble MD simulations for four different sets of coupling parameters. These are shown as horizontal lines.

least two of the vapor values calculated from the Gibbs ensemble method are in reasonable agreement with the direct simulations of the two-phase system. The remaining two values from the Gibbs ensemble simulation are somewhat high when compared to the direct simulation.

Publication

B.J. Palmer. "Generalization of the Gibbs ensemble molecular dynamics calculation to rigid molecule systems." (in preparation).

Ecological Science

Coplanar PCB Congener Separation and Quantitation

Lisa F. Lefkovitz, Thomas J. Gilfoil (Marine Sciences Laboratory)

Project Description

A number of DOE facilities currently have identified sites where polychlorinated biphenyls (PCBs) are present and pose a threat to both human and ecological health. These include Oak Ridge, Lawrence Berkeley Laboratories, Stanford Linear Accelerator, and the Portsmouth, Ohio, facility. Presently we are analyzing PCBs in air samples collected in the 200 Area of the Hanford Site as part of the Hanford Environmental Monitoring Program. The Hanford Site has been found to have mixed plutonium/ PCB waste that will need remediation. If the level of hazard coming from the PCBs can be determined based on the coplanars, rather than on total PCBs, there is a chance that the amount of material that needs remediation could be reduced.

PCBs consist of over 200 individual compounds. The coplanar congeners are considered to have a high level of toxicity compared with other noncoplanar PCBs. The toxicity of these congeners has been estimated to be equivalent to that of 2,3,7,8 tetrachlorinated dioxin. The ability to identify and quantify these highly toxic, coplanar PCB congeners is valuable for any study involving assessment of the risk posed by PCB contamination both in the marine and nonmarine aquatic environments, as well as in terrestrial systems where PCBs are highly persistent and readily bioaccumulated. Currently, the only available method to analyze for the coplanar compounds involves using expensive and complex techniques, such as high-resolution gas chromatography with high-resolution mass spectrometry. The purpose of this work was to demonstrate a simpler and less costly separation and analysis using a newly developed liquid chromatographic column coupled with gas chromatography/mass spectrometry with negative chemical ionization (GC/MS NCI).

Technical Accomplishments

Analytical work to achieve the separation of coplanar congeners using high-performance liquid chromatography coupled with quantitation using GC/MS NCI was completed. Separation of 3 coplanar PCBs (PCB 77, PCB 126, and PCB 169) and 1 semiplanar congener (PCB 81) from the other 100 or so PCB congeners generally present in environmental samples was accomplished. Initial testing involved confirming the method and determining detection limits based on the limitations of the instruments. These instrument detection limits (IDLs) are presented in Table 1.

PCBs tend to accumulate in organic-rich soils and sediments and aquatic tissue in concentrations that begin to pose both human and ecological health risks. The ability to isolate the extremely toxic coplanar PCB congeners from over 100 other PCB congeners in these complex matrices is a valuable tool. Methods were developed to isolate these compounds in specific matrices including soils, aquatic sediment, and fish tissue. Method detection limits (MDLs) were developed for tissue by spiking seven replicates of a clean mussel tissue sample. MDLs were calculated by multiplying the standard deviation of the replicate results by the Student's t-value at the 99th percentile for n = 7. Tissue MDLs are presented in Table 1.

Table 1. PCB Coplanar IDLs and Tissue MDLs

PCB Congener IUPAC Number	IDL[a] (ng/g)	Tissue MDL[b] (ng/g wet weight)
PCB 77	0.0074	0.031
PCB 81	not determined	0.021
PCB 126	0.0012	0.0043
PCB 169	0.0006	0.0033

(a) IDL assumes that 20 grams of sample were analyzed.
(b) MDLs were determined using 20 grams of tissue.

Electronics and Sensors

A Real-Time Adaptive Intelligent System for Sensor Validation

Francis G. Buck, Ray Pugh (Engineering and Analytical Sciences)
Daniel R. Sisk (Environmental Technologies)
Tye R. Blackburn (Decision, Safety and Risk Management)

Project Description

The objective of this project was to develop a functional real-time system-level sensor input validation diagnostic for typical open and closed loop process systems. The purpose of this research is to provide the capability for on-line engineering and operational support for reducing both the risks and the cost of operations and maintenance for industrial plants, utilities, and other process applications.

Sensors are used to measure process variables for control, monitoring, and data collection systems. The accuracy and validity of the sensor input greatly affects the product result which uses the sensor input data. To ensure that reliable input is used, a mechanism for validating or ensuring that the input is correct and flagging incorrect data is required. A sensor validation process can be developed at the system level (i.e., a group of individual components with sensor inputs) such that the system's internal dynamics (i.e., mechanical, hydraulic, and electrical energy balances aspects) of the process can be used to monitor, compare, evaluate, and determine acceptability of sensor inputs.

Technical Accomplishments

In this project, we used an integration of model-based reasoning, neural networks, and expert system artificial intelligence software paradigms to develop the validation module for the system in Figure 1. The modeled system is an example of typical open and closed loop fluid systems used for heat transfer. As with an electrical circuit, an energy balance around the "loop" can be used to verify if the flow out of a node point is equal to flow into the node. Using this simple approach with a combination of direct measured values (sensor inputs) and derived values (calculated values from sensor inputs, and design parameters and constants) an automated process was developed to evaluate the multiple resultant flow determinations to authenticate the validity of the "external" flow sensor value for flow. Within the system, expectant flows at the point in question (sensor node point) can be derived by various means such as from pumps, heat exchangers, valves, piping, and other sensor inputs from other "node locations" within the system and compared to the sensor input value under validation. This process is then applied to all sensor inputs in the system.

The two main advantages of this approach are that the process is independent of the type of sensors used and that it provides an individual sensor value replacement or "virtual sensor" for sensor inputs that are determined to be invalid.

The developed sensor validation diagnostic has the capability to determine the condition state of components (i.e., on/off; running/shut down) and matches the level of a human operator in monitoring deviations in sensor value drift for any hydraulic (open/closed system). The Sensor Validation Module provides the capability to fully automate this operator function. A higher level of precision can be achieved, but is dependent on system operating temperature and fluid characteristic parameters.

The modular concept of the validation diagnostic provides the functional capability to replicate the system sensor validation methodology to specific systems by use of the developed standard set of component library files containing component and system generic characteristics which are then normalized for plant system uniqueness. This allows the system sensor validation methodology to be easily adaptive and portable to industrial, chemical, manufacturing, and power generation facilities in a cost-effective manner.

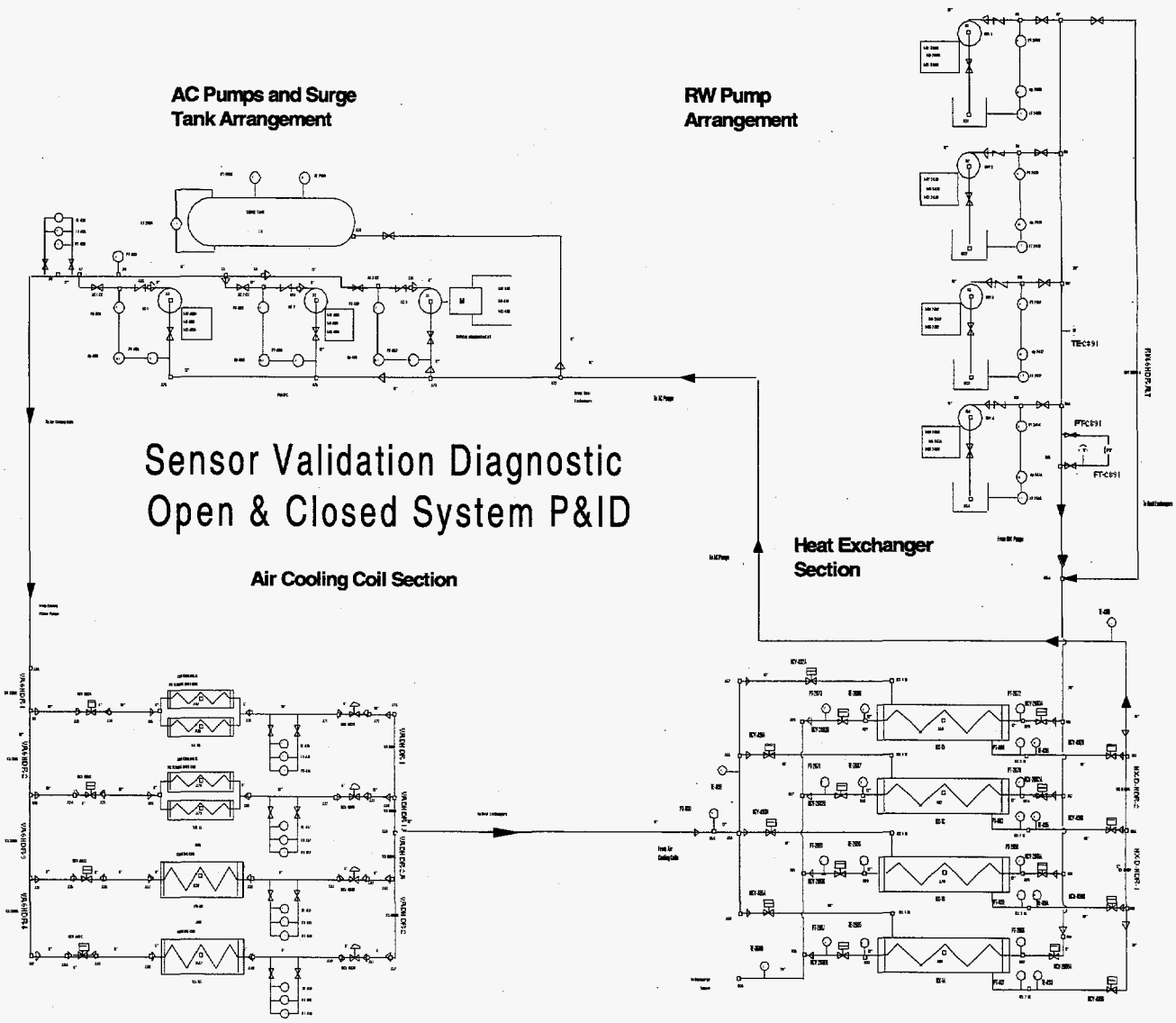

Figure 1. Sensor validation diagnostic open and closed system P&ID.

Automotive Exhaust Sensor for Engine Control

Jeffrey W. Griffin (Sensors and Measurement Systems)

Project Description

The objective of this project was to develop an inexpensive infrared exhaust vapor sensor that can be installed in all private and commercial internal combustion vehicles and that can be used for the purposes of engine control and/or monitoring engine emissions for environmental compliance.

Technical Accomplishments

Evaluation of Commercial Hydrocarbon Sensor

A commercial hydrocarbon vapor sensor (PointWatch™) manufactured by Detector Electronics Corporation, Minneapolis, Minnesota, was evaluated for its suitability as an automotive exhaust sensor. This device was exposed to calibrated concentrations of toluene vapor (a major constituent of automobile exhaust) and the lower detection limit was found to be around 50 to 100 ppmv, inadequate sensitivity for automotive applications.

Design and Fabrication of Improved Vapor Sensor

Since the optical absorption cell length of the PointWatch device is only 15 cm, it was decided to design and build a modified sensor with a gas cell length of 200 cm to improve sensitivity. The modified sensor, shown in Figure 1 employs a light-emitting diode source manufactured by Telcom Devices Corp., Camarillo, California. This infrared source has an output power of 0.12 mW at a wavelength of 3.28 micron. A commercial, pulsed incandescent infrared source manufactured by Ion Optics Inc. was also evaluated but was found unacceptable. The optical detector is a thermoelectrically cooled lead-selenide device manufactured by Infrared Industries, Inc., Orlando, Florida. A laboratory evaluation of the new vapor sensor is currently in progress.

Alternative Design for Automotive Exhaust Sensor

The prototype vapor sensor described in Figure 1 will probably not meet the cost goals required for an automotive sensor system. Near the end of this project an alternative conceptual design was developed which eliminates the need for the infrared source and vapor cell. This device is depicted in Figure 2. In operation, this device observes infrared emissions in the 3.3 micron spectral region from hot gases exiting the exhaust system. The automobile exhaust pipe serves as the "vapor cell" and signal detection is via lock-in amplifier with a timing signal derived from the engine ignition system.

Since this design incorporates only one electro-optical component (the detector) and minimal hardware, its cost would be significantly lower.

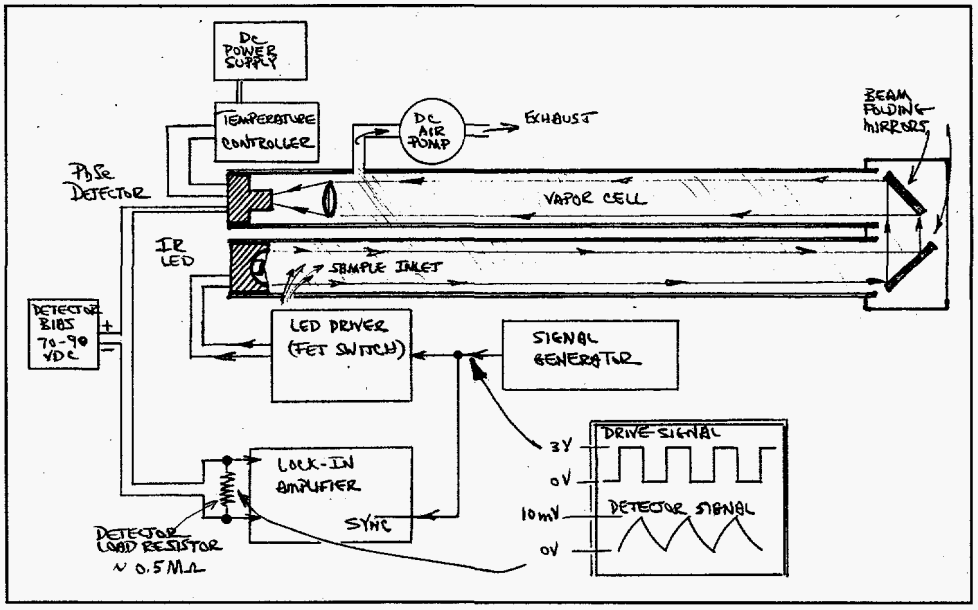

Figure 1. Long pathlength exhaust vapor cell.

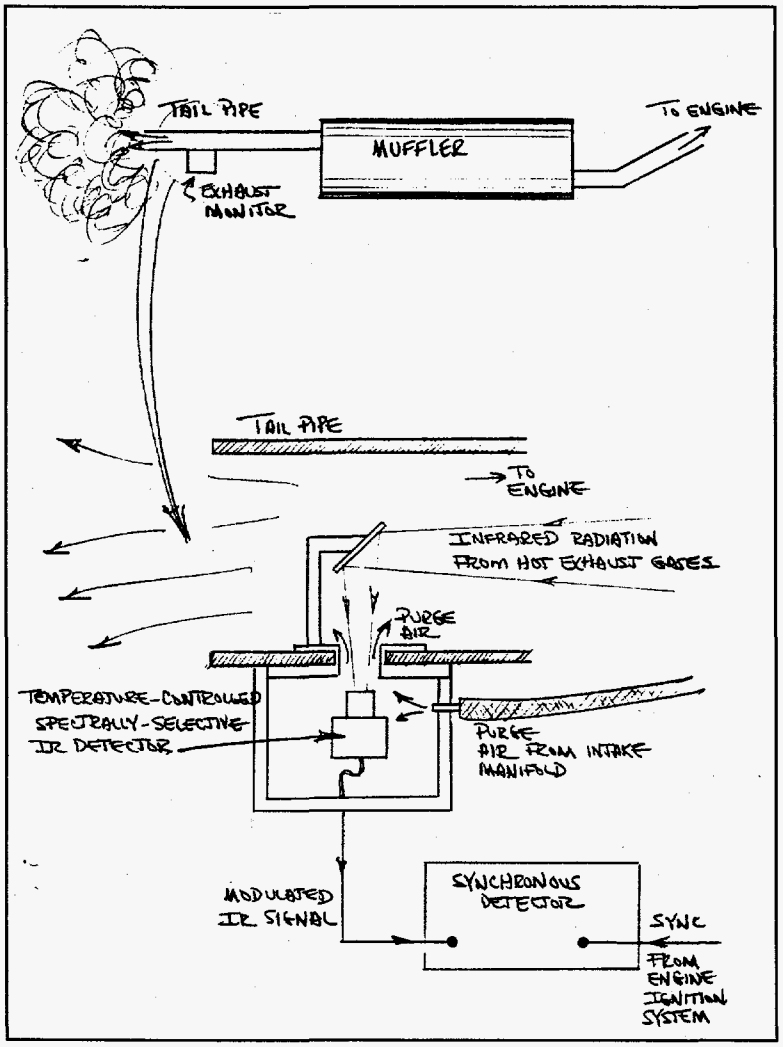

Figure 2. Exhaust radiometer.

Cylinder Design for Reduced Emission Origins

Charles F. Windisch, Gregory J. Exarhos, Nancy J. Hess (Materials Sciences)

Project Description

The principle objective of this project was to develop a real-time optical sensor for the determination of oil film viscosity within the combustion chamber of a spark ignition engine or at the main engine bearing surfaces. Characterization of the oil film in the combustion chamber was expected to provide insight into the interactions between the oil film and hydrocarbon fuel mixtures that can have a profound influence on engine emissions, wear, and overall performance. Measurements at bearing surfaces can provide insight regarding localized wear phenomena. Fluorescence emission was targeted for this application because of the high intensity optical signal that results under laser excitation and the possibility for collecting the fluorescence signal using optical fibers which would facilitate coupling to an engine under operating conditions. The work reported here demonstrated that not only can viscosity be measured in situ in real time, but that this technique also can be used for acquisition of spatially resolved information. In addition, a precise measurement of fluorescence intensity allows estimation of oil film thickness. Commercially available fiber-optic systems have been acquired that facilitate acquisition of polarized fluorescence spectra with only minor optical modification.

Technical Accomplishments

Fluorescence depolarization measurements were performed using vertically polarized cw laser light as an excitation source to probe the degree of orientation in a population of dopant dye molecules. Molecular size, molecule-solvent interactions, and solvent viscosity all influence the rotational relaxation time of the dye molecule and hence, the anisotropy of the emitted fluorescence. The depolarization ratio, which is a quotient of the parallel to the perpendicular components of the fluorescence emission, correlates with the carrier solvent viscosity. A dopant concentration at the parts per million level is introduced into the lubricating oil and induces little effect on the physical or chemical properties of the oil. Identification of an appropriate dopant molecule for a particular application then becomes a principal task of this research.

Initial results demonstrated that the viscosity of lubricating oil measured by traditional kinematic methods can be related to the measured fluorescence depolarization ratio of dye molecules introduced into the oil as a probe. Fluorescence depolarization measurements were acquired on several test dyes introduced into a variety of commercial lubricating oils including Red Line base stock, fully-formulated Pennzoil 5W-30 and Castrol 30W oils. The dye molecules investigated include BTBP, DDCI, coumarin, Nile Red, and ß-carotene. The experiments were conducted at several temperatures considered to be characteristic of oil films within the cylinder of a combustion engine. Two of the dye molecules, Nile Red and ß-carotene, were found to either decompose in oil solutions under laser excitation or to be chemically unstable at elevated temperatures. As shown in Figure 1, the fluorescence emission of BTBP and coumarin dye molecules exhibit systematic changes in depolarization ratio with increasing temperature signifying a decrease in fluid viscosity. Coumarin requires deep blue excitation for intense fluorescence emission. Similar studies conducted by Hoult et al. also demonstrated that the intensity of coumarin fluorescence emission from oil films thinner than 125 microns is linear with film thickness (Hoult and Rifai 1985; Hoult et al. 1988). These experimental results, coupled with previous results derived from this work, suggest that polarized fluorescence intensity measurements could be used to determine film viscosity and film thickness simultaneously.

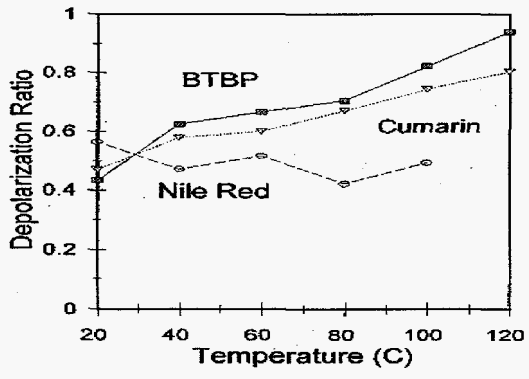

Figure 1. Temperature dependence of the depolarization ratio of three different dye molecules in lubricating oil. Earlier experiments established a direct correlation between depolarization ratio and oil viscosity.

Fiber-optic systems can be assembled from components that are commercially available and which can greatly facilitate excitation and collection of fluorescence emission signals from an operating engine. One such design by Shaw et al. (1992) is shown in Figure 2. Our initial measurements of the depolarization ratio involved dispersion of the collected fluorescence emission by a spectrometer and intensity analysis of the dispersed fluorescence emission bands. Such high-energy resolution is not necessary once the relevant fluorescence transitions have been identified. The spectrometer can be replaced with narrow band pass filters that only allow transmission of selected fluorescence wavelengths of interest. Intensity measurements can then be made with either photodiode, photomultiplier, or CCD detectors.

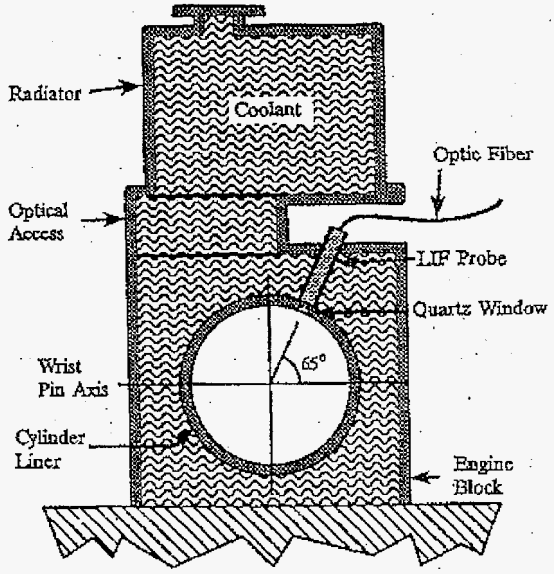

Figure 2. Schematic of optical fiber probe installation in combustion chamber.

However, fiber-optic collection of polarized fluorescence spectra requires the use of polarization preserving optical fibers such as Newport single mode fiber series F-FSP, F-SPV, and F-SPA fibers. Results of this work demonstrated that the probe dye molecules, neutral yellow (BTBP), DDCI, and coumarin are appropriate probe molecules for viscosity measurements in oil at elevated temperatures. A split polarizer arrangement where the top half passes parallel polarized light and the bottom half passes perpendicularly polarized light was demonstrated as a means to simultaneously measure the anisotropic polarized emission for both polarizations. The procedure developed here allows time resolved viscosity measurements to be performed on a millisecond or submillisecond time scale depending upon the signal to noise ratio and the molecular rotational relaxation time.

References

D.P. Hoult, and M. Rifai. 1985. "Measurement of oil film thickness on piston lands." Third Symposium on Energy Engineering Sciences, Pennsylvania State University, October 8-10.

D.P. Hoult, J.P. Lux, V. Wongs, and S.A. Billian. 1988. "Calibration of laser fluorescence measurements of lubricant film thicknesses in engines." SAE Paper #881587, 1988 SAE Transactions 97.

B.T. Shaw II, D.P. Hoult, V.W. Wong. 1992. "Development of engine lubricant film thickness diagnostics using fiber optics and laser fluorescence." SAE paper #920651, International Congress and Exposition, February 24-28, 1992, Detroit, Michigan.

Improved Fiber-Optic Sensor

Norman C. Anheier (Sensors and Measurement Systems)

Project Description

The introduction of fiber-optic sensor technology has revolutionized many industries. The Bragg fiber-grating sensor is one of the most current and promising fiber-optic sensor development areas. Fiber-grating sensors are intrinsic sensors that can be distributed within a single optical fiber. Fiber gratings have applications in communications, sensing, and signal processing. As a sensor, fiber gratings respond principally to temperature and strain. They can be used as a generic transducer to measure many different physical parameters indirectly through a strain measurement. Fiber-grating sensors have been installed in many civil structures, such as bridges and dams to measure the structures integrity. This project was focused on developing prototype devices using fiber-grating sensors.

Technical Accomplishments

During FY 1996, an extensive literature search was performed to identify research activities relating to fiber-grating sensors. In May, the Second Pacific Fiber Optic Sensor Workshop was attended in Troutdale, Oregon. Leading researchers in the field of fiber-optic sensors presented their research on this emerging technology and discussed the limiting components hindering progress. One prominent component was the lack of a low-cost Bragg grating signal processing system, also known as a demodulator. This demodulator provides the magnitude of strain and location on a distributed fiber-grating sensor system. Laboratory efforts were directed at developing low-cost demodulation techniques.

Components needed to build a fiber-grating demodulator were procured and a demodulator, based on a low-coherence interferometer (LCI), was assembled. Low-coherence light from an edge-emitting light-emitting diode was launched into a fiber-optic coupler (Figure 1). The fiber coupler is arranged in a Michelson interferometer configuration. As the scanning mirror path length coincides with the path length of one of the reflectors in the sensor arm, an optical interference burst is measured at the detector (Figure 2). The optical reflectivity is obtained by squaring the magnitude of the

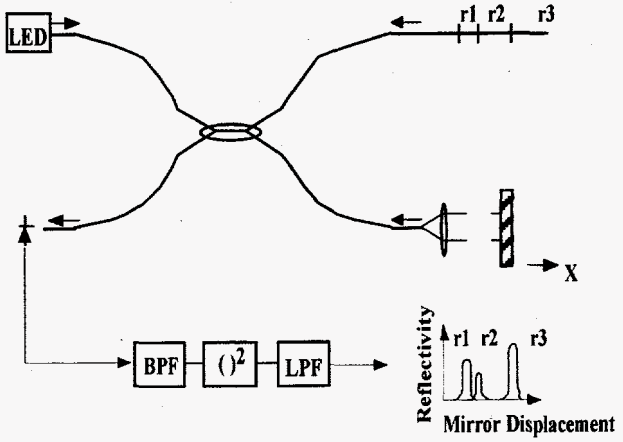

Figure 1. A low-coherence interferometer.

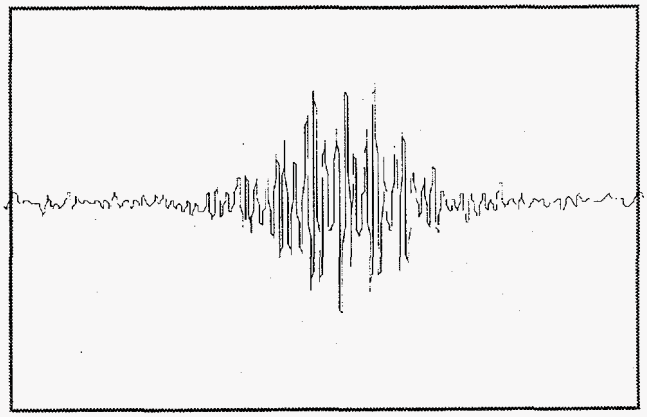

Figure 2. Detection of optical interference burst.

detector signal. The location of the reflector surface can be calculated from the scanning mirror position. The low-coherence interferometer in Figure 1 was tested in the laboratory.

A stack of partially reflecting mirrors was used in the sensor arm. A LabView™ program was written to control the scanning mirror positioning stage and process the detector output.

Figure 3 shows the low-coherence interferometer scan of the stacked mirrors. The two closely spaced interference

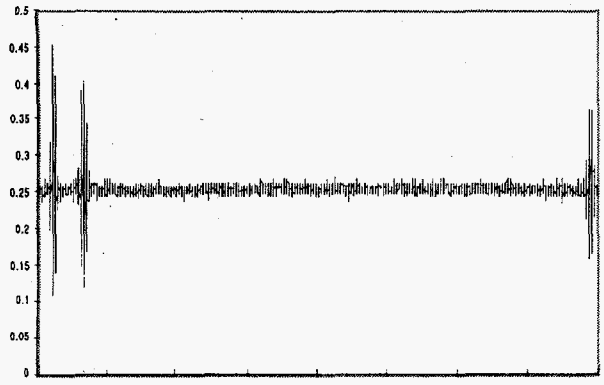

Figure 3. A low-coherence interferometer scan output.

bursts represent the distance between the rear surface of the top mirror and the front surface of the second mirror (0.227 mm). The distance between the second and third burst is the second mirror thickness (4.92 mm).

The low-coherence interferometer can be extended to measure strain-induced changes in fiber-grating sensors by adding an autocorrelator to the low-coherence interferometer in Figure 1.

The second portion of this project was an in-house fiber-optic sensors workshop. A fiber sensor video series was procured and a workshop was organized to view these tapes and entertain discussions on collaboration possibilities. Two collaboration interests were identified including the low-cost demodulator work and a fiber optic beta sensor for a paper web process.

Ultrasonic Measurement of Elastic Properties of Bone

Gerald J. Posakony, Robert V. Harris, Jr., James R. Skorpik,
Joe C. Harris (Engineering and Analytical Sciences)
Yong Liang (Materials Interfaces and Processes)

Project Description

Osteoporotic changes generally result in loss of bone mass in the cancellous (spongy) structure of the bone and can lead to compressional fractures at the head of the femur and/or degradation in the vertebrae. Early diagnosis is important in identifying the condition and assessing the efficacy and skeletal response of therapeutic intervention or medication intended to mitigate such conditions. Radiographic procedures, such as dual energy x-ray adsorption (DEXA), are presently the most widely accepted methods for detecting osteoporosis, but they require special equipment and facilities and are relatively expensive.

The objective of this project was to develop and demonstrate a simple, noninvasive ultrasonic system as an alternate method for detecting and measuring loss or change in the density of cancellous structures in the human body. While ultrasonic technology is inherently limited by the cellular nature of the cancellous structure of bone in that it provides relative rather than quantitative data, it can be used as a rapid and inexpensive means for screening persons that might be candidates for more detailed examinations. The goal for the work was to design, fabricate, and validate the performance of a compact, low-cost ultrasonic system for measuring low-density bone mass that could indicate conditions such as osteoporosis.

Technical Accomplishments

In research performed in FY 1994 and 1995, the relationship between ultrasonic attenuation and bone density in 100 cadaver calcanea (heel bones) provided a correlation coefficient between 0.83 and 0.87. Considering the potential inherent variations in the measurement, this was considered an excellent response and was the basis for work proposed in FY 1996. In developing this relationship, sections cored from the lower portion of the calcaneum were infused with fluid to simulate blood marrow, and the ultrasonic attenuation in the cancellous structures was measured using a pulse-transmission technique. Figure 1 is the plot of attenuation versus density at a frequency of 800 kHz. The results of these studies were encouraging, but all work was achieved under laboratory conditions. To make a determination as to whether the results could be used on live humans, a portable instrument that duplicated the performance of the laboratory equipment was needed.

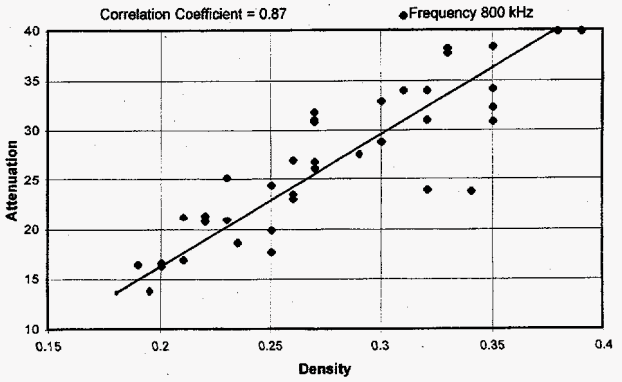

Figure 1. Plot of attenuation versus density.

The activities and accomplishments in FY 1996 can be divided into three areas: 1) instrumentation and optimization of transducers, 2) technology verification, and 3) advanced concepts.

Instrumentation and Transducer Optimization

Design and performance specifications were established, parts were assembled, and the system was fabricated. The first model had a number of shortcomings that were primarily related to the dynamic range and low-level signal linearity. These issues were resolved and the unit was tested and made ready for validation testing. Because of delays in obtaining parts, delivery of the unit was not completed until August, but tests showed it to be performing very well. A photograph of the ultrasonic system is shown in Figure 2. This unit includes the ultrasonic pulser and receiver, variable frequency control to optimize transducer performance, sync signal, radio frequency signal output, and both DC and meter readout. This compact, stand-alone unit provides voltage measurements that convert the attentuation values into numbers that can be used to screen for low, intermediate, and high density conditions.

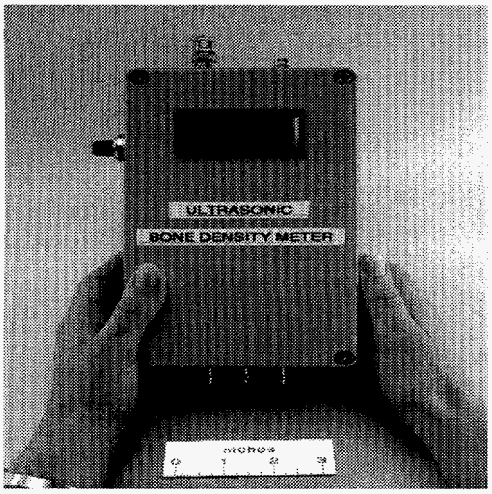

Figure 2. Ultrasonic bone density meter.

During tests it was found that the size of the sound beam was very important in obtaining reproducibility. Various combinations of units were studied. Because the bone structure and density of the calcaneum vary widely with position on the heel, beams as large as 12 to 13 mm could include both dense and sparse areas of bone. A 6 mm beam (lead pencil size) was found to be near optimum for both the transmitter and receiver. A focused horn design was used to achieve the desired beam size. Re-evaluation of the frequency showed that an operating frequency between 750 and 800 kHz was near optimum. Lower frequencies did not display the attenuation characteristics desired and higher frequencies gave inconsistent results.

Cancellous structures are irregular, complex cells and their interaction with the ultrasonic waves result in attenuation of the energy that propagates through the structure. Several attempts were made to mathematically model the structure and to be able to relate cell size and structure with the ultrasonic attenuation measurements. If such a relationship could be established, the attenuation data might provide quantitative rather than qualitative data. It was found that the cancellous bone structure was too complicated to model using known equations.

Ultrasonic System Verification

To establish the performance of the new ultrasonic system, cored bones used in prior studies were infused with water and measurements were made comparing the results of the new system with the laboratory equipment. Results showed nearly identical patterns and values. Several hundred tests were performed by two individuals one of whom had no prior experience with the measurement procedure. Values obtained by the two individuals were within 5% and were very close to measurements made in the previous year. This is considered well within any experimental error.

Development of the bone density meter was a major milestone in the program as it provided the ultrasonic system and procedure needed for future studies that might be made on human subjects.

Advanced Concepts

Throughout the present project the relationship between ultrasonic attenuation and density has been stressed. Ultrasonic measurements provide a relative measure of density. While density has value and is the principal means for determining bone loss as measured by radiographic techniques, in discussions with various doctors the most desired value would be to measure bone strength. An advanced concept to measure bone structure and relate this to strength was studied in the latter part of the project.

Ultrasonic methods are used for in vitro studies to determine bone strength. By measuring the longitudinal and shear velocities of small sections of bone and obtaining Poisson's ratio, the strength of that bone section can be calculated. However, this procedure is generally applied to cortical bone and would be difficult to use in cancellous structure.

A concept was projected to measure bone strength based on the percentage of bone versus non-bone of the cancellous structure. Fifty of the cored sections of calcaneum bones used in the attenuation studies were selected for the study. The cored sections were sliced in half and the area through which the attenuation measurements had been made were photographed. Because the cored sections are quite small, the photographs were expanded by a factor of four and the selected areas were optically scanned to define the ratio of bone (trabeculae) to open or void areas. This measurement provided a percentage of bone and non-bone. Initial results were disappointing as no correlation between percentage of bone and attenuation could be established. The photographs showed both small and large cell areas and also showed a number of planar structures where trabeculae lay across the perpendicular to the sound beam which could influence the results. A second observation was that the larger number of small versus large cells may have biased the results in favor of higher bone percentages. Further work is needed to separately define the ratio of large versus small cells. Bones with a greater number of large cells could conceivably have lower strength, but as of this date this remains a hypothesis.

Health Protection and Dosimetry

Optical In Vivo Blood Characterization and Multivariate Analysis

Norman C. Anheier, Kirk M. Remund, Don S. Daly, Timothy J. Peters (Sensors and Optical Systems)

Project Description

The development of optical biomedical sensing techniques is currently an area of increasing interest and activity. A particular category of optical sensing applications that has been receiving a great deal of attention of late is blood chemistry sensing. Frequently, the ultimate goal of optical blood chemistry sensing research and development is a noninvasive miniature sensor. Some blood chemistry parameters being targeted are concentrations of O_2, CO_2, and glucose. However, achieving the necessary accuracy and utility in noninvasive sensors for these and other chemical parameters requires knowledge of viable, robust blood optical signatures associated with the target blood chemistry parameter. The situation is made considerably more difficult by the severely limiting optical characteristics of intervening tissue. There are many commercially available noninvasive sensors for O_2, pulse, and other blood parameters. Some of these sensors have proven value due to accuracy, ease of operation, and simple calibration. The success of these sensors drives the interest for complementary sensors that detect other blood chemistry parameters.

The objective of this project is to develop a methodology that allows identification of near infrared spectroscopic signatures of blood chemistry parameters. Once useful signatures are identified, data can be used to predict analyte concentrations in the blood stream. An initial study (Case I) focused on three common anti-cancer drugs. These included methrotrexate (MTX), cis-platinum (CIS), and doxorubicin (ADR). The spectral data analysis for these compounds was performed using multivariate statistical analysis techniques. Noninvasive, in vivo, or implantable blood chemistry sensing devices and methods may be possible if the statistical techniques successfully correlate absorption to analyte concentration.

Technical Accomplishments

The FY 1995 study showed a null result for Case I analytes; however, the instrument measurement procedures, sample preparation and handing protocols, and data analysis were in place to enable the efficient performance of additional case studies of other analytes of importance.

During FY 1996, additional funding was used to further investigate this measurement procedure. The Case II study looked at the Case I analytes using both 0.5 mm and 1.0 mm absorption path lengths. Using these extended path lengths put the water bands in saturation, but it was hoped that subtle anti-cancer absorption features would be evident. Again this study showed a null result for Case II analytes. A final Case III study looked at glucose solutions.

Glucose Detection Tests

Tests were conducted using the Cary V spectrophotometer to determine the absorption spectrum of different concentrations of glucose in saline solution. The purpose of the tests were to determine if concentrations of glucose, in simple solutions of glucose and saline, could be detected using absorption measurements.

Two sets of glucose concentrations were mixed. The glucose concentration of the two sets are detailed in Table 1 below. The two sets were mixed separately to determine detection limits due to variability of mixing. The saline solution (0 mg/dL) was the same for both sets and the same saline solution that was used for the glucose concentration mixtures.

Table 1. Glucose Concentration of Two Mixed Sets

Glucose concentration (mg/dL)	
Set #1	Set #2
0.00	0.00
63.48	63.65
126.95	127.30
253.90	254.60
507.80	509.20
1015.60	1018.40

Each mixture was placed in a liquid cell holder and placed in the Cary V spectrophotometer. The spectrophotometer was set to run from 2500 nm to 1400 nm (4000 to 7143 cm^{-1}). The absorbance was measured every 0.06 nm. The results show the strong water absorption bands at 1450 nm, 1900 nm, and 2500 nm. In the tests, set #1 was first measured, then set #2, then set #1 was remeasured to determine the variation of the instrument. The samples were held at room temperature, there was no provision in the instrument to hold them at a constant temperature.

Glucose Statistical Analysis Summary

The statistical analysis was run on data from the final glucose/saline samples. The analysis was composed of two parts.

The first part was an analysis to determine which channels had absorbances that correlated well with the reference glucose concentrations of the samples. A genetic algorithm approach was used to identify these channels. The genetic algorithm reduced the number of channels to be used in a calibration exercise from 16,000 down to just over 5,000. The diagnostic checks (e.g., root mean squared error for prediction) from the genetic algorithm results indicated that calibration models fit using such selected channels by the genetic algorithm would yield poor predictions of glucose concentrations. Absorbances at two wavelengths (i.e., 2152 and 2272 nm) were also looked at to see if there was separation in the spectra due to differing glucose concentrations. These two wavelengths were identified by a glucose instrument patent (Harjunmaa et al. 1993) as being predictive of glucose. Glucose signal could not be distinguished from noise at these two wavelengths (Figure 1).

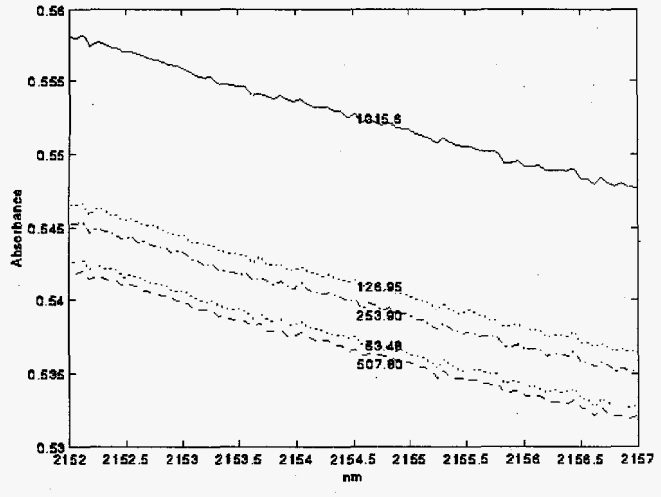

Figure 1. Set 1 Run 1, absorption spectra labeled by glucose concentration (mg/dL).

Partial Least Squares and Multiple Linear Regression were used to fit calibration models to the spectral data. Partial Least Squares models were fit using all 16,000 wavelengths as independent variables in the analysis with glucose as the dependent variable. The model had a very high calibration error and prediction error. No attempt was made to use the genetic algorithm selected wavelengths since it was found earlier that the models using these variables performed very poorly for glucose prediction. A Multiple Linear Regression model was fit using the two wavelengths identified by the glucose instrument patent. This model also had very poor predictive capability.

Various transformations of the data were made to see if glucose signal could be discovered. Mean centering (used in the model fits discussed above), saline spectra subtraction, and first order differencing (i.e., estimate of first derivative) were each used. None of these methods turned up any glucose signal in the spectra.

Temperature Influence on Concentration

To verify glucose concentration, a Glucometer®3 Diabetes Care System was used to measure the concentration of the glucose. The results are shown in Table 2. Tests on a reference standard provided by the instrument indicated that the standard deviation in the instrument reading was zero (below measured value). Repeated tests on the 63.65 mg/dL sample indicated the standard deviation in the measuring technique to be $\pm$ 3 mg/dL. The instrument can measure glucose levels between 20 and 500 mg/dL. Acceptable blood sugar levels are between 50 and 250 mg/dL.

Table 2. Measured Glucose Concentration of Two Mixed Sets as a Function of Temperature

	Glucose concentration (mg/dL)		
	Temperature of samples		
Set #1	42°F	59°F	72°F
0.00	Lo	Lo	Lo
63.48	68	82	114
126.95	153	188	203
253.90	271	335	370
507.80	Hi	Hi	Hi
1015.60	Hi	Hi	Hi

	Temperature of samples		
Set #2	46°F	60°F	72°F
0.00	Lo	Lo	Lo
63.65	75	82	130
127.30	175	213	243
254.60	263	329	402
509.20	Hi	Hi	Hi
1018.40	Hi	Hi	Hi

The results in Table 2 are plotted in Figure 2 and indicate that the change in glucose concentration as a function of temperature is a linear relationship, and the slope and intercept are both dependent on the amount of glucose in the mixture. The results also indicate that the actual concentration was different than the mixture stated on the bottles, but the results did verify that the concentrations were in the same order as the mixtures. Hence, the results in the first section of this report were still valid.

Conclusion

This study attempted to predict aqueous analyte concentrations using near infrared spectroscopic signatures. While in principle this approach seems reasonable, we found that detecting useful absorption features extremely difficult even using laboratory spectrometers. We conclude that these measurements confounded by two issues. First, aqueous-phase were measurements are dominated by strong water bands that overlap weak analyte signatures. Increasing the optical path length serves only to increase the water band interference. Second, as demonstrated in Figure 2, temperature plays a large role in the concentration measurement of the analyte. In addition, temperature can affect the water band shape to a greater extent than changes analyte concentration. Therefore temperature-induced spectra variations can overwhelm weak analyte signatures.

Reference

H. Harjunmaa, Y. Mendelson, and Y. Wang. 1993. *A Non-Invasive Method and Apparatus for Measuring Concentration of Analytes in Living Tissue.* International Publication Number WO93/00856, International Application Number: PCT/US92/00784, January 21.

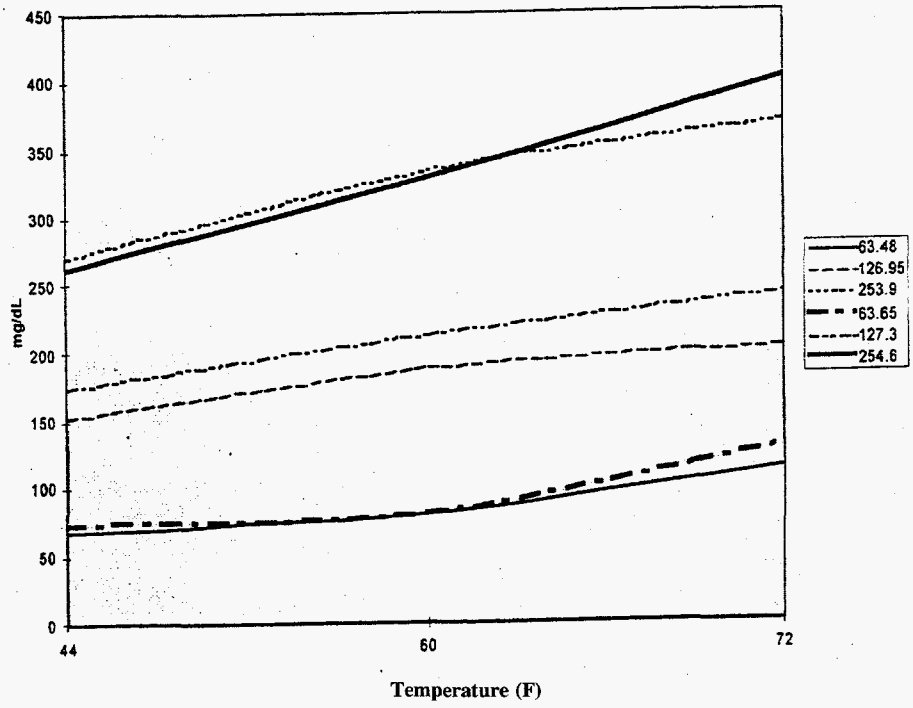

Figure 2. Glucose concentration vs. temperature measured using a Glucometer® 3.

PBPK-Based Breath Analysis Instrumentation

Karla D. Thrall (Health Protection)

Project Description

The assessment of the potential for health effects and the need for protective measures require the accurate measurement of exposure and the ability to translate these measurements into dose. Exposure data provide a basis for assessing compliance with standards, for evaluating adequacy of standards, and for developing improved risk estimates. The development of the PBPK-Based Breath Analysis instrumentation will provide the ability to more accurately assess occupational exposures to volatile organic compounds on the individual worker level.

Technical Accomplishments

Funding for this project was received late in FY 1993, and initial activities focused on demonstration of feasibility of the system. We were able to purchase the simulation and optimization software, SimuSolv (The DOW Chemical Company, Midland, Michigan), and a PBPK model for CCl_4 was extracted from the literature and successfully run on our SimuSolv system. Collaborative analytical activities using a trace atmospheric gas analyzer (TAGA) mass spectrometer verified that the detection limit for CCl_4 in exhaled breath using the breath analysis instrumentation and human breath spiked with CCl_4 post-exhalation was 10 parts per billion (ppb).

In FY 1994, the human breath-inlet device at another laboratory was remodeled for use with laboratory rats, and a series of animal studies were conducted to demonstrate proof-of-principle on the system. In the first set of experiments, conducted using a TAGA located at PNNL, animals were injected with a single dose of CCl_4 via an indwelling jugular vein cannula. In this experiment, it was possible to immediately monitor CCl_4 in the exhaled rat breath using the breath analysis instrumentation. This data was subsequently modeled using a modified PBPK model that allowed for simulation of concentrations of CCl_4 that would be present in exhaled breath which compared well with the animal data. Furthermore, this model was able to be run "backwards" using the initial data points collected over the first 1 minute (approximately 40 data points) to estimate what the initial peak blood level should have been. The estimated value was found to be 98.7% of the amount that was known to have been injected.

In the second set of experiments, using a TAGA located at another laboratory, animals were given a single oral dose of CCl_4 at various dose levels. As before, it was possible to immediately monitor for the real-time exhalation of CCl_4. However, under the conditions of oral dosing, it was also possible to detect chloroform (a metabolite of CCl_4), and ethane, pentane, and acetone, which serve as biomarkers of lipid peroxidation (i.e., toxicity).

Efforts in FY 1995 focused on using the exhaled breath experimental data collected in the previous year to develop a preliminary PBPK model to describe the oral uptake of CCl_4 and to compare the model simulations for exhaled breath concentrations with the actual data. Additional modeling efforts were initiated to develop a preliminary PBPK model to describe the uptake, tissue distribution, metabolism, and elimination of benzene to predict the levels of benzene in exhaled breath and benzene metabolites in the urine that should be measurable in humans exposed to various levels of benzene occupationally. This model will be extensively used in the upcoming activities focusing on benzene exposure assessment at Savannah River.

In FY 1995, a significant move forward toward the development of the monitoring system for field use was achieved by the award of general research equipment funding to purchase a field portable mass spectrometer developed and marketed by Teledyne Electronic Technologies. The atmospheric sampling glow discharge ion source (ASGDI) for the mass spectrometer was not optimized for sensitivity or selectively until February 1996, thus the system was inoperable until that time.

Activities in the final year of support (FY 1996) have focused on laboratory tests to expand on previous studies monitoring the exhaled breath of rats treated with carbon tetrachloride for the parent compound, chloroform (the initial metabolite) and acetone, ethane, and pentane as markers of lipid peroxidation (biomarkers of toxicity). Unfortunately, the exhaled breath experimental data collected during these studies was not comparable to results from previous experiments. It is planned that these experiments will be repeated at some later date.

Publications and Presentations

K.D. Thrall and D.V. Kenny. 1996. "Evaluation of a carbon tetrachloride physiologically based pharmacokinetic model using real-time breath-analysis monitoring of the rat." *Inhalation Toxicology* 8:251-261.

D.V. Kenny, K.D. Thrall, and P.J. Callahan. 1996. "Real-time analysis of breath for carbon tetrachloride and its metabolites." Presented at the Conference on Advances in Toxicology and Applications to Risk Assessment, Wright-Patterson Air Force Base, Ohio, April 23-25.

Real-Time Dosimetry for Therapeutic Radiation Delivery

Mary Bliss (Nuclear Chemistry)
Richard A. Craig (Sensors and Management Systems)

Project Description

This project used existing technology to begin development of a device to measure the delivered dose of therapeutic radiation in real time. The objective of this project has been to demonstrate the feasibility of using current technology to develop a flat-panel-type radiation detector capable of providing real-time dosimetry for the delivery of therapeutic radiation. Previous efforts in FY 1994 and FY 1995 have confirmed the potential for application of PNNL's neutron-sensitive optical fiber technology to real-time dosimetry for boron neutron capture therapy (BNCT).

Technical Accomplishments

Experiments have been performed using fluxes typical of those in BNCT (i.e., 10^{10} n/cm^2/sec) and have been measured with a single fiber. This prototype testing of a neutron-flux monitor indicates that dosimetry based on the tested detector concept, in support of the traditional calculations, is practical. The detector provides immediate neutron-flux information, and by implication, dose information. The data also indicate that gamma-ray dose information may also be derived from the detector output.

The sensor showed no signs of saturation, even at the highest fluxes. The response of the sensor was linear with reactor power at the higher ($\geq$10 kW) reactor powers. This indicates that the prototype can provide a proper measure of the flux and, by inference, the dose related to neutron reactions.

At lower powers, ($<$10 kW) the residual gamma-ray flux was large enough that the detector response was not linear with reactor power. Even though the pulse-height threshold had not been optimized for gamma-ray rejection, the gamma-ray interference is quite small. The gamma-ray sensitivity can be reduced by more than an order of magnitude by increasing the threshold bias by 50%. This should, for practical purposes, eliminate gamma-ray interference in the BNCT environment for which the fields are many orders of magnitude smaller than in the reactor-tube environment.

Detectors were operated in a thermal neutron flux of 10^{10} neutrons/cm^2/sec and an epicadmium flux of approximately the same order of magnitude for periods in excess of an hour. A detector was left in the reactor gamma-ray field for 16 hours and showed no apparent degradation. Radioactive activation of various detector package components occurred, as expected.

Overall, although work remains before the concept can be brought into the clinical setting, it appears that the problems are tractable. The concept continues to have promise for measuring neutron fluxes for epithermal beams and can be readily adapted to provide real time dose rate information for conventional gamma-ray/x-ray therapy.

Publication and Presentation

M. Bliss, R.A. Craig, D.S. Sunberg, Y.C. Harker, J.R. Hartwell, and J.R. Venhuizen. 1996. "Progress Towards Development of Real-time Dosimetry for BNCT." Presented at the Seventh International Symposium on Neutron Capture Therapy for Cancer, Zurich, CH, September (proceedings in preparation).

Hydrologic and Geologic Sciences

Development of a PC-Based Watershed Modeling and Visualization Package

Mark S. Wigmosta (Hydrology)
John S. Risch (Remote Sensing)

Project Description

The objective of this project was to produce an advanced, PC-based watershed modeling and visualization package by linking PNNL's existing hydrology and terrain visualization models through a common representation of surface topography. The modeling package allows the user to interactively examine spatial and temporal patterns of simulated hydrologic properties (e.g., snow cover or soil moisture) by "flying" or "driving" through the watershed. The modeling system will support a variety of DOE needs, ranging from studies of global environmental change to evaluating the impacts of various land use management or restoration options on watershed hydrology and water resources.

Technical Accomplishments

PNNL-Watershed was designed to provide a spatially-distributed representation of hydrology-vegetation dynamics at the topographic scale described by digital elevation model (DEM) data. Digital elevation model data are used to model topographic controls on absorbed solar radiation, precipitation, temperature, and downslope water movement. The PNNL Terrain Visualization System (Smart Terrain) uses digital elevation data in a Triangular Irregular Network (TIN) to provide an accurate, three-dimensional representation of surface topography. Smart Terrain allows a user to move interactively through the modeled landscape.

PNNL-Watershed originally used a square-grid network to represent surface topography (i.e., elevation data are specified at regular distances on a square-grid). A major limitation of this method is that areas of low relief are modeled at the same resolution as areas of high relief (e.g., a broad flood plain is modeled at the same resolution as mountainous terrain). In the TIN approach used by Smart Terrain grid cells are triangles of various sizes depending on the local topography, allowing areas of high relief to be modeled in greater detail that areas of low relief. This approach provides a higher quality representation of topographic features with fewer grid cells. As part of this project, PNNL-Watershed was restructured to allow the model to be run over square-grid or TIN representations of topography. PNNL-Watershed was also modified to run on both workstations and PCs.

The Smart Terrain TIN-generation algorithm was modified to provide the ability to segment and constrain the TIN generation process using supplemental vector geographic information. This capability was added to support two principal requirements. The first of these is the need to isolate the TIN-generation process to occur within the boundaries of the watershed only, using a polygonal boundary description. The second requirement is the need to generate a geometrical representation of the terrain capable of supporting the PNNL-Watershed channel-flow model. This was accomplished by using vector definitions of stream courses, applying monotonically decreasing elevation values to the x, y stream vector coordinates, and using the resulting three-dimensional vector stream definition to constrain the TIN generation such that the resulting TIN is split along the stream vector breakline. This results in the generation of a TIN with triangles that directly abut the stream segments, enabling the hydrologic output from the TIN-based watershed hillslopes to be directed into the appropriate segments of the channel-network.

The watershed modeling and visualization system was applied to the American River Watershed, Washington. The Smart Terrain-format terrain model of the watershed was derived from the same United States Geological Survey digital elevation model data used in the watershed modeling. In addition, a number of raster overlays were developed, including 1) a shaded relief image of the digital elevation model, 2) a color-coded elevation map, and 3) a series of PNNL Watershed Model output maps showing snowpack conditions and the spatial distribution of soil moisture at representative times during the period of the model run. A Windows-based user interface was also developed that enables users to quickly and easily set up and modify watershed model parameters to simulate the effects of storm events on the hydrology of a modeled watershed.

Presentation

M. S. Wigmosta, W. A. Perkins, L. R. Leung, and J. S. Risch. 1996. "Application of a linked climate-hydrology model to a mountain watershed." 1996 Fall Meeting of the American Geophysical Union, San Francisco, California.

Marine Sciences

Development of a Lagrangian Particle-Tracking Method for Quantifying Fluxes in the Near-Shore Marine Environment

Lyle F. Hibler (Marine Technology)
Paul J. Farley (Ocean Processes)

Project Description

The objective of this project was to couple oceanic dispersion modeling with Lagrangian drifter field programs. This coupling provides a method for more accurate representation of oceanic dispersion and contaminant transport. The drifter design (Figure 1) was tailored to coastal environments; to follow surface currents and to be tracked by a differential global positioning system (DGPS). We implemented a particle trajectory algorithm in an applied modeling effort, and await the results of a field program at the site for integration of DGPS observed trajectories with those estimated by the new algorithm.

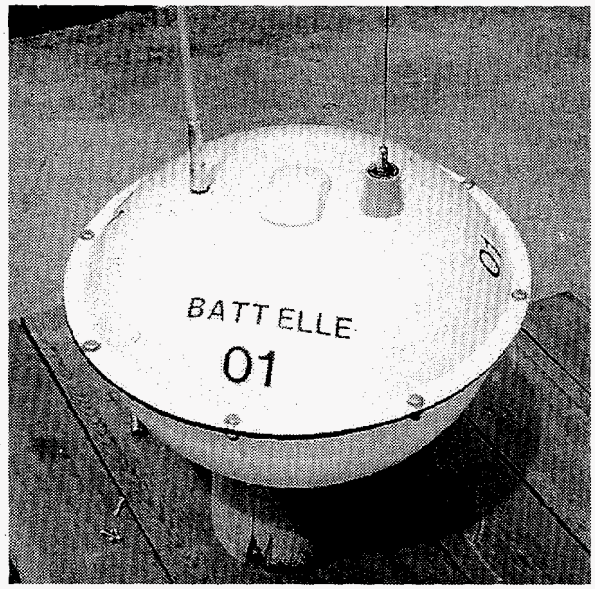

Figure 1. Differential GPS-tracked drifter.

Technical Accomplishments

Four tasks completed during FY 1996:

1. redesign of the DGPS drifter
2. a field test within Sequim Bay
3. a field demonstration
4. implementation of a drifter trajectory algorithm in the Ob Estuary Model.

1. Drifter Redesign

After several field deployments, a few hardware shortcomings became apparent. A block diagram of the drifter electronics is shown in Figure 2. The new features and components of the drifter are listed below:

- *Power Supply Cost and Capacity*. Sealed lead-acid batteries replaced lithium batteries to reduce maintenance costs and to address safety considerations.
- *GPS Message String Compatibility with Peripheral Software*. The original OEM GPS card used a proprietary message string that cannot be used with commercial tracking software; the new hardware (Trimble SV6) multichannel differential-ready GPS card was chosen. This card outputs standard unmodified NEMA 83 message strings at 1-second updates and it is completely compatible with tracking software.

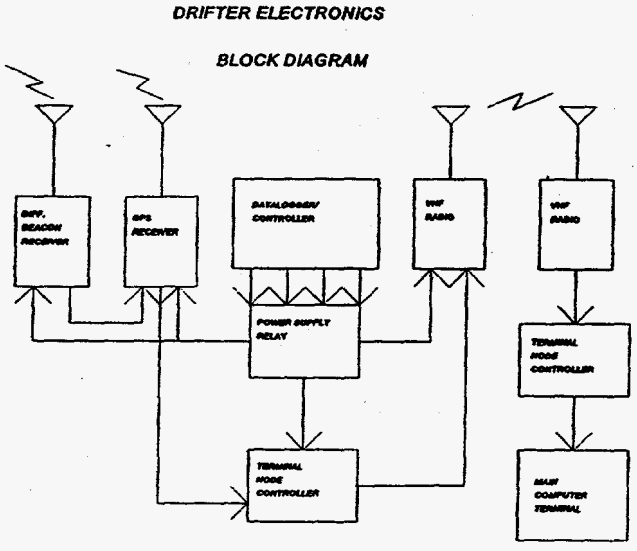

Figure 2. DGPS Drifter component schematic.

- *External Interface with Microprocessor and Power Supply Recharge*. The drifter is now fitted with an eight-conductor, water-tight, pluggable connector that allows the battery to be recharged, the microprocessor to be reprogrammed, and the terminal node controller to be reconfigured without opening the housing.

- *Telemetry Radio*. A Ritron radio has been selected to replace the ICOM radio. This radio is PC-programmable and is available in an unblocked version for government use. This radio is also designed for digital data transmission, making it ideal for this application.

2. Field Test in Sequim Bay

The DGPS drifter was tested in Sequim on June 23, 1996. The drifter was released at the mouth of Sequim Bay on an incoming tide and its position was tracked for 1 hour. This trajectory is shown in Figure 3.

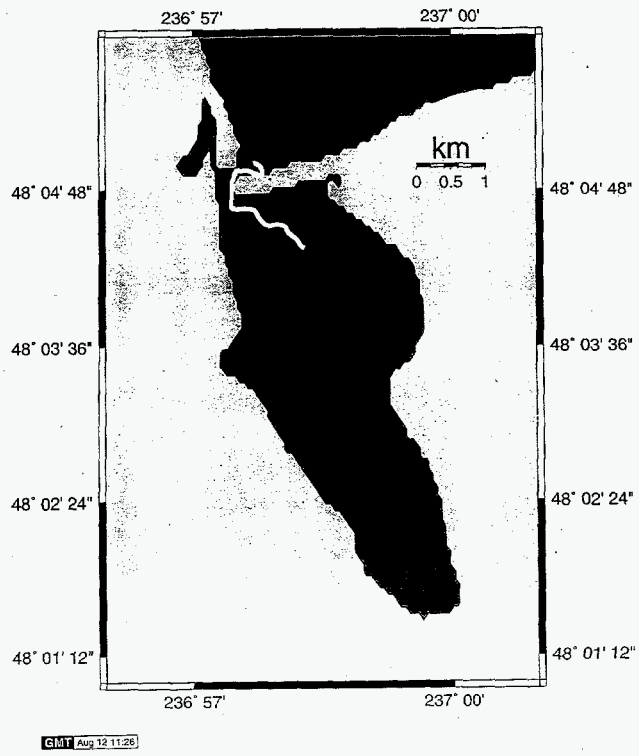

Figure 3. DGPS Drifter track, June 23, 1996, 3 to 4 p.m.

3. In-Water Field Demonstration

A 2-day field deployment/demonstration was provided. This was requested after an initial presentation.

4. Trajectory Algorithm Implemented in Finite Element Model

The particle-tracking algorithm was incorporated into the RMA2 finite-element model. The trajectories were estimated using the flow-field estimated by the model application to the Ob Estuary as part of the Office of Naval Research (ONR) Arctic Nuclear Waste Assessment Program (ANWAP). Random perturbations to the deterministic flow paths were introduced and scaled according to specified eddy-viscosities and computed current magnitudes. Full use and verification of this capability will be established when results of the ongoing ANWAP field program are completed. Examples of three modeled trajectories are shown in Figure 4.

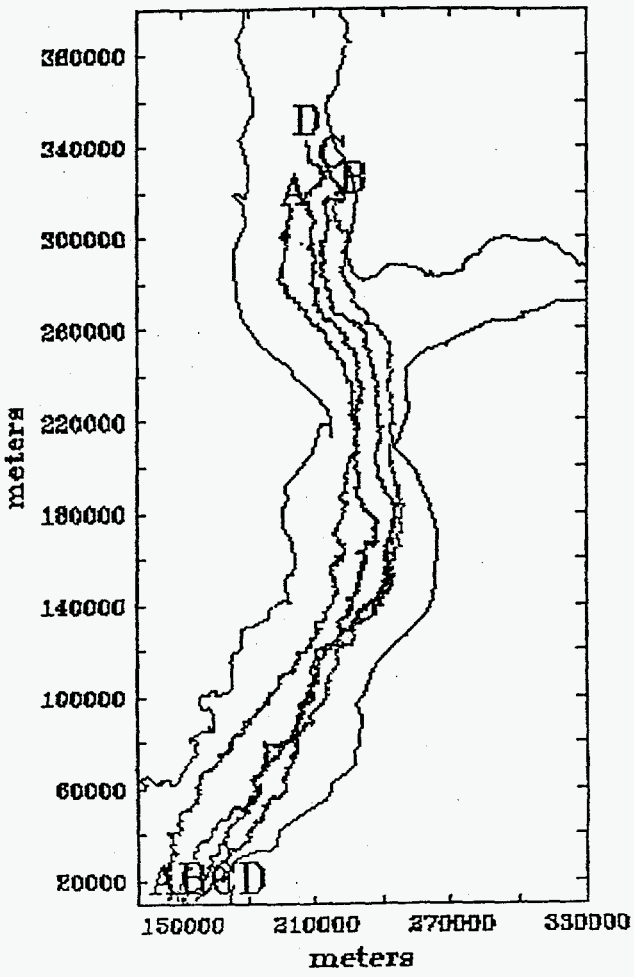

Figure 4. Modeled DGPS Drifter trajectories in the Ob Estuary.

Publication

T. Paluszbiewicz. 1996. "Differential GPS-tracked drifter." Battelle Marine Sciences Laboratory, Sequim, Washington.

Remote Sensing of Coastal and Marine Environments with Airborne Multisensor Pod System (AMPS)

Ronald M. Thom, Lyle F. Hibler (Marine Sciences Laboratory)
Gregg M. Petrie (Remote Sensing)

Project Description

The objective of this project was to use existing data bases provided by the DOE's Airborne Multisensor Pod System (AMPS) to capture coastal processes at high spectral and spatial (scale ~2 m) resolutions and exploit these data sets to:

- improve our understanding of important coastal processes
- develop a better understanding of how information captured at different scales can be better integrated
- develop methods to predict other coastal conditions (e.g., Bathymmetry) not apparent in the imagery.

Technical Accomplishments

The project emphasized the exploitation of AMPS and serves as a proof-of-principle application for the system while demonstrating its potential for successful deployment and practical use. The work in 1996 included:

- construction of land cover maps of human development features (e.g., roads, buildings) and natural habitats (e.g., marshes, mud flats)
- modeling predictions of bottom conditions based on wave crest characteristics in the imagery.

The multisensor imaging pod is a package of airborne remote sensing devices that includes high resolution cameras (visible and infrared), a narrow-band hyperspectral sensor for digital imaging in visible and near-infrared ranges, a multiple broadband spectral imager, a high-resolution video camera, and a low-light video camera. Marine and coastal images from a synthetic-aperture radar and the multisensor imaging pod were collected near the U.S. Army Corps of Engineers Field Research Facility near Duck, North Carolina, on October 15-24, 1994, (aka Mission Five).

The overflight we used was made during the DUCK94 and Coastal Ocean Process experiments funded by Office of Naval Research and the National Science Foundation. These images are accompanied by an outstanding collection of ground-truth measurements of water temperature, directional wave spectra, tidal elevations, current velocities, conductivity-depth-temperature profiles, acoustic-Doppler current profiles, chlorophyll, and suspended sediment. In the future, we hope to use the images to:

1. compare remotely sensed estimates of water temperature, suspended-sediment concentrations, and phytoplankton distribution with ground-truth measurements
2. catalog and interpret coastal processes uniquely observable with remote sensing, such as fronts, water-mass distributions, beach and bar topography, surface-wave refraction, and phytoplankton patchiness
3. determine the scale and distribution of observable features, and their signal in lower-resolution satellite images.

Materials Science and Engineering

Advanced Energy Storage Materials

Peter C. Rieke, Bruce C. Bunker, Jun Liu, Mira A. Josowicz, Scott A. Chambers, Li-Qiong Wang (Materials and Chemicals Sciences)

Project Description

A new class of energy storage devices called ultracapacitors are currently being developed to meet the increasing power density needs of the transportation and communications industries. Unfortunately, the material with the highest demonstrated capacitance per unit weight, hydrated ruthenium oxide, is scarce and very expensive. Objectives of this project include preliminary studies of energy storage mechanisms in conductive oxide films such as ruthenium oxide, and exploration of the manipulation of the redox and solid-state chemistry of mixed-valence oxide films. This project is limited to identifying promising oxide materials systems and experimental techniques that would provide the basis of a broader program. The proposed work will impact the use of conductive oxides in a wide range of applications including capacitors, batteries, catalytic devices, and electronics.

Technical Accomplishments

Ruthenium dioxide is recognized as one of the most efficient materials for use in ultracapacitors. However, its mechanism of operation remains unclear. Pore size and crystallite size influence the amount of charge stored per unit weight of material. Recent work using hydrous $Ru(OH)_2$ suggest that the bulk of the material is involved in charge storage. However, experiments on electrodes prepared with significant amounts of crystalline RuO_2 suggest that charge storage is confined to the surface of the material.

To address these mechanistic issues we have prepared single-crystal RuO_2 electrodes by molecular beam epitaxy. The method of preparation was varied to introduce variable amounts of defects in the crystal structure. Transmission electron microscopy (TEM) and atomic force microscopy (AFM) were used to characterize the electrode structure, and cyclic voltametry was used to characterize the electrochemical behavior. The resulting electrodes were non-porous and nominally single crystal except for the presence of grain boundary defects.

A very high-quality RuO_2 electrode was prepared and examined by transmission electron microscopy. Very few defects were present and the RuO_2 showed near perfect registry with the underlying TiO_2 substrate. A second sample was cycled in 1M H_2SO_4 at 50 mV/sec. Repeated cycling did not significantly influence the voltamogram. The transmission electron microscopy of the cycled samples was not substantially different and thus cyclic voltametry did not significantly influence the electrode structure. The atomic force microscopy scan for the sample showed a distinct texture consisting of needle-like units approximately 50 x 200 nm having a distinct orientation. The sample is moderately rough with relief variation of up to 10 nm.

The cyclic voltametric scans were obtained from -0.6 to 1.0 V versus Hg calomel electrode at 50 mV/sec. A very well-defined redox wave is observed at about 475 mV and was assigned to the Ru^{+3}/Ru^{+4} redox couple. The charge passed during oxidation from 400 mV to 800 corresponds to complete 1-electron oxidation of a layer approximately 0.87 Å thick or 25% of a monolayer of RuO_2. Clearly only the very near surface regions are involved in redox reactions and potential cycling does not adversely influence this outer layer.

The above sample constituted our base line sample with which others are compared. Other samples were prepared with thicker layers or at lower temperatures to increase the defect density.

The transmission electron microscopy for a 450 Å thick RuO_2 film prepared by sequential deposition of 150 Å layers at 600, 450, and 425°C showed significant differences. Registry of the RuO_2 layers extends through the first 150 Å but began to degrade slightly in the second layer. The top layer consisted of poorly ordered crystalline domains about 30 Å in diameter. During preparation this sample gave a well-defined low energy electron diffraction pattern suggesting that on a larger scale the sample is fairly well ordered. The sample does not contain pores nor is it amorphous. The atomic force microscopy of this showed distinct crystal edges and the sample appears to have irregular steps. We believe that this structure is the result of a high density of crystal defects being expressed at the sample surface. This view is consistent with the defect structure shown in the above transmission electron microscopy.

The cyclic voltametric behavior is radically different. Broad capacitor-like behavior was observed with approximately an order of magnitude greater current than the base line sample. No distinct redox waves are present although some small irregularities are present that might be interpreted as residual redox waves. The area under

the oxidation curve from -0.3 to 0.8 V taken at 50 mV/sec corresponds to complete 1-electron oxidation of 11 monolayers or 34 Å of RuO_2. This is over a factor of 10 difference in charge storage capacity compared with that of the above nearly perfectly crystalline sample. The 34 Å depth of reaction assumes complete 1-electron oxidation but the data of the nearly defect-free sample show that highly crystalline regions do not undergo significant redox reaction except at the surface. This leads us to the conclusion that the active electrode region is the defect structure that occurs across the grain boundary mismatches.

The cyclic voltametric data is also consistent with this view. Oxidation/reduction requires the incorporation of compensating charge in the bulk of the electrode. This is apparently impossible in the highly crystalline regions but is possible in the defected regions. The rate of mass transfer is apparently slow enough that distortion of the cyclic voltametry curves occurs. This effect requires substantially greater study through variation of cyclic voltametry scan rate or using impedance techniques.

In conclusion, the electrochemical behaviors of single-crystal RuO_2 electrodes that contain various crystal defects have been compared. The behavior of the least defected electrode reveals that electrochemical activity is confined to the surface of the crystalline material and that it is not possible to cause hydrogen intercalation by electrochemical means. The electrochemical behavior of this electrode is substantially different than that previously reported. The reasons are not clear but this work suggests that small differences in defect structure can have dramatic influence on the electrochemistry. Electrodes that contain significant amounts of defects do exhibit a distributed redox behavior that may be useful in ultracapacitor devices. The mass of charge passed in these electrodes suggests that proton insertion occurs to a few tens of nanometers along the defected regions.

Publication and Presentation

The above work was presented at the fall 1996 National Electrochemical Society Meeting in San Antonio, Texas. The work will also be published in the symposium proceeding as P. Rieke et al., in *Electrochemical Capacitors II*, F. M. Delnick, D. Ingersoll, X. Andrieu and K. Naoi, editors, PV96-25, p 35, The Electrochemical Society Proceedings Series, Pennington, New Jersey.

Coatings Characterization

Gordon L. Graff, Charles Windisch, Li Wang, Kim Ferris, Jun Liu (Materials Sciences)

Project Description

The primary objective of this research is to utilize state-of-the-art scanning electron microscope, TEM, nuclear magnetic resonance, and Raman characterization to investigate fundamental mechanisms controlling thin film growth. Detailed characterization will be performed on deposited films, on deposition solutions, and on precipitates (particles) forming in the bulk solution.

Technical Accomplishments

Since slow deposition rates remain a technical limitation to our solution derived coatings, detailed solution, substrate, and thin film characterization are required to understand fundamental mechanisms and rate limiting processes controlling film growth. Previous work indicated that the extremely rapid hydrolysis and condensation reactions that occur in aqueous solutions of Sn^{4+}, Zr^{4+}, and Ti^{4+} cations may limit film growth since solution conditions favor a burst of nucleation with little subsequent growth. In addition, detailed TEM studies showed that thin film growth mechanisms are fundamentally different on polymeric substrates than on SAM-containing metal substrates.

During FY 1996, a detailed study of solution speciation and hydrolysis reactions was undertaken on the TiO_2 deposition system. Extensive Raman, nuclear magnetic resonance, and modeling efforts were performed on titanium lactate solutions in an attempt to gain a detailed understanding of the film growth mechanism. Raman and nuclear magnetic resonance studies convincingly showed that the Ti^{4+} cations were positioned between the hydroxyl and carboxyl groups in the lactate anion. Molecular modeling also predicted the identical chelated titanium lactate structure in solution. Quantitative nuclear magnetic resonance and Raman showed the lactate/Ti^{4+} ratio in solution to be approximately 1.4-1.7 to 1. This result conflicts with the proposed structure of titanium lactate existing in the literature. Using molecular models and assuming sixfold Ti^{4+} coordination, oligomeric structures were constructed with all possible combinations of nonbridging, twofold, and threefold oxygens. The models show that the starting solution species is a titanium lactate oligomer containing three to five Ti^{4+} species.

Raman experiments also showed that the onset of titanium oxide precipitation resulted in release of free lactate anion into solution. Thus, destabilization of the Ti-lactate complex in a pH regime (pH 3 to 4) in which Ti^{4+} is highly supersaturated, results in rapid hydrolysis and condensation reactions to form a titanium oxide film. Potentiometric titrations performed on dilute Ti-lactate solutions also confirmed this reaction mechanism. Titrations results showed the onset of precipitation when the equivalents of added acid/base precisely matched the lactate concentration in solution.

Understanding of this film growth mechanism is significant since it facilitates titanium oxide film growth under more benign solution conditions (pH = 3 to 4) than conventional hydrolysis reactions (pH = -0.7).

Publication

G.L. Graff, C.H. Windisch, L.Q. Wang, K.F. Ferris, and S. Baskaran. "Mechanisms of TiO_2 thin film growth from aqueous titanium lactate solutions." (in preparation).

Die Casting Materials

Ed L. Courtright (Materials and Chemical Sciences)
Darrell R. Herling, Eric A. Nyberg (Materials Processing)

Project Description

The objective of this project was to develop information on improving the process of automotive die castings. This work focused on identifying ceramic materials that could be used as coatings that will extend the life of dies used in making aluminum castings.

Several material candidates were tested in contact with molten aluminum to establish their compatibility and to determine if interfacial reactions occurred. We hope to find a material that will increase the die life by a factor of 5X. The results obtained during the course of this investigation indicated that one or more ceramics are inert to molten aluminum and therefore, warrant development as coating systems for commercial die applications.

Technical Accomplishments

While the stated objective of this development effort was to develop coating systems for protecting the steel dies used in aluminum die casting operations, it was decided that initial compatibility studies could be better performed with monolithic materials rather than coatings. Chemically pure coatings of stoichiometric composition often require some initial developmental effort because of problems with adherence to their substrates and this issue must be addressed and solved before the coatings are functional.

In view of the limited funding available for this project, it was decided to hot press ceramic powders into small, round bars and then immerse these in a molten aluminum bath at 700°C for up to 6 hours or more. The materials chosen for initial investigation included CrB_2, TiB_2, TiN, BN, and $Cr_{23}C_6$. Two steel materials were chosen as control samples: a maraging steel, and a H-13 tool steel. The latter is typically used as the die material in most die casting operations.

Small test samples were held at one end with a wire and immersed into a molten aluminum bath. As shown in Figure 1, there was no surface reaction with titanium diboride (TiB_2) compared with the H-13 steel which suffered extensive surface reaction. The maraging steel sample also suffered extensive reaction and the TiN bar was observed to have a lesser, but detectable, interfacial reaction. Both the chromium diboride (CrB_2) and boride nitride (BN) samples were also observed to be relatively inert. The inertness of chromium diboride is of particular interest because a coating of this material can be applied to a large complex die configuration by boriding the surface of a chromium-based steel, an expensive pack cementation process. Also, titanium diboride or boron nitride coatings would have to be applied by either physical or chemical vapor deposition processes, which are expected to be much more costly.

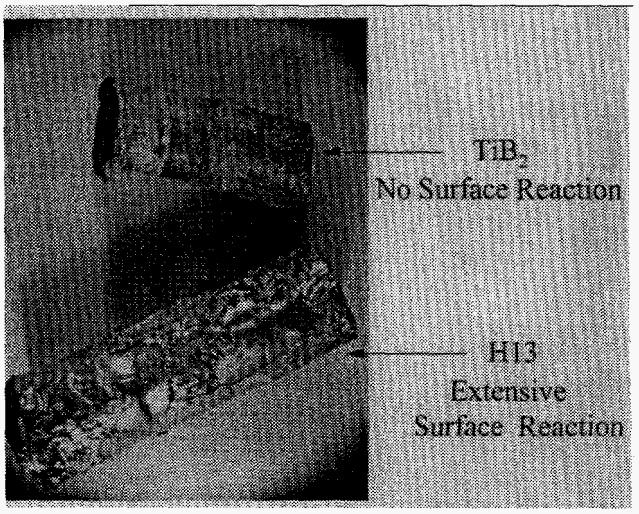

Figure 1. Die casting die coatings evaluations post-immersion testing results in A339 aluminum at 700°C for 6 hours.

High Performance Barrier Coatings Using Polymer Multilayers

John D. Affinito (Materials Sciences)

Project Description

The objective of this project was to develop a new vacuum deposition technology capable of depositing polymer/oxide (or polymer/metal) multilayers, which are useful as high performance permeation barriers for food and other packaging applications. An R&D/prototype production vacuum roll coater designed for multilayer thin film deposition onto flexible substrates in a roll-to-roll configuration was adapted for use in this work (see Figure 1). The machine is capable of simultaneous deposition of polymer, metal, semiconductor, oxide, nitride, or carbide thin film multilayer structures.

Technical Accomplishments

The polymer multilayer (PML) process for flash evaporation of monomer fluids has been combined with magnetron sputtering and e-beam evaporation in a web coating operation and used to fabricate polymer/oxide barrier layers on 0.002 inch thick polyester substrates. A PML polymer smoothing layer is deposited followed by oxide/PML pairs of layers. Barriers were fabricated with 1, 2, 3, 7, and 33 PML/oxide pairs. For single oxide layer barriers, permeation rates for O_2, as low as 0.00017 cc/100 in^2/day (or 0.00255 cc/m^2/day), were obtained while H_2O permeation rates less than 0.001 gm/100 in^2/day (or 0.015 gm/m^2/day) were obtained. These rates should be compared with current food packaging industry goals of 0.1 cc O_2/100 in^2/day or 0.1 gm H_2O/100 in^2/day.

Scanning electron micrograph data were presented that indicates the PML layer is decoupling the substrate defects from the oxide film by presenting the growing oxide with an ultra-smooth pseudo-substrate upon which to grow. Thus, the permeation rate becomes gated by the defect density (or bulk diffusion rate) intrinsic to the oxide layer and not by the substrate induced defects.

Experimental Methods and Apparatus

Figure 1 is a schematic of the vacuum web coater. The system can, and does, accept many types of substrates such as flexible polyester, polyethylene, metal foils, and various types of fabric. Of the many unique features of

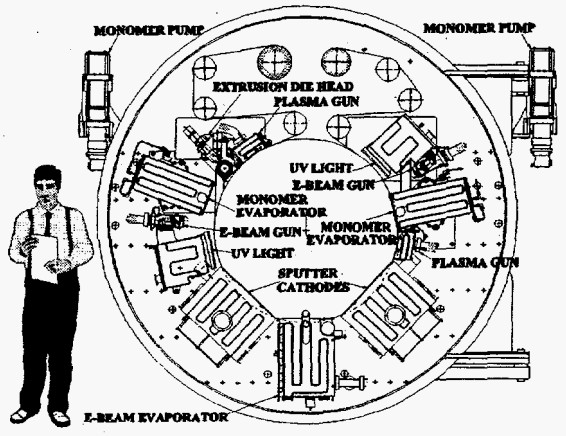

Figure 1. The modular design of the PML web coater permits many, and varied, deposition processes to be carried out simultaneously.

this system, of particular importance to this work is the fact that, in a single pass through this system, as many as seven sequential layers, including PML layers, may be deposited. This permits polymer/oxide/polymer layers to be deposited on the substrate before anything else touches the surface.

The PML process is an evaporative process that begins with the working monomer, a reactive organic liquid, being degassed. The PML process may deposit films ranging in thickness from a few tens of angstroms to tens of microns at substrate speeds as great as 600 linear meters per minute.

Experimental Results

For this work, roll-to-roll depositions of PML/Al_2O_3/PML coatings on 0.002 inch thick polyester were carried out. Two types of Al_2O_3 coatings were examined: sputter deposited and electron beam evaporated. For all of the oxide layers, the oxide deposition is preceded and followed by a PML deposition. All PML layers were cured (cross-linked) with ultraviolet radiation.

Figures 2 and 3 summarize the permeation data for those samples that we measured. Focusing on Figure 2, it is apparent that sputtered oxide layers produced better

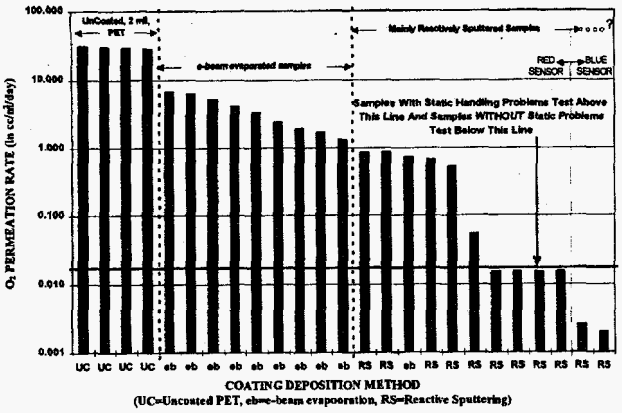

Figure 2. O_2 permeation rates of PML/oxide barrier films deposited under various conditions.

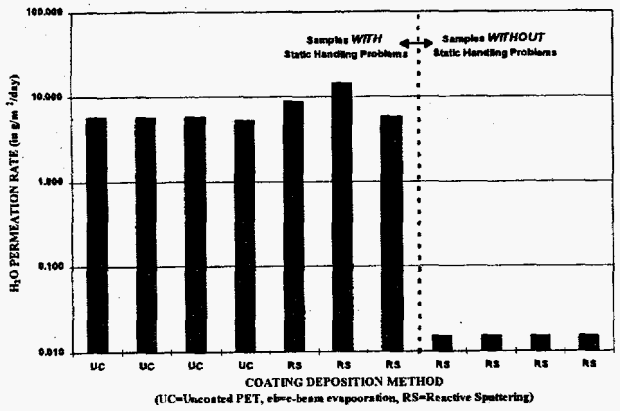

Figure 3. H_2O permeation rates of PML/oxide barrier films deposited under various conditions.

barriers than did electron beam evaporated oxide layers. Further, those sputtered samples whose substrates did not experience pre- and post-deposition handling problems due to static electricity performed much better than samples that had static problems. We believe the static problems to be traceable to the humidity at the time the substrate was wound from the master core to the web coater core.

It is clear, however, that there is a marked difference between the three sets of samples. The first group, with Al_2O_3 layers sputtered in the humid summer, had no static build-up problem and permeation rates for both O_2 and H_2O were well below current food packaging industry goals. The control samples of polyester had the O_2 and H_2O permeation rates expected from 0.002 inch thick polyester. The second group, with Al_2O_3 layers sputtered during the winter as the humidity was plummeting, had a great deal of static build-up and had good O_2 barrier properties, but only equal to, or slightly better, than current food packaging industry goals. However, this second group had H_2O permeation rates that were the same, or slightly worse, than what would be expected from bare polyester. The third group of samples was fabricated at the driest point in the low humidity cycle. These samples used electron beam evaporated Al_2O_3 and demonstrated the worst static build-up problems of all of the samples. As well, though only slightly worse than the industry goals for O_2 permeation, the O_2 permeation of these samples was at least two orders of magnitude higher than the samples in the first group with sputtered Al_2O_3 layers, fabricated in the humid summer, that had no static buildup problems.

Figure 4 presents scanning electron micrograph photographs of bare polyester substrate, metallized polyester substrate, and polyester substrate with a PML smoothing coating. This scanning electron micrograph data suggests a mechanism for the enhanced barrier properties we have observed and described above. We propose that plain oxide coatings are ultimately limited in performance by pinholes that arise due to the inherent surface roughness of the polymer substrate, as well as scratching of the oxide layer as the coated substrate is wound up after oxide deposition. To prevent this, we propose that the PML layers perform two functions: the first PML layer smooths the substrate surface so that the substrate defects are decoupled from the subsequent oxide film deposition; and the second PML layer protects the oxide layer from scratching as the coated substrate is wound up.

Conclusions

All three sets of samples measured showed O_2 permeation rates below the current state of the art. Two sets of the samples had O_2 permeation rates better than industry goals and one of those was about 3 orders of magnitude below those goals—near the detection limits of the instrumentation. H_2O permeation rates for the best O_2 sample set was also nearly 2 orders of magnitude better than industry goals - below the detection limits of the instrumentation. The intermediate O_2 sample set, still a factor of 2 better than industry goals, was no better than bare polyester for H_2O permeation. H_2O permeation measurements were not made on the worst O_2 sample set. Not enough work has been done to clearly determine the source of these variations in measured permeation rates. There is anecdotal evidence, but not proof, to support the premise that electrostatic charging of the web leads to electrostatic discharge that can damage the coating. Under this scenario, the electrostatic discharges produce pinholes in the coating that act as permeation channels for O_2 and H_2O species. Follow-on work should test the electrostatic discharge damage theory. This could be done with the PNNL deposition system by, within a single run, switching between ultraviolet and electron beam curing of each of the PML layers. Thus, the two PML layers could be cured with all four combinations (UV/UV, UV/EB, EB/EB, and EB/UV) during a single

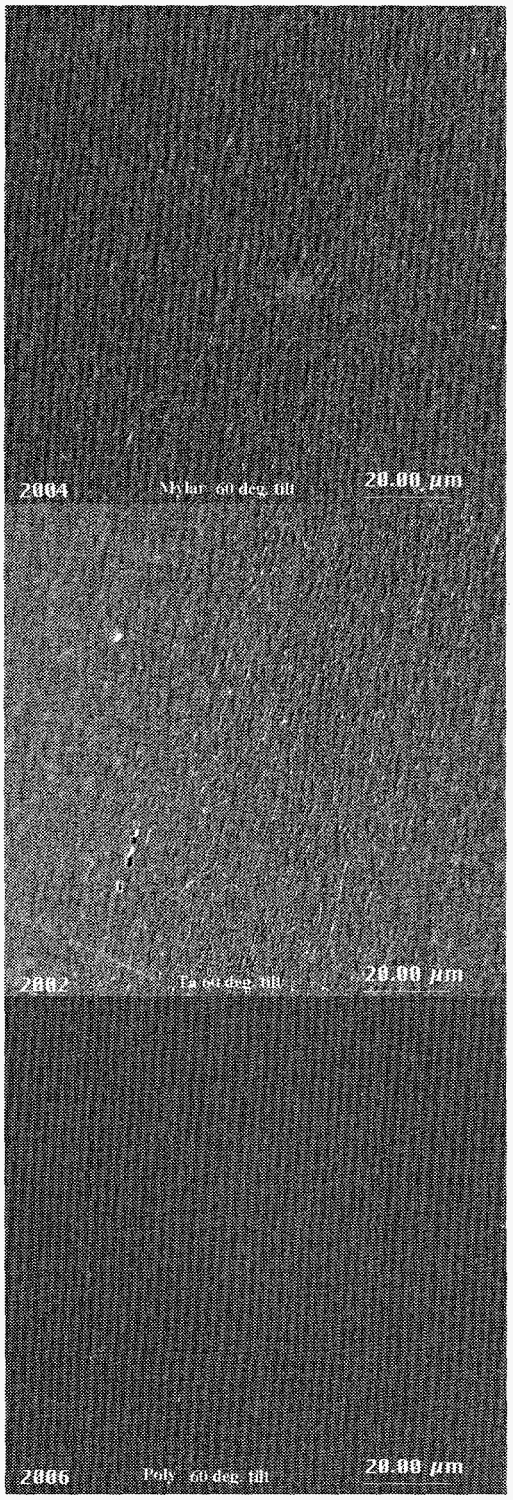

Figure 4. SEM photographs that depict the ability of a PML layer to smooth a rough surface. The *TOP* shows the surface of virgin polyester. The *MIDDLE* shows a polyester surface with a 250 Å coating of sputtered tantalum metal. The *BOTTOM* shows a polyester surface with a 1 μm PML coating.

experiment at constant oxide deposition. This will isolate run-to-run variations due to static/ humidity, substrate, or oxide deposition technique.

Those variations, if any, that arise due to the method of oxide deposition can also be discovered by running these four-way cure experiments with various oxide deposition techniques.

In any case, it is clear that, in some form, PML-based barrier layers can be produced with high optical transmission and extremely low permeation to O_2 and H_2O and, presumably, to other species as well.

Publications and Presentations

J.D. Affinito, M.E. Gross, C.A. Coronado, G.L. Graff, E.N. Greenwell, and P.M. Martin. 1996. "A new method for fabricating transparent barrier layers." Presented at the International Conference on Metallurgical Coatings and Thin films 96, April, San Diego, and accepted for publication in the proceedings in a future volume of *Thin Solid Films*.

J.D. Affinito, M.E. Gross, C.A. Coronado, G.L. Graff, E.N. Greenwell, and P.M. Martin. 1996. "Polymer-oxide transparent barrier layers." Presented at the 39th annual meeting of the Society of Vacuum Coaters, May, Philadelphia, and accepted for publication in the proceedings.

High Porosity Dielectric Films Through Biomimetic Processing

Suresh Baskaran, Jagan R. Bontha, Paul J. Bruinsma, Nancy J. Hess, Jun Liu (Materials and Chemical Sciences)

Project Description

Templating processes that mimic biomineralization are useful in the design of advanced inorganic materials. The objective of this research was to synthesize inorganic porous films with controlled dielectric properties from surfactant-templated precursor solutions. Highly porous ceramic films have potential as low K' interlayer dielectrics in advanced semiconductor devices. Nanoporous ceramic films also have applications as thermal barriers, as advanced catalysts and catalyst supports, and in other structures useful in environmental remediation.

In this project, low dielectric constant silica films were synthesized by engineering ordered nanoscale porosity in the films. The synthesis approach was based on self-assembly of inorganic/organic structures by condensation of ceramic precursors on organic surfactant micelles during high evaporation-rate processing. Processing parameters for controlling pore size, pore structure, and film thickness in mesoporous silica films on silicon substrates were investigated. A simple spin-coating technique was used to synthesize low K' films. The role of solution chemistry in pore structure design and development in these spin-coated films was studied.

Technical Accomplishments

Porous films were synthesized by spin-coating a solution containing tetraethyl orthosilicate (TEOS), ethanol, water, hydrochloric acid, and a cationic surfactant on polished silicon wafers. The surfactant/TEOS molar ratio was varied to control the pore-volume fraction in the final film and to optimize the ordering of the pores. The spin-coated films were heat treated to 550°C, and evaluated by x-ray diffraction and ellipsometry. From the variations in d-spacing and the height of the primary x-ray peak with surfactant/TEOS molar ratio, it was apparent that pores with hexagonal ordering could be obtained up to surfactant/TEOS molar ratios of ≈0.15. Ellipsometric results demonstrated that high porosity and low refractive index (low dielectric constant) can be obtained with high surfactant loadings. The vol% porosity and refractive index as a function of the surfactant/TEOS molar ratio are shown in Figure 1. A film dielectric constant of <2 at optical frequencies was inferred from the measured refractive index, indicating

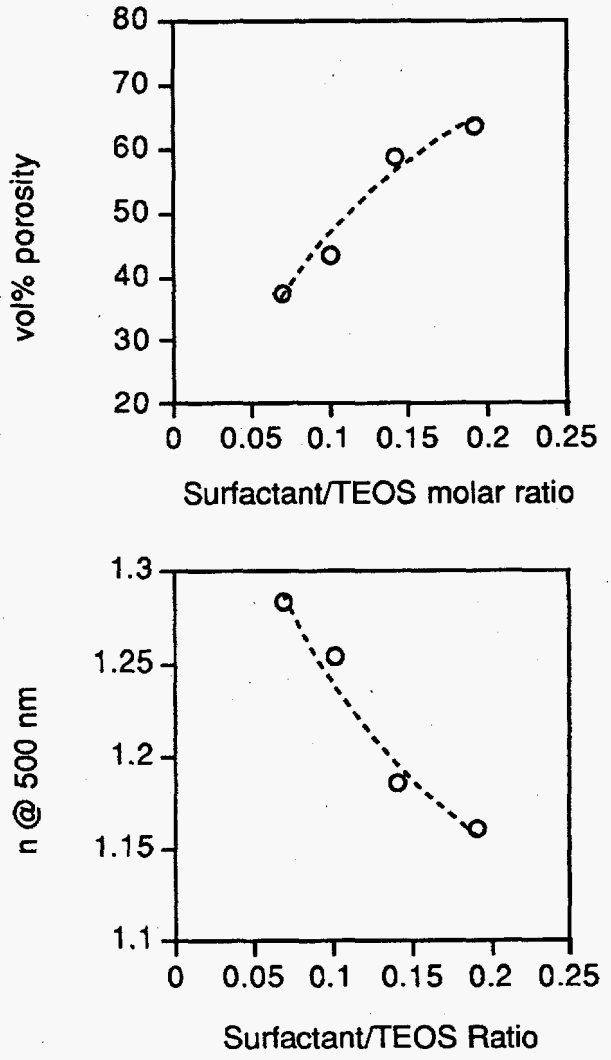

Figure 1. Film porosity and refractive index as a function of the surfactant/TEOS molar ratio.

refractive index, indicating that spin-coated mesoporous films are potentially useful in low K' applications.

Publication and Presentation

J. Liu, J.R Bontha, A.Y. Kim, and S. Baskaran. 1996. "Preparation of continuous mesoporous films on porous and dense substrates." In *Proceedings of Symposium on Microporous and Macroporous Materials*, MRS Spring Meeting, San Francisco, California, April 8-12.

High Temperature Catalytic Materials

Kalahasti S. Ramesh, John G. Darab (Materials and Chemical Sciences)
John L. Cox, Timothy L. Hubler (Environmental Technology)

Project Description

The objective of this project is to identify and develop new catalytic materials for high-temperature (> 1000°C) applications. New catalytic materials will be prepared and their structure (physical, chemical, and catalytic properties) investigated under controlled experimental conditions. Initially, the class of refactory metal oxides referred to as hexaaluminates, with the general formula $MO.6Al_2O_3$, are targeted for study. This class of materials is known to have high thermal stability (1500°C) and afford the opportunity to tailor catalytic activity and selectivity through suitable lattice substitutions for the aluminum (Al^{+3}) and the alkali metal (M^{+2}).

At present, improved catalysts that can withstand high temperatures are a roadblock to improved efficiency, economics, and reduced environmental impact of a number of energy and chemical processes. These include catalysts for combustion, steam/natural gas reforming, internal combustion engine pollution abatement, and hot-fuel gas cleanup. Catalytic combustion of methane is an area of interest for the development of stationary gas turbines, which is the technology of choice for new electricity loads. Japanese industry is currently far ahead of the U.S. in this area of catalysis R&D. Solid oxide fuel cells are another important area for high-temperature (> 1000°C) catalyst research. Catalyst stability and durability at these high temperatures are of paramount importance to all these advanced energy/environmental technologies.

Technical Accomplishments

Conventional methods for preparing high surface area, single phase, hexaaluminates, including 1) solid-state reaction of the component oxides at elevated temperature and 2) wet chemical co-precipitation have not been entirely satisfactory. As the number of metal components in the hexaaluminates increase, these methods of synthesis become even less satisfactory. This problem has been circumvented by using a sol-gel method of synthesis, specially tailored for the multicomponent hexaaluminates targeted for investigation. Table 1 lists the catalysts prepared along with characterization data.

Table 1. Catalyst Characterization Data

Material Composition	Bulk Density g/cc	Surface Area, m^2/g 1300°C/6h	1400°C/2h	Phases, XRD
$SrAl_{12}O_{19}$	0.91	7.3	6.9	100%$SrAl_{12}O_{19}$
$Sr_{.8}Pr_{.2}Al_{12}O_{19}$	1.10	6.0	3.4	75%$Sr_{.8}Pr_{.2}Al_{12}O_{19}$ +25% amorph.
$Sr_{.8}Ce_{.2}Al_{12}O_{19}$	1.08	1.4	1.2	75%(95%$SrAl_{12}O_{19}$, 5%CeO_2)+25% amorph.
$Ca_{.8}Pr_{.2}Al_{12}O_{19}$	1.09	6.0	4.8	100%$Ca_{.8}Pr_{.2}Al_{12}O_{19}$
$Ca_{.8}Ce_{.2}Al_{12}O_{19}$	1.24	9.5	8.6	85%(75%$CaAl_{12}O_{19}$, 20%CeO_2, 5%Al_2O_3) +15% amorph.

The preparation of unsubstituted hexaaluminates was found to be straightforward and can be accomplished by any one of a number of approaches so long as sufficient calcination temperature and time are employed. The sol-gel method, because of the intimacy of component contact, allows hexaaluminate phase development at a lower calcination temperature. Preparing substituted hexaaluminates is much more challenging. Aside from the stoichiometry requirement, cation size and charge must be carefully selected with respect to substitution in the mirror plane or spinel block. The failure of Ce^{+4} substituted hexaaluminate to form is thus attributed to its being too small (85 pm) and the charge too great to substitute in the mirror plane and its being too large to substitute for Al^{+3} (53.5 pm) in the spinel block. The ionic radii of the Pr^{+3} (99 pm) on the other hand is sufficiently close to Sr^{+2} (118 pm) and Ca^{+2} (100 pm) to permit substitution.

The observed order of thermal stability of the prepared materials was $SrAl_{12}O_{19} > Ca_{0.8}Ce_{0.2}Al_{12}O_{19} > Sr_{0.8}Ce_{0.2}Al_{12}O_{19} > Ca_{0.8}Pr_{0.2}Al_{12}O_{19} > Sr_{0.8}Pr_{0.2}Al_{12}O_{19}$. These results are consistent with other reported investigations on means for stabilizing aluminas where additions of alkaline earth metals, Ca, Sr, and Ba result in the formation of hexaaluminate when calcined at high temperatures which maintain high surface area even at temperatures up to 1450°C. These results on stability enhancement of aluminas point to the importance of inhibition of mass transport by the addition of stabilizing components whether it suppresses the phase

transformation by forming a stable crystalline structure (as in the case of the hexaaluminates) or retards the sintering of the surface structure by hindering surface diffusion or preventing nucleation. The hexaaluminates have shown superior thermal stability to many candidate catalysts for high-temperature catalytic combustion, including a large number of simple transition metal oxides and first row transition metal perovskites.

The catalytic activity of the prepared hexaaluminates toward methane combustion were also studied in a packed-bed micro-flow reactor. The results are shown in Figure 1 and reported in Table 1. Each catalyst exhibited a characteristic S-shaped curve which begins with low methane conversion where the rate is controlled by the kinetics of the chemical reactions on the surface of the catalyst. As the temperature increases, the rate increases and heat builds up to the point where the catalyst "lights-off" resulting in a rapid increase in methane conversion, followed by the tailing off of conversion due to lack of fuel supply and/or air to the catalyst. The observed order of catalyst activity for the catalysts based on the $T_{10\%}$ was none ≈ dense Al_2O_3 ≤ $Ca_{0.8}Pr_{0.2}Al_{11}O_{19-\alpha}$ < $Sr_{0.8}Pr_{0.2}Al_{11}O_{19-\alpha}$ < $Ca_{0.8}Ce_{0.2}Al_{11}O_{19-\alpha}$ < $Sr_{0.8}Ce_{0.2}Al_{11}O_{19-\alpha}$ < $SrAl_{12}O_{19}$.

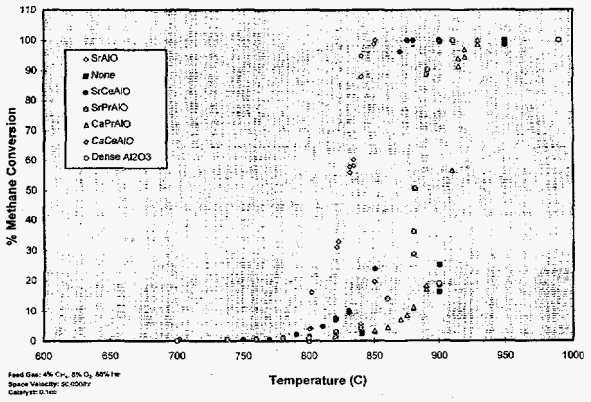

Figure 1. Combustion catalyst activity (catalyst calcined at 1200°C/4h).

The procedure used in determining catalyst activity also revealed information about reaction mechanism. Invariably the initial catalyst activity decreased, quite abruptly in some cases, to an apparent steady-state value. This phenomenon was examined in some detail for $Sr_{0.8}Pr_{0.2}Al_{11}O_{19-\alpha}$ and $Sr_{0.8}Ce_{0.2}Al_{11}O_{19-\alpha}$. This decrease in catalyst activity is consistent with the bulk or lattice oxygen contributing to the oxidation. Hence, initially the catalyst is saturated with oxygen so that conversion is high, but since the rate of methane oxidation is more rapid than the replenishment of the lattice oxygen, as the available oxygen becomes depleted, the conversion slows until it eventually reaches a steady-state value which depends upon temperature, space velocity, catalyst, and reactant composition. If poisoning or sintering of the catalyst were responsible for the decrease in activity, we would not expect the initial activity to be restored by oxygen treatment in the absence of methane as was seen in the sequential tests performed at 890°C. This model of methane combustion over metal oxide catalysts has been evoked by others and takes the rate expression shown in Equation (1) where k_1 is the rate associated

$$\text{Rate} = k_1 P_{CH4} + k_2' P_{O2}^{0.5} P_{CH4} \qquad (1)$$

with the lattice oxygen and k_2' for the chemisorbed oxygen.

Publications and Presentations

K.S. Ramesh, J.L. Cox, J.J. Kingsley, T.L. Hubler, and J.G. Darab. "Catalytic combustion over hexaaluminates." Ceramic Transactions Series, *Catalyst Materials for High Temperature Processes,* M. Misono, P.L. Gai, and K.S. Ramesh, Eds., American Ceramic Society (in press).

J.G. Darab and K.S. Ramesh. "Hexaaluminates for high temperature catalytic applications (A Review)." *Journal of Materials Science* (in preparation).

T. Hubler, K.S. Ramesh, J.L. Cox, and J. Darab. 1995. "Modified hexaaluminates for high-temperature oxidation catalyst application." Presented at the 98th Annual Meeting of the American Ceramic Society, Indianapolis.

K.S. Ramesh. 1996. "New materials for catalytic combustion." Invited Seminar at the Institute of Materials, University of Oregon, Eugene, March.

K.S. Ramesh. 1996. "Novel catalyst materials for automotive exhaust catalyst." Invited Seminar at the University of Washington, Seattle, February.

K.S. Ramesh, J.J. Kingsley, and J.L. Cox. 1995. "Synthesis and properties of hexaaluminates for catalytic combustion." Presented at the Annual Session of the American Ceramic Society, Cincinnati.

Intelligent Organic/Inorganic Composites

Jun Liu (Materials Sciences)

Project Description

This project aims to combine intelligent organic molecules with inorganic materials to form a new class of intelligent composites. The inorganic material functions as a structural framework and defines the scale and the microstructure of the composite, such as the pore size, pore geometry, and pore connectivity. These organic molecules interact with the environment to provide a specific function. The applications of such materials for controlled release of expensive chemicals and for binding toxic heavy metals have been investigated.

Technical Accomplishments

There has been a growing interest in "intelligent molecules" made of soft aggregates of organic polymers. Because of the specific functional groups, these organic materials can respond to a change in environmental conditions, or can specifically react with chemical agents. Materials scientists have been using and advancing composite materials based on metals, ceramics, and plastics for decades. The science and technology of such hard materials have been well established. Unfortunately, these hard materials do not actively interact with the environment and the product serves to provide only one particular function, such as mechanical strength.

This project aims to combine the inorganic material and the soft organic material to form an intelligent composite. The ceramic material functions as structural framework and defines the scale and the microstructure of the composite, such as the pore size, pore geometry, and pore connectivity. The organic material is incorporated into or co-synthesized with the ceramic material. These organic molecules are the intelligent component of the composite that can respond to an environmental change or provide specific interactions.

The main accomplishments in 1996 are summarized below.

Materials Development for Controlled Release of Expensive Chemicals

In FY 1996, we made a presentation about the smart materials we were working on to scientists and researchers from the Northwest region's agricultural community. The composite materials have been identified as having great potential for applications that are relevant to the economy of the Northwest. For example, insect pheromones have been widely investigated for pest control, but few delivery systems have been effectively demonstrated. The existing delivery systems, including polymer matrix encapsules, cannot meet the requirements of the applications.

We have synthesized polymer materials that can switch between different states. These polymers are used to trap pheromones. Unlike traditional polymers, the release rate in the polymer matrix can be controlled and fine tuned for particular applications. This will greatly increase the effectiveness and reduce the cost of pest treatment using biologically derived agents.

The phase transition, with respect to solvent conditions and temperature is shown in Figure 1. The loading and unloading of several pheromones have also been demonstrated.

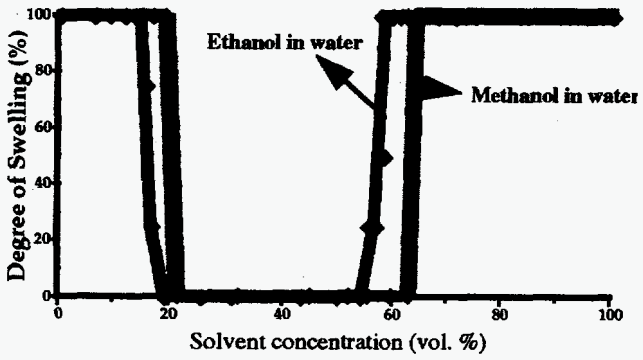

Figure 1. Phase transition (degree of swelling) of the polymers as a function of solvent concentrations.

Binding of Heavy Metals to Self-Assembled Molecules on High Surface Area Supports

The binding of the heavy metals and the interfacial molecular conformation were investigated. The molecular ordering at the interface was established using a solid-state nuclear magnetic resonance technique (see Figure 2). The new materials showed extremely high efficiency in removing heavy metals from both aqueous and nonaqueous waste streams. Distribution coefficients as high as 300,000 have been obtained for Hg. The materials have also shown very high selectivity in the presence of other actions, such as Na, Ba, etc.

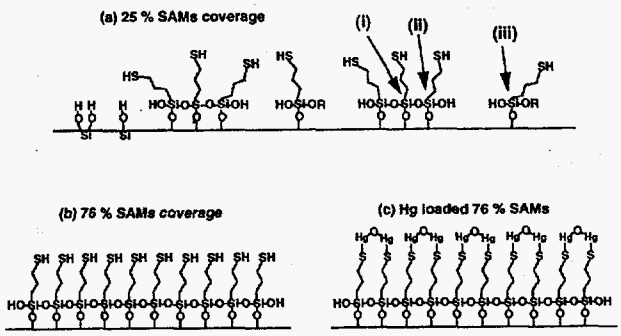

Figure 2. Molecular ordering of functional molecules at the interface as revealed by NMR.

Publication

X. Feng, G.E. Fryxell, L.-Q. Wang, and J. Liu. "Self-assembled monolayers on mesoporous supports (SAMMS)." *Science* (to be submitted).

Materials Synthesis and Processing for Flat Panel Displays

Barbara Tarasevich, Suresh Baskaran, Gordon Graff, Larry Chick, Nancy Hess, Jun Liu (Materials and Chemical Sciences)
Alan Joly (Chemical Structure and Dynamics)

Project Description

The objective of this work is to develop novel phosphor materials for flat panel displays. Emissive flat panel displays are critical to a new generation of imaging and display technologies, such as monitors, laptops, large screens, and head-mounted displays. Their commercialization has been limited, however, due to the lack of highly efficient, chemically stable phosphors that operate at low voltages. In general, phosphor formation is a "black art" — with a lack of understanding of how to control and optimize luminescence through solid-state band structure and by controlling macroscopic particle/cluster properties and microscopic crystal/dopant structure. New phosphor materials for flat panel displays will be developed by teaming several novel materials processing technologies developed at PNNL. Nanostructured phosphors will be developed using mesoporous matrices as templates, and particulate phosphors will be developed using a combustion process for the formation of submicron particles. These processes have significant advantages over conventional methods in that complex materials can be synthesized with controlled dopant levels and submicron to nanosized structures.

Technical Accomplishments

Two approaches were used to form novel low-voltage phosphors involving micron-scale and nanoscale synthesis:

- Particulate zinc gallate phosphors were developed using combustion synthesis methods and were modified by variations in cation concentration.
- Nanostructured quantum phosphors were formed using mesoporous matrices as templates.

Phase pure zinc gallate and materials deficient in zinc were developed and characterized using x-ray diffraction, transmission electron microscopy, and inductively coupled plasma. Figure 1 shows photoluminescence spectra for zinc gallate powders at 254 nm excitation. The spectra show broadband emission centered at 490 nm due primarily to three radiative crystal field split transitions of gallium: $^4T_2$,$^4T_1$, and ^2E to $^4A_2$.

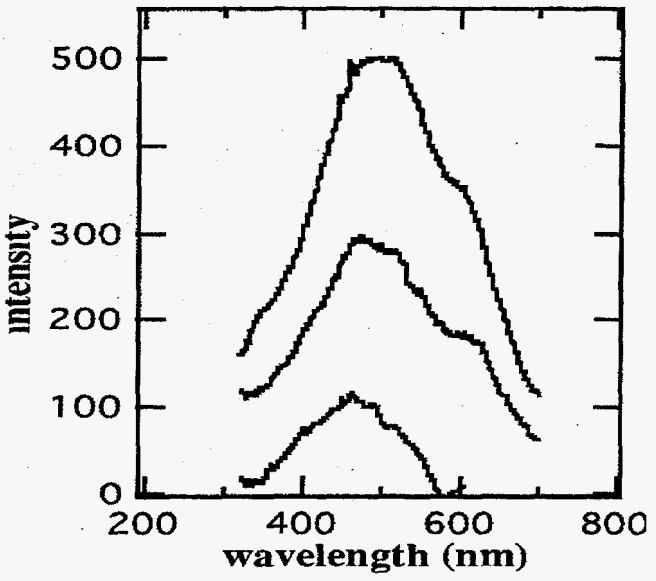

Figure 1. Photoluminescence of zinc gallate powders at 254 nm.

Interestingly, the luminescence intensity increases with decreasing zinc concentration. The mechanisms for this enhancement of luminescence are not known but may be due to effects of zinc deficiency on the octahedral coordination and symmetry of gallium. Ongoing work involves characterization of materials by catholuminescence to obtain efficiencies in lumens per watt which can be compared to conventional materials.

Quantum structures consist of 10 Å to 100 Å semiconducting clusters isolated within a dielectric or higher band gap material. These devices are of interest because quantum confinement controls the band structure meaning that the color emitted can be tuned by varying the cluster size. More importantly, these systems can have very high luminescent efficiencies. Nanostructured cadmium sulfide and ZnO phosphors were formed using mesoporous silica matrices. Figure 2a shows a TEM micrograph of a cross section of 40 Å mesoporous silica.

Figure 2b shows photoluminescence excitation and emission spectra for the cadmium sulfide nanocomposites. The spectra for cadmium sulfide show an excitation peak at 390 nm. This peak is blue shifted from the 477 nm

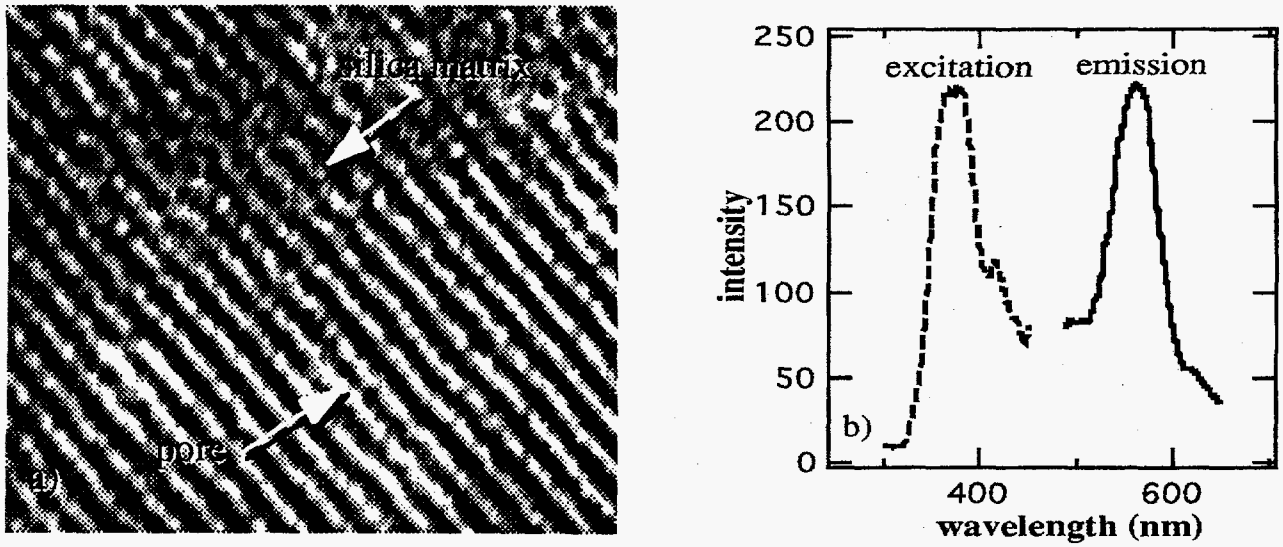

(a) (b)

Figure 2. a) TEM micrograph of mesoporous silica showing longitudinal section of 40 Å cylindrical pores. b) photoluminescence spectra of CDs precipitated within 30 Å mesoporous silica showing quantum confinement.

excitation peak expected for bulk cadmium sulfide suggesting quantum confinement of the 30 Å diameter precipitates. The emission peak is at 560 nm indicating transitions involving defect states and not donor/acceptor recombination across the band gap.

We have demonstrated the synthesis of zinc gallate particulate phosphors with good blue photoluminescence and cadmium sulfide and ZnO nanophosphor materials exhibiting strong photoluminescence due to quantum confinement. Further work will allow us to characterize the materials by cathodoluminescence, optimize properties, and understand luminescence mechanisms in macroscopic and quantum structures.

Publication

B. J. Tarasevich, L. Chick, and C. Coyle. "Formation of zinc gallate phosphors by combustion synthesis." *Journal of Materials Research* (to be submitted).

Mesoporous Materials

Jun Liu (Materials Sciences)

Project Description

The objective of this project is to develop novel high surface area mesoporous materials for industrial and environmental processes. In 1996, we developed a new templating route for making mesoporous zirconia materials. High surface area zirconia is a potential candidate for an environmentally benign solid acid catalyst. We also explored the application of mesoporous materials as energy storage material and as new environmental remediation agents.

Technical Accomplishments

The discovery of ultra-large porous zeolite has greatly expanded the possibilities of designing open porosity materials for a variety of applications. The new materials are characterized by pore diameters that can be adjusted between 1.5 nm and 20 nm through synthesis conditions and by the monodispersity and ordering of the pores. However, many industrial and environmental applications require the materials to have a range of chemical compositions and specific surface chemistry that cannot be satisfied by existing mesoporous materials. In 1996, the research thrust of this project was to 1) overcome the weakness of the existing mesoporous materials, 2) expand the field of application of mesoporous materials, especially to the areas that are unique to PNNL, and 3) further scientific understanding and strengthening of our position in this research area.

The main results are summarized below.

New Templating Route Developed for Making Mesoporous Materials Using Amphoteric Surfactants

Cationic surfactants, anionic surfactants, and nonionic surfactants have been used in the synthesis of mesoporous materials according to the literature. The templating effect has been attributed to the ionic or hydrogen binding between the head group and the ceramic precursors. However, the head group size was usually affected by the binding of the ceramic precursors and the synthesis was difficult to control. We have for the first time used amphoteric surfactant as the template. The large cationic group in the head area was not affected and determined the geometry of micelles, and the ceramic precursor was bound to the anionic portion of the surfactant through covalent bonding. The new templating route is illustrated in Figure 1a as compared to existing synthesis methods. The interfacial bonding was established by nuclear magnetic resonance and is illustrated in Figure 1b.

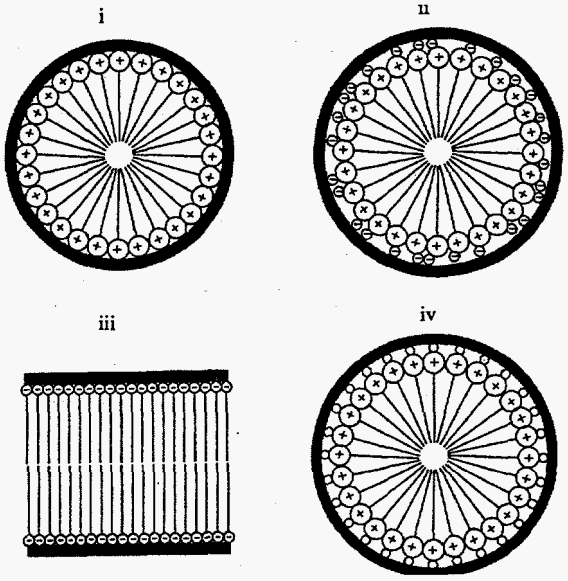

Figure 1a. Comparison of the several typical bonding conformations: (i) cationic, (ii) ion mediated, (iii) anionic, (iv) amphoteric.

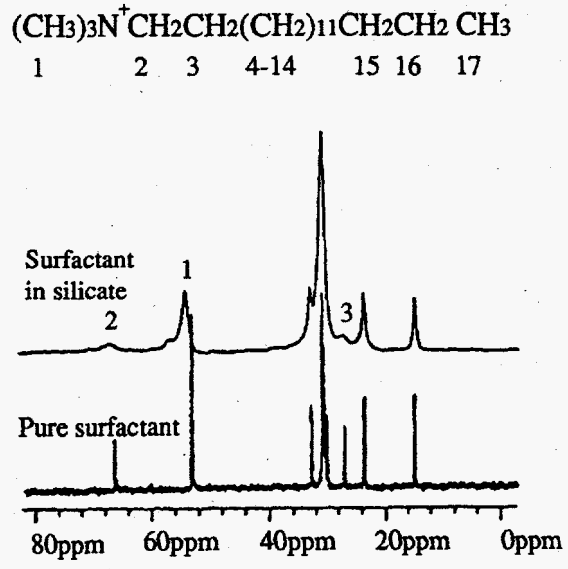

Figure 1b. Line broadening and shift indicate the ceramic precursor binds to the anionic portion, not the cationic portion, of the head group.

New Mesoporous Materials Developed, Self-Assembled Monolayers on Mesoporous Supports

To systematically vary the surface chemistry and to design specific binding sites on the surface for catalytic and environmental applications, functional groups were attached to mesoporous silica to form a novel material: self-assembled monolayers on mesoporous supports (SAMMS). A population density of 75% of the self-assembled monolayers has been achieved. The SAMMS material is illustrated in Figure 2. This material not only finds immediate application in environmental remediation, it also opens enormous possibilities for designing more complicated functional structures and composites. The SAMMS material has demonstrated very high efficiency for removing heavy metals from aqueous and nonaqueous waste streams under a variety of conditions.

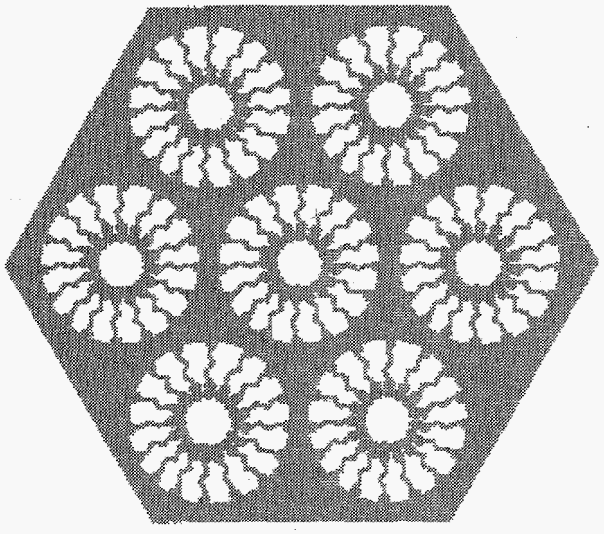

Figure 2. Schematic illustration of the SAMMS.

Modeling and Understanding of the Self-Assembly Processes

A simple molecular dynamics model has been developed to model the formation of high order structures of surfactants in the presence of the ceramic precursors.

This is the first and the only model available to date that is able to qualitatively predict the binding of ceramic precursors to the surfactant head groups and its effect on the micellar structures.

Nuclear magnetic resonance has been used to study the molecular dynamics and conformation in surfactant ceramic precursor solutions. The global and molecular disorder-to-order transformation has been established, as illustrated in Figure 3.

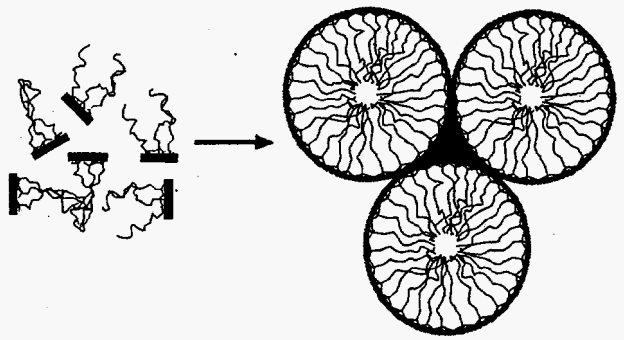

Figure 3. Local and global disorder-to-order transition as revealed by NMR.

Publications

L.-Q. Wang, J. Liu, G.J. Exarhos, and B.C. Bunker. 1996. "Investigation of the structure and dynamics of surfactant molecules in mesoporous silicates using solid-state ^{13}C NMR." *Langmuir* 12, 2663-2669.

J. Liu, A.Y. Kim, and J.W. Virden. 1996. "Preparation of mesoporous spherulites in surfactant solutions." *J. Porous Materials*, 2, 201-205.

J. Liu et al. "Self-assembly in the synthesis of ceramic materials and composites." *Advances in Colloidal and Surface Science* (invited review article, in press).

B.J. Palmer and J. Liu. "The effect of solute-surfactant interactions of micelle formation in surfactant solutions." *Langmuir* (in press).

A.Y. Kim, P. Bruinsma, and J. Liu. "Synthesis of mesoporous zirconia using amphoteric surfactant." *J. Chemical Communication* (in press).

Nanoparticle Processing

Beth L. Armstrong (Materials Sciences)

Project Description

The overall goal of the nanoprocessing project was to investigate material fabrication processes of nanoparticles into pellets, thin films, membranes, and bulk ceramics while building material processing capabilities at PNNL. The objectives for FY 1995 were refined to properly process the above mentioned forms such that unique material properties (high surface area, unique surface chemistry, and controlled porosity) would be maintained. Efforts for FY 1996 added ultrafine powder consolidation for catalysis, membrane separation, and catalytic membrane reactor applications.

Until the development of the Rapid Thermal Decomposition of precursors in Solution (RTDS) process, attaining nanoparticulate materials in large quantities was difficult and very expensive. Competing technologies are now only just beginning to provide nanoparticulate materials in pound quantities. Thus, processing nanoparticulates into large, bulk components was simply not feasible due to a lack of material with reproducible characteristics. Even if the materials were available, processing of nanoparticulates into bulk components is extremely difficult due to the high surface area of the powders, typically >200 m^2/gm, and the hygroscopic nature of the powders themselves. These powders do not flow or pack well due to the high surface areas and excess water.

During FY 1994, consolidation of RTDS products was investigated for structural ceramic applications. With such applications being judged inappropriate for the RTDS powders, efforts in FY 1995 focused on using RTDS and mesoporous powders for catalytic applications. The issues of processing ultrafine powders were still similar to the objectives set in FY 1994. These issues included overcoming problems of consolidating powders with highly hydrated surfaces, maintaining high surface activity, and fabricating mechanically robust components. These components must retain their high pore volume after processing to facilitate high reactivity and mass transport.

During FY 1996, efforts built on an alternative ultrafine synthesis process developed at PNNL, the glycine nitrate process. The glycine nitrate process, which is now scaled-up commercially, produces nanocrystalline, complex stoichiometry oxides by a combustion synthesis process. Aqueous precursors, such as metal nitrates, and glycine are mixed and heated to autoignition to produce a "fluffy" ash composed of hard agglomerated particles. Unlike the RTDS derived powders, the glycine nitrate process-based powders have lower surface areas, typically >10 m^2/gm, and therefore are less prone to hydration. However, compaction was still difficult due to the agglomerated nature of the resulting powders.

Technical Accomplishments

This project was separated into three sections: 1) ultrafine material consolidation, 2) mesoporous material consolidation, and 3) catalytic membrane consolidation.

Ultrafine Material Consolidation

Partially (4Y-PSZ) and fully stabilized (8Y-FSZ) zirconias were synthesized using a modified version of the glycine nitrate process. Due to the high autoignition temperature required to form crystalline zirconia, the glycine was replaced with urea buffered with carbohydrazide. The glycine nitrate process powders were uniaxially pressed at 64.2 MPa and cold isostatically pressed at 137.9 MPa. Initial sample sizes were approximately 21 mm in diameter by 1 to 3 mm thick. A variety of heat treatments were evaluated to determine the optimal sintering conditions. The compacts were heated 2°C/min to 5°C/min to the sintering temperature (1100°C to 1400°C) and held at the selected temperature for 2 hours in air. As anticipated, sintered densities increased with increasing sintering temperatures for all compositions (Figure 1).

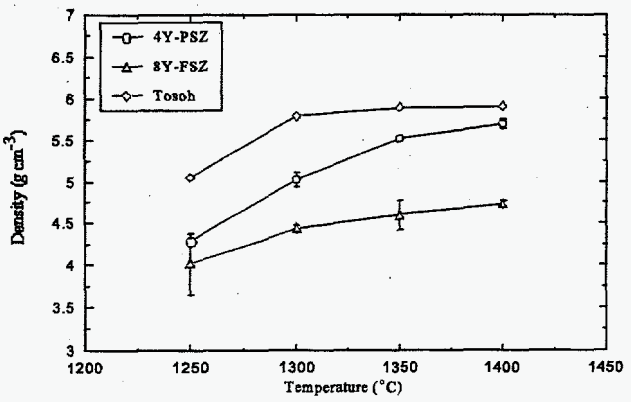

Figure 1. Sintered densities of glycine nitrate process-synthesized zirconias.

However, neither the glycine nitrate process-modified 4Y-PSZ and 8Y-FSZ pellets sintered to full theoretical density. The 4Y-PSZ pellets showed an average 10% increase in relative density over the 8Y-FSZ pellets. To determine if full theoretical density could be realized for the 4Y-PSZ material without the use of high pressures, a set of milling experiments were run. Pellets were pressed from 4Y-PSZ powder that was ball milled for 16 hours, shaker milled for 16 hours, or shaker milled for 16 hours and calcined at 650°C for 0.5 hour. Pellets were sintered at 1300°C for 2 hours.

The sintered densities increased with increased work or decreased agglomerate size. Ball milling produced sintered densities of 5.69 gm/cc, shaker milling of 5.76 gm/cc, and the calcined-shaker milled samples showed the most improvement of 5.82 gm/cc. The average grain size distribution for the calcined-shaker milled pellet was 100 to 200 nm. This showed that even though the powder did not densify at lower sintering temperatures than are typical of submicron zirconias, the grain size was smaller than reported for the submicron-sized materials.

Mesoporous Material Consolidation

Based on the results of the consolidation of the mesoporous silicas during FY 1995 (using the aqueous synthesis technique evaluated on the "Catalyst Development and Testing" project during FY 1994 and 1995), we continued consolidation efforts on larger sample sizes (~50.8 mm diameter pellets) on the Catalyst Development and Testing project directly. Support was provided to uniaxially and isostatically press and densify pellets for electrochemical separation applications.

Catalytic Membrane Consolidation

Originally, the fabrication of a porous, open ended, silica tube was planned for ultrafiltration applications. Due to unplanned fiscal cutbacks in the project, this task was eliminated from the project scope.

Publication and Presentation

B.L. Armstrong. "Consolidation of nanocrystalline ZrO_2." *Materials and Manufacturing Processes,* Vol. 12, No. 2 (in press), and presented at the ASME Conference, Johns Hopkins University, Baltimore, Maryland, July (invited).

Nanoparticle Science

Larry A. Chick (Materials Sciences)

Project Description

During FY 1996, this project investigated the use of alternative fuels for combustion synthesis of ceramic powders. The "burn" characteristics of the production process, as well as the properties of the resulting powders were of prime concern. Alternative fuels hold the possibility of allowing a more exact tailoring of the powder produced to fit varying applications. Rate of production, material cost, particle size, and phase purity are all directly related to the combustion process which will change drastically with the fuel chosen.

Technical Accomplishments

Typically, in the production of $La_{0.7}Ca_{0.31}CrO_3$ materials by combustion synthesis, glycine is used as a fuel leading to the glycine nitrate process. For this study, 10 fuels were investigated including glycine. The study began by looking at the burn characteristics of these 10 fuels and their effect on the production of $La_{0.7}Ca_{0.31}CrO_3$ powder. To study the burn characteristics, the flame temperature, ignition temperature, and amount of remaining water at time of ignition were observed for each fuel. The ignition temperature and remaining water values were collected by use of a constructed apparatus as shown in Figure 1. The flame temperature was monitored by use of a two-color optical pyrometer. The powders produced in each test were collected and several of their properties were measured. BET analysis was performed on each powder to determine the surface area. Results are listed in Table 1.

The early experiments showed that the burn characteristics were influenced by a large number of variables outside of the fuel chosen. Sample geometry (relating to the geometry of the container during the burn) and heating rate often had significant influences on the resulting burn characteristics. To minimize these effects, the geometry was held constant and designed so that the precursor solution would be arranged as a thin layer in a flat bottom dish. This was chosen as the layout to minimize the effects of uneven heating. The heating rate was also controlled by keeping the sample distance from the hot plate constant and keeping the setting of the hot

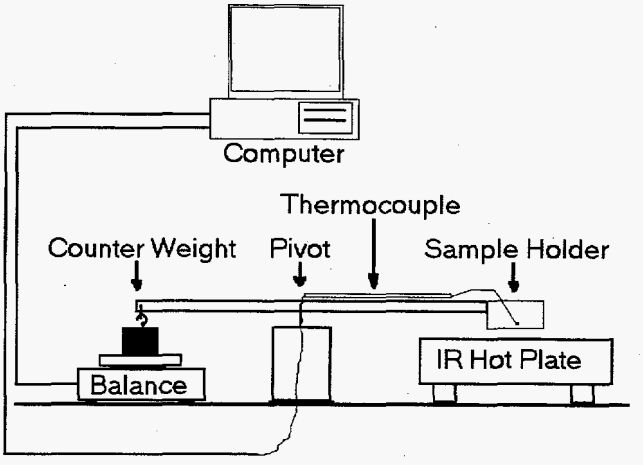

Figure 1. Experimental apparatus for measuring the wt% residual water and the ignition temperature of precursor solutions for combustion synthesis.

plate constant. It was found that combustion tended to begin at an edge of the thin film, where the water content was locally lower, and then spread through the thin film sample. As a result, it was sometimes difficult to assign a definite ignition temperature and water content to a given fuel solution.

A series of experiments involved systematic variation of the solution heating rate. The results showed that the residual water content at the point of ignition decreased with slower heating rates for some fuels, such as valine, but remained relatively constant for others, such as glycine. Data for valine are shown in Figure 2. At high heating rates (short time to ignition), the solution ignited when there was still as much as 25% water present. At much slower heating rates, the residual water was essentially gone when ignition occurred. Residual water is expected to decrease the flame temperature, because it absorbs heat without reacting to release chemical energy. Figure 3 shows that, indeed, the measured flame temperature decreases with increasing residual water. The calculated adiabatic flame temperatures show the same trend, although they are much higher, due to the non-adiabatic conditions of the experimental combustions.

Table 1. Data on Combustion Synthesis Fuels

Fuel	Weight	Formula	BET Surface area, m^2/g	Ignition Temp., °C	Flame Temp., °C
Alanine	89.09	$H_2NCH_2CH_2CO_2H$	20.6	182.45	1511
Anthranilic Acid	137.14	$H_2NC_6H_4CO_2H$	42.2	158.53	
Arginine	174.20	$H_2NC(NH)NH(CH_2)_3CH(NH_2)CO_2H$	25.7	171.42	1473
Carbohydrazide	90.09	$H_2NNHCONHNH_2$		180.80	
Glutamic Acid	147.13	$HO_2CCH_2CH_2CH(NH_2)CO_2H$	30.9	160.92	1312
Glycine	75.07	$H_2NCH_2CO_2H$		216.75	
Methionine	149.21	$CH_3SCH_2CH_2CH(NH_2)CO_2H$	34.8		
Proline	115.13	$HOCOCH(CH_2)_3NH$	25.6	167.92	1487
Sucrose	342.30	$C_{12}H_{22}O_{11}$			
Valine	117.15	$(CH_3)2CHCH(NH_2)CO_2H$	13.8	156.64	1493

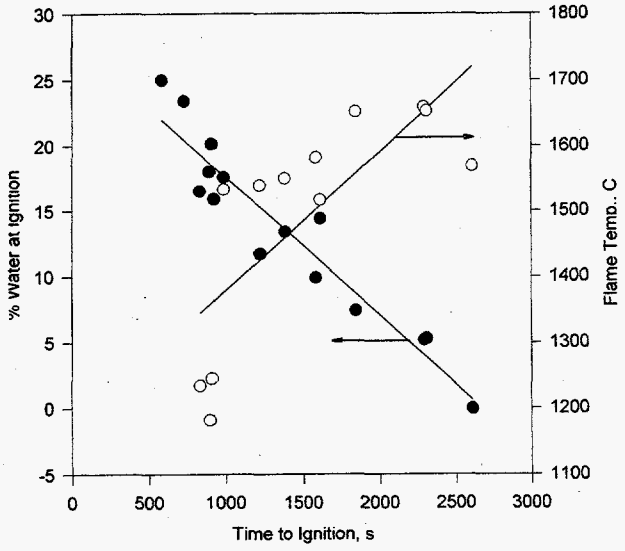

Figure 2. Percent water at ignition and flame temperature versus time to ignition for nitrate-valine solution precursor.

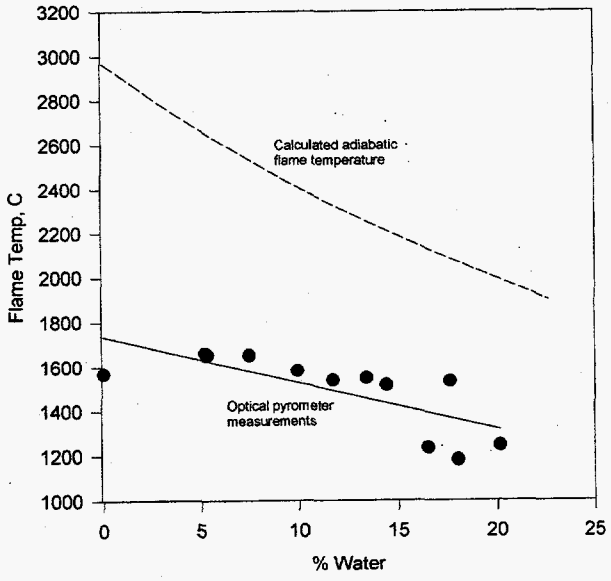

Figure 3. Flame temperature versus percent water at ignition for nitrate-valine precursor solutions, measured and calculated for adiabatic conditions.

Ordered Mesoporous Membranes and Thin Films

Jun Liu (Materials Sciences)

Project Description

This work aims to produce ceramic membranes and thin films with uniform porosity adjustable in the nanometer size range based on nucleation and self-assembly of surfactant liquid crystalline structures on functionalized surfaces or at liquid-liquid interfaces. In FY 1995, formation of free-standing thin films on a liquid-liquid interface was demonstrated. Nanoporous membranes on porous supports were prepared using a diffusion reactor. In FY 1996, this method was further optimized and high quality, continuous, transparent mesoporous films have been prepared. The structures of the mesoporous film were characterized by x-ray diffraction and transmission electron microscopy.

Technical Accomplishments

The discovery of ultra-large porous zeolite like materials is considered a landmark in the history of synthesis of molecular sieve type materials. The new materials are characterized by pore diameters that can be adjusted between 1.5 nm and 20 nm through the synthesis conditions and by the monodispersity and ordering of the pores. Unfortunately, these materials can be prepared only in powder form. One of the most important applications of such materials will be membranes and films. In 1994 and 1995, PNNL scientists used a new synthesis route to make membranes and films based on the discovery of a heterogeneous nucleation mechanism. In FY 1996, the objective was to further develop the synthesis procedure and to optimize the synthesis conditions.

In FY 1996, the interfacial reaction method was optimized to prepare continuous mesoporous films on porous supports. The films produced have the desired characteristics of mesoporous film for separation and purification purposes: continuity, uniform micro-structure, and free of defects. A porous support was placed between two compartments—one containing a silicate solution and the other a surfactant solution. The silicate and surfactant solutions diffused into the support to form a stable mesoporous interfacial film. Under optimum conditions (e.g., temperature), a very uniform and transparent film was formed in the middle of the porous support where the surfactant and silicate solution met. Based on transmission electron microscopy (TEM) and x-ray diffraction (XRD), the mesoporous film appears to have formed through the following mechanism: the surfactant mixed with the silicate at the interface to form flexible, rod-like micelles, and these silicate-surfactant micelles condensed into an insoluble interfacial film consisting of random-packed micelles. (See Figures 1a and 1b.)

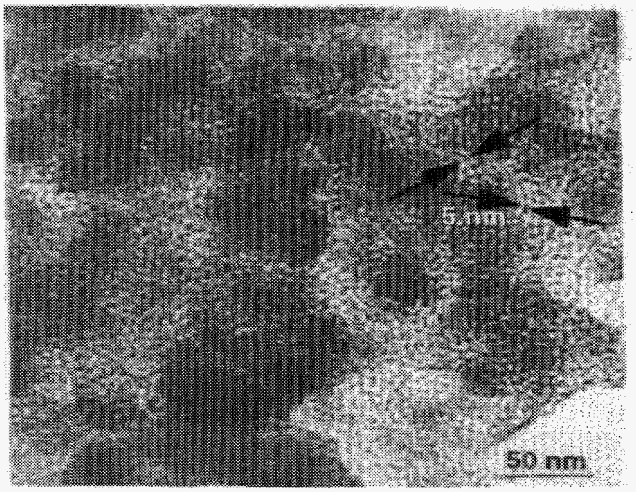

Figure 1a. TEM micrograph showing the random packed micelles in the mesoporous film.

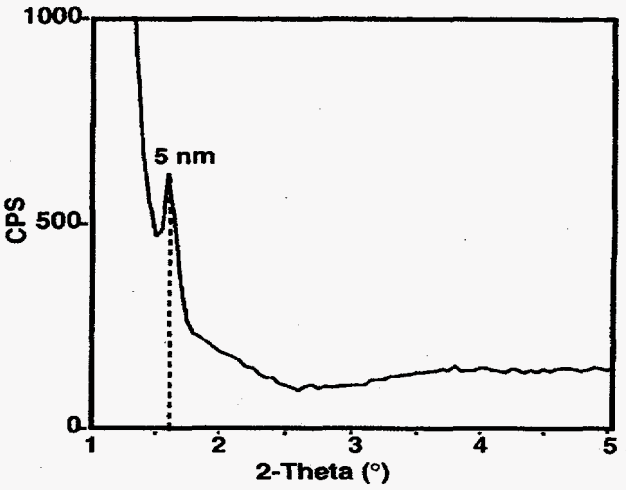

Figure 1b. Low angle XRD pattern showing a typical peak corresponding to the micellar structure in the film.

A joint effort with another project led to the development of a fast, simple spin coating method for making high-quality, transparent mesoporous films on dense substrate. In this method, the starting solution is

a homogeneous mixture of surfactant and silicate. The solution was spun onto a substrate and dried fast. This produced a mesoporous film with a strong (100) reflection in x-ray diffraction. Transmission electron microscopy suggests that it consists of mesoporous structures and the ordering starts from the substrate. The advantages of this approach include: simple and fast preparation, high quality, controlled thickness over a wide range, and thermal stability during calcination. The total porosity and the wall thickness also can be adjusted, which is not possible in any other methods.

The supported films developed under this project may find applications as separation membranes, sensors, low dielectric coatings for semi-conducting devices, and electrode devices for ultracapacitors. The spin coated films may find applications as electrodes in ultracapacitors.

Publication

J.A. Bontha, J. Liu, and A.Y. Kim. "Preparation of continuous mesoporous films based on interfacial reactions." *Chemistry of Materials* (submitted).

Shape Selectivity Porous Catalysts

Bruce C. Bunker (Advanced Processing)

Project Description

The objective of this project was to synthesize novel and supported heteropoly acid catalysts to replace Friedel-Crafts metal halide catalysts. Traditional Friedel-Crafts catalysts include aluminum chloride and boron trifluoride materials. However, they both are very corrosive, can be used for only one catalyst cycle, and create a hazardous waste. After one catalytic cycle, the deactivated catalysts cannot be regenerated and therefore must be disposed of in a landfill. Numerous chemical companies are looking for alternative Friedel-Crafts catalytic materials for use in special chemical, commodity chemical, and low molecular weight polymer or resin synthetic processes. Recent publications have indicated that heteropoly acids possess the closest surface acidity to aluminum chloride and boron trifluoride materials, however, heteropoly acids have low surface area (about 5 m^2/g), poor thermal stabilities, and also have shown inadequate regeneration characteristics.

The approach used in this project was to synthesize and characterize stabilized heteropoly acid catalysts by incorporating/supporting heteropoly anions in the pores of mesoporous silica. Mesoporous silica has tailored structure and porosity. The novel acid catalysts based on mesoporous silica were expected to provide superior catalytic activities, improved thermal stabilities, and added product shape selectivity.

Technical Accomplishments

Impregnation was the main method pursued in the early stage of this project since it is well understood and convenient. In order to better retain heteropoly acids within the pores of supports, two more synthetic routes were also explored, namely, in situ synthesis of heteropoly acid materials within the pores of mesoporous silica, and one-step synthesis of mesoporous silica-supported heteropoly acid catalysts. Various mesoporous silica with a pore size range from 30 Å to 100 Å were studied. Solid state ^{31}P nuclear magnetic resonance was used as a major tool to ensure the desired Keggin structure of heteropoly acid is retained in the synthesized catalytic materials.

With the impregnation method, several interesting features were found. First, pore size is important for the efficient dispersion of heteropoly acid anions. Since the size of heteropoly acid is quite large (typically about 12 Å), it is almost impossible to disperse heteropoly acid anions on mesoporous silica with a pore size distribution $\leq$ 30 Å. Dispersion of heteropoly acid anions on supports was successfully achieved when using silica with pore size distributions of 65 Å or 100 Å as supports. Second, special care has to be taken in the preparation of heteropoly acids solution. Otherwise, unsuccessful impregnation of Keggin type heteropoly acids can result. In addition, acidity of catalysts was severely lost due to decomposition of Keggin structure by surface basic species whenever supporting materials were not chemically treated prior to impregnation. A series of leaching tests indicate that heteropoly acid anions were better retained ($\geq$ 90 wt %) when supports with smaller pores like 30 Å mesoporous silica were used and less than 10 wt% heteropoly acid was impregnated. Mesoporous supported heteropoly acids show improved thermal stability as evidenced by their decomposition temperature of 570°C for 30 Å mesoporous silica supported $H_3PW_{12}O_{40}$ as opposed to 500°C of pure $H_3PW_{12}O_{40}$. Since mesoporous silica has large surface area (about 1000 m^2/g) compared with that of heteropoly acids (about 5 m^2/g), heteropoly acids are still highly dispersed on mesoporous silica even at a 70 wt% loading. Therefore, it is not surprising to see significantly improved catalytic activities of mesoporous silica supported heteropoly acid in the tested alkylation of *tert-butyl* phenol by styrene. For the comparison purpose, the activities of amorphous silica and carbon-supported heteropoly acids, as well as sulfuric acid were also tested with the same model reaction. Experiments show superior activity of mesoporous silica-supported heteropoly acids as well as added shape selectivity to mono-alkylated product as opposed to multi-alkylated products.

In situ synthesis of heteropoly acids within the mesopores of silica does not succeed. The major obstacle is the acidifying intermediates of heteropoly acids have much larger size than that of mesopores.

One-step synthesis of mesoporous silica-supported heteropoly acids showed partial success.

Publication and Presentation

A.Y. Kim, Y. Wang, L.Q. Wang, and B. C. Bunker. "Mesoporous silica supported heteropolyacid catalysts." (to be submitted).

Y. Wang, A. Y. Kim, S. Li, J. Liu, and B. C. Bunker. 1996. "Solid heteropolyacid catalysts based on mesoporous silica." MRS Spring Meeting, San Francisco. April 8-12.

Solution Chemistry

Gordon L. Graff, Bruce C. Bunker, Suresh Baskaran, Lin Song (Materials Sciences)

Project Description

New coating materials and techniques are important to industry not only to extend the useful life of components but also to allow the substitution of lighter-weight materials. Research efforts are focused on the development of corrosion resistant, chemically resistant, catalytic, and/or ultraviolet-blocking coatings that can be deposited from inexpensive, aqueous salt solutions.

Technical Accomplishments

TiO_2

Methods were developed in FY 1996 to uniformly coat 4 x 6 inch (and larger) polycarbonate substrates. Both smooth and complex shaped substrates were coated and tested in accelerated ultraviolet aging test. Preliminary results show usable lifetime extensions of three to four times for our biomimetic coatings when compared to the best commercial ultraviolet blockers currently available for polycarbonate. Thorough experimentation was completed to define the useful deposition regime (pH, concentration, temperature) for successful TiO_2 thin film deposition. In an effort to further enhance the ultraviolet absorbing characteristics of our coatings, organic blockers are being incorporated into the thin film during solution deposition. Spin coating and dip coating methods have also been investigated in an attempt to produce thicker films for improved ultraviolet attenuation.

ZnO

Solubility diagrams for aqueous Zn solutions show an increased tendency for oligomeric speciation in basic over-acidic solution conditions. In FY 1996, extensive experimentation was conducted on Zn solutions between pH 7 and pH 12. Film growth was demonstrated, but film quality was still not good. Film thicknesses of approximately 1 micron were possible, but the films were porous and opaque. Though the possible attenuation of ultraviolet radiation using ZnO may be superior to TiO_2, the deposition of optical quality films using this method does not seem possible.

Membrane Development

Our TiO_2 deposition process was used to coat the surface and internal pore structure of an asymmetric polysulfone membrane used in gas separation. Measurements conducted at an outside laboratory showed a fourfold improvement in the O_2/H_2O selectivity of the membrane. The mechanism for this difference is thought to be the modification of the pore distribution after film deposition. Figure 1 shows the normalized pore volume versus pore size for the native and TiO_2-coated membrane.

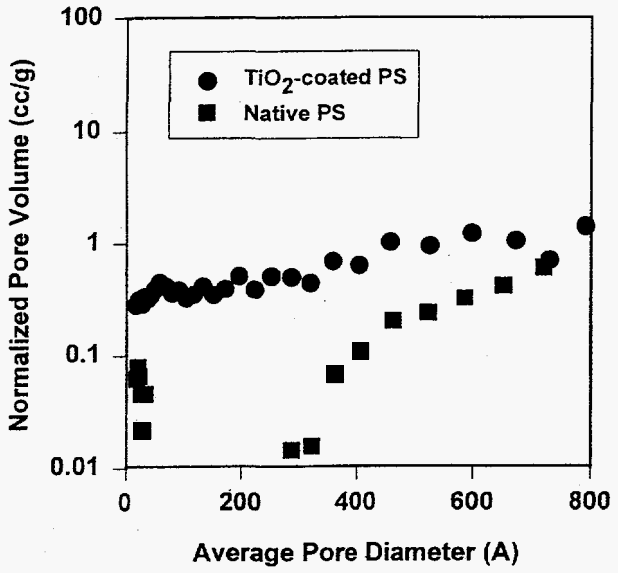

Figure 1. Normalized pore volume versus pore size for native and TiO_2-coated membrane.

Based on these findings, a membrane permeation apparatus for measuring O_2/N_2 selectivity was designed and assembled (Figure 2). After calibration, the system was used to measure gas permeability and selectivity on biomimetic-coated membranes. Commercial polysulfone membranes with molecular weight cutoffs of 100,000 and 10,000 were coated with varying thicknesses of FeOOH, SnO_2, TiO_2, and octacalcium phosphate. Permeabilities measured on the SnO_2 and TiO_2 coated substrates showed a two- to threefold reduction over the native 10,000 MW membranes, indicative of pore size reduction. Unfortunately, none of the samples tested showed improved selectivity for oxygen over nitrogen. Several possible explanations exist for this. First, the inorganic coating may have no effect on gas permeability. Second, the presence of small defects (cracks, pinholes) in the membrane can completely falsify permeation tests. This is typically overcome by deposition of a polymeric "gutter layer"

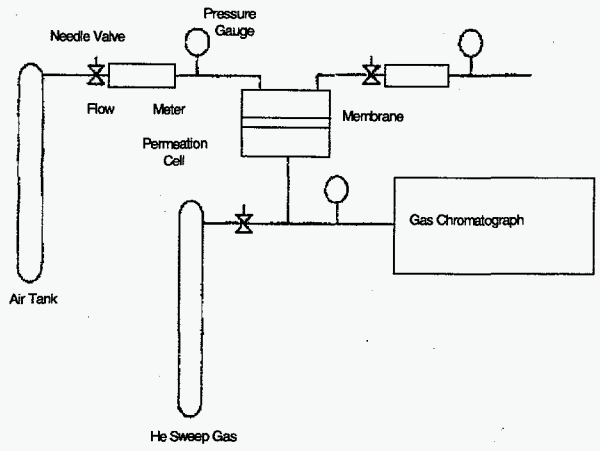

Figure 2. Membrane permeation apparatus.

that seals the large defects. Testing of the "coated" membranes complete with sealing layer should be conducted before final conclusions can be reached.

Publications

G.E. Fryxell et al. 1996. "Nucleophillic displacements in mixed self-assembled monolayers." *Langmuir*, 12, pp. 5064.

P.C. Rieke et al. 1995. "Biomimetic thin film deposition." Proceedings of the 4th Japan International SAMPE Symposium, pp. 565.

M. Agarwal et al. "Low temperature chemical synthesis of zirconia films" *J. Am. Ceram. Soc.* (submitted).

S. Baskaran et. al. "TiO_2 thin films on organic interfaces through biomimetic processing." *J. Am. Ceram. Soc.* (submitted).

Surface Modification

Suresh Baskaran, Gordon L. Graff (Materials and Chemical Sciences)

Project Description

Previous research at PNNL has demonstrated that carefully tailored organic interfaces will catalyze the nucleation and growth of ceramic thin films from aqueous solutions. Thus, if the surfaces of target substrate materials can be correctly modified, low temperature and ambient pressure deposition of ceramic coatings can be directly achieved on complex shaped and/or temperature sensitive substrates. Unfortunately, a limited number of useful surface modification schemes (particularly for plastics) have been developed. This research effort is dedicated to the rapid development of industrially useful surface modification schemes for consumer plastics (polycarbonate, polyvinyl chloride, nylon, acetal, polyethylene, acrylic, polystyrene).

Technical Accomplishments

To date, the most common surface modification technique used in biomimetic mineralization has been the self-assembled monolayer—a short alkyl silane coupling agent which can be covalently attached to the surfaces of metal oxides. This technique is not industrially acceptable since it requires multiple synthesis steps in high purity organic solvents and the self-assembled monolayer is mechanically fragile (readily scratches off). Further, self-assembled monolayer techniques are not readily applicable to polymeric substrates. Currently, only one surface modification technique (sulfonation of polystyrene) has been developed for plastics that successfully induces ceramic film formation. Similar surface modification schemes must be devised for other industrially useful polymers such as polycarbonate, acrylic, acetal, polyvinyl chloride, nylon, polyethylene, and polypropylene. The modification schemes must also be kept simple, inexpensive, and environmentally benign.

Emphasis during FY 1996 was placed on functionalization of polycarbonate and polypropylene surfaces. Initially, simple gas phase sulfonation reactions were attempted on both polymers. Contact wetting angles (water) for polycarbonate dropped from 75° to 85° to less than 10° for the sulfonated surface. Since polycarbonate contains two aromatic rings per monomer unit, these results were consistent with previous findings on polystyrene surfaces. These surfaces effectively stimulated mineral deposition. Direct sulfonation had little or no effect on native polypropylene surfaces, with only slight changes in wetting angle after surface treatment. In addition, the reacted polypropylene surfaces were ineffective in stimulating film deposition.

Surface plasma treatments were previously attempted on polycarbonate and polypropylene with limited success. In FY 1996, a new process was developed involving low energy corona treatments followed by gas phase sulfonation. This surface modification scheme resulted in superior crystal nucleation surfaces on polypropylene, but had only marginal improvement on the film growth properties of polycarbonate.

An extensive study was also conducted to directly attach functional sites through chemical tethers to the aromatic groups of polycarbonate. Solvent selection presented a particular challenge on the reactive polycarbonate surface. Nearly all of the solvents that could be used for Freidel-Crafts reactions (chloromethylation, bromomethylation, carboxlyation) were not available for us since they cause polymer damage. Only petroleum ether (hexanes) showed no visible damage on polycarbonate after 24 hours of exposure, so mixed solvent systems were utilized. Chloromethylation reactions in hexanes, acetonitrile, and hexane/$MeCl_2$ gave slight decreases in contact wetting angles (from 80° to 60°) but the surface damage was excessive for optical applications. Similar results were obtained for the bromomethylation reactions. The best results were obtained by acylation of polycarbonate with cyclic anhydrides. Contact angles for maleic acid surfaces were 30°, and polymer surface damage was minimal. Deposition of titanium oxide films was also demonstrated on the acylated polycarbonate substrates.

Synthesis of Model Inorganic Ion Exchange Materials

James E. Amonette (Environmental Dynamics and Simulation)

Project Description

The long-term objective of this project is to develop and demonstrate the capability to synthesize environmentally relevant phase-pure minerals and related inorganic compounds. Our focus in FY 1996 has been on layered-hydroxide compounds consisting of octahedrally coordinated sheets of Al, Mg, and/or Fe(II) cations. The interest in these compounds stems from 1) their similarity to the octahedral sheets in the clay minerals that dominate the cationic chemistry of soils and sediments and their potential ability to serve as templates for the controlled synthesis of these minerals, 2) their potential use as high-charge inorganic anion-exchange materials in neutral and alkaline systems, and 3) their potential ability to provide a variety of octahedral environments for Fe(II) in a form that is readily analyzed by advanced surface-science techniques, thus allowing progress to be made in understanding the molecular-scale structural factors that control solid-phase Fe redox potentials. Most of our effort in FY 1996 involved refinement of a novel synthesis technique for high-charge hydrotalcite-like compounds (HTLCs) that essentially eliminates inorganic carbon from the interlayer regions and, thus, allows much greater freedom in their subsequent use, whether as anion exchangers, templates for clay-mineral synthesis, or specimens for surface studies of Fe redox chemistry. Smaller-scale efforts were devoted to formation of the layered Fe(II) compounds and to a review of smectite synthesis methods.

Technical Accomplishments

Novel Synthesis Approach

Hydrotalcite-like compounds consist of brucite-like, $[Mg(OH)_2]$ layers where partial substitution of smaller M(III) cations for M(II) has occurred yielding positive charge. This layer charge is compensated by anions, e.g., CO_3^{2-}, located in the interlayer region (along with adsorbed water). For applications involving ion exchange, CO_3-free high-layer-charge HTLCs are desirable. The CO_3^{2-} anion, due to its high charge density, is retained strongly in the interlayers—resulting in a low or nonexistent anion-exchange capacity under ambient conditions. High layer charge, i.e., $x > 0.33$, where x is the M(III)/[M(III) + M(II)] ratio, has been difficult to achieve in CO_3^{2-} systems, and prior to our work, no CO_3-free, high-charge HTLCs were reported.

Typically, Mg/Al HTLCs are synthesized at pH 10 where the solubilities of the end member Mg and Al phases are similar. At pH below 10, the solubility of the Al phase decreases and that of Mg increases. We hypothesized, therefore, that by decreasing the pH during the crystal-growth stage of synthesis, we could increase the degree of Al substitution in the HTLC, while at the same time decreasing the potential for CO_3^{2-} ions to be incorporated into the structure. To further minimize the incorporation of CO_3^{2-}, we modified an earlier published method in which terephthalate [TA, p-$C_6H_4(COO)_2^{2-}$] is used as the interlayer anion instead of CO_3^{2-}.

The results of bulk chemical analysis for a typical series of samples (x of starting solution = 0.33) show the x values of the products obtained at pH 10, 8.5, and 7.5 (Samples A, B, and C, respectively) were essentially the same as the starting solution, indicating coprecipitation (Table 1). The sample obtained at pH 6.5 (D), on the other hand, had the highest x (0.45) yet reported for low-CO_3^{2-} HTLCs. Separate analyses of the samples on a 5-nm scale by scanning electron microscopy/energy-dispersive x-ray spectrometry confirmed these results.

Table 1. Characteristics of HTLCs

	Sample			Anion suite[c]	
pH	c_o[a]	a_o	x[b]	TA	C_{inorg}
	---Å---			---mol%---	
A(10)	14.2	3.036	0.34	69	31
B(8.5)	14.2	3.038	0.34	76	24
C(7.5)	14.1	3.024	0.37	95	5
D(6.5)	13.9	3.002	0.45	98	2

(a) c_o is the d_{001} for the TA peak
(b) x of starting solution was 0.33
(c) Based on total-C and inorganic-C data

To gain a better understanding of changes in the structures of these compounds during the titration, considerable effort was spent characterizing the products. Elemental analysis of the products and the washing solutions (data not shown) suggested that the mechanism for formation of the high-layer-charge HTLCs involves the active removal of Mg^{2+} from, and simultaneous incorporation of solution-phase Al^{3+} into, the octahedral sheet. These results are consonant with the divergence in the solubilities of $Mg(OH)_2$ and $Al(OH)_3$ as pH decreases from 10 to 6.5. Powder x-ray diffraction analysis showed a steady decrease in the a_o ($2d_{110}$) and c_o (d_{001}, interlayer spacings for TA) lattice parameters as layer

charge (i.e., x) increased (Table 1). The relationships between x and the lattice spacings were linear ($r^2 > 0.99$) and consistent with formation of a solid-solution series for structural ions of different radius and charge. Taken together, these structural and chemical data suggest that the formation of high-layer-charge HTLCs is likely due to homogeneous structural changes rather than to simple dissolution and precipitation of separate phases. This is further evident from the formation of an HTLC with $x \approx 0.42$ when Sample A was titrated to pH 6.5 with 2% HNO_3 instead of the Mg/Al nitrate solution. In addition to x-ray diffraction and bulk data, analysis of the washings from this sample confirmed the loss of Mg and the rearrangement of Al in the structure. Similar treatment of a CO_3-HTLC (i.e., no TA present) failed to produce a high-layer-charge compound suggesting that the nature of the interlayer anion plays a significant role in the process. Evidently, TA anions stabilize the structure so that it can accommodate higher degrees of substitution.

Given the importance of the interlayer anions, we further characterized the composition of the interlayer anion suite. Samples obtained at pH 10 and 8.5 contain TA, CO_3^{2-}, and HCO_3^- (Table 1). Carbonate species were present in these products even though none were added to the system intentionally and excess TA was present throughout the precipitation process. These species are likely atmospherically derived. On the other hand, samples C and D contain very little CO_3^{2-} or HCO_3^-. The x-ray diffraction data also show the removal of CO_3^{2-}/HCO_3^- by changes in the relative intensities of the 0.73-nm and 1.4-nm peaks (data not shown). These two peaks correspond, respectively, to CO_3^{2-}/HCO_3^- and TA (long axis perpendicular to the hydroxide sheet) in the interlayer. Analyses by ^{13}C cross-polarized, magic-angle-spinning nuclear-magnetic-resonance (CPMAS-NMR) spectroscopy (Figure 1) and Fourier-transform infrared spectroscopy (data not shown) confirmed these changes in the amounts of TA and carbonate species. In particular, it is evident that essentially no inorganic C is present in the high-layer-charge sample formed at pH 6.5 and that the environment of the TA anion is changing as the pH decreases (Figure 1).

In summary, our work with HTLCs suggests that the cations in the hydroxide sheet are surprisingly labile when TA is the interlayer anion. Manipulation of this characteristic opens new possibilities for the synthesis of materials with layered hydroxide structures.

Epitaxial Precipitation of $(Mg,Fe^{2+})(OH)_2$

From aqueous solution we precipitated several brucite and Fe(II)-bearing brucite phases on sheets of muscovite

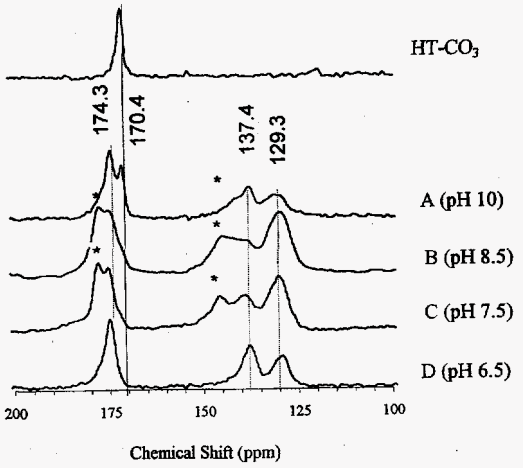

Figure 1. ^{13}C CPMAS-NMR spectra of pure-CO_3^{2-} HTLC (top) and four HTLCs synthesized using the TA method.

in an attempt to produce single-layer atomically flat specimens suitable for analysis by advanced surface-science techniques. Exposure of the Fe(II)-bearing specimens to oxygen resulted in a rapid change in color, indicating that we were successful in maintaining Fe(II) during the synthesis. Further characterization of these specimens by tapping-mode atomic-force microscopy showed the presence of small (10- to 40-nm diameter) platelets on the surface having a typical thickness of about 5 nm. These results were encouraging, but further refinement is needed.

Review of Smectite Synthesis Methods

We continued work on an extensive critical review of the different approaches used to synthesize smectite clay minerals. The review will be submitted for publication in June 1997.

Publication and Presentation

R.K. Kukkadapu, M.S. Witkowski, and J.E. Amonette. 1997. "Synthesis of a low-carbonate high-charge hydrotalcite-like compound at ambient pressure and atmosphere." *Chemistry of Materials* 9:417-419.

R.K. Kukkadapu, M.S. Witkowski, and J.E. Amonette. 1996. "High-charge hydrotalcite-like compounds in the Mg^{2+}-Al^{3+}-terephthalate system." In Program and Abstracts, p. 102. The Clay Minerals Society, 33rd Annual Meeting, Gatlinburg, Tennessee, June 15-20.

Molecular Science

Bonding and Structure of Organic Ligands at Oxide/Water Interfaces

Calvin C. Ainsworth (Earth Systems)
Donald M. Friedrich (Chemical Structure and Dynamics)

Project Description

The objective of this research is to examine the sorption chemistry of organic ligands at the solid-water interface by application of state-of-the-art optical spectroscopic methods. In support of this objective, research was performed 1) to develop sensitive spectroscopic methods using steady-state and time-resolved laser induced fluorescence in novel ways that allow spectroscopic interrogation of organic ligands at the solid-water interface at low, environmentally relevant sorbate surface coverage ($\leq$ 1%); and 2) to identify and characterize the nature (bonding, structure, and dynamics) of interfacial organic species. The objective was accomplished.

Technical Accomplishments

Interactions between organic ligands and minerals at the solid-water interface are integral to many processes occurring in soils and subsurface materials. These processes include contaminant transport, soil formation, and diagenesis. Often, these interactions are characterized as surface complexation reactions and are assigned a structure based on inadequate data. Under these conditions, modeling efforts are little more than exercises in curve fitting. In order to better understand and simulate important aqueous-mineral interfacial phenomena, it is crucial to obtain spectroscopic data concerning speciation, structures, and dynamics of organic ligands at the aqueous-mineral interface under controlled conditions that are still relevant to the natural environment.

The current investigations are performed using salicylate anion (o-hydroxybenzoate) as probe and colloidal Al_2O_3 as the mineral interface. The salicylate was chosen because it is a fluorophore reported in the literature as a model compound for the study of organic ligand-surface speciation (bonding, structure) as a function of important geochemical variables (pH, ionic strength, surface loading). Al_2O_3 was chosen because of its spectroscopically benign nature (infrared and ultraviolet transmittance, weak Raman interference). Most experiments are performed in constant temperature, dilute suspensions (1 g/L) of colloidal Al_2O_3 (mean particle size 70 nm) with geochemically relevant low concentrations of organic ligand (10^{-6} to 10^{-7} M).

Speciation of salicylate adsorbed on aqueous colloidal alumina (δ-Al_2O_3) was determined by polarized fluorescence excitation spectroscopy at low surface coverage (2% to <10%). Adsorption isotherms and pH and ionic strength edges suggest the existence of both inner-sphere and outer-sphere salicylate surface complexes. Spectroscopic characteristics of inner-sphere surface-salicylate complexes (one bidentate and two monodentate) were identified through comparison of suspension spectra with remarkably similar fluorescence and excitation spectra of solution phase Al(III)-salicylate complexes. The large fluorescence Stokes shift of the aqueous salicylate anion is highly sensitive to complexation structure, resulting in spectral shifts characteristic of the aluminum binding in the three inner-sphere salicylate complexes. These species appear to be present even at extremely low surface coverage, and the relative distributions are dependent on pH, ionic strength, and the relative concentrations of alumina and salicylate. Fluorescence polarization anisotropy measurements, both steady-state and time-resolved, demonstrate that the bidentate and monodentate surface complexes do not undergo rotational reorientation on the time scale of the fluorescence (t_f = 4.5 ns), consistent with inner-sphere, polar covalent binding of these salicylate complexes to alumina surface sites. At high surface coverage, time-resolved anisotropy measurements suggest the existence of a surface salicylate species that is rotationally hindered (τ_{rot} = 30 ps) relative to free solution phase salicylate ions (τ_{rot} = 20 ps). This behavior is consistent with an electrostatically bound outer-sphere complex suggested earlier by the pH and ionic-strength sorption edges.

The kinetics of surface complexation were studied using a combination of the high power laser excitation, stopped-flow apparatus, and sensitive intensified diode array detection system to study the reaction of salicylate with surface alumina sites. The formation of Al(III)-salicylate complexes both on colloidal alumina in aqueous suspension and in homogeneous aqueous Al(III) solutions as a function of time were monitored via the change of the fluorescence emission spectra after fast mixing of the solutions using the stopped-flow technique. Two argon laser excitation wavelengths were used, 300 nm (near the absorption maximum) and 334 nm (on long wavelength absorption edge of the bidentate complex). The emission

spectra of salicylate in alumina suspension within the first 3 minutes after solution mixing are shown in Figure 1 (A,B). The free salicylate, bidentate complex, and monodentate complex binding through the carboxylate group all strongly absorb light at 300 nm. As seen from Figure 1A, the emission maximum shifts from 415 nm (corresponding emission of free salicylate and the monodentate complexes) toward 382 nm (corresponding to the more stable bidentate complex) within minutes. At 334 nm, only the bidentate complex and the monodentate complex binding through the phenoxide group absorb. The emission spectra excited at 334 nm show maxima around 382 nm even at the beginning of the reaction and the emission intensity increases as the reaction time increases. Experiments conducted within 12 hours indicated that for the complexation in alumina suspension the reaction slows down significantly after a few minutes and completion of the reaction takes more than 12 hours. For complexation in homogeneous phase at pH 3.3, the reaction completes within 10 minutes.

The intensity change at various combinations of excitation and emission wavelengths were recorded on the Spex fluorimeter. Typical plots of the logarithm of the difference of the emission intensities at infinite reaction time (fit from the actual data) and at different reaction times are shown in Figure 2 together with their linear least-square fits. Under the solution conditions of this work, the metal ions (in aqueous Al(III) solutions) or the metal ion sites (in alumina suspensions) are in much excess. As expected, the reaction is pseudo-first-order. The pseudo-first-order rate constants, k, obtained from slopes of plots are independent of the initial concentration of salicylate. As shown in Figure 2, in homogeneous phase the reaction follows a single first-order kinetics. However, multiple first-order paths coexist in the reaction with alumina suspension, implying the complexity of the heterogeneous reactions. Such multiple reaction paths are presumably indications of the formation of multiple species at the same time as well as conversion between species. The concentration of salicylate in suspension was kept well below the site density determined from macroscopic sorption measurements (approximately 1 per nm^2). Because the bidentate complex is the majority species and forms rapidly even in suspension, the slower components may represent bidentate binding to minority sites or sites that reformed to bidentate complexation after initial (possibly monodentate) binding of the salicylate.

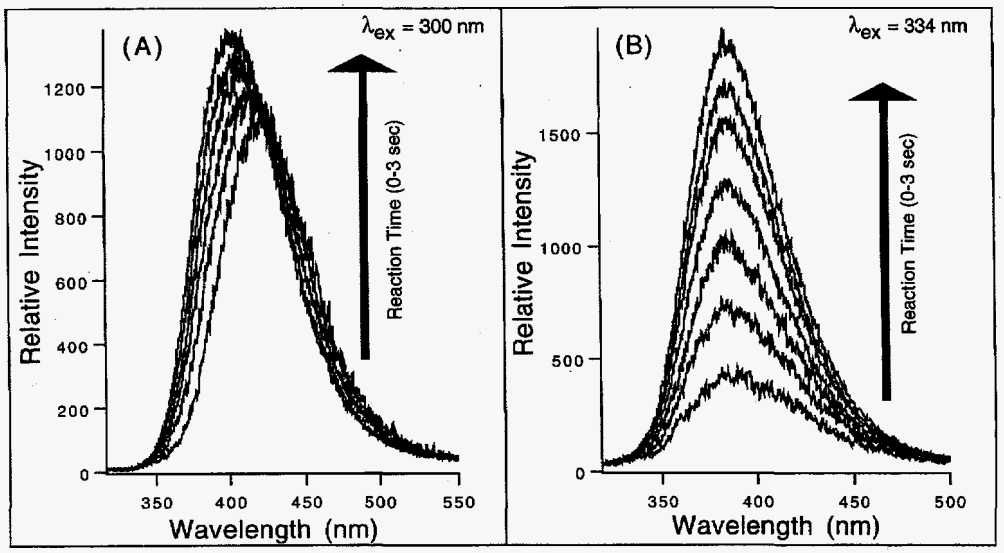

Figure 1. Fluorescence emission spectra of salicylate in aqueous alumina suspension at pH 6.1 and ionic strength of 0.01 M as a function of time within the first 3 seconds. Reaction Time (0-3 sec). (Al_2O_3) = 1 g/L. (salicylate) = 2 x 10^{-6} M.

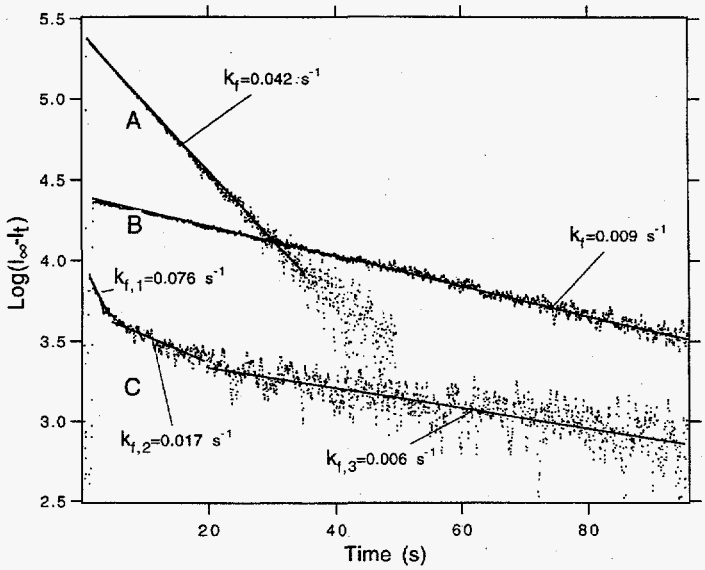

Figure 2. Plots of log (I_∞-I_t) as a function of time and their linear least-square fittings. The solution/ suspension conditions are: A: Homogeneous aqueous solution, (Al[III]) = 0.002 M, (salicylate) = 2 x 10^{-5} M, pH 3.3, Ionic strength = 0.01 M. B: Homogeneous aqueous solution, (Al[III]) = 0.002 M, (salicylate) =2 x 10^{-5} M, pH 2.0, Ionic strength = 0.01 M. C: Heterogeneous aqueous suspension, (Al_2O_3) = 1 g/L, [salicylate] =2 x 10^{-6} M, pH 6.1, Ionic strength= 0.01 M.

Publications and Presentations

Z. Wang, C.C. Ainsworth, D.M. Friedrich, P.L. Gassman, and A.G. Joly. "Characterization of salicylate-aluminum oxide surface complexes by polarized fluorescence spectroscopy." *Geochimica Cosmochimica Acta* (submitted).

Z. Wang, D.M. Friedrich, C.C. Ainsworth, and P.L. Gassman. "Effect of multiple light scattering on emission anisotropy from turbid suspensions." (in preparation).

Z. Wang, D.M. Friedrich, C.C. Ainsworth, and P.L. Gassman. "Excited state proton transfer and conformational relaxation of salicylate anion and its aluminum complexes in aqueous and alcoholic solutions." (in preparation).

Z. Wang, C.C. Ainsworth, D.M. Friedrich, and P.L. Gassman. "Mechanism of salicylate formation of salicylate-Al_2O_3 surface complexes. Stop-flow kinetics study." (in preparation).

D.M. Friedrich, Z. Wang, C.C. Ainsworth, and P.L. Gassman. 1996. "Speciation of salicylate surface complexes in aqueous alumina suspensions by polarized fluorescence excitation spectroscopy." American Chemical Society: Spring Meeting, Symposium on Environmental Heterogeneous Processes, New Orleans, March 24-28.

Z. Wang, D.M. Friedrich, C.C. Ainsworth, and P.L. Gassman. 1996. "Probing metal ion complexation with salicylic acid and its derivatives with excited state proton transfer and luminescence anisotropy." American Chemical Society: Spring Meeting, Symposium on Environmental Heterogeneous Processes, New Orleans, March 24-28.

High Resolution and Solid State NMR Studies of Proteins and DNA-Adducts

Gary P. Drobny (University of Washington)

Project Description

In collaboration with Professor Paul Hopkins (Chemistry, University of Washington), quantities of DNA with cross-linking lesions were synthesized and studied by high resolution nuclear magnetic resonance. The effects that these lesions have on sequence specific interactions between Cro repressor and the OR3 operator sequence were studied.

In collaboration with Professor Pat Stayton (Bioengineering, University of Washington), charge mutants of Protein G were synthesized and labeled with 13C and 15N. The solution structure of these mutants were studied using nuclear magnetic resonance spectroscopy.

Also, Streptavidin, a 13 kDa protein was prepared and labeled with 13C and 15N. We used the 750 MHz nuclear magnetic resonance spectrometer at PNNL to investigate the feasibility of studying the structure of this protein in its free and biotinylated form.

Technical Accomplishments

The remarkable hierarchical structure of hard tissues such as bone and teeth is generated through the interrelated regulation of compartment solution chemistry, the molecular/cellular receptor biology that governs cell responses to mineral phases, and the crystal engineering capabilities of biomolecules such as proteins. A number of biological proteins have been isolated that interact with and control the growth of calcium-containing crystalline phases such as hydroxyapatite and calcium oxalate (the principal mineral phase of kidney stones). An important class of these proteins are the non-collagenous acidic proteins found in bone tissue, in salivary fluids, and in urinary compartments. These proteins can function as promoters of crystal nucleation when immobilized in the extracellular matrix where they are involved in controlling crystallite orientation and morphology, and can also function as inhibitors of biomineralization through the recognition of growing crystal faces in supersaturated environments such as the mouth, kidney, bladder, and in bone.

While a great deal of information has been accumulated on the molecular biology of biomineralization and many proteins involved in biomineralization have been identified, there is little known of the detailed structure-function relationships used by proteins to directly control crystallization processes. In particular, the absence of structural information within this important class of proteins has made it difficult to elucidate the molecular recognition mechanisms used in crystal engineering.

Several of the acidic proteins have been purified and their ability to control in vitro mineralization processes is well documented. Important examples are osteocalcin, osteonectin, bone sialoprotein and osteopontin from bone tissues, and the proline-rich acidic proteins such as statherin found in salivary fluids. Statherin is isolated from salivary compartments and functions as an effective inhibitor of hydroxyapatite secondary nucleation and can also serve as a nucleation promoter when immobilized to solid surfaces. The human gene for statherin has been cloned and its primary sequence is characterized by a negatively charged N-terminus consisting of an Asp-Ser-Ser-Glu-Glu-Lys sequence, and the serines are post-translationally phosphorylated to add to the anionic character. There is no direct three-dimensional structure information available for statherin, but molecular modeling and secondary structure predictions suggest that the N-terminus has a predilection for a-helix formation. The presence of secondary structure in other acidic proteins has also been predicted and hypothesized to play a role in crystal recognition through lattice-matching mechanisms. Peptides from this N-terminus of statherin have been shown to bind effectively to hydroxyapatite seed crystals and to inhibit their further growth in metastable supersaturated solutions.

We report here a preliminary solid-state nuclear magnetic resonance determination of the conformation of one such N-terminal statherin peptide on a hydroxyapatite crystal surface. The peptide is derived from the first six amino acids of statherin (N6), with the sequence D-pS-pS-E-E-K (where pS denotes phosphorylated serine). Secondary structure of the N6 peptide on a hydroxyapatite crystal surface was elucidated by measuring the distance between C1 carbonyls on adjacent, 13C-labeled amino acids. Distances between nuclear magnetic resonance-active nuclei in the solid state can be determined to high

accuracy using magic angle sample spinning (MASS) and windowless dipolar recouplings (DRAWS) pulse techniques. For example, distances of up to 5.5+ between 13C spins and 10+ between 19F spins can be determined using DRAWS.

Figure 1 shows the amplitude of transverse 13C magnetization as a function of the duration of dipolar recoupling irradiation obtained from an N6 peptide labeled with L-serine-1-13C at pS2 and pS3. Juxtaposed with the experimental data are simulated "dipolar dephasing curves" for a range of secondary structures, characterized by the Ramachandran angle f. The data fall closest to simulations that are characteristic of an alpha helical secondary structure.

These preliminary results show that solid-state nuclear magnetic resonance techniques like DRAWS can be used to determine the secondary structure of biopolymers adsorbed onto high surface area crystals. The sensitivity of the DRAWS experiment is high (figure inset A is the MAS spectrum of pure N6, inset B is N6 adsorbed onto hydroxyapatite) and we believe that the structure of peptides with molecular weights of up to 10 to 20 kDa may ultimately be determined by these techniques.

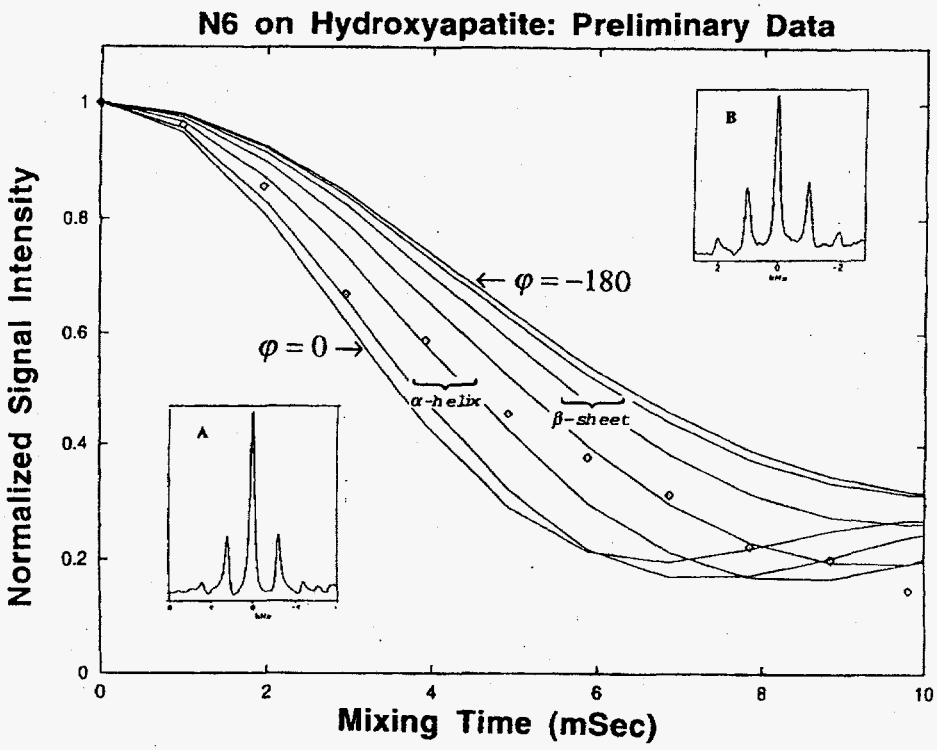

Figure 1. N6 on hydroxyapatite, A) CPMAS spectrum of bulb N6, doubly labeled; B) CPMAS spectrum of N6 adsorbed onto hydroxyapatite.

Identification and Structural Determination of Paramagnetic Species Using Pulsed EPR

Michael K. Bowman (Macromolecular Structure and Dynamics)

Project Description

This project seeks to develop and demonstrate magnetic resonance techniques for the characterization of reactive species on the surface of potential catalysts and of free radical species in solids. The focus is on high resolution pulsed electron paramagnetic resonance (EPR) techniques that will be capable of resolving complex spectra from overlapped species.

The key intermediates in many chemical reactions, especially those catalyzed by enzymes or oxide surfaces are free radicals. The identification and characterization of these free radicals is a key step in understanding the mechanism and mode of action. Magnetic resonance, particularly electron paramagnetic resonance, is an excellent spectroscopic method for the study of these free radical intermediates because it is uniquely selective for and sensitive to free radicals.

Technical Accomplishments

We have continued the study of Lewis acid sites on the surface of γ-alumina. These are the catalytic sites of many industrially important catalysts and can, in fact, destroy chlorinated hydrocarbons. However, there appear to be a number of different Lewis acid sites on alumina surfaces. Some are quite reactive and are responsible for the complete destruction of molecules and the formation of coke on the surface of the catalysts which limits the operating lifetime of the catalyst. Consequently, catalysts are often modified to remove the most reactive sites and leave behind sites with reduced activity but better selectivity. Two such surface modifications use boric or phosphoric acid to treat the surface.

We introduced a diamagnetic molecule onto the activated, surface-modified catalyst. Those molecules that reach a catalytically active site react to form a free radical bound to that site. Thus, we selectively introduced our probe free radicals into those Lewis acid sites which retained catalytic activity. The electron paramagnetic resonance spectra show three different types of bound species interacting strongly with aluminum on the surface and another radical species without significant interactions. Phosphoric-acid-modified surfaces show all three bound species, but in different proportions depending on the extent of surface treatment. On the other hand, the boric-acid-modified catalysts show only one bound species. It appears that surface modification controls activity and selectivity of the alumina catalysts by changes in the relative amounts but not the kinds of active Lewis acid sites.

A second related question concerns how these radical species were formed. Are the radicals the result of oxidation or reduction of the quinone and Lewis acid site? To help resolve this, we have modified pulsed electron paramagnetic resonance techniques, such as ENDOR, TRIPLE, and HYSCORE, specifically for these mixtures of overlapping species.

The pulsed ENDOR and TRIPLE spectra, Figure 1, allow us to unravel the overlapping spectra and obtain the hyperfine couplings of proton and aluminum nuclei for each of the species. In the case of the radical with no significant hyperfine interaction with aluminum nuclei at the surface, we find large proton hyperfine couplings that agree well with quantum mechanical calculations of those couplings for the anthraquinone radical cation, but not for the radical anion.

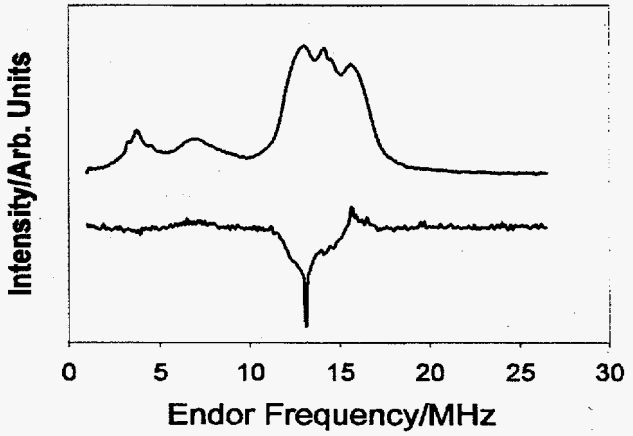

Figure 1. Pulsed EPR spectra of radicals produced from anthraquinon on the surface of activated γ-alumina. A) The pulsed ENDOR spectrum arises from all four types of species on the surface and shows peaks from proton and aluminum nuclei. B) The pulsed TRIPLE spectrum is selective for only one of these species and shows which peaks belong to the other species.

These results indicate that we might be able to determine the catalytic properties of the different types of Lewis acid sites by quantitative correlations between the catalytic properties and the species measured by electron paramagnetic resonance. Thus, if we could obtain structural and chemical information from electron paramagnetic resonance experiments concerning the Lewis acid sites we observe, we could then begin to correlate structure with function for this catalytic system and to provide predictive tools for catalyst design.

The electron paramagnetic resonance spectra show that at least two of the Lewis acid sites at which radicals form are coordinatively unsaturated so that the probe molecule we use, a quinone, forms a tight complex between its oxygen atom and aluminum in the Lewis acid site. We observe strong complexes with substantial spin delocalization onto one aluminum and onto two aluminums. This suggests that one site contains a single coordinatively unsaturated aluminum while the other is missing a bridging oxygen.

Publication and Presentation

R.I. Samoilova, S.A. Dikanov, A.V. Fionov, A.M. Tyryshkin, E.V. Lunina, and M.K. Bowman. "Pulses EPR study of orthophosphoric and boric acid modified γ-alumina." *Journal of Physical Chemistry* (in press).

R.I. Samoilova, S.A. Dikanov, A.V. Fionov, A.M. Tyryshkin, E.V. Lunina, and M.K. Bowman. 1996. "CW and pulsed EPR study of orthophosphoric and boric acid modified γ-alumina." 38th Rocky Mountain Conference, Denver, Colorado, July 21-26.

NMR Studies of Altered DNA-Protein Complexes

Michael A. Kennedy (Macromolecular Structure and Dynamics)

Project Description

During FY 1996, we focused on studies of the human DNA repair protein XPAC. XPAC is thought to be the first protein involved in the recognition of DNA damage. Previous studies on the sequence and cloning of XPAC have reported it to consist of 273 amino acid residues with a corresponding molecular weight of 31 kD. XPAC has also been shown to contain a zinc finger DNA binding domain that falls into a class which has been identified in the chick erythroid transcription factor GATA-1. This class of zinc finger is unique in that only a single copy of the zinc finger is necessary for specific binding to DNA. This binding is accomplished by a core zinc finger which contains an alpha helix that interacts in the major groove of DNA and an "arm" that interacts in the minor groove of DNA. Our goals in studying this protein include using nuclear magnetic resonance spectroscopy to determine the structure of XPAC, complexes of XPAC with damaged DNA, and complexes of fragments of XPAC with damaged DNA.

Technical Accomplishments

Our initial studies focused on determining the structure of a synthetic 40-residue fragment of XPAC (XPAC40) which contains the core of the zinc finger domain. Nuclear magnetic resonance data in Figure 1A shows the fingerprint region of a NOESY spectrum that enables proton assignments for the peptide, in addition to the expected crosspeaks in the "sequential walk" from (n)-αH τo - (n+1)NH. Additionally, crosspeaks are observed that indicate β-sheet structure. Furthermore, a secondary chemical shift analysis indicates the presence of α-helix in the region of the N-terminal region of the peptide. Based on this nuclear magnetic resonance data, a restrained molecular dynamics structure was generated and is shown in Figure 2B. In comparison to the GATA-1 structure (Figure 2A), the two-strand anti-parallel β-sheet at the N-terminal region and the α-helix at the C-terminal region is preserved, however the overall orientation of the individual structural elements are not precisely conserved. This is not surprising considering that the GATA structure was determined as part of a complex with DNA whereas the XPAC fragment was determined in the absence of DNA.

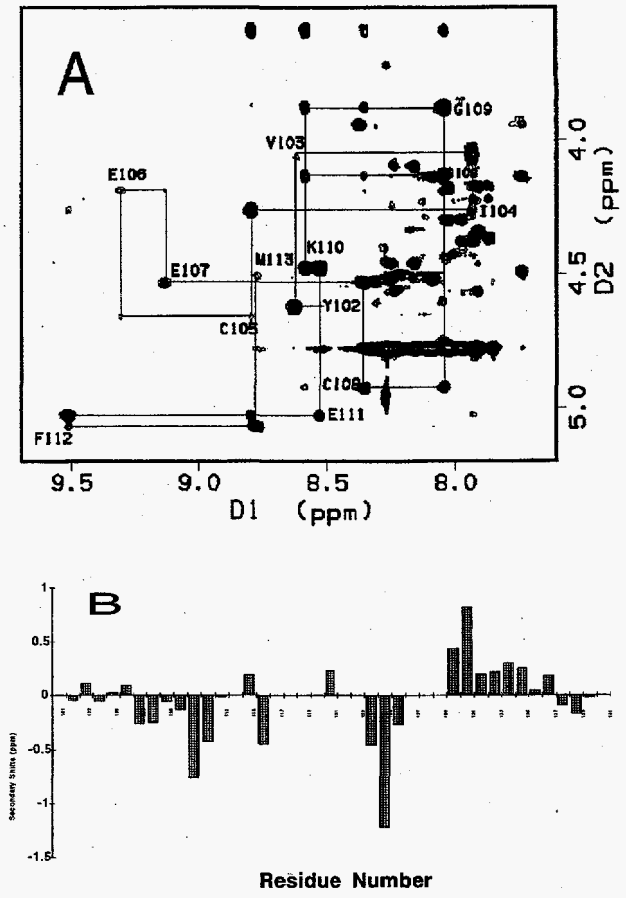

Figure 1. A) 750 MHz NOESY spectrum of XPAC40 at 25°C. The horizontal and vertical lines join crosspeaks between sequential (n)-αH τo - (n+1)NH protons. B) Plot of secondary chemical shifts relative to random coil values.

In pursuit of the structure of the intact XPAC, we prepared a clone of a shortened fragment of the XPAC protein that is missing the first exon and is short of the C-terminal 54 residues. Figure 3 shows preliminary data collected at 750 MHz on this protein. The heteronuclear single quantum coherence {^{15}N-^{1}H} spectrum shows 114 resolved residues out of 161 total residues (7 of which are prolines). This shows that 74% of the expected crosspeaks are resolved. Additional data is currently being collected to enable complete structural determination of this protein.

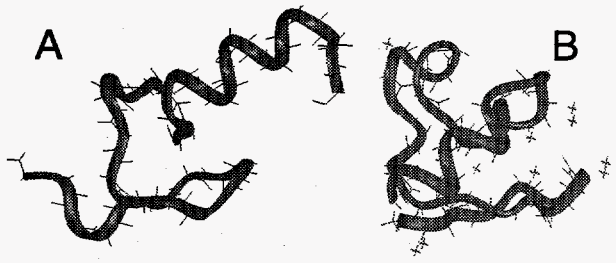

Figure 2. A) Structure of zinc finger DNA binding domain taken from NMR derived structure complexed with its consensus promoter DNA sequence (published by Omichinski et al., of the NIH group), B) Our NMR based restrained molecular dynamics structure of XPAC40.

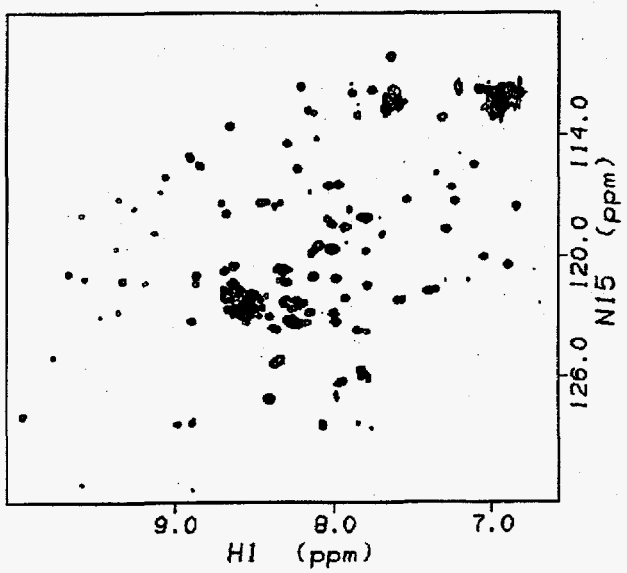

Figure 3. 750 MHz {1-H-15N}-HSQC shown in the amide proton to amide nitrogen region of the spectrum. See text for discussion of data.

Publications and Presentations

J.R. Tolman, J.M. Flanagan, M.A. Kennedy, and J.H. Prestegard. "NMR evidence for slow collective motions in cyanometmyoglobin." *Nature Structural Biology* (submitted).

G.W. Buchko and M.A. Kennedy. 1996. "^{1}H NMR conformational studies of the zinc-finger domain from the human excision repair protein XPA." 37th Experimental NMR Conference, Asiolomar, California, March 17-22.

G.W. Buchko and M.A. Kennedy. 1996. "^{1}H NMR conformational studies of the zinc-finger domain from the human excision repair protein XPA." XCII International Conference on Magnetic Resonance in Biological Systems, Keystone, Colorado, August 18-23.

Novel Synthesis of Metal Cluster/Polymer Composites

Mira A. Josowicz (Materials and Interfaces)
Scott A. Chambers (Materials and Chemical Sciences)

Project Description

The objective of this research was to develop a detailed understanding of the mechanism(s) of spontaneous, in situ formation of metal clusters and their size distributions in electroactive polymers. This knowledge will impact the following areas: 1) the rational design of conducting polymer/metal cluster composite materials for specific gas/solid interactions that are important for the fabrication of chemical sensors and separation membranes; 2) enhancement of conductivity and stability of organic semiconductors for molecular electronic devices; and 3) fabrication of modified electrodes for selective, environmentally friendly electrocatalytic conversion processes, such as energy-efficient fuel cells, electrochemical detoxification processes, and high storage density and lightweight batteries.

Technical Accomplishments

Interfacial reactions taking place during synthesis of conducting polymers, nucleation of metal clusters into the polymer matrix, or exposure to vapor or gas molecules of the novel composite materials result from electron exchange between electron donor or acceptor molecules. Understanding of the basic mechanism of electron transfer at the polymer-electrolyte interface and at the polymer-gas interface are critical issues for developing materials that can efficiently tailor an electron exchange based on weak or strong charge transfer interactions. An interplay between the outlined charge transfer processes was investigated by designing experiments associated with the study of interfacial reactions governed by physical and chemical factors of the polymer matrix.

First, voltammetry has been used to study the effects of anions of supporting electrolytes and the effects of substituents on the aniline monomer on oxidation potentials and morphology of the synthesized polyaniline. It was observed that the polymerization rate of aniline in hydrochloric acid is slower than in sulfuric, sulfanilic, or phosphoric acid. Consequently, the morphology of the films varied from smooth to granular to netlike type, respectively. Also, it became evident that the anions of the used acids did not exert any significant effect on the redox characteristics of the polyaniline films. Correspondingly, polymerization of aniline monomers with different substituents placed in meta- or ortho-positions by itself or in the presence of aniline as co-monomer in sulfuric acid was initiated. From the cyclic voltammetric data it became evident that oxidation of the corresponding anilines is more difficult with the increasing electrophilic character of the substituents. It appears that there is an optimum potential range, i.e., reactivity of the aniline radical cation intermediate, which favors radical cation coupling in the follow-up reaction to yield polymeric films. Thus, under these conditions, polymerization occurs only for the parent aniline. The substituted anilines such as 2-carboxylic acid, 2-sulfonic acid, 3-carboxylic acid, 2-chloro, 3-cyano-, and 3-nitro-aniline do not yield polymers. Thus, the reactivity of the "as formed" radical cation intermediates increases. The primary effect is reflected by the increase of the oxidation potentials of the monomers. Thus, with an increase of the reactivity of the formed intermediates with respect to other nucleophiles present in the solution (i.e., solvent), an "escape" polymerization reaction takes place in the vicinity of the Pt-electrode. Another possibility is, that the effect of the strongly electron withdrawing groups on aniline is leading to destabilization of the radical cation intermediate making the radical cation coupling reaction unfavorable.

The UV/VIS spectra of protonated polyaniline films polymerized in the presence of sulfuric acid or phosphoric acid exhibited different features. In the spectrum of polyaniline obtained from sulfuric acid, two absorption bands are seen which correlate to the energy band gap of approximately 3.9 eV and to the polaron transition within the energy band gap band of 1.6 eV. In the spectrum of polyaniline obtained from phosphoric acid, only one wide absorption band around 2.5 eV is seen. It is assumed that this energy band results from a combination of two transition states originated from an intra-chain absorption leading to formation of a "molecular" exciton with a positive charge placed on benzoid units and the negative charge centered on the quinoid units which overlap with the π-π^* antibonding transition associated with the energy band gap. The relative work function values of the two films as measured in reference to the same gold grid electrode were of the same magnitude, suggesting that both films exhibit the same affinity for an electron.

In the Raman spectra for both films, the same vibration stretches can be identified. Furthermore, the ratio of the C-C stretching of quinoid rings at 1586 cm^{-1} and the C-C stretching of benzenoid rings at 1612 cm^{-1}, in both films is identical. Thus, all findings support the statement that both films are of the same structural composition.

Interactions between polyaniline and silver cations were monitored by placing polyaniline films immediately after their cyclic voltammetric deposition which had ended with the potential of -0.1 V (in reference to saturated calomel electrode) in the solution of 0.1 M silver nitrate. Continued equilibration in the silver nitrate solution for 2 hours was monitored by recording UV/VIS spectra. The increasing intensity of the absorption of the PANI films suggest an increase of film conductivity. The energy band gap position remains at the same position but the polaronic band was shifting from 1.9 eV to approximately 2.5 eV. As a result of that process, silver agglomerates were formed in the polyaniline film. From the inspection of the polyaniline films with the optical confocal microscope, information was obtained that the clusters are of metallic origin, their density is high, and that the agglomerates are varying in size.

Stripping of the metallic silver metal was possible by sweeping the potential of the silver composite polyaniline film between -0.4 and + 0.4 V in 1 M hydrochloric acid.

Redox reactions between the polyaniline films and silver cations have been captured by recording Raman spectra after the silver nucleation. The results provide the information that silver nucleation causes the ratio of quinoid to benzoic units to be higher when the polyaniline films were doped originally with HSO_4^- as compared to the polyaniline films doped with the $H_2PO_4^-$. The observed molecular vibrations were shifting to higher energy when the silver nucleation took place in the polyaniline film deposited from phosphoric acid. This implies that the silver was incorporated into the polyaniline matrix in different binding energy states.

From the XPS studies on silver cluster supported on solid state substrate, the chemical shift of Ag 3d5/2 binding energy depends on silver coverage and cluster size. As compared with the bulk silver sample, Ag 3d5/2 = 367.9 eV, very small silver particles usually are causing a negative binding energy shift and with an increase coverage of the sample the energy shifts are approaching the binding energy of the bulk metal. The "as identified" Ag energy bands in the polyaniline films deposited from sulfuric acid were 368.9 eV and from phosphoric acid 368.3 eV. The atomic percent of the identified silver was 3.8 for the PANI-HSO_4^- as compared to 5.7 for the PANI-$H_2PO_4^-$. A detailed examination of the silver Auger lines detectable in XPS has provided the kinetic energy data of 355.9 and 358 eV for the PANI-HSO_4^- and PANI-$H_2PO_4^-$, respectively. The Auger chemical shift data confirmed the Raman data indicating different chemical environment for the silver present in the polyaniline matrix. It can be postulated that the imine nitrogen is more susceptible to acceptor binding in the PANI-HSO_4^- film leading to a polyaniline-silver complex formation. In the case of PANI-$H_2PO_4^-$, the imine nitrogen has already been protonated by the hydrogens of the phosphoric acid due to the doping of aniline, so that the silver is incorporated in its metallic form.

X-ray photoelectron spectroscopy data obtained for polyaniline films polymerized from aniline-2-sulfonic acid or 3 anilinobenzoic acid in the presence of aniline in sulfuric acid have identified the binding of Ag-O which would correlate to the electrostatic interaction between the aniline substituents (-COOH- or -HSO_4^-) and the Ag^+.

Presentations

J. Janata and M. Josowicz. 1996. "Potentiometric sensors for ions and gases." Masaryk University, Brno, Czechoslovakia, March 1.

J. Janata and M. Josowicz. 1996. "Chemical modulation of work function." Schloss Ringberg, Germany, March 7.

J. Janata. 1996. "Non-Nernstian potentiometry in gas phase." Gordon Research Conference, Colby-Sawyer College, New London, New Hampshire, July 29.

Numerical Solution of the Schrödinger Equation

Robert J. Harrison (Theory, Modeling, and Simulation)

Project Description

We have been working toward a fully numerical solution of the electronic Schrödinger equation. Mainstream ab initio methods adopt the algebraic approximation by using basis sets at all levels of theory to turn the numerical problem of solving Schrödinger's equation into a large, sparse, eigenvalue problem. At the lowest level of theory, molecular orbitals are expanded in a finite 1-particle basis set, usually chosen as atomic centered orbitals. The underlying 1-particle basis has recently emerged as the main source of error in conventional ab initio calculations. Yet more recently, it has become apparent that the algebraic approximation leads to inferior scaling of computational expense with respect to both required accuracy and system size, when compared to possible numerical alternatives. Thus, numerical solution of effective one- and two-electron approximations to the many-electron Schrödinger equation promises both greater accuracy and significantly decreased computational expense.

Technical Accomplishments

In the preceding years, we identified the free-space Poisson equation as a prototypical problem. Initial efforts, focused on FEM methods, attempting to generate compact and accurate representations of molecular charge distributions in the KASKADE package. We adopted a quintic polynomial basis and a modified adaptive grid generation and modified the program to prove the feasibility of solving the free-space Poisson equation in this framework. The wavelet approach was investigated in order to be able to make a meaningful comparison of the two schemes. Initial work in one dimension indicated that standard bases were inappropriate for the largely smooth molecular wave functions. After some investigation we adopted the multi-wavelet basis (due to Alpert). This basis is derived from a piecewise linear combination of polynomials and in contrast to other orthonormal wavelet bases has a closed form and is readily computed permitting direct quadrature and straightforward analytic manipulation. Extensive formal and algorithmic work then ensued in order to detail how the Green's function to the Poisson equation could be applied in a rapid (i.e., $O(N)$) fashion. Code to compute the necessary matrix elements has been implemented and verified to be internally consistent and also has the correct long-range values and symmetries. However, even given these matrix elements, much work remains to realize an efficient implementation of the Green's function. Follow-on funding has been received to complete this evaluation and to develop other major components of the three-dimensional wavelets code such as compression, addition, and multiplication of functions.

In the past year, we have focused on developing prototype problems and solutions for the two-electron problem which includes most of the complexity of the many-electron system. A finite-element code was developed for the two-electron atom Hartree-Fock wave function for the purpose of understanding the approach to the known asymptotic behavior. Such an understanding is critical to a compact representation of the two-electron wave function. It was observed that asymptotic behavior was approached amazingly rapidly; indeed a simple two-term wave function, based on the asymptotic behavior at small and large distance, could reproduce the exact wave function within 1% over the entire domain. FEM formalism was developed for the exact solution of the two-electron atom, also with the aim of studying asymptotics, but this was not implemented. Effort was also directed at preparing KASKADE to treat the six-dimensional two-electron polyatomic wave function which required development of additional elements and data structures.

The Development of a Dissociative Model for Water

Sotiris S. Xantheas (Theory, Modeling, and Simulation)

Project Description

The objective of this project was to develop a flexible dissociative interaction potential for water by using a data base derived from first principles calculations. Such a tool can address scientific issues resulting from the heterolytic hydrolysis of water enabling us to:

- quantify the changes in the structural, energetic, and spectral properties of water induced by a solute or interface
- describe the hydrolysis of water due to solutes (ions or salts) and mineral interfaces
- study the proton transfer process in aqueous solutions
- model redox processes in condensed phases.

The molecular-level understanding of these fundamental processes is the cornerstone in addressing a variety of environmental problems at the Hanford Site associated with:

- speciation of heavy atoms in solution
- leaching/dissolution of radioactive species from glasses
- processes in waste tanks (i.e., H_2 generation, chromate reduction).

Technical Accomplishments

A new functional form was used for the interaction potential in order to alleviate the problems of existing models, such as:

- the O-O distance collapses "too early" with cluster size
- the H_3O^+ is too strongly polarized resulting in an incorrect geometry
- the R(O-H) distance in hydroxide is too short
- the clusters up to the hexamer are too strongly bound (between 1.5 and 2 times).

The new functional form used is:

$$V = \sum_{i=1}^{n_H-1}\sum_{j>i}^{n_H}\frac{q_i q_j}{r_{ij}} + \sum_{i=1}^{n_H}\sum_{j=1}^{n_o}\left(\frac{q_1 q_j}{r_{ij}} + \frac{\alpha}{r_{ij}^{12}} + \frac{\beta}{r_{ij}^{6}}\right)$$
$$- \sum_{i=1}^{n_H}\sum_{j=1}^{n_o} q_i \frac{\vec{\mu}_j \bullet \vec{r}_{ij}}{r_{ij}^{3}} S_{OH}(r_{ij},\gamma) + \sum_{i=1}^{n_o-1}\sum_{j>1}^{n_o}\left(\frac{q_i q_j}{r_{ij}} + \frac{\delta}{r_{ij}^{12}} + \frac{\varepsilon}{r_{ij}^{6}}\right)$$
$$- \sum_{i=1}^{n_o}\sum_{j\neq i}^{n_o} q_i \frac{\vec{\mu}_j \bullet \vec{r}_{ij}}{r_{ij}^{3}} + \sum_{i=1}^{n_o}\sum_{j>1}^{n_o}\frac{\vec{\mu}_i \bullet T_{ij} \bullet \vec{\mu}_j}{r_{ij}^{3}}$$
$$+ \sum_{i=1}^{n_H-1}\sum_{j>1}^{n_H}\sum_{k=1}^{n_o}\frac{1}{2}k_\theta(\theta-\theta_e)^2\, S_{HOH}(r_{ij},r_{jk},\lambda)$$

where

$$S_{OH}(r_{ij},\gamma) = \tanh(\gamma r_{ij}^2)$$

$$S_{HOH}(r_{ij},r_{jk},\lambda) = \exp\left\{-\lambda\left[(r_{ij}-r_e)^2 + (r_{jk}-r_e)^2\right]\right\}$$

In this expression, q denotes the charge, μ the dipole moment, r the various OH and O-O distances, θ the HOH angle and α,_β,_γ,_δ,_ϵ,_λ_ are constants determined by the fitting process. The induced dipole moment on each water is solved self-consistently in the field of the neighboring fragments.

The potential model is:

- flexible - accounts for changes in the internal coordinates of water due to the environment
- dissociative - accounts for the heterolytic dissociation of water into OH^- and H^+ ions
- polarizable - accounts for environment-dependent field.

The functional form of the potential function suggests that an accurate description of both the intramolecular potential energy surface (PES) of water, as well as several intermolecular PESs involving two water molecules and several ionic fragments with water is required. Many of the data needed for the parametrization have not been (cannot be) measured experimentally (i.e., the dipole moment function for water and the water dimer structure and binding energy).

A data base was created with structural, energetic, and spectral information for the H_2O, OH^-, H_3O^+, $(H_2O)_n$, $OH^-(H_2O)_n$ and $H_3O^+(H_2O)_n$ obtained from first principles calculations. We also assembled a nonlinear squares code that reads in subsets of this information and fits the potential parameters.

The intramolecular potential energy surface and dipole moment function for water were computed in order to ensure proper description of the monomer total dipole moment with changes in the internal coordinates. The total dipole moment has contributions from the formal charges used on the atoms (-2 for oxygen +1 for hydrogen) as well as the moment induced due to the presence of protons at short range.

In order to fit the O-O parameters, ab initio calculations on the water dimer were performed. The family of augmented correlation consistent basis sets (aug-cc-pVxZ, x=D, T, Q, 5) of Dunning and co-workers (Dunning 1989; Kendall et al. 1992) and a hierarchy of electron correlation methods from second- to fourth-order Moller-Plesset perturbation theory (MP2, MP4) and a coupled-cluster description of the electronic wave function including single, double, and triple replacements [CCSD(T)] were used. The complete basis set (CBS) extrapolated O-bond length for the water dimer was estimated at 2.907 Å (MP2), 2.913 Å (MP4), and 2.914 Å [(CCSD(T)], respectively. The (CBS) electronic energy difference at the optimal geometries was computed at -4.94 (MP2), -4.85 (MP4), and -4.86 kcal/mol [CCSD(T)], respectively (Xantheas 1996; Feyereisen et al. 1996). The variation of the results with basis set and level of correlation suggest that a relatively accurate description of the intermolecular interaction can be achieved at the MP4/aug-cc-pVTZ level. We have therefore computed the potential for the water dimer corresponding to the minimum energy path (MEP) along the O-O intermolecular mode. The corresponding potential is shown in Figure 1 where it is compared to the Matsuoka-Yoshimine-Clementi (MCY) potential (Matsuoka et al. 1976). The results of Figure 1 suggest that the MCY potential is more anharmonic than the ab initio potential.

In order to fit S_{OH} in Equation (1), an accurate description is needed of the proton affinity of water as well as the path for the proton attachment in order to form H_3O^+. The proton affinity of water (electronic energy differences, ΔE_es) at the MP2/aug-cc-pVDZ level is -168.9 kcal/mol, only 1.3 kcal/mol away from the MP2 CBS limit of -170.2 kcal/mol, suggesting a rapid convergence with basis set size at the MP2 level of theory. MP2 also performs well in comparison to CCSD(T); the corresponding proton affinity at the CCSD(T)/aug-cc-pVDZ level is -170.2 kcal/mol, only 1.4 kcal/mol away from the CBS limit of -171.6 kcal/mol.

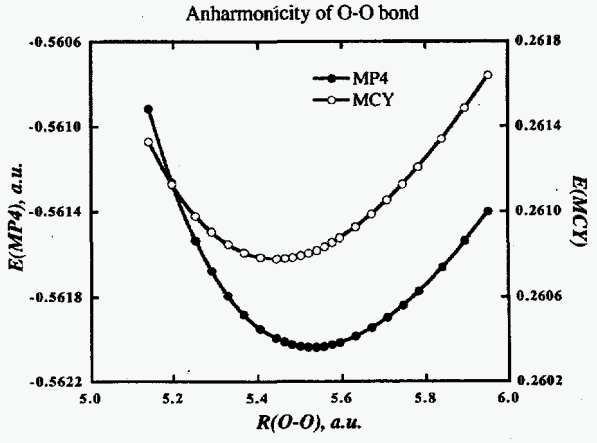

Figure 1. Ab initio (MP4/aug-cc-pVTZ) and MCY potential along the intermolecular O-O mode for the water dimer.

The MEP for the proton association along the O...H^+ coordinate at the MP2/aug-cc-pVDZ level was computed and used to fit S_{OH} in Equation (1). The comparison of the ab initio with the potential MEP is shown in Figure 2. The potential predicts a value of -164.0 kcal/mol for the proton affinity of water. Although the agreement is satisfactory around the minimum and at large ($R \geq 4$ Å) separations, there is substantial deviation in the $2\text{Å} \leq R < 4$ Å region, probably attributed to inadequacies in the charge-dipole cutoff function in this range. This proposition suggests that the O-O and O-H parameters might have to be fitted simultaneously. Therefore, the reduced three-dimensional PES for the proton transfer between two water molecules in $H_5O_2^+$ at the MP2/aug-cc-pVDZ level of theory was computed. The surface was obtained by varying both R(O-O) and R(O...H^+)

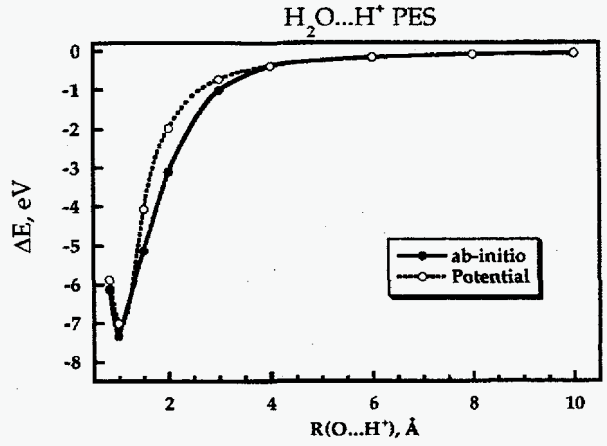

Figure 2. Minimum energy path (MEP) for proton association of water along the R(O...H^+) coordinate: comparison between MP2/aug-cc-pVDZ and interaction potential.

and optimizing the rest of the internal coordinates of the system. It is shown in Figure 3. It exhibits a single very flat minimum at R(O-O)=2.4 Å and R(O...H^+)=1.2 Å, contrary to previous calculations (Tortonda et al. 1993) at the HF level of theory which have found a surface with a double minimum.

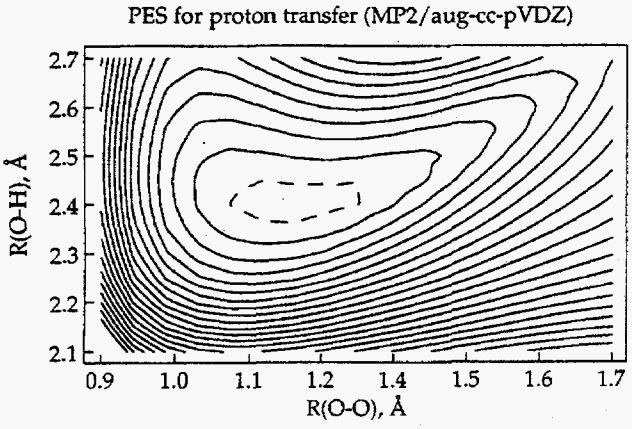

Figure 3. Reduced potential energy surface for proton transfer in $H_5O_2^+$ at the MP2/aug-cc-pVDZ level of theory. Contour increment: 0.25 kcal/mol.

Plans are to refine the parameters of the potential by using the reduced potential energy surface corresponding to the proton transfer in $H_5O_2^+$ and to benchmark its ability to reproduce results for larger clusters and macroscopic thermodynamic properties of water.

References

T.H. Dunning, Jr. 1989. *J. Chem. Phys.* 90, 1007.

M.W. Feyereisen, D. Feller, and D.A. Dixon. 1996. *J. Phys. Chem.* 100, 2993.

R.A. Kendall, T.H. Dunning, Jr., and R.J. Harrison. 1992. *J. Chem. Phys.* 96, 6796.

O. Matsuoka, E. Clementi, and M. Yoshimine. 1976. *J. Chem. Phys.* 64, 1351.

F.R. Tortonda, J-L. Pascual-Ahuir, E. Silla, and I. Tunon. 1993. *J. Phys. Chem.* 97, 11087.

S.S. Xantheas. 1996. *J. Chem. Phys.* 104, 8821.

Tumor Formation in Cells and Tissues Studied by Means of Liquid-State and Solid-State NMR

Robert A. Wind (Macromolecular Structure and Dynamics)

Project Description

The main objective of this project is to improve the characterization of tumors by means of nuclear magnetic resonance (NMR) methodologies. The investigations were carried out by in vitro liquid-state and solid-state nuclear magnetic resonance and by localized in vivo nuclear magnetic resonance spectroscopy. The in vitro experiments were performed on healthy mammary tissues obtained from female Fischer rats, on R3230AC mammary tumors implanted in the animals, and on normal epithelial cells and malignant cells extracted from the tissues. The in vivo investigations were carried out on mice bearing hepatic tumors resulting from exposure to dichloroacetate (DCA) in their drinking water. In all cases differences were observed between the normal and diseased cells and tissues. Two collaborations have started to use the results of this project in a medical application and in a health-related environmental research project.

Technical Accomplishments

The importance of both in vivo and in vitro nuclear magnetic resonance imaging and spectroscopy for the detection and characterization of tumors has long been recognized. It was found that several parameters, that can be determined by these techniques, are different in healthy and tumorous tissues. Examples are the water concentration and mobility, and the intensities of certain lipids and water-soluble metabolites. However, the results are often ambiguous, as many different types of tumors and other lesions give similar results, and as a large scatter in the results often makes the differentiation between healthy and tumorous tissues difficult. We have undertaken several approaches which might improve this situation:

1. We have extended the liquid-state nuclear magnetic resonance methodologies to higher fields than is used today.

2. We performed high-resolution solid-state experiments on frozen samples. This makes it possible to investigate structures and dynamics of large-molecular weight molecules such as phospholipids, proteins and nucleic acids, which can not be observed with 'standard' liquid-state nuclear magnetic resonance techniques. Moreover, solid-state nuclear magnetic resonance makes it possible to study the tissues for a long time without degrading the samples, and to obtain information about slow motions in the samples, normally overshadowed by fast overall molecular tumblings.

3. We started evaluating the diagnostic potentials of in vivo localized nuclear magnetic resonance spectroscopy. In order to minimize the scatter in the results arising from individual differences in the subjects, model inbred rodent lines were used.

The in vitro nuclear magnetic resonance measurements included a liquid-state ^{1}H and ^{13}C nuclear magnetic resonance study and a solid-state ^{13}C nuclear magentic resonance investigation of mammary tumors implanted in rats; the in vivo measurements focused on ^{1}H spectroscopy of liver tumors in mice. During FY 1994 and 1995, the emphasis was placed upon the in vitro spectroscopy work. During FY 1996, this work was continued with experiments on other samples in order to investigate the reproducibility of the results, and the first in vivo experiments were performed. Below we shall discuss the progress of these projects in FY 1996 separately.

The in vitro liquid-and solid-state nuclear magnetic resonance measurements were performed on healthy mammary tissues obtained from female Fischer rats, on R3230AC mammary tumor tissues implanted in the animals, and on healthy mammary epithelial cells and tumor cells extracted from the tissues. The liquid-state nuclear magnetic resonance experiments were performed at 4°C in magnetic fields of 11.7 and 17.6 tesla, whereas the solid-state experiments were carried out in a field of 9 tesla at -100 and -40°C. For the solid-state experiments the samples were quickly frozen after excision (tissues) or preparation (cells) at -78°C, and preserved at this temperature prior to the measurements. Following are the main results: 1) the liquids nuclear magnetic resonance results are very similar in both fields, so that higher fields do not offer specific advantages; 2) the T_1 values of the water protons are very similar in healthy and tumor tissues, but the T_2 values are significantly different; 3) both the liquid-state ^{1}H and ^{13}C spectra and the solid-state ^{13}C spectra of the healthy tissue is dominated by the triacylglycerols present in the adipose tissue. Analysis of the liquid ^{13}C spectra gave as a result that the average chain length of the fatty acids is

~17 carbon units, with about 30% saturated, 28% mono-unsaturated, 39% double-unsaturated and 3% triple-unsaturated fatty acids; 4) the ^{1}H and ^{13}C spectra of the tumor tissues and the cells differ markedly from that of the healthy tissue, and are mainly due to cellular lipids and proteins. As such, nuclear magnetic resonance might be useful to detect small amounts of transformed cells in a tissue; 5) compared to the liquid ^{1}H and ^{13}C spectra of the normal cells the liquid spectra of the tumor tissues and tumor cells show an increased amount of mobile lipids. The chain lengths of these lipids were found to be similar in all samples; 6) the solid-state ^{13}C spectra of the tumor tissues and the tumor cells were very similar, but showed some significant differences with the spectrum of the normal cells. The main difference is a reduced relative intensity of the line due to the methylene chains in the tumor samples, which has been associated with changes in local mobilities occurring in the cells after tumorigenesis. The spectral differences virtually disappear if the samples are preserved at ambient temperatures, emphasizing the importance of the quickly freezing the samples; and 7) at -100°C differences in nuclear relaxation times can be used to separate the lipid spectrum from that of the proteins.

The in vivo ^{1}H nuclear magnetic resonance experiments could not be carried out on the rats used in the in vitro measurements, as our equipment is capable only of handling small rodents like mice. As mice with mammary tumors were not available, it was decided to perform the experiments on B6C3F1 male mice chronically exposed to 2 g/L dichloroacetate in their drinking water. During this exposure a variety of benign and malignant lesions are developing in the livers of these animals, such as clear cell foci, clear cell adenomas, adenomas, adenocarcinomas, and carcinomas. These animals are part of a research program studying the changes in cell division and tumor growth induced by active metabolites of chlorinated hydrocarbon solvents widely distributed in DOE sites. The in vivo ^{1}H nuclear magnetic resonance spectra of the lesions might help in characterizing the different types of lesions without having to sacrifice the animals, and in identifying the transformation of these lesions from benign to malignant. Ultimately, the data will be used to develop realistic non-linear dose-response relationships for non-genotoxic carcinogens used in risk assessment modeling. The experiments were performed in an external field of 11.7 tesla. Figure 1 shows a magnetic resonance image of a cross section in the abdominal region of a mouse taken 43 weeks after the initiation of the exposure. The (enlarged) liver is clearly visible, and in the lower right-hand corner a large lesion can be observed, which was identified as an adenoma by histology analysis. Figure 2 shows three proton spectra, obtained in the tumor (1), and two liver regions (2 and 3), indicated in Figure 1. Intensities are observed mainly at 0.9, 1.3, 5.0, and 5.3 ppm, corresponding to protons in methyl groups,

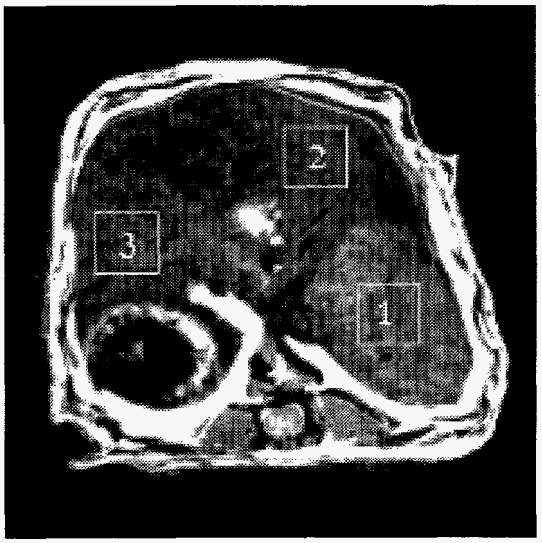

Figure 1. In vivo MR image of a mouse liver after 43 weeks of exposure to DCA. In the lower right hand corner, a large adenoma is observed.

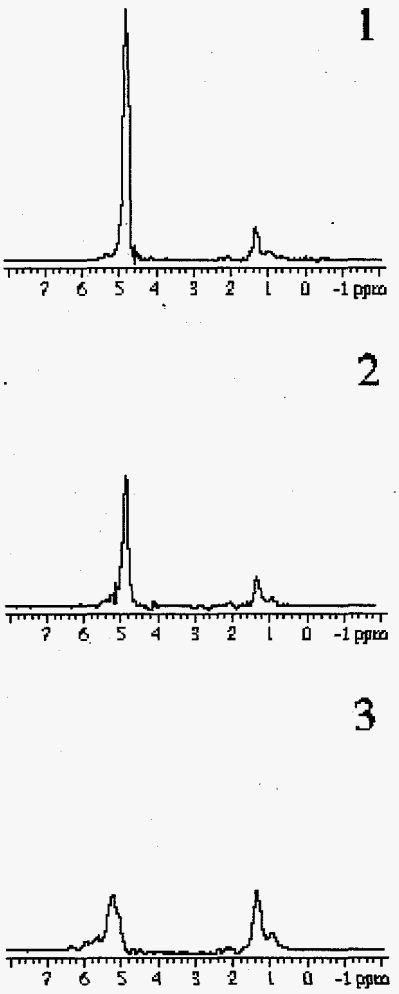

Figure 2. Localized ^{1}H in vivo NMR spectra of the regions 1, 2, and 3 indicated in Figure 1.

methylene groups, water, and protons attached to unsaturated carbons, respectively. It follows that the tumor spectrum shows an increased water intensity, probably indicative of the large cell concentration, but the results obtained in the in vitro measurements of the mammary tumor are not confirmed. The intensities of the lines associated with the lipid protons are the same in the tumor as in the adjacent liver region 2, and actually less than those in the more remote liver region 3. Also, the latter region seems to contain more unsaturated lipids than the other two regions. Whether all these results are significant and/or lesion-specific is under investigation.

Publications and Presentations

R.A. Wind, B.A. Concannon, K.M. Groch, D.N. Rommereim, and R.A. Santos. "An investigation of rat mammary healthy and R3230AC tumor tissues and cells by means of solid state ^{13}C NMR." *Solid State NMR* (in press).

R.A. Wind, B.A. Concannon, K.M. Groch, D.N. Rommereim, and R.A. Santos. "Healthy and tumorous rat mammary cells studied by solution ^{1}H and ^{13}C NMR." (in preparation).

K.M. Minard, R.E. Bull, and R.A. Wind. "Detection of hepatic lesions in mice exposed to dichloroacetate with high-field in vivo MRI." (in preparation).

R.A. Wind. 1995. "Tumor formation in cells and tissues studied by magnetic resonance." Physics General Seminar, University of Utah, October.

R.A. Wind. 1995. "In vivo and in vitro NMR studies of the effects of exposure to toxic chemicals." Colorado State University, October (invited presentation).

R.A. Wind. 1995. "Tumor diagnosis in cells and tissues by NMR methodologies." Colorado School of Mines, October (invited presentation).

R.A. Wind. 1995. "Tumor formation in cells and tissues studied by magnetic resonance" Special Biophysics Seminar, University of California at Berkeley, October.

R.A. Wind, R.A. Santos, K.M. Groch, and D.N. Rommereim. 1995. "Solid and liquid NMR studies of the R3230AC mammary adenocarcinoma in model Fischer Rats." International Chemical Congress of Pacific Basin Societies, Hawaii, December (invited talk).

R.A. Wind, K.M. Groch, A. Jurkiewicz, D.N. Rommereim, and R.A. Santos. 1996. "An investigation of rat mammary healthy and R3230AC tumor tissues and cells by means of solid state ^{13}C NMR." 37th ENC, Asilomar, March.

Process Science and Engineering

Advanced Instrumentation Real-Time Acoustic Planar Imaging of Dense Slurries - RAPIDS

Alireza Shekarriz (Fluid Dyanamics)

Project Description

The objective of this project is to demonstrate how an ultrasonic imaging system can be used to determine the local rheology of process mixtures in real-time. Two different sets of parameters are important for rheological measurements: 1) local viscosity and 2) local strain rate (shear and extension). The local strain rate can be measured by locally measuring the velocity profile in the flow. The velocity profile is determined from following the motion of tracers in the flow as has commonly been done in particle image velocimetry. Local viscosity is linked to the pressure drop in the pipe. Knowledge of the rheology of the fluid in real time provides the tool for process control and optimization and flexible manufacturing. Such information also provides information such as how homogeneous the process mixture may be.

Technical Accomplishments

During FY 1995, we investigated the feasibility of using a novel approach for measuring the fluid velocity profile in a circular pipe. The feasibility of this technique was initially demonstrated in FY 1995 using an existing ultrasonic imager called RTUIS (real-time ultrasonic imaging system). During FY 1996, the application of the technique for a fully developed viscometric flow of a non-Newtonian fluid was demonstrated. To reduce the degree of experimental complexity and measurement difficulties associated with a full-field imager such as RTUIS, an array of ultrasonic transmitters and receivers were used for measurement of the velocity profile across the pipe section.

Figure 1 is the pipe loop setup used for making the velocity and pressure drop measurements with 0.1 wt% Carbopol 980 as the working fluid. This setup consisted of a 1/3 hp flexible impeller pump capable of producing high pressure heads at the desired flow rates, a positive-displacement flowmeter for accurate reading of the flow rate, and a straight 20-foot section of pipe to produce a fully developed flow. The flow rate tested was at 13.3 L/min which yielded a Reynolds number of ~6.5 which is well below the transition point. Thus, it is expected that the flow is fully developed over more than 99% of the length of the 20-foot section of pipe. Also, care was taken in ensuring that the pipe section is straight and will not produce any secondary flows prior to the test section, the location at which the ultrasonic transducers are located.

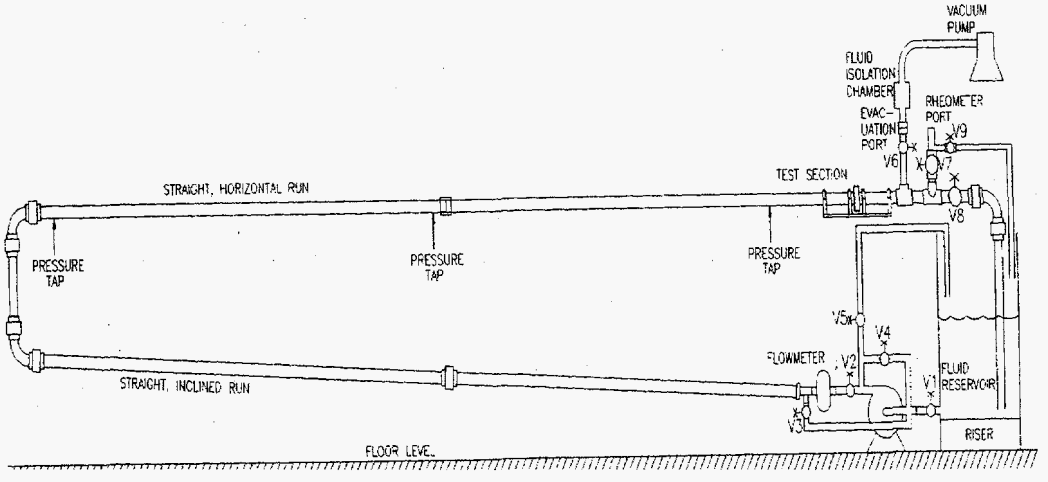

Figure 1. Flow loop setup for ultrasonic velocity profile measurement.

A sample of the mixture was then taken for off-line measurement of the fluid rheology using a Bohlin® VOR rheometer (Figure 2). The fluid rheology, for a range of shear rates of 0.01 to 10 s^{-1}, was found to be represented well by the Herschel-Bulkley model.

$$\tau=\tau_o+K|\dot{\gamma}|^{n-1}\dot{\gamma} \qquad (1)$$

In the above equation, τ_0 is the yield stress (2.75 Pa), K is the consistency factor (2.5 Pa.s^n), $\dot{\gamma}$ is the shear rate, and n is the behavior index of the fluid (0.6). It is clear from Equation (1) that the fluid is extremely shear thinning and the laminar fully developed velocity profile of this fluid in the pipe is reported to be significantly different from its Newtonian counterpart. An analytical solution exists for presenting the velocity profile in this case, and this profile is given for the particular rheology, as will be discussed further when comparing to the data.

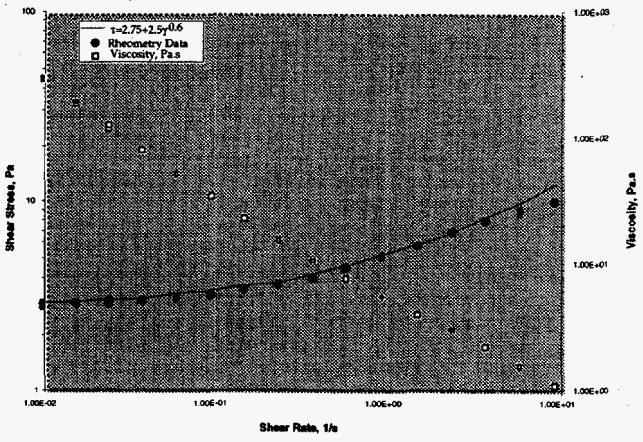

Figure 2. Rheology of the non-Newtonian working fluid, 0.1 wt% Carbopol 980.

Four pairs of focused 3 MHz ultrasonic transducers were used to image the flow along the diametrical axis of the pipe. The transducers were located an axial distance of 9 mm downstream of a thin resistive wire used for local heating. The line-of-sight of the transducers were normal to the plane in which the heated wire was positioned. At time t=0, a short pulse of charge was released into the heating wire using a capacitor, which resulted in heating of the fluid in the vicinity of the wire. The signal received at various receiving transducers was monitored immediately after the capacitor discharge and tracked for approximately 2 seconds. The time of flight or delay time of the disturbance at each transducer location was measured. The local velocity was inversely proportional to this delay time. Figure 3 shows two typical time traces recorded at the receiving transducers which monitored

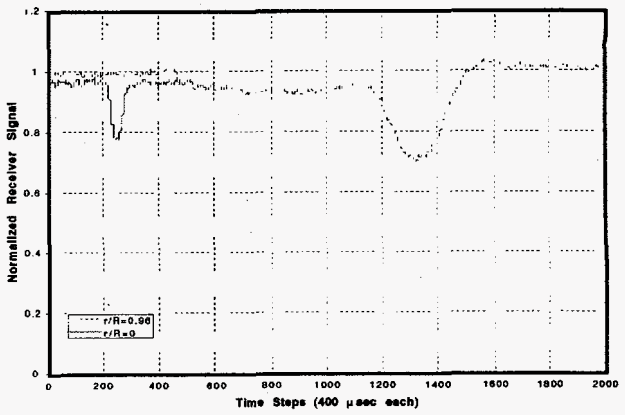

Figure 3. Time trace of signal received at two different transducers.

the radial locations of r/R=0 and 0.96, at the center of the pipe and near the pipe wall, respectively. Note that due to a higher velocity in the center of the pipe, the signal at the center transducer (r/R=0) is received much sooner than what is received at the last transducer (r/R=0.96). The dip in the time trace for the transducer at r/R=0.96 is much broader than that in the center of the pipe due to a slower velocity and higher diffusion time.

Figure 4 is a plot of the local velocity at various radial locations in the pipe. The error bars on each data point are a measure of the uncertainty in both the velocity and position measurements. The position uncertainty is due to the finite width of the ultrasonic beam at the measurement point and the velocity uncertainty is mainly due to thermal inertia of the wire and its surrounding fluid. Although this thermal inertia was accounted for, the actual delay time of the wire and fluid to a heat pulse is a function of the local heat transfer coefficient, which is unknown for this class of fluids.

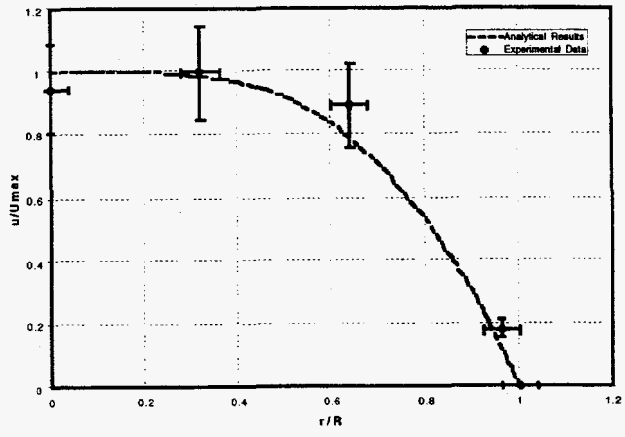

Figure 4. Velocity profile across the pipe. The line is the analytical predictions based on the rheology presented in Figure 2.

To investigate how closely the current velocity measurements represent the actual fluid velocity, a model was used based on a closed form solution of the equations of motion for fully developed laminar flow of a yield-pseudoplastic fluid in a pipe (Park et al. 1989).

$$u/U_m = \left[\frac{n}{2F(1+n)}\right]\left[(F-Y)^{\frac{1+n}{n}} - (F\cdot\frac{r}{R}-Y)^{\frac{1+n}{n}}\right] \quad (2)$$

In Equation (2), u is the local velocity at the radial location r, R is the radius of the pipe, U_m is the mean velocity of the flow, n is the behavior index, and Y and F are parameters which depend on the pressure gradient in the pipe, yield stress of the material, and the characteristic shear rate, all defined in Shekarriz and Brenden (1995). This model predicts that the velocity within the core region remains constant and drops suddenly outside the core. The size of the core is a function of the yield stress of the fluid. Note that the measured distribution and predictions agree within 15%, when the velocity is normalized with respect to the maximum velocity in each case. These measurements however, were found using a delay correction, which appears to be somewhat impractical for fluid flows with properties which could change as a function of time. Thus, although the above technique seems feasible, it is concluded that it would not be practical. A more practical approach would be to use a Doppler technique for measurement of the velocity profile.

References

J.T. Park, R.J. Mannheimer, T.A. Grimley, and T.B. Morrow. 1989. "Pipe flow measurements of a transparent non-Newtonian slurry." *Journal of Fluids Eng.*, Vol. 111, pp. 331 - 336.

A. Shekarriz and B.B. Brenden. 1995. "Planar ultrasonic imaging of a two-phase mixture." *Journal of Fluids Eng.*, Vol. 117, No. 2, pp. 317-319.

Publication

A. Shekarriz, B.B. Brenden, and H.K. Kytömaa. "Planar ultrasonic technique for visualization and concentration measurement in dense slurries." *Journal of Powder Technology* (accepted).

Advanced Spot Welding of Aluminum Automotive Sheet

Mark T. Smith, Huaxin Li (Materials Sciences)

Project Description

Resistance spot welding of aluminum alloys is a critical requirement for the development of aluminum-intensive structures and vehicles. Resistance spot welding lends itself to the high volume production rates associated with automotive manufacturing and is currently in widespread use for the manufacture of steel automotive bodies and components. Conventional resistance spot welding techniques developed for steel encounter a number of difficulties when applied to aluminum alloys due to the following characteristics: 1) high thermal and electrical conductivity, 2) surface oxide films, 3) high softening rate with increasing temperature, and 4) high shrinkage during cooling. As a result, resistance spot welding of aluminum requires higher welding current density for a given weld nugget size (compared with low carbon steel), results in decreased electrode life because of electrode pickup (contamination), and has difficulty maintaining consistent weld nugget size and strength because of irregular resistance of the surface oxide films.

The objective of this project is to demonstrate a unique resistance spot welding technique for aluminum sheet that uses a special filler metal disk to improve weld quality, reliability, and surface finish. The technique results in significantly higher current density for a given power input, is compatible with existing high-volume automotive resistance spot welding technology, and has the potential to eliminate/minimize electrode pickup (contamination).

Technical Accomplishments

This technique incorporates a special filler metal disk that is placed between the aluminum sheets that are being spot welded. Test results on 1 mm thick 6061 aluminum alloy sheets welded using flat-flat electrodes have shown that filler metal/resistance spot welding can dramatically improve almost all of the problems found during conventional resistance spot welding. By using filler metal/resistance spot welding, the following improvements have been achieved: 1) reducing/ eliminating electrode contamination; 2) eliminating/ minimizing surface indentation and deformation; 3) increased weld nugget size that was twice as big as that produced by conventional resistance spot welding; 4) maintaining consistent weld nugget size; and 5) eliminating the need for cleaning, particularly at faying surfaces. Failure by peeling testing occurs in base metal around the weld nugget. Metallographic investigation shows favorable oval nugget shape on cross section. The ratio of major axis to minor axis is 7 with major axis being 6.5 mm long.

Welding of 3.2 mm thick 6061 and 5083 aluminum alloy sheets was done using one flat and one curved electrode. Fracture by peel fracture tests again failed in the base metal. Metallographic analysis found that a brazing-bonded corona ring was formed around the weld zone (fusion zone and heat affected zone) if a filler metal disk was used. The bonded corona seemed to be formed because the molten filler metal wetted, diffused into base metal, and formed a joint under the electrode pressure (like pressure brazing). Because the joint was limited on the surfaces, the original microstructure in the corona was not changed during welding (no softening). The bond was strong because peeling fracture occurred in the base metal along the border of the corona ring (see Figure 1).

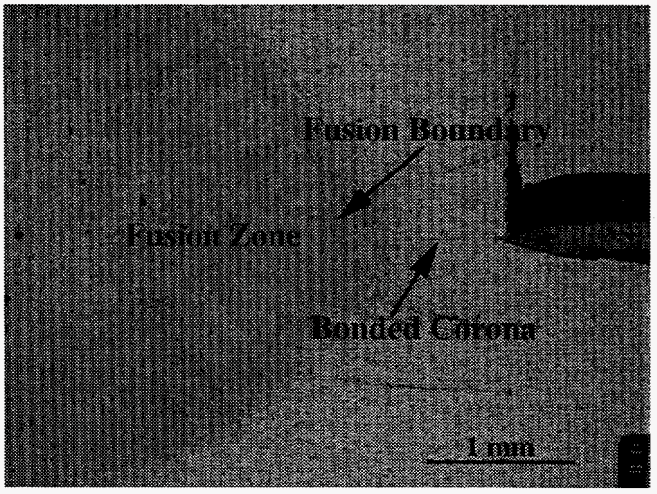

Figure 1. Filler metal resistance spot welding joint. Fractured in the base metal along brazing-bonded corona. The base metal is a 3.2 mm thick 6061 aluminum sheet.

Welds made by conventional resistance spot welding were fractured in the heat affected zone along the fusion line (the border between fusion zone and the heat affected zone) as shown in Figure 2. The joined area in the filler metal/resistance spot welding (fusion zone plus brazing bonded zone) was 61% bigger than the traditional nugget size. Tensile-shear strength filler metal/resistance spot welding is 20% stronger and welds are tougher than conventional resistance spot welding.

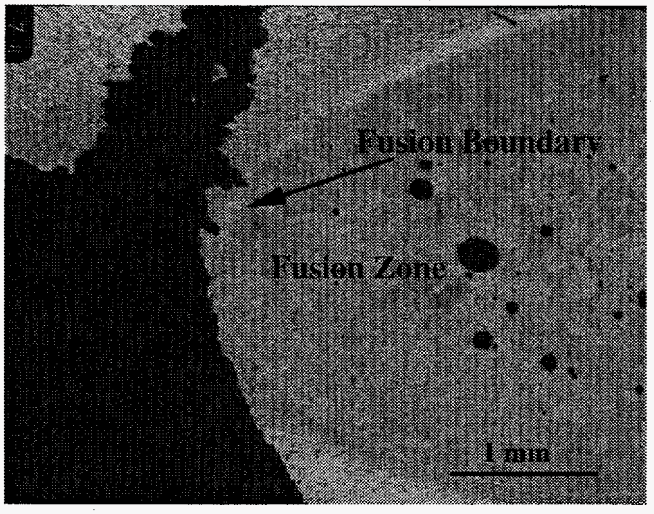

Figure 2. Conventional resistance spot welding joint. Fractured in the heat affected zone along fusion boundary. The base metal is a 3.2 mm thick 6061 aluminum sheet.

In summary, the filler-metal-assisted resistance spot welding can provide improved weld microstructure (less porosity and cracks) and joined size, which increases peeling strength, tensile-shear strength (by producing the brazing-bonded corona), and joint toughness when compared to conventional resistance spot welding. Future work is aimed at understanding the controlling mechanism of weld formation during filler metal/resistance spot welding and to make the filler metal/resistance spot welding more user friendly.

Alkane Oxidation

Ward E. TeGrotenhuis, Steven R. Billingsley (Process Technology)
Donald M. Camaioni, John C. Linehan (Atomic and Molecular Chemistry)

Project Description

The objective of this project was to advance the ALKOX technology for producing alcohols from alkanes by developing a more economical overall process, collecting supporting experimental data, and addressing outstanding technical issues. The scope was to focus on one application and one chemistry pathway, for which a process flowsheet, mass and energy balances, and a refined economic analysis would be developed. The process was to be validated through laboratory experimentation, engineering analyses, and process flow modeling. Technical feasibility was to be established and critical issues addressed, such as overall conversion factors, reaction conditions, residence times, reactor configurations, separation efficiencies, and overall heat recovery.

Technical Accomplishments

Oxidation of hydrocarbons is central to the production of numerous products and materials, including solvents, plastics, textiles, adhesives, fuels, and other consumer products. Typically, alcohols are the intermediate feedstocks for producing many of these products, but cannot be produced by direct oxidation from alkanes, because the alcohol is more reactive than the original alkane in an oxidative environment. Therefore, indirect routes are required, such as the conversion of methane to syn-gas in the production of methanol. These indirect routes typically involve low conversion rates, low yields, and high energy consumption.

ALKOX chemistry represents a new direct oxidation route for producing alcohols from alkanes. The process involves conversion of an alkane to an ester intermediate in a primary reactor, which is subsequently hydrolyzed to the alcohol in a second reactor. To form the ester, a redox reaction involving Cu(I) and oxygen produce a hydroxyl radical, which removes a hydrogen atom from the alkane. The alkyl radical then reacts with Cu(II) and trifluoroacetate to form the triflouroacetate ester, which is stable at reaction conditions. This reaction can be carried out at room temperature and pressure, and can achieve very high conversion of alkanes to corresponding alcohols. The technology has been reduced to practice for methane and cyclohexane. Additional innovation has occurred, including photolysis of TiO_2 to initiate the reaction. Cyclohexanol production was selected as the subject for this project, because the base economics are more favorable than for other alternatives.

The project was successful in developing a process showing significantly improved process economics, as well as in resolving several important technical issues. The revised economic analysis has improved the projected return on investment from 22% to 74% for a 200 million pound per year plant with a 20-year life, as determined from a detailed ASPEN model of the process. The improved economics were achieved primarily through reduced operating costs associated with back-end separations. The most significant driver was the experimentally determined equilibrium coefficient for the hydrolysis reaction, which was much more favorable than previously assumed, allowing a significant reduction in excess water that has to be recovered and recycled. In addition, an improved reactor design was proposed, which would simplify the downstream unit operations. Improvements were also made to the flowsheet for back-end separations in order to combat azeotropes and to reduce the heat duty associated with distillation.

The experimental objectives of the project were to validate the base chemistry, and to complement the process modeling effort. Additional data were collected on the photocatalytic version of the ALKOX reaction. The original experiment, in which TiO_2 is deposited on hollow silica spheres doped with Pd, was repeated and results verified. In addition, other catalysts were shown to work, including powdered TiO_2, both with and without Pd doping. The catalyst also worked without adding either Cu(I) or Cu(II) ions to the solution. Without added Cu ions, both cyclohexyl ester and a dimer of cyclohexane were produced. However, on running for extended periods, reaction solutions developed yellow to brown colors in all cases, indicating byproduct formation, although GC analyses did not show significant quantities of byproducts. The potential for byproduct formation is reduced by the new reactor concept. Operational cost estimates adopted for the reactor are more conservative than previously assumed, which somewhat dilutes the savings mentioned above.

Additional experiments were performed to support modeling of the process downstream of the primary reactor. To properly define the downstream conversion and separation problem, data were collected in phase equilibria in the primary reactor. Second, equilibrium coefficients for the hydrolysis reaction,

Cyclohexyl trifluoroacetate Ester + Water ↔
Cyclohexanol + Trifluoroacetic acid (TFA)

were measured at several water to acid ratios. This resulted in the most significant discovery impacting process economics. A favorable equilibrium coefficient of 0.3 was measured at a water to acid ratio of 5:1 at 30°C, which represents a significant decrease from the prior assumed water to acid ratio of 50:1. This reduction in excess water dramatically decreased the operating costs associated with downstream separations, which had been consumed in reboiler duty to vaporize the large amount of water cycling through the process. For example, annual offsite steam costs for the representative plant decreased from the previous estimate of $100 million to $13.6 million.

The remaining unit operations in the revised flowsheet were modeled using property estimators built into the ASPEN software. The resulting mass and energy balances from the ASPEN simulations were used to revise the economic analysis, which not only increased the projected return on investment from 22% to 74%, but improved the level of confidence in the economic analysis.

The project has successfully advanced the ALKOX technology for cyclohexanol production, primarily through developments in the process down stream of the primary reactor, resulting in substantially improved economics. However, technical and economic issues remain principally with the primary reactor. Efforts are required to identify the preferred catalytic pathway, which will then allow experimental determination of conversions, yields, and efficiencies. These, along with a reactor design, will solidify the economic picture of the technology.

Development of Small-Scale Reformer for Hydrogen Production

Anna Lee Y. Tonkovich (Process Technology)

Project Description

The objective of this project was to demonstrate the viability of a membrane reactor for efficient small-scale hydrogen production. Methane reforming was targeted initially. A high-temperature and high-pressure membrane reactor was designed and constructed to accommodate the reactions of interest. It was expected that near unit hydrocarbon conversions can be achieved in the single-pass reactor. New membrane materials and new fabrication procedures for existing materials to facilitate in situ hydrogen separation were investigated to support long-range development of hydrogen production technologies. Strong industrial interest has been expressed upon successful demonstration of this technology, which includes high per-pass conversion and pressurized permeate hydrogen.

Three tasks were scoped: 1) membrane fabrication of known materials and permeance testing, 2) investigation of new materials for hydrogen separation, and 3) investigation of high-pressure reactor sealing protocols and subsequent reactor demonstration.

Technical Accomplishments

The first task was conducted in conjunction with an affiliate membrane development project, "Gas Selective Thin Film Barrier Materials." This system was widely recognized in the literature as providing high hydrogen flux rates and resistance to hydrogen embrittlement, but long-term membrane durability under reaction conditions is unknown. Further, these coatings represent over an order of magnitude reduction in membrane thickness over unsupported membranes.

The direct coating of Pd and Pd-alloys on support tubes was found to be unsatisfactory. The surface roughness was too great to coat defect-free membranes. Additional work was initiated to investigate surface smoothing layers. No membrane to date has demonstrated complete defect-free operation, but the defect density has dropped dramatically. The final membrane evaluated in the project has a finite number of defects (<0.75 defects per cm^2) compared to coatings without a smoothing layer (>100 defects per cm^2).

The second task investigated new materials for hydrogen separation. New candidate materials for permselective hydrogen separation, including strontium-substituted ytterbium cerates, (Sr,Yb)CeO3 were evaluated. These materials would be used in an electrochemically "driven" mode by applying an electrical potential across the dense membrane layer. As well as attaining hydrogen flux levels useful for the devices of interest, this driven operation mode would allow transport "up" the hydrogen partial pressure gradient. Under most operating conditions, the driven flux should be largely independent of the hydrogen partial pressure gradient. Fluxes near 1 sccm/cm^2 have been measured at 900°C, through 2 mm-thick membranes at 4% H_2 in the upstream gas. While these materials offer attractive features, they are prohibitively expensive to be scaled-up in an industrial process. Further, the necessary hydrogen flux requirements for the process exceed those measured in existing thick membrane disks by several orders of magnitude. The material cost and necessary development to produce ultrathin membranes makes these materials ill-suited for bulk industrial use and better suited in sensor applications.

The third task centered on the design and demonstration of a high-temperature and high-pressure membrane reactor. Construction of the reactor module was made using a specialty alloy (Haynes 230) to permit the required severe reaction conditions. A six-bolt flange maintains module seal for high-pressure operation. The membrane is bonded to a dense ceramic tube, which extends from the reaction zone and slides through the flanged seal for hydrogen removal under high retentate and permeate pressures.

The lack of fabricated defect-free membranes did not permit the complete evaluation of the reactor under real-world reforming conditions. Benchmark tests of the reactor were completed with the insertion of a dense tube where the membrane is housed to evaluate the fixed-bed reactor operation under similar conditions. As a function of temperature from 300°C to 750°C and up to 50 psig, the fixed-bed performance approaches thermodynamic equilibrium. Evaluation of the reactor with the hydrogen permselective membrane is expected to produce much higher hydrogen yields per pass.

Presentation

A.L.Y. Tonkovich. 1996. "The future of membrane reactors for the chemical and petroleum industries." Invited lecture at the ACS Spring Conference, New Orleans, Louisiana, March.

Electroactive Materials

Johanes H. Sukamto, Scot D. Rassat (Process Technology)

Project Description

The preparation and characterization of electroactive materials for the development of a new ion-exchange process was the focus of this activity. In this process, the redox properties of the electroactive materials are exploited to uptake and elute the target ions. In particular, both the uptake and elution steps are affected by the application of an electric potential and the passage of a stoichiometric number of electrons. Therefore, no chemical additives were required (i.e., secondary waste is greatly minimized), power consumption is minimized, and the target ions can be recovered in pure form.

Technical Accomplishments

Film characterization procedures were identified and included cyclic voltammetry, potential step, quartz crystal micro-gravimetry, and impedance analysis. Both cyclic voltammetry and potential step experiments were used to evaluate the electroactive film capacity. However, to conduct the stability studies (i.e., capacity as a function of time), the existing control programs required modifications. A quartz crystal microbalance system was assembled and the control software was written. In addition, an impedance system was acquired and tested. Several experiments with different Ni substrates were performed. The Ni substrates used were Ni plated onto a Pt substrate, Ni sheets, and Ni plated onto a Au substrate. A standard Watts bath was used to plate Ni on Pt, but the bath aggressively corroded the Au substrates on the quartz crystal microbalances. This demonstrated that the composition of the bath used for Ni plating is an important consideration in developing the Ni deposition procedure. After the nickel ferrocyanide film was deposited, the electroactive film was tested in various solutions: 0.5 M Na_2SO_4, 0.67 mM $CsNO_3$, and mixtures of the two. Cyclic voltammetry and potential step cycling results qualitatively showed that films were stable and that they preferentially uptake cesium over sodium. Cyclic voltammetry and potential step cycling results (in terms of both capacity and stability) were qualitatively consistent with results obtained from the quartz crystal microbalance.

Nickel hexacyanoferrate films prepared using proprietary methods were shown to have twice the capacity and to be much more stable than films prepared according to methods published in the literature, as shown in Figure 1.

Furthermore, one of the PNNL films has comparable uptake and elution rates as compared to the literature film while it has nearly twice the capacity as shown in Figures 2 and 3.

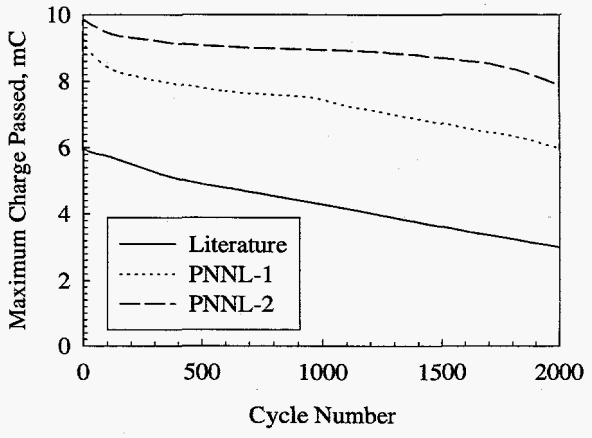

Figure 1. Comparison of stability for literature, PNNL-1, and PNNL-2 films.

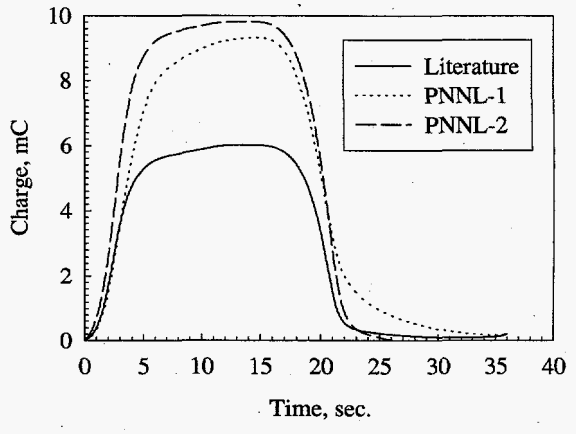

Figure 2. Comparison of the uptake and elution rates for literature, PNNL-1, and PNNL-2 films.

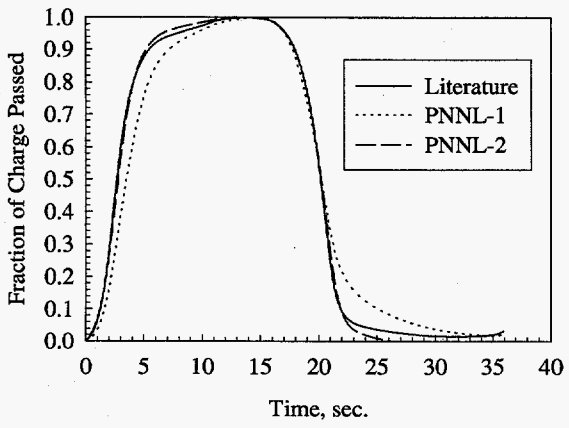

Figure 3. Same as Figure 2 but normalized with respect to the maximum charge.

Preliminary XANES/EXAFS measurements to determine the coordination chemistry were completed. A theoretical study of the film formation processes was initiated; the role of nickel oxide, both the native and the oxide formed during film formation, was studied.

Publications and Presentations

M.A. Lilga, R.J. Orth, J.P.H. Sukamto, S.M. Haight, and D.T. Schwartz. "Metal ion separations using electrically switched ion exchange." *Separation Science and Technology* (submitted).

M.F. Buehler, J.P.H. Sukamto, M.A. Lilga, W.E. Lawrence, and J.E. Surma. 1996. "Separation of Cs from Hanford waste using potential modulated ion exchange." 1996 AIChE Spring Meeting in New Orleans, February 25-29.

J.P.H. Sukamto, S.D. Rassat, R.J. Orth, M.A. Lilga, W.E. Lawrence, J.E. Surma, and R.T. Hallen. 1996. "Separations using electroactive materials for DOE tank waste applications." 189th Meeting of The Electrochemical Society, Los Angeles, California, May 5-10.

Electroconversion

Wesley E. Lawrence (Process Technology)

Project Description

The objective of this project was to develop a safe electrochemical-based nonthermal alternative to open burning for the conversion of hazardous energetic waste materials, such as high explosives, to innocuous species or into useful products. Process development included examination of the process chemistry and an evaluation of the process performance through testing with high explosive materials.

Technical Accomplishments

Within the Department of Energy, thousands of nuclear weapons will be dismantled generating a large volume of explosive wastes. Similarly, within the Department of Defense, weapons demilitarization is anticipated to generate over 180 million pounds of energetic material in the next decade. This demilitarization of U.S. weapons has created a need for treatment technologies that are clean, safe, and efficient as traditional methods of disposal are not considered desirable. Traditional methods of energetic material destruction include incineration or open burning/open detonation. For example, the DOE Pantex plant in Amarillo, Texas, processes about 100,000 pounds of high explosives annually by outdoor burning. This method of treatment releases significant amounts of toxic chemicals into the environment and requires extensive handling of high explosives by personnel. Therefore, alternative high explosive destruction technologies are receiving increased interest. Electrochemical conversion is being evaluated to address these treatment needs as it offers unique advantages over incineration and other conventional thermal and high-pressure processes. Electrochemical treatment processes are conducted near ambient temperatures and pressures. This reduces maintenance, improves reliability, and reduces costs, because exotic materials and special process equipment are not required to address high-temperature and high-pressure corrosion and safety concerns. Electrochemical treatment is inherently clean, because only electrons are added to the process, which minimizes the generation of secondary waste. In addition, electrochemical processes are intrinsically modular. This contributes to scalability and minimal process downtime, electrochemical cells can be easily connected and disconnected from a process train to be repaired or replaced. Systems may be either skid- or truck-mounted for transport to the treatment site.

An evaluation of the electrochemical conversion of high explosive material was conducted. Electrochemical reduction testing was undertaken to demonstrate the desensitization and/or destruction of high explosives. Direct electrochemical reductive destruction of a high explosives; specifically, cyclotetramethlyene tetranitramine (HMX), was demonstrated in both water and water/cosolvent systems. Dimethyl sulfoxide (DMSO) was evaluated as the primary cosolvent because of excellent solvating properties, ability to swell the viton binder in plastic-bonded high explosive material, and excellent oxidative and reductive stability. DMSO is also used at Pantex for high explosive recovery. The reduction of HMX in water and cosolvent systems is shown in Figure 1. The rate of destruction obtained was 31 μg/C for the pure water at -2.0 V (SCE) with the rate decreasing to approximately 21 μg/C for cosolvent concentrations >25% by volume. At 100% concentration of the cosolvent, the high explosive is strongly solvated and difficult to reduce. However, at lower cosolvent concentrations, the electrochemical reduction of the high explosive was observed to proceed at intermediate rates, while providing for a higher high explosive solubility in solution than in water alone.

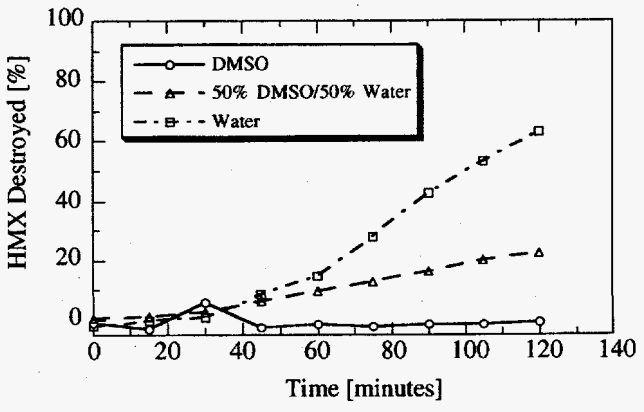

Figure 1. HMX destruction for H-cell electrolysis in water and co-solvent solutions. Applied potential was -2,0 V (SCE) with platinum working and counter electrodes. Cell separator was Nafion 450.

The stability of the cosolvent was investigated under both oxidative and reductive conditions. Under reductive potentials up to -2.0 V (SCE), the DMSO did not degrade. Under oxidative conditions, the DMSO showed stability in acid solutions. These results indicate that DMSO is stable under practical process operating conditions.

Liquid chromatography, ion chromatography, and mass spectrophotometry were used to provide a cursory identification of the primary high explosive materials and reduction intermediates. The secondary N-nitramines in acid solution such as HMX are expected to undergo a six-electron reduction to the corresponding unsymmetric hydrazine where in neutral and alkaline solution the nitroso derivative is formed. Other investigators have demonstrated the reduction of N-nitrosamines to their corresponding hydrazines, where lower yields of the hydrazine were obtained for aromatic compounds under low pH as their tendency for hydrolysis or rearrangement is greater than the aliphatic substrates. HMX is believed to undergo similar reactions as the reduction of nitro groups forms a cyclic ring with unsymmetric hydrazine groups. In acidic solution, an HMX nitro group would be reduced through a six-electron reaction. Therefore, complete reduction of the nitro groups for HMX would require 24 electron equivalents provided the ring does not undergo cleavage. Full decomposition of the high explosive requires cleavage of the ring resulting in the formation of several intermediate compounds. The explosive potential of these intermediates, the reduced HMX compound, is significantly decreased. Liquid chromatography results for the electrochemically reduced high explosive indicates that the heterocyclic ring is cleaved and several intermediates at low concentration are being produced. The ring cleavage creates difficulties for synthesis or recovery of intermediates; however, the primary objective to desensitize the high explosive material is achieved.

Destruction testing was conducted with HMX in both a batch cell and recirculating flow cell. Destruction rates up to 17 μg/C were obtained. Solvents including DMSO and methanol were evaluated as well as electrolytes such as sulfuric acid and ammonium acetate. For the electrochemical process, >99% destruction extents for HMX were observed (Figure 2). Increasing the high explosive material concentration and optimization of solvents and electrolyte are expected to increase destruction rates.

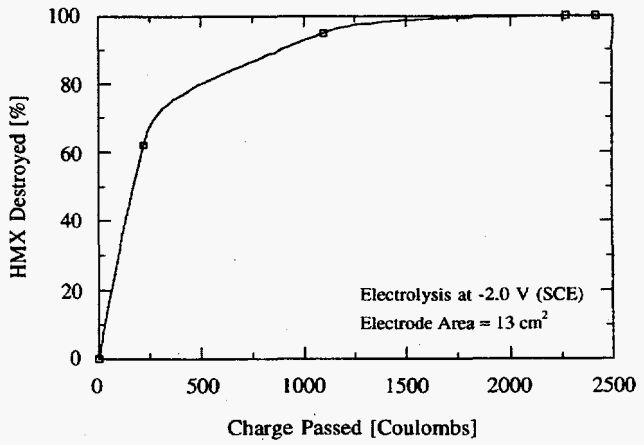

Figure 2. HMX destruction as a function of the charge passed. Platinum working and counter electrodes. Nafion 450 separator. Electrolyte 0.1 N sulfuric acid.

A preconceptual process flowsheet was developed to address concerns associated with traditional methods of treating high explosives by taking advantage of the benefits offered by electrochemical processes. The preconceptual flowsheet takes into consideration issues of reducing personnel exposure through reduction in handling, emissions of toxic gases, and the generation of secondary waste streams. The preconceptual process is envisioned to consist of a solubility controlled dissolution of high explosives to minimize handling of the material. The desensitized stream would be treated through a direct or indirect reduction. This approach would generate minimal secondary waste as compared to other technologies such as base hydrolysis. The binder material would be filtered or oxidized to carbon dioxide and water. The thermal and chemical stability of the cosolvent enables it to be returned for use in the dissolution process.

Under the conditions evaluated, synthesis or recovery of intermediates would be difficult as several intermediates at low concentration are formed during the reduction. However, these results show that electrochemical reduction is a viable approach for high explosive desensitization and destruction. This approach not only has applicability to HMX, but also to other nitrated organics such as RDX.

Formation of a Contaminant Barrier by Injecting Metallic Sulphate Colloids

Kirk J. Cantrell, Daniel I. Kaplan, James E. Amonette, John S. Fruchter (Water and Land Resources Management)

Project Description

One of the new technologies being developed at PNNL for the in situ remediation of aquifers contaminated with oxidized compounds (such as chlorinated solvents and chromate) involves the creation of, and subsequent contact of groundwater with, a permeable reduced zone in the aquifer sediments. Two approaches using different forms of reduced iron (Fe) have been proposed to create the reduced zone.

The first approach relies on the injection of colloidal-sized zero-valent-Fe [Fe(0)] particles into subsurface sediments. As this Fe(0) is oxidized to Fe(II) and eventually to Fe(III) oxyhydroxides by groundwater, it is available to react with oxidized contaminants. Although the use of Fe(0) for this purpose is relatively well known, PNNL's approach involving colloidal particles is novel and extends application of the technique to greater depths than possible with the trench-and-fill approach required for emplacement of Fe filings.

The second approach involves reduction of the Fe(III) already present in sediment clay minerals to Fe(II) by reaction with a soluble reductant such as hydrosulfite ($S_2O_4^{2-}$, also known as dithionite). The excess reductant and reaction byproducts are withdrawn through the same well used for injection leaving the Fe(II) in the clay minerals to react with groundwater constituents (oxygen and contaminants). This approach is novel in that native minerals are used to perform the actual remediation (although pre-reduced clays can also be injected in sediments lacking suitable Fe-bearing clays) and formation of Fe(III)-oxide precipitates during oxidation is avoided.

Although the utility of Fe(0) for reduction of chlorinated solvents has been shown in the literature, the rate constants given vary widely. And, aside from one preliminary experiment with CCl_4, essentially nothing was known about the efficacy of Fe(II)-clay for remediation of chlorinated solvents. Thus, in addition to determining the feasibility of reductive dechlorination by Fe(0)-colloids and Fe(II)-clay, the objective of this project was to compare the relative rates of dechlorination by these two reductants. The scope involved batch kinetic studies conducted in collaboration with the Environmental Sciences Department at Heritage College in Toppenish, Washington.

The purpose of this research was to further develop permeable reactive barriers composed of reductants that destroy or remove contaminants from solution. Reducible contaminants are especially mobile because of their propensity to evade adsorption by most geological materials. They include halogenated-hydrocarbon compounds (e.g., trichloroethylene, tetrachloroethylene, and carbon tetrachloride), and a number of oxidized metals and radionuclides (e.g., CrO_4^{2-}, MoO_4^{2-}, TcO_4^-, UO_2^{2+}, and NpO_2^+). The first goal of this project was to increase the utility of the dithionite in situ redox barrier to include remediation of TCE contaminated groundwater. The second goal was to further develop an alternative method of forming an in situ redox barrier by injecting a suspension of zero-valent (metallic) iron colloids into the flow path of a contaminant plume.

Unlike other in situ contaminant-mitigating barriers in which large volumes of geological material must be excavated to form a trench, these technologies only require that a series of temporary injection and extraction wells be installed. An alternative installation method would use directional drilling to install the barrier. These approaches can greatly reduce the cost of barrier emplacement and greatly extends the depth to which this technology can be used.

Technical Accomplishments

A series of batch experiments were conducted using samples of carbonyl-Fe colloids (1 to 2 μm) and of bentonite clay containing about 6 wt% Fe. The Fe(0) colloids were exposed to oxygenated water for 8 days before use to help remove the protective organic coatings added at manufacture to prevent oxidation. The bentonite, in turn, was treated with dithionite to reduce the structural Fe, washed to remove the excess reductant and byproducts, and stored in an anoxic chamber before use. Three Fe treatments, each containing 3.6 mmol of reductive capacity as Fe(0)-colloids, Fe(II)-clay, or a 50:50 mixture of both [i.e., 1.8 mmols each of Fe(0) and Fe(II)], were prepared in 20-mL headspace vials in the

anoxic chamber. A synthetic groundwater and enough trichloroethylene or CCl_4 to yield a final concentration of about 3 $\mu g\ mL^{-1}$ in 16 mL were added to these vials and then they were sealed, removed from the chamber, and incubated with gentle shaking at room temperature. Controls containing contaminant and no reductant, or reductant with no contaminant, were also prepared. After suitable periods (up to 6 weeks), the gas in the headspace of the vials was sampled and the concentration of trichloroethylene, CCl_4, $CHCl_3$, and other possible volatile degradation products was determined by gas chromatography using a flame-ionization detector.

After an initial rapid decrease in trichloroethylene concentration with the Fe(0) and the Fe(II)-clay treatments (Figure 1), slow pseudo-first-order degradation rates were seen with half-lives of 34 days [Fe(0)] and 17 days [Fe(II)]. Although the Fe(II)-clay was about twice as effective as the Fe(0), both treatments were slow. The mixture of the two Fe reductants, however, proved to be synergetic, yielding a pseudo-first-order half-life of only 53 hours and complete degradation of the trichloroethylene in 2 weeks.

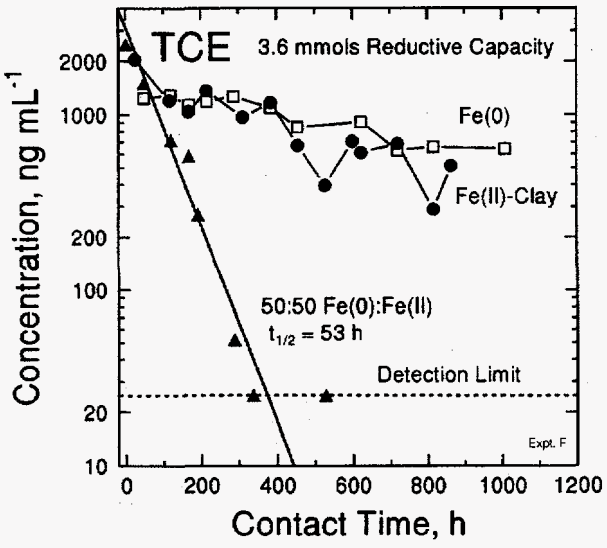

Figure 1. Rates of TCE degradation at room temperature by equivalent amounts of Fe(II)-clay, Fe(0) colloids, and a 50:50 mixture of the two.

With the Fe(II)-clay treatment, the only volatile degradation product(s) observed was an increase in the "air spike" at the beginning of the chromatogram (not shown), suggesting the possible formation of highly volatile compounds such as ethane, ethene, or chloracetylene during the reduction. For the Fe(0) and mixed Fe(0)/Fe(II)-clay treatments, the same air-spike increase was seen along with several minor unidentified peaks. Thus, the Fe(0) process involved pathways yielding a variety of volatile and less-volatile products.

A similar pattern in relative degradation rates was seen with CCl_4 (Figure 2, top). The Fe(0) yielded the slowest degradation rate (83-hour half-life), the Fe(II)-clay was roughly an order-of-magnitude faster (8.5-hour half-life), and the 50:50 mixture yielded the fastest degradation rate (3-hour half-life) after an initial delay of about 8 hours. These rates, however, were independent of reactant concentration (i.e., zero-order rather than pseudo-first-order), suggesting that a catalytic process with a limited number of continually saturated reaction sites was involved.

Chloroform ($CHCl_3$) was seen as the primary volatile degradation product in the treatments involving Fe(II)-clay (Figure 2, bottom). In addition to degrading the CCl_4 more rapidly, the mixed Fe(0)/Fe(II)-clay treatment also yielded more $CHCl_3$, which in turn degraded at a very slow rate (~250-hour half-life). The degradation rate for $CHCl_3$ in contact with Fe(II)-clay could not be determined. With either reductant, however, the

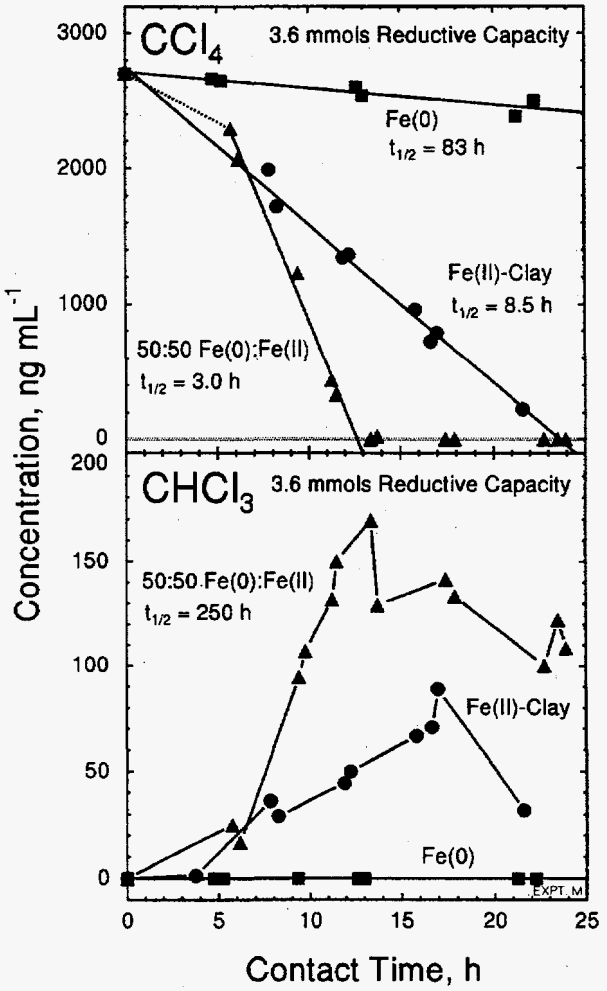

Figure 2. Rates of CCl_4 degradation (top), and $CHCl_3$ production and degradation (bottom) at room temperature by equivalent amounts of Fe(II)-clay, Fe(0) colloids, and a 50:50 mixture of the two.

maximum amount of $CHCl_3$ produced amounted to <7% of the CCl_4 that degraded, suggesting that most of the degradation products were nonvolatile. One degradation mechanism consistent with this result would be a free-radical mediated polymerization process. Verification of this mechanism, however, requires further study of the particle surfaces.

We surmise that the strong synergetic effect of combining the Fe(0)-colloid and Fe(II)-clay reductants likely results from the ability of the clay to promote corrosion of the Fe(0) surface. In practical terms, injection of Fe(0) colloids into the subsurface should yield a similar effect due to interactions with the clay minerals present. At this point, it is not clear whether the type of clay mineral or its Fe content have a bearing on the degree of synergism.

In summary, both approaches involving Fe were effective in degrading trichloroethylene and CCl_4, albeit with half-lives on the order of days or weeks. A mixture of Fe(0)-colloids and Fe(II)-clay, however, proved synergetic and yielded rates of degradation with half-lives of 53 hours for trichloroethylene and 3 hours for CCl_4. The volatile products of trichloroethylene degradation seemed to differ for the two reductants, but a sequential dechlorination mechanism yielding $CHCl_3$ as the only volatile product was observed for CCl_4 with both reductants. Although less $CHCl_3$ was produced by the Fe(II)-clay than by the Fe(0)-colloids, the majority of the CCl_4 degradation products were not volatile.

The major technical accomplishment achieved during FY 1996 for these tasks was demonstrating that shear-thinning fluids greatly enhance the injectability of zero-valent iron colloids in porous media.

This work also determined that the use of shear-thinning fluids greatly improves the emplacement profile of suspensions of micron size Fe^0 particles in porous media relative to suspensions without shear-thinning fluids. Use of these fluids will also permit the use of much lower flow rates than would be possible without them. Lower injection rates are desirable because it will decrease the number of injection wells required to emplace the barrier, thereby decreasing the installation cost of the barrier. This will greatly increase the range of subsurface environments where this emplacement technology can be used. It was also found that vinyl polymer was superior to gum xanthan and carbo-xymethyl cellulose because the vinyl polymer suspensions created the lowest backpressure, resulting in the highest hydraulic conductivity. The results of this work also indicate that additional data collected from column experiments at various suspension concentrations would allow the development of a simple empirical model for predicting the emplacement of the Fe^0 colloids as a function of suspension flow rate, concentration, and total throughput.

Publications and Presentation

K.J. Cantrell, and D.I. Kaplan. "Injection of colloidal Fe^0 particles in sand columns with shear-thinning fluids." *J. Environ. Eng.* (in press).

K.J. Cantrell, and D.I. Kaplan. "Zero-valent iron colloid emplacement in sand columns." *J. Environ. Eng.* (in press).

D.I. Kaplan, K.J. Cantrell, T.W. Wietsma, and M.A. Potter. "Formation of a chemical barrier with zero-valent iron colloids for groundwater remediation." *J. Environ. Qual.* (in press).

J.E. Amonette, E.J. Camacho, and H.R. Divanfard. 1996. "Reduction of chlorinated hydrocarbons by Fe(II)-bearing smectite." Abstracts with Program, The Clay Minerals Society, 33rd Annual Meeting, Gatlinburg, Tennessee, June 15-20, p. 20.

Gas-Phase Corona Scaleup

William O. Heath (Process Technology)

Project Description

The gas-phase corona reactor (GPCR) technology is being developed as an alternative to thermal treatment for removing pollutants from gas streams (Heath et al. 1994). The technique uses gaseous electrical discharges (corona) to form a nonthermal plasma capable of initiating chemical reactions. Nonthermal plasmas typically operate at 30°C to 100°C but produce energetic electrons that create radicals and other reactive species normally associated with high-temperature (>500°C) reactions. The primary benefits are the potential for low energy requirement and low cost.

The typical GPCR device (Figure 1) is a coaxial cylinder with an inner metal electrode, an outer tube made of quartz, and dielectric pellets filling the annular gap. A screen in contact with the outside surface of the tube serves as the ground electrode. The inner electrode is connected to a high-voltage (20 to 30 kV) ac power supply operated at 60 Hz. The quartz tube serves as the reaction vessel and as a dielectric barrier to inhibit direct charge transfer between electrodes.

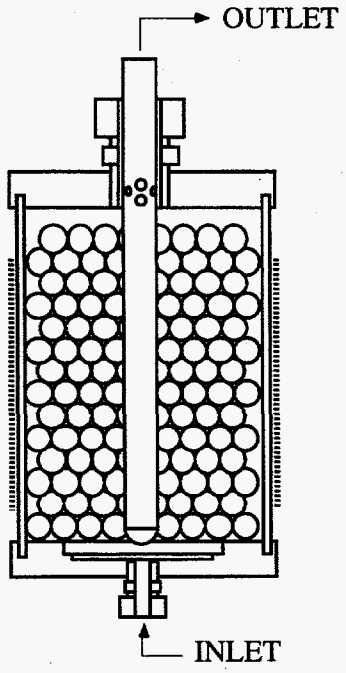

Figure 1. Schematic of gas-phase corona reactor.

A key issue for producing large-scale GPCR devices is the ability to couple electrical power to the gas stream flowing through the reactor so as to create a suitable plasma. Strong electric fields must be established throughout the reactor, and the ability to create these fields depends in a complex way on the dimensions and size of the reactor. The scaling parameter that encompasses these unknowns is the electrical impedance, which varies with voltage geometry, and time. In turn, the throughput capacity of the reactor depends on the power density of the plasma. The objective of this project was to investigate the ability to control power coupling in GPCR devices by altering either the power frequency or the electrical impedance characteristics of the power system.

Technical Accomplishments

Equations for predicting the impedance of coaxial GPCR devices were developed based on the equivalent electrical circuit for a GPCR device shown in Figure 2.

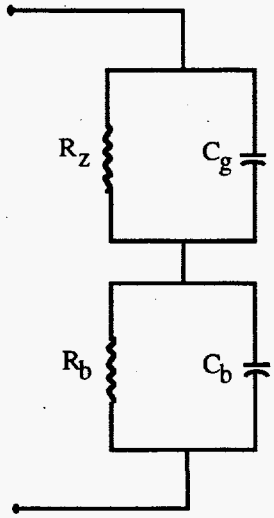

Figure 2. Equivalent circuit for reactor.

In the equivalent circuit, the reactor bed is considered to consist of a nonlinear resistance, representing the ionized gas (plasma) in parallel with capacitance, representing the packing material and non-ionized gas. The bed is in

series with the dielectric barrier, represented as a capacitance in parallel with a resistance.

The resistance of the ionized gas is estimated by solving the poisson equation for the electric field distribution in a coaxial cylinder geometry:

$$\frac{1}{r}\frac{\partial(Xr)}{\partial r} = \frac{4\pi\rho_i}{\kappa_g}$$

In selecting this equation, the assumption is made that sufficient charge density is created in the discharge so as to influence the field distribution. The analytical solution to the poisson equation was then used to calculate the following expression for R_z, which depends nonlinearly on the overvoltage within the reactor, defined as $V_r - V_s$.

$$R_z = \frac{r_b^2}{8\pi L_R\left(\frac{\mu_+\mu_e}{\mu_+ + \mu_e}\right)\xi_f\varepsilon_v\kappa_o\kappa_g\left(|V_r| - V_s\right)}\ln\left(\frac{r_b}{r_a}\right)$$

When the absolute value of V_r falls below V_s, the discharge ceases, R_z becomes infinite, and the bed impedance is dominated by the capacitive term, C_g:

$$C_g = \frac{2\pi L_R(\kappa_b - \kappa_g)\kappa_0}{(1-\varepsilon_v)\ln\left(\frac{r_b}{r_a}\right)}$$

The terms ξ_f and ε_v in the above expressions model the presence of the dielectric packing within the reactor. Expressions for the capacitance C_b and resistance, R_b, of the dielectric barrier are calculated as:

$$C_b = \frac{2\pi L_R\kappa_b\kappa_o}{\ln\left(\frac{r_c}{r_b}\right)}$$

$$R_b = \frac{\rho_b}{\pi L_R}\ln\left(\frac{r_c}{r_b}\right)$$

Using these expressions to approximate the nonlinear impedance, Z_r, of a GPCR device, the voltage at the interior of the dielectric barrier is expressed as

$$V_r = E_s\left(1 - \frac{Z_b}{Z_r}\right)$$

which can be solved via iterative calculations in the frequency domain. The current, I_r, flowing through the equivalent circuit is then determined by the expression

$$I_r = \frac{E_s}{Z_r}$$

which can be plotted in the time domain. Figure 3 plots calculated values of the voltage on the inside of the dielectric barrier (V_r) and the external current (I_r) versus time over one half cycle (180°C) given a typical applied voltage (E_s) at a frequency of 60 Hz and assuming a 2.5-cm reactor with a ground-screen length of 8 cm operated with argon.

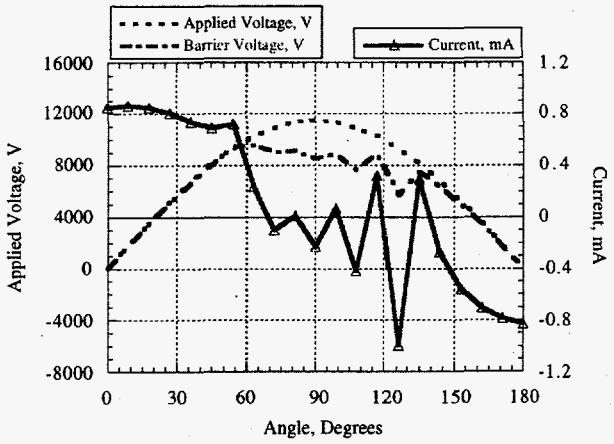

Figure 3. Calculated values of current and voltage over one-half cycle.

The impedance (current and phase) characteristics of a corona reactor were measured as a function of frequency from 60 Hz to 4680 Hz using a 2.5-cm reactor with a ground-screen length of 8 cm. Figure 4 plots the results in terms of the reactor admittance (one over impedance) versus frequency. The reactor admittance, Y_r, was determined from experimentally measured values of reactor power as:

$$Y_r = \frac{P_r}{E_s^2,\text{rms}}$$

As shown, the admittance increased linearly with frequency to roughly 3240 Hz, where a maximum is reached. This suggests that an ionic resonance is achieved where the average time required for ions to drift across the bed region approaches the time period of a half cycle, equal to 0.3 ms at 3240 Hz. An estimate of the frequency for ionic resonance is given by:

$$2f_r \approx \left(\frac{\mu_+ \mu_e}{\mu_+ + \mu_e} \right) \frac{V_{r,rms}}{r_b^2}$$

which equals 3850 Hz under the experimental conditions (26.6°C, 730 torr) and using an rms value of 5.79 kV from the calculated values plotted earlier in Figure 3. Beyond the resonant frequency, the decline in admittance would be expected because of ion drift limitations and from an increase in impedance caused by dielectric heating at higher frequencies.

Table 1 compares calculated values (Figure 3) with measured values (Figure 4) at 60 Hz for power, current, voltage, phase angle and overall impedance as well as barrier capacitance and bed capacitance determined experimentally using Lissajois plots (Manley 1944).

Table 1. Comparison of Calculated and Predicted Values

Parameters	Calculated	Measured
Power, W	1.33	1.36
Current, mA	0.58	0.63
Phase Angle, Degrees	73.7	74.5
Barrier Capacitance, pF	203	217
Bed Capacitance, pF	13.2	26.2
Impedance, MΩ	49.8	48.7
Resonant Frequency, Hz	3850	3240

As shown, the calculated values were found to very closely match measured values. A similarly close match between predicted and calculated values was found from additional data obtained with a much large reactor operated with dry air.

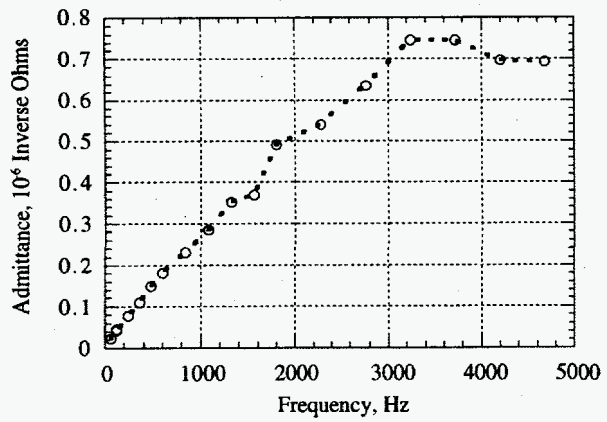

Figure 4. Reactor admittance versus frequency.

The production of nitrous oxide in gaseous discharges is well known, and has been used as a means of estimating the power absorbed in a gas (Helfritch 1993). Figure 5 presents data on the formation of nitrous oxide. The dotted line corresponds to a theoretical yield 250 eV/molecule, equivalent 0.928 ppm per J/L.

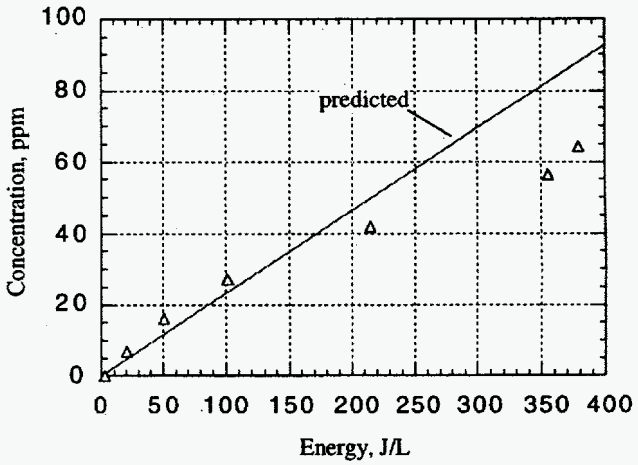

Figure 5. Production of nitrous oxide.

As shown, the levels of nitrous oxide were slightly less than what would be predicted, suggesting perhaps one fifth of the power delivered to a GPCR is lost via conductive heating rather than absorbed by the gas.

Conclusions and Recommendations

Equations for predicting the current-voltage behavior of GPCR devices were found to compare well with experimental data, and can be used to optimize the design of coaxial GPCR devices. However, further development will be required to predict initiation voltages, particularly as a function of operating frequency.

References

W. O. Heath, S. Barlow, T.M. Bergsman, D.E. Lessor, T. Orlando, A. Peurrung, and R.R. Shah. 1994. "Development and analysis of high-energy corona process for air purification." PNL-SA-24432 S. Proceedings of the Third International Conference on Advanced Oxidation Technologies for Water and Air Remediation, London, Ontario, June 25-30.

D. J. Helfritch. 1993. "SO_2 and NO_x removal from flue gas by means of lime spray dryer followed by electron beam irradiation." *Nonthermal Plasma Techniques for Pollution Control*. Springer Verlag, Heidelberg.

T. C. Manley. 1944. *The Electrical Characteristics of the Ozonator Discharge*. Trans. Electrochemical Soc., Vol. 84, pp. 83-96.

Hydrogen-Free Processing of Metallic Sodium Mixed Waste

Glenn W. Hollenberg (Process Technology)
David L. Baldwin (Atmospheric Chemistry and Spent Fuel)

Project Description

The objective of this project was to study alternate novel processing routes for mitigation of reactor sodium, with its known "reactive metal" hazard classification. The development of a hydrogen-free process, with resulting nonhazardous or less-hazardous disposal form, would eliminate safety and disposal issues normally resulting from the conventional reaction of sodium with water. The metal oxide mitigation of sodium process was developed to meet this need. Seven candidate metal oxide materials were selected based on thermodynamic considerations and experimentally tested. Two common metal oxides were predicted and found to have adequate reaction rates, for complete reaction, but not be overly exothermic. Small-scale scoping studies led to larger demonstrations (up to 35 g Na) of the final two feed materials, as confidence in process control grew. The result of this research provides a simple nonhydrogen generating process for safe disposal of radioactive alkali metal mixed waste, and for a simplified decontamination and decommissioning approach for sodium-cooled reactors such as those located on DOE sites and in France, Russia, and Japan.

Technical Accomplishments

Sodium was used as a coolant in numerous sodium-cooled reactors such as FERMI, EBR-II, and FFTF. Coolant sodium, contaminated with radioactive constituents or activated itself, represents a mixed waste because of the "reactive metal" hazard classification for metallic sodium. Nearly 500,000 gallons of low-level radioactive sodium exists in the DOE complex, including the FFTF and EBR-II coolant loops. In addition, small quantities of highly contaminated sodium resides in certain shielded hot cells.

A facility capable of treating nonradioactive sodium exists at the INEL, which uses the well-established process of reacting sodium with water or caustic to form a sodium hydroxide product. Large quantities of hydrogen are exhausted from this facility during operation. A planned modification to the INEL facility, for treating radioactive sodium, was estimated to cost $60 million, however, safety questions remain.

The thermodynamics of the process provides insights into which metal oxides can theoretically react with sodium and at a given exothermic energy level. Some metal oxides were predicted to be extremely exothermic and were experimentally found to be far too vigorous, with temperatures reaching much greater than 1000°C. In contrast, others were predicted to generate no exothermic reaction, and were experimentally found to not react at all, but only become wetted. The intermediate energetic oxides were found, in the scoping tests, to have intermediate characteristics between the two extremes noted above.

In most of these cases, the product after reaction consisted of a slag mixture of the reduced feed material and sodium oxide.

The metal oxide mitigation of sodium process was typically completed in several steps: 1) mixing of the molten sodium and metal oxide, 2) initiation of reaction at a selected temperature, 3) thermal ramp due to the exothermic reaction, and 4) cooldown. Over 45 reaction experiments were conducted with reactor grade sodium in an inert atmosphere glove box. A stainless steel reaction vessel was used to contain the reactants and a hot plate or tube furnace was used to initiate the reaction. The temperature of the reactants was measured by embedded thermocouple. After the reaction was completed, products were characterized by x-ray diffraction, mass balance and residual sodium metal analysis. Presence of residual sodium metal was tested for and indicated by microscopic reaction with water.

For one selected metal oxide, the reaction initiated spontaneously within a minute after mixing at the mixing temperature, with the reaction temperature ramping to exothermic temperature. The reaction products resulted in a dense metallic disk as shown in Figure 1, consisting of a composite of the reduced feed material plus sodium oxide. No trace of sodium metal residue was detected.

For another selected metal oxide, the reaction product was a highly porous, low density, crumbly product. No trace of sodium metal residue was detected.

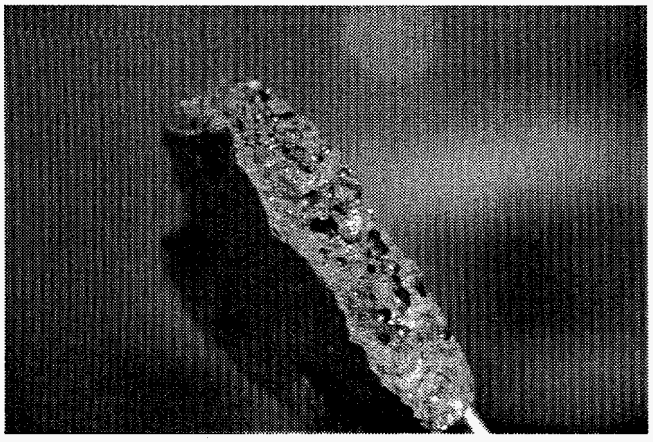

Figure 1. Final disposal product resulting from sodium/metal oxide reaction. "Hockey Puck" product is composed of the reduced feed material plus Na_2O. No trace of Na metal remains.

Interactions with FFTF and EBR-II staff identified some advantages/disadvantages for the approaches. One candidate material provides a dense, rock-like product, but the existence of Na_2O in the product may limit acceptance as a waste form. The second candidate material provides a more controllable initiation process and a completely nonhazardous waste, but the product is powdery or crumbly in comparison to the more dense product.

Conclusions

There are several conclusions which can be drawn based on experience with sodium technology:

1. A successful, novel method, not previously described in the literature, has been developed with the nonhydrogen-generating metal oxide mitigation of sodium method for sodium mitigation.

2. By use of selected metal oxide feed materials, controlled reactions with sodium can be conducted with bounded thermal transients($<900°C$). These reactions form the basis for relatively simple treatment technologies which might be applied either as waste processing or decontamination and decommissioning.

3. Products from the reactions indicated above mitigate the "reactive metal" nature of sodium metal. Depending on local regulations at the time, they may be directly buried or incorporated into a waste form such as low-level waste glass.

4. A batch process for small legacy containers of sodium may directly result from this work; however, additional effort is necessary to develop a continuous process that may be usable for treatment of bulk sodium.

Presentations

G.W. Hollenberg. 1996. "Hydrogen-free processing of sodium metal waste." ANL-W seminar, May 24.

D.L. Baldwin, and G.W. Hollenberg. 1996. "Hydrogen-free processing of sodium metal waste." FFTF presentation, May 16.

Hydrogen Separation Technology Using the CHASP Process

Jagannadha R. Bontha, Dean E. Kurath (Process Technology)

Project Description

The overall objective and scope of the work was to conduct proof-of-principle experiments to establish the separation capabilities of the CHASP process. CHASP is a separation process developed by researchers at PNNL for the separation and concentration of enriched (or heavy) water. The process exploits the differences in the physical properties, i.e., the extent of hydrogen bonding that occurs between normal and enriched water, to achieve the desired separation. Separation is achieved by introducing a third component into the mixtures of normal and enriched water. At appropriate operating conditions, the third component introduces a phase change into the system which is a result of the hydrogen bonding nature of the water species. The partitioning of the enriched and normal water species between the phases created due to their differences in the hydrogen bonding strengths determines the separation capabilities of the CHASP process.

Technical Accomplishments

Funding in FY 1994 was used to build an experimental test unit to establish the differences in the hydrogen bonding strengths of enriched and normal water species and to determine the separation factors.

In FY 1995, initial experiments were conducted using D_2O and the phase change promoter. These experiments helped identify the thermodynamic equilibrium conditions at which a phase change occurs within the system. The thermodynamic equilibrium data when contrasted with the data for normal water, shown in Figure 1, indicated large differences in the conditions at which a phase change can be introduced with D_2O as opposed to H_2O. Using the thermodynamic equilibrium data for D_2O as a basis for the operating conditions, experiments were conducted using mixtures of D_2O and H_2O to determine the achievable separation factors. However, the dissociation of D_2O when mixed with H_2O to form HDO, indicated that the thermodynamic equilibrium data with HDO water should be determined to establish the operating conditions for the process.

In FY 1996, experiments were conducted using HDO and the phase change promoter to identify the thermodynamic equilibrium conditions at which a phase change occurs within the system. These results, also shown in Figure 1, indicate that even with HDO, the conditions at which the

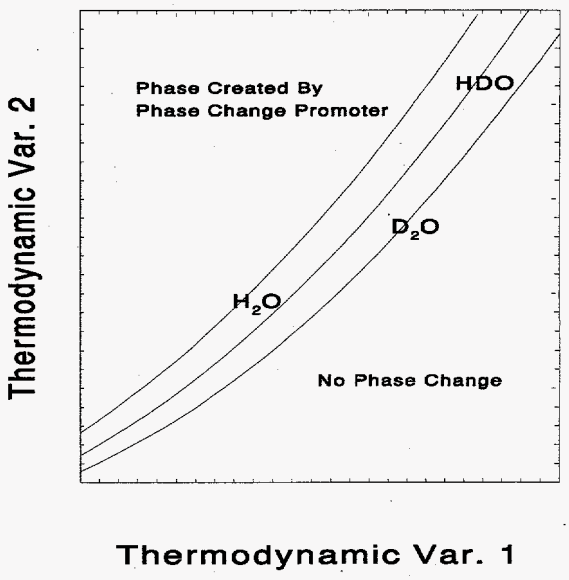

Figure 1. Thermodynamic equilibrium data for H_2O, HDO, and D_2O in the presence of a phase change promoter. For operating region above the curve, there will be the formation of a new phase and for operating region below the curve, no new phase formation occurs.

phase change occurs are much different than those with normal water species. Experiments were then conducted with mixtures of HDO and H_2O at different relative concentration of the individual species and different operating conditions to establish the achievable separation factors. The results are shown in Figure 2 where the separation factor is plotted as a function of the relative concentration of the HDO in the feed solutions at different operating conditions. The results in Figure 2 indicate that, within the experimental errors associated with the separation of the different phases and the analysis of HDO concentration in the two phases, the separation factor was independent of the relative concentration of HDO in the mixture and the operating condition. The separation factor was found to be on average of about 1.3 (i.e., on average about 30% of HDO is concentrated in the new phase created by the phase change promoter). Although the separation factors are relatively lower than the normally preferred range of 5 to 10, we believe that the CHASP process could still be a viable alternative due to the extremely low capital and operating costs associated with the CHASP process as opposed to the more conventional combined electrochemical and catalytic exchange (CECE) process for the recovery of enriched water.

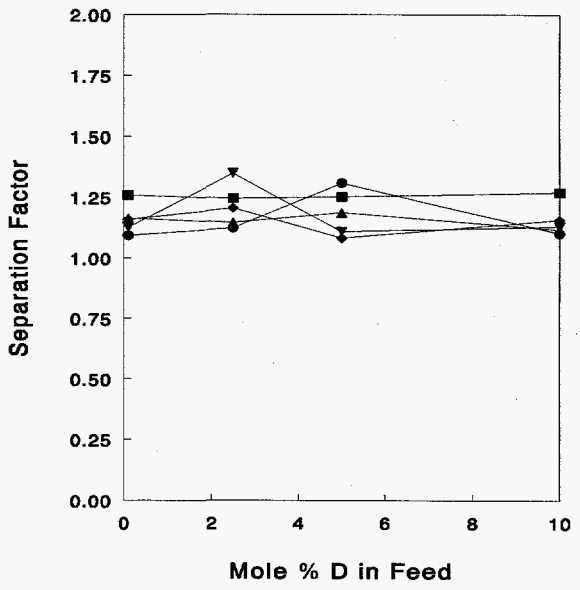

Figure 2. Deuterium separation factors achieved using the CHASP process at different operating conditions.

In Situ Stabilization of Mercury by Apatite

Loni M. Peurrung, Xiandong Feng (Process Technology)
Shas V. Mattigod (Applied Geology and Geochemistry)

Project Description

Treatment of mercury-contaminated soils, groundwater, and other wastes remains a difficult environmental challenge. This project investigated a variety of candidate materials for use as chemical stabilization agents for mercury. Materials studied included phosphate- and sulfur-bearing minerals that are known to precipitate insoluble forms of heavy metals and prevent their migration in the environment. The project included both theoretical investigations of the mercury stabilization agent thermodynamics and experimental investigations of mercury retention and waste form durability.

Background

Materials capable of sequestering and stabilizing heavy metals in contaminated soils and groundwater are receiving increased attention as a method of reducing remediation costs. Mercury is a particularly difficult metal to stabilize due to the variety of chemical forms it can take in the environment. Sulfur-bearing minerals have been investigated by some researchers to precipitate mercury as an insoluble sulfide. However, this process generates hydrogen sulfide gas, must be carefully pH balanced, and additives are necessary to prevent microbial degradation of the stabilized mercury.

Recent work at PNNL and elsewhere has demonstrated that apatite can be used to immobilize hazardous metals in contaminated soils. Apatite, a natural phosphate-bearing mineral, reacts with dissolved metals to form a new mineral matrix that is highly insoluble in water. Apatite has been proven to be effective on a wide range of heavy metals and radionuclides, including lead, zinc, cadmium, strontium, and uranium. However, there have been no investigations of the effectiveness of apatite on mercury. Mercury, like these other heavy metals, tends to be in the +2 valence state in the vadose zone, forming complexes with hydroxide and other anions under normal soil pH and Eh conditions.

Mercury is a recognized toxin and a difficult remediation problem in soils and groundwater. The current remedial approach for these materials is excavation and disposal. If in situ treatment of soils were effective, excavation could be avoided. Moreover, mixing a stabilization agent into previously excavated materials could allow them to be reclassified as nonhazardous waste, substantially decreasing disposal costs. Based on prior work with apatite, treatment is expected to cost roughly $50 per treated ton of soil versus hundreds or thousands of dollars per ton for treatment and disposal alternatives.

Technical Accomplishments

The purpose of this project was to conduct proof-of-principle demonstrations on the effectiveness of candidate stabilization agents on mercury. We selected four materials for evaluation:

- ground phosphate rock (natural, mined apatite, $Ca_5(PO_4)_3OH$)
- monocalcium phosphate [$CaHPO_4$]
- sodium sulfide (used in commercial treatment)
- a Battelle-developed material (SAMMS).

SAMMS is a manufactured material consisting of a substrate coated with a monolayer of functional groups. The potential advantage of SAMMS over simple treatment with mercury sulfide is in SAMMS' nature as a manufactured material.

The first three candidate materials were mixed with soil spiked with mercury. A control sample (no treatment) was also prepared. The soil and its mercury speciation were selected to mimic actual waste at the DOE Oak Ridge site. The SAMMS material was tested on liquid streams, a surrogate Savannah River tank water and a surrogate waste oil. (While actual waste samples would have been preferred, they are radioactive, mixed wastes. Substantial expense would have been involved in obtaining and working with these materials.)

After a two-week incubation period, the soil samples and the mercury-loaded SAMMS material were subjected to a toxicity characteristic leaching procedure (TCLP), the EPA test for establishing effectiveness of stabilization methods. Leachate concentrations for the treated soils were then compared to that from the untreated control. (While it was our original intention to repeat these tests after several incubation periods, funding was substantially reduced in June, preventing further study.)

The results of the TCLP tests are shown in Figure 1. Leaching extracted 8.9% of the mercury from the untreated soil sample. Sodium sulfide treatment was the

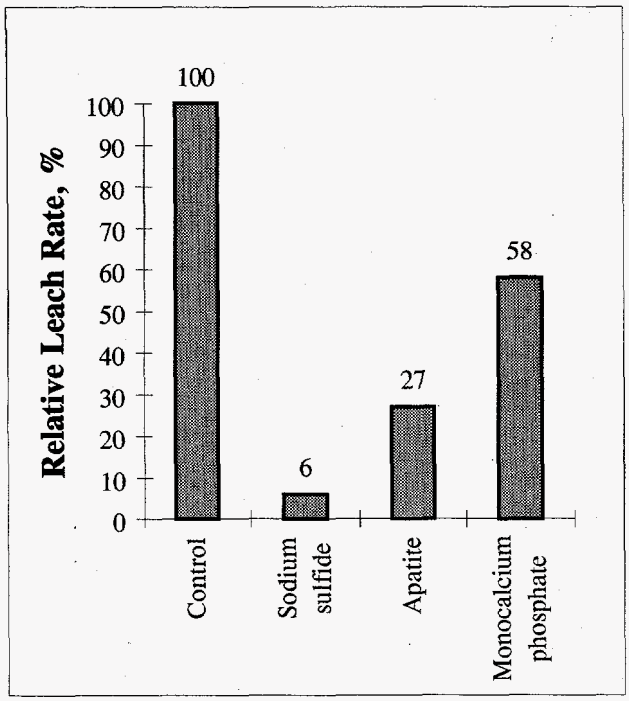

Figure 1. Treatment effectiveness for the three soil additives.

most effective, reducing the leach rate by 94%. Apatite treatment was the next most effective at 73%. Monocalcium phosphate resulted in a leach rate reduction of only 42%. These data represent attenuation observed after only a two week incubation period. It is known that reactions of solid phosphates in soils have slow reaction kinetics. Hence, the results of this short-term incubation may be a poor predictor of long-term reactions that would furthur attenuate the mobility of mercury. The effectiveness of the long-term incubation with phosphates could not be evaluated due to the mid-year budget reductions. Therefore, the results of the short-term incubation tests should be considered only as a proof of principle.

The SAMMS material was not tested as a soil additive due to the mid-year budget reduction. However, SAMMS was used to treat two liquid streams in column studies: a surrogate Savannah River tank waste and pump oil. For the tank waste study, the pH was varied from 3 to 9. The inlet concentration of mercury was 6200 ppb, and a volume of waste equal to 38 times the column volume was treated. For the pump oil, the inlet concentration of mercury was 12,100 ppb, and the waste volume treated was up to 100 column volumes. Each waste stream was passed through the SAMMS column only once.

Treatment by SAMMS reduced the mercury concentration in the surrogate tank waste to less than 1 ppb. Moreover, the SAMMS material subsequently passed a TCLP, leaching 0.2 ppb of mercury or less. The mercury was extracted from solution with an effectiveness equivalent to an adsorption constant, K_d, of about $3x10^5$.

For the pump oil, the outlet mercury concentration was 66 ppb after 20 column volumes (for a K_d of 3600) but rose to 635 ppb after 100 column volumes (for a K_d of 1800). The SAMMS material once again passed a TCLP, with a leachate concentration of only 1.8 ppb. (The limit for disposal of mercury-containing wastes is 200 ppb.)

Conclusions

The conclusions of the work are that apatite and other phosphate-containing materials seem to be only moderately effective as stabilization agents for mercury. However, the SAMMS technology appears to be a promising method for extracting mercury from wastes and forming a stable, TCLP-durable waste form.

Presentations

The work was presented July 16, 1996, in Oak Ridge, Tennessee, at a Battelle-sponsored seminar, "Selected Environmental Technologies." Attendees included federal and contractor representatives from the Oak Ridge Site and others from the surrounding area.

Ionizing Radiation Assisted Processing of Hazardous Wastes

Charles H.F. Peden (Materials and Interfaces)

Project Description

Recent research at PNNL has uncovered the possibility of using common photochemical oxidation catalysts, such as TiO_2, as gamma radiation catalysts for the oxidation of organics, or reduction of metal species present in the Hanford tanks. Ionizing radiation (gamma, beta, alpha) generates electron-hole pairs in inorganic semiconductors which should lead to similar surface mediated redox chemistry as that known for optically excited samples. The most common metal oxide substrate for photoelectrochemical reactions is TiO_2, an environmentally benign material. Initial work has focused on studying gamma catalyzed chemistry on TiO_2. Future efforts will extend this study to include wider bandgap oxides, such as zirconium dioxide which is known to be stable in high radiation fields.

Technical Accomplishments

In the past year, we have performed additional proof-of-principle experiments again using EDTA as a model compound. Destruction of EDTA, a major component of tank wastes, has been accomplished over TiO_2 and ZrO_2 catalysts using gamma irradiation. These have focused on issues related to the dependence of reaction on catalyst composition, solution pH, and the presence of impurities such as Sr. We also performed experiments demonstrating the capability to reductively precipate metal cations from solution.

Engineering Bounding Study

Based on preliminary engineering data obtained in the first (partial) year of funding on this program, we were able to estimate the effectiveness of a potential process that uses this technology.

We envision that treatment of tank waste could be performed in reactors utilizing the existing ^{137}Cs capsules stored at the Hanford Site, although other gamma sources could be used. A reactor could use 20 to 50 ^{137}Cs capsules. Assuming each capsule still contains about 45,000 Ci, we have 1.67×10^{15} disintegrations/second/capsule. A single ^{137}Cs capsule will yield 1.42×10^{15} 0.66 MeV gamma particles per second. This is equivalent to 2.97×10^{20}, 3.2 eV photons/second (where 3.2 eV is the bandgap of TiO_2). Assuming the reactor is constructed such that we absorb 50% of the energy in the reaction volume, and that we have 10% conversion into useful chemical events, we have 1.48×10^{19} reactions/second/capsule or 2.47×10^{-5} mol/s/capsule. This is an effective gamma value of about 1.5, while our initial experimental gamma value has been a factor of 2 to 3 times better. Tank AW106 is 3.8 mM in EDTA and has a volume of 2.6×10^6 liters. Using the lower calculated efficiency, it would take 4450 days to process the supernate of Tank AW106 for a reactor that used a single ^{137}Cs capsule. Therefore, a 20-capsule reactor will process this tank's supernate in 222 days while a 50-capsule reactor will only require 89 days.

Radiocatalysis of EDTA by TiO_2

Studies of the dependence of reaction on catalyst composition, solution pH, and the presence of Sr were continued this year. While these studies are not yet complete, a number of preliminary conclusions can be drawn from the data obtained to date.

The presence of a small amount of Pd in the TiO_2 catalyst formulation appears to enhance the performance of the material by at least a factor of 4. This behavior is commonly observed in TiO_2 photocatalysts because the precious metal serves to promote the separation of charge (electron/hole pairs) of the semiconductor. This is due, in part, to enhanced electron transfer reaction rates on the precious metal relative to pure TiO_2. A continuous supply of air, bubbled through the reaction mixture, led to increased EDTA destruction efficiencies. We believe that this is due to the need to maintain the concentration of dissolved oxygen in the reaction mixture.

Studies of the effect of solution pH, and the presence of Sr on EDTA destruction efficiencies were also continued in this past fiscal year and extended to include reaction in the gamma reactor. Reactivity dropped monotonically with increasing pH by a total factor of about 2 between a pH of 4 and 14. Based on a recently proposed reaction mechanism, this behavior is expected for photocatalytic organic oxidations in aqueous solution. The effect of Sr was also assessed because it is possible that complexation of EDTA might reduce its reactivity. No significant effects of Sr were observed.

The suitability of radiocatalyzed chemical reactions for performing important waste remediation processes has not been assessed. The range of potential redox

reactions will be dependent upon the reducing ability of the excited conduction band electron and the oxidizing ability of the valence band hole. This range will be dictated, for the most part, by the flatband position and the bandgap of the semiconductor. The e-/h+ pair chemistry of wider bandgap materials has not been adequately examined due, in large part, to the fact that atmospheric filtered sunlight does not provide significant intensity of deep ultraviolet (this limitation does not exist with ionizing radiation). Also, photoelectrochemical studies require electrodes which exhibit sufficient electrical conductivity. This criteria is difficult to meet for insulating materials such as ZrO_2 without heavy doping. However, using ionizing radiation there are a much greater range of radiocatalyzed redox processes that can be explored with a wide bandgap material such as ZrO_2. For example, the conduction band of ZrO_2 is higher than that of TiO_2, resulting in greater reduction capability in ZrO_2. The reducing ability of the conduction band electron is very important in accessing redox potentials for reductive deposition of metals from high-level mixed waste. This is schematically illustrated in Figure 1, where the flatband positions of n-doped TiO_2 and ZrO_2 are shown at pH=0 relative to the redox potentials for Cu^{2+} and Ni^{2+} reduction to metal. As suggested by this figure, Cu metal deposition should proceed on TiO_2, but Ni deposition should not. In fact, our preliminary results show that reductive precipitation of Cu metal readily occurs when a Cu^{2+} solution containing a TiO_2 catalyst is exposed to gamma irradiation, but Ni deposition does not occur.

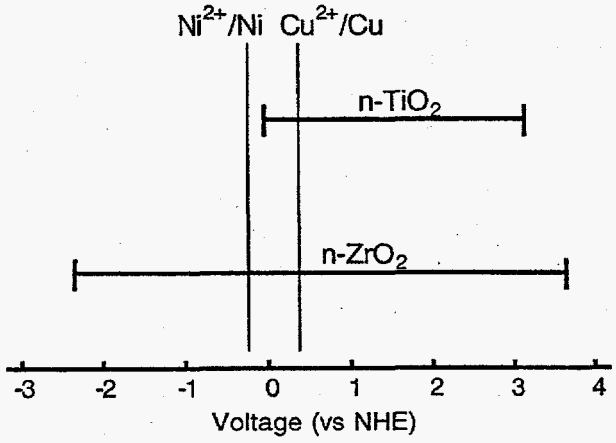

Figure 1. Flatband potentials of n-TiO_2 and ZrO_2 at pH=0. Also plotted are the redox potentials for Cu^{2+} and Ni^{2+} reduction to metal.

Publications and Presentations

J. Janata, J.C. Linehan, W.J. Shaw, C.H.F. Peden, J.L. Daschbach, and A. Heller. 1995. "Gamma ray destruction of EDTA catalyzed by titania." *Interface* 4(3)149.

J.L. Daschbach, J.C. Linehan, W.J. Shaw, M.A. Henderson, C.H.F. Peden, J. Janata, and A. Heller, "Ionizing radiation induced catalysis on titania particles." In *Environmental Applications of Ionizing Radiation*, W.J. Cooper, R. Curry, and K.E. O'Shea, Eds., John Wiley & Sons, New York (in press).

J. Janata, J.C. Linehan, W.J. Shaw, C.H.F. Peden, J.L. Daschbach, and A. Heller. 1995. "Gamma ray destruction of EDTA catalyzed by titania." 188th Electrochemical Society Meeting, Chicago, Illinois, October.

C.H.F. Peden, J.C. Linehan, W.J. Shaw, J. Janata, J.L. Daschbach, and A. Heller. 1995. "Gamma ray destruction of EDTA catalyzed by titania." International Chemical Congress of Pacific Basin Societies, Honolulu, Hawaii, December.

C.H.F. Peden, J.C. Linehan, W.J. Shaw, J. Janata, J.L. Daschbach, and A. Heller. 1996. "Gamma ray destruction of EDTA catalyzed by titania." 11th International Catalysis Conference, Baltimore, Maryland, July.

Kinetics, Scale-up, and Demonstration of Uranium Bioprecipitation Technology

Michael J. Truex, Brent M. Peyton, Nancy Valentine (Bioprocessing)
Yuri A. Gorby (Environmental Microbiology)

Project Description

Previous research at the U.S. Geological Survey and PNNL has identified a biological mechanism to remove heavy metals from aqueous streams (Gorby and Lovley 1992; Gorby and Truex 1993). This technology utilizes bacteria that can use certain metal species as electron acceptors. In the process, a soluble metal is reduced and forms an insoluble compound that can be removed from solution by filtration or precipitation. The process is applicable to remediation of uranium, chromium, cobalt, and potentially other multivalent metal species with the appropriate oxidation/reduction potential and solubility characteristics. Examples of maximum concentrations that can be biologically processed are 50 mM uranium, 10 mM cobalt, and 1 mM chromium.

In order to apply this concept in a flow-through reactor at full-scale, more information was needed regarding the kinetics of both the reduction reaction and the precipitation step. The objective of this project was to obtain the basic kinetic coefficients for the process using a simulated waste. These experiments will provide data for use in defining treatability protocols, process optimization, and conceptual design.

Technical Accomplishments

Uranium reduction was successfully performed using bacteria immobilized in calcium alginate. Experimental data quantified the relative effects of diffusion-driven mass transfer, microbial reduction, and binding to calcium alginate in relation to the rate of uranium uptake from bulk solution for the tested system. The solution pH and carbonate concentration affect binding of uranium to calcium alginate due to changes in the properties of the dominant species complex. This property was used to separate microbial reduction and alginate binding phenomena in different treatments so that rates for the individual processes could be determined.

Results confirm the quick uptake of uranium by alginate that has been observed by other researchers. Inclusion of microbial uranium reduction in an alginate system increases the capacity for uranium uptake but mass transfer limitations of the immobilized cell system prevent significant benefits from the added reaction. From these data, models of suspended cell microbial uranium reduction systems (from previous year LDRD results), alginate-based uranium sorption systems, and systems that combine alginate sorption and microbial reduction were developed and can be used to determine the most appropriate system for application to a specific waste stream.

Publications

M.J. Truex, B.M. Peyton, N.B. Valentine, and Y.A. Gorby. "Uranium reduction kinetics of a dissimilatory Fe(III)-reducing bacterium under non-growth conditions." *Biotechnol. and Bioeng.* (in press).

B.M. Peyton, M.J. Truex, N.B. Valentine, and Y.A. Gorby. "Comparison of metal reduction rates for suspended- and calcium-alginate-immobilized bacteria." (manuscript in preparation).

Liquid Corona Process Development and Novel Electrode Scale-Up

Gary B. Josephson (Process Technology)

Project Description

This project focused on demonstrating proof of principle for three developments to improve the effectiveness and applicability of the process called "liquid corona": 1) improving the efficiency of the process by altering the composition of the gas phase above the liquid, 2) improving the efficiency of the process by adding catalysts to the liquid, and 3) determining whether application of high frequency alternating current power through a dielectric can create a large area volume filling plasma. The third development issue has been identified as critical to scaling up the technology for practical application.

Background

Liquid corona is a term used to describe an electrical process that generates active chemical species and has been shown to effectively destroy some recalcitrant materials of interest to DOE remediations, i.e., perchloroethylene and carbon tetrachloride. The term liquid corona is an easy name for the process, but it is not really accurate. The corona is not actually in the water but in the gas phase and immediately on the liquid surface which serves as an electrode. It should be noted that corona discharge is not merely another configuration of electrolysis where chemical reactions are accomplished by charge transfer oxidation and reduction. Work done by Hickling and Davies (1952) proved that charge transfer is only a minor factor in corona discharge and that the chemical effects are fundamentally different. Most noticeably, many equivalents of chemical reaction can be accomplished for each electron of charge transfer. Each electron accelerating through the electric field collides with many gas molecules creating other charged particles and neutral active species (free radicals and atoms). Depending on the conditions of the discharge, active species accounting for between 8 and 180 reactions have been measured for each electron of charge transferred. These can bring about ionization, excitation, or dissociation of solvent molecules by collision, in addition to charge transfer reactions observed in a typical electrochemical process.

Liquid corona is most similar to radiolysis or electron beam processes and the concepts and ideas developed in radiation chemistry can be directly applied to this type of corona discharge process (Hickling and Linacre 1954). However, there are some noteworthy differences between the two processes. For example, although the energy per electron in liquid corona is relatively low (~ 100 eV) as compared to most ionizing radiation ($\sim 10^4$ to 10^7 eV), the dose rate can be extremely high. As measured by Hickling, for a current of 0.075 A, the number of singly charged gaseous ions reaching the solution surface per minute was 2.8×10^{19}. Assuming an average energy of 100 eV, the dose rate for liquid corona amounts to 2.8×10^{21} eV min^{-1}. This is significantly higher than the dose rate normally used in radiolysis ($\sim 10^{16}$ to 10^{20} eV cc^{-1} min^{-1}). Therefore, the amount of chemical change which can be affected in liquid corona is much greater than that in radiolysis, and high concentrations of substrate can be used. Furthermore, under these conditions, impurities seem to have much less effect (Hickling 1964). Thus, liquid corona is unique and novel because it can bring about chemical changes that are similar to those which result from ionizing radiation however, the energy input is of the order of electrochemical process.

Earlier research into the phenomenon at PNNL indicated that the effectiveness of the process could be enhanced for certain types of materials by changing the gas composition. That research also identified that the point-to-plane plasma possessed characteristics that would make it impossible to scale-up the process by parallel multiplication of the point-to-plane electrodes. Another approach would be necessary.

Technical Accomplishments

This project demonstrated proof of principle to enhance the technology. Based on the results of this project, it was identified that titanium dioxide and iron oxide improved the oxidation of pentachlorophenol. Conditions for application of the technology using catalysts were established. Additionally, it was determined that for materials which are less oxidizable than pentachlorophenol, changing the composition of the

gas phase improved the performance. Gases that improved performance were demonstrated and included hydrogen, argon, helium, and in some cases nitrogen. The conditions for application of the technology using alternative gases were established. Significant development of these two novel enhancements remains to be done.

For the technology to be applied on a large scale, it is necessary to deliver several amps of current to a large area of water surface. Previous work had demonstrated that such a condition would not be possible using many point electrodes. This project demonstrated that a large area plasma could be created using a solid dielectric barrier and high frequency alternating current power. In these tests a plasma of 25 cm^2 was maintained with alternating current power and frequencies of 500 to 5000 Hz. Current densities up to 0.16 mA/cm^2 were demonstrated. The maximum current density was not determined in this project.

Several different configurations of electrode and types of dielectric were tested. These included the following: plate coated with two thicknesses Al_2O_3, plate coated with ZrO_2, rod coated with Al_2O_3, rod coated with ZrO2, plate coated with a proprietary coating from a corona coating supplier, a plate sputter coated with Al_2O_3, a plate enclosed in a quartz dielectric. Other that the sputter-coated electrode, all the coated electrodes were coated by the process known as plasma spray. In the plasma spray process, granules (or powder) of the oxide are aspirated through a flame onto the piece to be coated. The flame melts or softens the particles which then stick on the item and fuse. The results of this type of coating is an accumulation of particles piled on top of each other. The interfaces may be totally or partially fused depending upon the conditions of the flame spaying operation. During this testing none of the electrodes with applied coatings could successfully create a large volume plasma. In every case, only a single column of high intensity plasma would form. The oscilloscope wave forms of these discharges appeared identical to the wave form of a bare metal electrode. It is hypothesized that either each electrode had a pinhole defect (invisible to the eye but big enough for atoms to pass) or the grain boundaries did not have a sufficient dielectric strength to maintain the field. Only the electrode enclosed in quartz successfully maintained a large area plasma.

Conclusions

The performance of the "liquid corona" can be enhanced by changing the conditions of the gas phase and/or adding a catalyst to the aqueous phase. These process modifications are apparently novel.

A large area plasma can be maintained using alternating current and a dielectric barrier on the electrode. The barrier, however, must not have defects or conductive grain boundaries. A homogeneous type barrier such as quartz is known to be a suitable barrier. Other types of glass or glass/ceramic may also be suitable.

References

A.J. Hickling, and R.J. Davies, 1952. *J. Chem. Soc.* 3595-3602.

A.J. Hickling, and J. Linacre. 1954. *J. Chem Soc.* 711-720.

A.J. Hickling. 1964. *J. Electroanalytical Chemistry*, 329-373.

Publication and Presentation

G. Josephson, A. Sharma, D. Camaioni. 1996. "Destruction of organic contaminants using glow discharge plasma." Presented at the ACS Conference, *Emerging Technologies in Hazardous Waste Management*, Birmingham, September 10-12, ACS Symposia Series, Vol. 8.

Liquid Metal Micropump

Donald J. Hammerstrom (Energy Division)
James H. Konynenbelt (Environmental Technology)

Project Description

Microactuators and small chemical diaphragm pumps were designed, fabricated, and tested to demonstrate the feasibility of developing pumps, actuators, or valves appropriate for emerging microchemical processes.

Introduction

Staff had shown in 1995 that the same Lorentz force actuation principles used by large liquid metal pumps hold for channels with diameters less than 1 mm. Obtainable static actuation pressures are directly proportional to pump geometries.

The high pressure, small volume actuator and pump combination may have high value for environmental, military, and biomedical applications. Pressures exceeding 40 kPa were experimentally obtained from a liquid metal microactuator test article the size of four stacked dimes during FY 1996. However, combined actuator and pump performance was not demonstrated.

Technical Accomplishments

A compact, high-pressure liquid metal actuator was designed and tested. The liquid metal actuator has no solid moving components, has high power densities, and has virtually unlimited actuation stroke. The actuator uses the Lorentz force electromagnetic actuation principle, in which electrical current is applied at right angles to a magnet flux imposed by a strong permanent magnet.

Theoretical calculations and computer simulations were performed to corroborate experimental results and resolve design issues. The complete compact device, about 4 mm high, can maintain a static pressure exceeding 40 kPa, and additional devices can be stacked to additively achieve even greater pressures. Each additional device adds less than 0.5 mm to the actuator thickness. Multiple atmosphere pressure actuators are conceivable. The actuator is proposed as a component for chemical pumps, fluidic valves, and a micro-ram.

A computer simulation electrical model was prepared to support observed experimental behaviors and predict the effects of any design modifications. The computer simulation code was configured to easily predict effects of geometry, electrode and liquid metal choice, electrode and channel dimensions, magnet flux, applied current, liquid metal average velocity, and presence or absence of peripheral conducting rings. The simulation code predicts voltage distribution, current density distribution, and total actuation pressure.

A number of methods for fabricating the pump were considered: electrodeposition, chemical etching, and various forms of delicate machining.

The chemical pump component adopted a conventional diaphragm pump approach. The diaphragm of the small chemical pump might be driven by either the liquid metal microactuator or by another actuator like a piezoactuator. Some experimentation was performed to manufacture more flexible diaphragms using etched diaphragm surfaces.

A more novel valveless pump approach was pursued to rectify chemical flow. Researchers manufactured small nozzles that might be tuned to rectify flow when pulsed at moderate to high frequency.

At PNNL, we have designed and fabricated several prototype liquid metal electromagnetic pumps and actuators that could find numerous applications. These prototypes demonstrate high reliability with few solid moving parts, extreme simplicity of design, and relatively high pressure at reasonable efficiency. Our tests indicate that pressures greater than 200 kPa are achievable in stacked spiral devices, with a corresponding efficiency of 5%. These specifications are attractive for applications such as micro-fluidic valves, microcompressors, microactuators to drive pumps for chemical delivery and sensing systems, and related equipment.

Membrane Separations

Richard T. Hallen, Wesley E. Lawrence (Process Technology)

Project Description

Membrane separations has been identified as a key component to the treatment, separation, and recovery of chemical components from complex waste streams, such as at Hanford and from industrial operations associated with the textile, pulp and paper, chemical, and mining industries. Development of membrane separation capabilities will be in the areas of recovery and reuse of both water and chemicals using membrane technologies. Specific areas of research include size and chemical selective membrane separation processing including micro-, ultra-, and nanofiltration, reverse osmosis membranes, and electro-assisted membrane separations (e.g., electrodialysis and electrokinetic).

In this project, efforts were concentrated on the development of lab and bench-scale membrane research capabilities to support resource recovery, pollution prevention, and zero discharge manufacturing. The capabilities were established for aqueous phase membrane processes. These capabilities are available for project specific evaluation of membrane technologies for the separation and recovery of chemicals from wastes. The capabilities are/have been used for testing and evaluating new membranes being development at PNNL, such as inorganic size and ion selective membranes. These membranes have the potential to be more robust, suffering less chemical and radiolytic degradation.

Technical Accomplishments

Membrane separations are very attractive for reducing energy consumption and allowing chemical recovery. Membrane separation technologies have replaced many distillation process because of the reduced energy consumption. The textile and chemical industries are just starting to recognized the great potential for recovery of valuable chemicals used in processing. Many of the industrial processes employed, such as dyeing in the textile industry, are only 70% to 90% efficient with millions of dollars of valuable chemicals going to waste treatment facilities. Membrane separations recover the chemical unchanged for reuse and generate little secondary wastes. Electrodialysis, through water splitting, can be used to recover acids and bases from neutralized process streams which are usually disposed of as salt.

Capabilities were developed to allow the demonstration of membrane separation technologies. Waste streams containing salts and metal ions were processed by membrane separation technologies. Electrodialysis and pressure filtration were the two of the key membrane technologies of interest. Electrodialysis can be used to recover salt or convert salts to the corresponding acid and base. Pressure filtration uses organic or inorganic membranes of varying pore size to perform selective removal of target species. Membranes for reverse osmosis only allow water to pass and can be used to generate drinking quality water. Nanofiltration membranes exclude large molecules usually above molecular weight of 200 and divalent ions but allow monovalent ions such as sodium and chloride to pass. Ultrafiltration membranes exclude high molecular weight compounds or particles from dissolved salts. Microfiltration membranes only exclude solid particles.

The initial efforts were focused on establishing the experimental capabilities to perform membrane separations. Lab and bench-scale systems were assembled or procured. The first research experiments focused on the separation and recovery of metal cations. The selectivity of membranes for separation of sodium and cesium mixtures was determined. The regeneration of neutralized acids and based was also demonstrated for sodium nitrate, the major component of Hanford tank wastes.

The membrane project shifted focused to the separation of inorganic anions. Specifically, the selectivity of membranes for phosphate, nitrate, and borate separations was determined. The experimental results showed that borate, used in nuclear power or chemical industries, could be economically removed from waste water for reuse.

PNNL participated in the NSF Center for Separations Using Thin Films at the University of Colorado as part of this project. The center allows for a broader interaction with university and industries involved with both preparation and implementation of membrane technologies.

Microchannel Separations

Dean E. Kurath (Process Technology)

Project Description

The objective of this project was to design, fabricate, and begin testing of a microchannel solvent extraction system to demonstrate enhanced mass transport and separations through the use of microchannels and microtechnology architectures. Microchemical separations systems offer the potential to enable compact, high throughput separations hardware, providing distributed processing for the treatment of DOE wastes. Miniaturized separations equipment has the potential to reduce costs associated with tank waste disposal and environmental restoration activities where conventional, centralized processing facilities traditionally require multi-billion dollar investments and long lead times (to accommodate both scale-up and design/construction efforts).

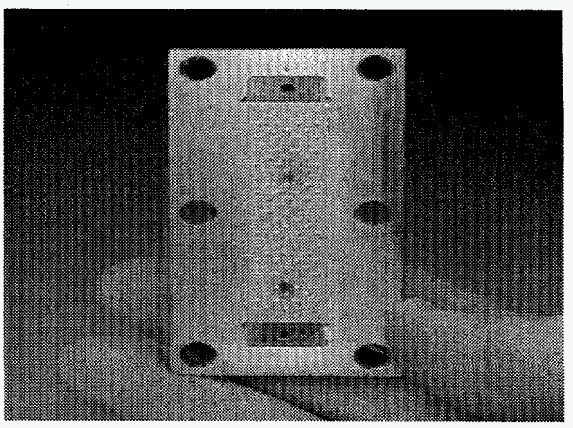

Figure 1. Microchannel solvent extraction test article.

Technical Accomplishments

Solvent extraction involves the contacting and subsequent separation of two immiscible liquids with mass transport occurring across the contact area. Macro solvent extraction hardware generally consists of devices in which mechanical work is performed to mix the two streams and achieve a high contact area. Subsequent separation of the two phases is often achieved by gravity or centrifugal force. High surface area mixtures may be difficult and slow to separate if emulsions are formed. Typically, the time required for mass transfer (assuming sufficient mixing of phases takes place) is relatively short compared to the time required to separate the phases. More generally, mass transport in a solvent extraction system may be maximized by having a high contact area to volume ratio, a small mass transport distance in each phase, and rapid phase separation.

During FY 1996, two separate microchannel solvent extraction designs were considered. One involved a membrane placed between the two phases and the other design did not have a membrane. It was decided to pursue the membrane-based contactor because of the ability of this design to operate in a countercurrent flow configuration. This mode of operation is generally more efficient than co-current flow.

A small microchannel device was fabricated (Figure 1) using electrodischarge machining to etch a microchannel into two plates. The membrane is placed between the two support plates. The two liquids enter opposite ends of the contactor and mass is transferred from one phase to the other. Commercially available membranes have been used to date to develop a baseline performance and to obtain performance data for comparison to commercially available contactors.

The test system currently being used to evaluate the microchannel solvent extraction device involves the extraction of iron from an aqueous feed of 0.2 M $Fe(NO_3)_3$ into HDEHP (di-2-ethylhexyl phosphoric acid) with dodecane as the diluent. This system was chosen for testing because the extraction process can be qualitatively monitored via a color change. Quantitation of the extraction process is achieved using ICP-AES to determine the iron content of the streams.

Preliminary testing and evaluation revealed that the dominant resistance to mass transfer was in the membrane. Since resistance to mass transfer is primarily determined by the diffusion path length through the membrane, microfabrication techniques are being employed to fabricate engineered microstructural membranes. These membranes contain ordered arrays of mesoscale and microscale pores. The ordered pore structure is expected to reduce the diffusion path length relative to the tortuous path normally found in conventional membranes. The diffusion path length will also be reduced by minimizing the thickness of the membrane.

Presentations

R. Wegeng, C. Call, and M. Drost. 1996. "Micro thermal and chemical systems." Presented at GOMAC 96, PNNL SA-27117, Pacific Northwest National Laboratory, Richland, Washington.

R. Wegeng, C. Call, and M. Drost. 1996. "Chemical system miniaturization." Presented in the Process Miniaturization session of AICHE's Spring National Meeting, February.

Microplasma Reactor

Joseph G. Birmingham, Bruce Lerner, Johanes H. Sukamto, Robert S. Wegeng (Process Technology)

Project Description

The objective of this project was to develop and demonstrate a miniature plasma (or ionized gas) reactor that uses micromachining fabrication techniques. The prototype microreactor produced a plasma that was revealed by experimental data and visual observations. The use for the micromachined plasma reactor is expected to be validated with additional testing. It is expected that the synthesis of temperature-sensitive and -reactive compounds and the decomposition of toxic or hazardous gases will be accomplished by a micromachined plasma reactor.

Mass production of microscale components and systems, using fabrication techniques developed for microelectronics, has the potential to make small-scale, distributed chemical processes economically attractive relative to centralized processes normally used today. Microtechnology has matured to the point where initial applications of microsensors are reaching commercialization, and powerful microactuators (that can be used as prime movers for pumps, valves, and other mechanical components) are under development within the U.S. and abroad. The development of the microchannel heat exchanger demonstrated successful operation of high heat fluxes during FY 1995. The design of the microreactor will be similar to a microchannel heat exchanger with two additional masking steps to deposit materials needed for the initiation of the plasma (or ionized gas).

Technical Accomplishments

The feasibility of processing gases and liquids with micromachined electrochemical reactors was the focus of this project. The design and development of two micromachined approaches, micromachined plasma reactor and microelectrochemical cell, was accomplished this year. The micromachined plasma reactor is a low-temperature, atmospheric pressure, packed/catalyst bed reactor that creates a plasma (or ionized gas) to enhance chemical reactions and can be configured with gas separation membranes. In FY 1996, the micromachined plasma reactor surpassed other plasma reactor technologies in the synthesis of ethylene, acetylene, and ethane from a flowing methane gas stream. The micromachined plasma reactor was designed and tested with gas separation membranes to convert methane.

Process gas through a micromachined plasma reactor-membrane system has the following advantages:

- upgrades the Btu content of the gas in the absence of oxidation reactions
- requires less than 10 W of power per CFM
- outperformed larger plasma devices at the same gas flow rate with 1/1000 the reactor volume at 1/4 the applied power.

The micromachined plasma reactor membrane system is unique in that the constant removal of product through the membrane should increase conversions.

Another micromachined device described as a micromachined electrochemical cell was fabricated. Initially, we designed a micromachined platform for electrochemical processing of liquid waste streams. It was postulated but unconfirmed that power consumption and suppression of side reactions would be curtailed due to the proximity of the electrodes in a micromachined electrochemical device. The primary objective was to show that power consumption and side reactions are minimized by minimizing the inter-electrode gap in a microelectrochemical cell.

Micromachined Plasma Reactor Fabrication

The micromachined plasma reactor is a synergistic combination of plasma (or ionized gas) and catalysts technologies. The design of the micromachined plasma reactor involved the deposition of metals by vacuum deposition techniques into ceramic channels. A machinable ceramic MACOR had channels cut with a slitting saw using conventional carbide tools. These microtechnology fabrication techniques were used to deposit 5 microns of aluminum metal and 50 microns of alumina (defect-free dielectric) in the MACOR structure. The overall reactor length was about 4 cm. The swagelock fittings served as both the electrical feed throughs and the conduit for the gas flows. In addition, a membrane imprint was milled into the micromachined plasma reactor to hold a polymeric material in the middle of the plasma as seen in the schematic diagram of Figure 1. Teflon™ tape was used to seal this reactor and worked adequately since the operating temperatures were close to ambient.

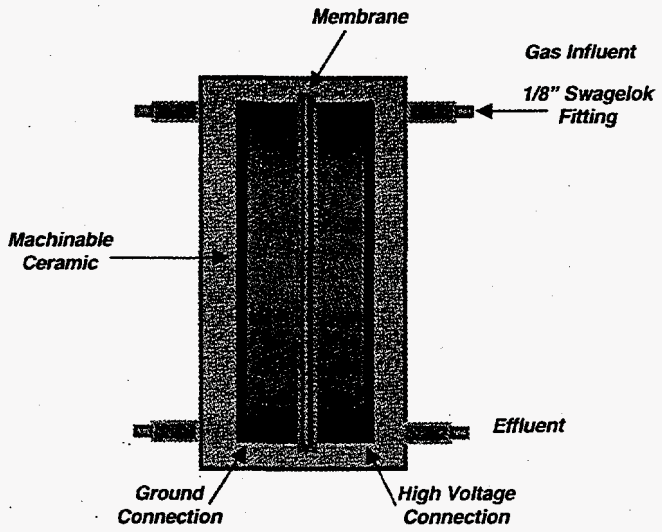

Figure 1. Membrane/plasma microreactor.

Microelectrochemical Cell Reactor Fabrication

Mass (and heat) transport are significantly enhanced within microchannels. For example, the augmentation of heat transfer in a microchannel has been demonstrated at Pacific Northwest.

Many industrial and urban liquid waste streams contain dilute concentrations of contaminants. Since many contaminants can either be reduced or oxidized, it appears that these waste streams should be amenable to electrochemical treatment. In most cases, these waste streams are not very conductive, they have a low ionic strength (or equivalently, a high ohmic resistance). Therefore, any electrochemical process operated at a reasonable current level requires a substantial applied potential, resulting in high operating costs and, possibly, safety/control issues compared to other oxidation/ reduction technologies.

In a typical electrochemical cell, there are at least two electrodes, an anode (where oxidation takes place), and a cathode (where reduction takes place). The applied potential between the anode and cathode is commonly viewed to consist of 1) the surface overpotential at the anode and cathode, and 2) the ohmic drop in the bulk of the solution. For any given applied potential or current, the surface overpotentials are dependent on the composition of the solution as well as the electrode materials since all of these determine the type of electrochemical reaction that will take place. The ohmic potential drop depends on the ionic strength of the solution and the separation distance between the electrodes. Therefore, for a given waste stream the total applied potential can be minimized by 1) choosing the appropriate electrode materials, 2) reducing the separation distance between the two electrodes, and/or 3) adding chemicals to the waste stream to change its composition.

Since the introduction of additional chemicals to waste streams is usually not desirable, this leaves the first and second options. With respect to the first option, much work has been published to the application of various electrode materials tailored for special reactions. To the best of our knowledge, the commercial use of electrochemical cells with inter-electrode gaps in the order of 100 μm has not been discussed in the literature. Reduction of the ohmic drop is advantageous not only from a safety standpoint since a lower applied potential can be used, but also from an economic viewpoint as a result of additional control/stability of the surface overpotentials and uniformity of the current/potential distribution. Differences in surface overpotentials in the order of tens of millivolts are sufficient to cause different reactions to occur, and to control the surface overpotentials to within tens of millivolts becomes more difficult as the applied potential increases to tens or even hundreds of volts.

After fabrication was completed, the electrochemical array was to be tested for at least one of the following applications:

1. removal of RCRA metal (e.g., Pb, Cd)

2. desensitization/detoxification of waste water contaminated with explosives (e.g., HMX, RDX, TNT).

However, insufficient funds were available to test the microelectrochemical cell.

Micromachined Plasma Reactor

Proof-of-principle experiments were conducted on a micromachined plasma reactor and a direct comparison was made with a standard plasma device. To illustrate different characteristics of the plasma created within the micromachined plasma reactor and other plasma device at the same flow rate, argon gas with about 10% methane was sent through the plasma reactors. The amount of conversion of methane was compared directly. The micromachined plasma reactor plasma was initiated a 1 kV and consumed about 10 mA as registered on the oscilloscopes and power display equipment. The total power deposited in the micromachined plasma reactor was measured to be close to 10 W of power in a micromachined plasma reactor space that was 1/1000 the volume of the larger plasma reactor. The high energy density plasma was so intense as to be seen glowing through the ceramic MACOR walls of the micromachined plasma reactor. The following results were found when sending the same argon and methane gas at the same flow rate through the two plasma reactors:

- the micromachined plasma reactor produced on average four times the amount of methane activation products at higher frequencies as the other plasma reactor configuration

- the micromachined plasma reactor had 1/1000 the reactor volume and consumed approximately 1/4 the electrical power.

Although several technical issues need to be resolved, the micromachined plasma reactor testing provided encouraging results in miniaturizing chemical reaction systems to create unique synthesis environments. The lower temperatures also allow the use of membrane materials such as polymers that could not survive at the higher temperatures commonly used in other hydrogen forming techniques. The inclusion of a membrane in the reactor allows for the removal of hydrogen selectively which drives a higher thermodynamic conversion. The result from the inclusion of a membrane mimicked the same trends found for the micromachined plasma reactor.

Nonaqueous Based Processing

Richard T. Hallen, Lawrence E. Bowman, John L. Fulton (Process Technology)

Project Description

The objective of this project was the development of a new processing technology, slashing, which is based upon carbon dioxide carrier/solvent to reduce energy requirements and prevent environmental pollution associated with waste water treatment and disposal.

This work demonstrated the potential use of carbon dioxide for applying and removing size to spun yarns for textile weaving, which required the development of new size materials which are soluble in carbon dioxide. New compounds and mixtures were examined to determine physical properties of the materials for application and processing. Actual yarn samples were treated and the physical properties of the yarns determined. Removal and recycling of the compounds was examined. Potential engineering designs for continuous treatment of fibers, warps, and fabrics at elevated pressure were identified. Specific approaches involve use of roller/seals similar to polymer extrusion processing and semi-continuous rope processing similar to jet dyeing.

Technical Accomplishments

The development of a nonaqueous slashing process requires reformulation of the size that is applied to the warp yarns and eliminating the use of water for application or removal. The specific strategy centers on implementing nonaqueous technologies involving use of 100% solids size and liquid carbon dioxide as a solvent replacement for water. The key to this effort is the development of a new polymeric size compatible with carbon dioxide, having the necessary physical properties.

Other nonaqueous technologies have been considered over the last two decades, but none have met industry's needs for cost-effective operation and minimal environmental impact while maintaining standards of high quality warp. These efforts have demonstrated the use of 100% solids sizes (hot melt application) and nonaqueous solvents (chlorinated hydrocarbons). The new system examined controls costs by using carbon dioxide, which is inexpensive and environmentally safe. While customizing this technology to meet the specialized needs of fabric manufacturing, we treated the entire sizing and desizing process to ensure the best success of a complete operation.

In laboratory experiments, we have been able to demonstrate the solubility of new classes of size compounds in liquid and supercritical carbon dioxide. These size compounds, separately and as mixtures, were then applied to single strands of 50% polyester/ 50% cotton spun yarns using the hot melt application technique. The amount of size added to the yarns was determined. The treated yarns were evaluated for strength and elongation at PNNL. Selected samples were sent to the Institute of Textile Technology for evaluation in simulated weaving tests, abrasion tests. Results have shown that selected formulations of the carbon dioxide soluble size mixtures meet or exceed the industrial standard, polyvinyl alcohol/starch mixtures.

Size removal by carbon dioxide was demonstrated using small squares of fabric that had the newly formulated sizes applied by the hot melt technique. The fabric was placed in an autoclave, sealed, and pressurized with carbon dioxide. The carbon dioxide was recirculated in the autoclave with a spinning impeller. The autoclave was depressurized and the fabric pieces removed for evaluation. None of the size remained on the fabric after treatment.

These results demonstrate the potential of carbon dioxide for increasing the energy efficiency and reducing the environmental impact of textile slashing.

Publications

L.E. Bowman, C.G. Caley, R.T. Hallen, and J.L. Fulton. 1996. "Sizing and desizing polyester/cotton blend yarns using liquid carbon dioxide as a replacement solvent." *Textile Research Journal*, 66(12) 795-802.

L.E. Bowman, R.T. Hallen, and J.L. Fulton. "Evaluation of new size formulations soluble in liquid and supercritical carbon dioxide." *Textile Research Journal* (manuscript in preparation).

Plasma Engineering and Prototype Development

Theresa M. Bergsmann, William O. Heath (Process Technology)
Russel G. Tonkyn (Chemical Structure and Dynamics)

Project Description

The gas-phase corona reactor (GPCR) technology is being developed as an alternative to thermal treatment for removing pollutants from gas streams (Heath et al. 1993). The technique uses gaseous electrical discharges (corona) to form a nonthermal plasma capable of initiating chemical reactions in a packed bed of dielectric pellets. Nonthermal plasmas typically operate at 30°C to 100°C but produce energetic electrons that create radicals and other reactive species normally associated with high-temperature (>500°C) reactions. The primary benefits are the potential for low energy requirement and low capital cost.

This project focused on understanding the rate (kinetics) of contaminant removal and the sensitivity of unwanted byproducts like ozone and NOx on reactor power. The rate of contaminant removal in a GPCR determines the size (thus capital cost) of the reactor required to treat a contaminated stream and the energy requirement (thus operating cost). Variables previously suspected of affecting the reaction kinetics included contaminant inlet concentration, stream humidity, composition of packing in the reactor, and the power per volume of reactor (power density). The power density was also thought to affect both the removal rate and the production of ozone and NOx.

The objectives of this project were to investigate 1) the kinetics associated with contaminant destruction in GPCR devices, 2) the effect of packing composition on removal kinetics, 3) the effect of humidity on energy use, and 4) the effect of packing composition and power density on ozone and NOx formation.

Technical Accomplishments

As a first step in modeling the kinetics of contaminant removal in a GPCR device, the following simplifying assumptions were made:

1. Rate effects owing to mass-transfer limitations can be neglected in a packed bed (Levenspiel 1989).

2. A packed bed operated in the turbulent regime functions as an ideal plug-flow reactor (Levenspiel 1989).

3. The reactor can be considered to operate at constant temperature and pressure.

4. Decomposition follows a pseudo first-order decay that can be described by a phenomenological rate equation that assumes removal rates are limited by the equilibrium concentration of one or more active species that react with the contaminant.

5. The bimolecular removal of active species can be assumed to depend only on the initial concentration of contaminant.

These assumptions lead to the following rate equation:

$$\ln\frac{C_i}{C_t} = \left\{\frac{\hat{P}\, k_p k_r}{k_q + C_0 k_r}\right\} t$$

The quantity in braces is equivalent to a first-order rate constant but includes the dependence on initial contaminant concentration. Defining the residence time, t, as the volume of the reactor divided by the rate of flow through the reactor, and the power density, $\hat{P}$ as the applied power divided by the reactor volume:

$$\hat{P}t = \frac{P_R}{V_R}\frac{V_P}{F_F} = \hat{E}$$

the product of power density and time is an energy density, $\hat{E}$. In terms of energy density, the rate equation can be restated as:

$$\ln\frac{C_i}{C_i} = \frac{\hat{E}}{\beta}$$

where,

$$\beta = \frac{\alpha_{q/r}}{k_p} + \frac{C_i}{k_p}$$

and,

$$\alpha_{q/r} = \frac{k_q}{k_r}$$

To evaluate the ability of this model to describe typical experimental results, tests were performed to evaluate carbon tetrachloride destruction at several concentrations in air. The model was found to provide an adequate fit of the data as shown in Figure 1, which plots specific energy versus starting concentration using two different reactor packing materials. Values of α and k_p correspond to the slope and intercept of lines fitted to the data:

$$k_p = \frac{1}{\text{slope}} \; ; \; \alpha_{q/r} = \frac{\text{intercept}}{\text{slope}}$$

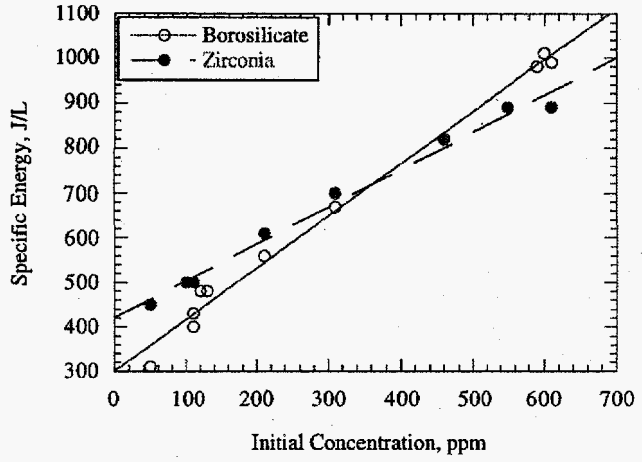

Figure 1. Effect of carbon tetrachloride concentration on specific energy.

Further experiments were performed on the destruction of trichloroethylene in air using a wide variety of reactor packing materials. Table 1 lists the kinetic parameters that were established for each packing material. The results suggested that mixtures of various packings may work better than any single packing for reducing energy requirements over a wide range of concentrations.

Table 1. Effect of Packing Material on Kinetics

Pellet Material	k_p L (J ppm)$^{-1}$	Alpha ppm^{-1}	Beta[a] J/L
Soda Lime	19.70	2342.06	113.82
Pt/Pd Alumina	-25.72	-1111.11	47.09
Biocarrier	16.76	1357.46	75.03
Borosilicate	-56.69	-3449.31	62.60
Chromia	44.66	5702.56	125.45
Molybdena	34.21	2549.04	71.60
Zirconia	55.68	4845.19	85.22

(a) Values for 100-ppm initial

Experiments were then performed to examine the effect of stream humidity on kinetic parameters for the destruction of trichloroethylene in air. We found the energy requirement to be roughly proportional to the logarithm of moisture, as shown in Figure 2. All of the data obtained at humidities from 0.1 to 70% RH, were well described by the following expression:

$$\beta = \beta_0 + k_{RH} \ln (\%RH)$$

although the real effect of moisture on the physical and chemical mechanisms involved with contaminant removal are apparently complex.

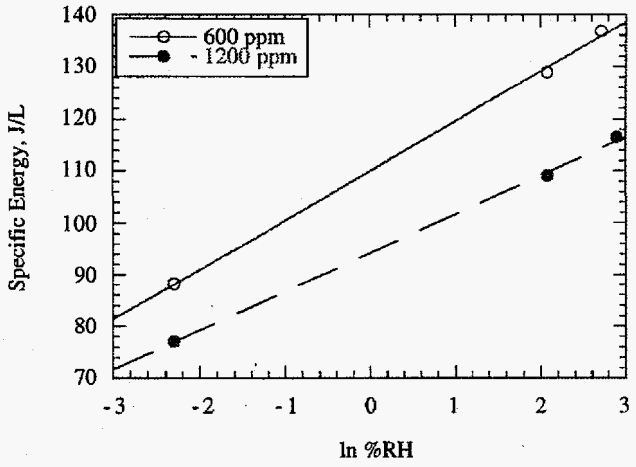

Figure 2. Effect of humidity on specific energy for trichloroethylene on soda glass pellets.

The formation of ozone and oxides of nitrogen in electrical discharges has been studied since the 1860s in connection with ozonizers for water purification. The initial step is the simultaneous formation of atomic oxygen, atomic nitrogen, and electronically excited nitrogen molecules via electron impact, and charged species primarily through electron attachment (forming negative ions) and electron impact ionization (forming positive ions). These energetic species eventually recombine to form stable (ground state) compounds.

Several experiments were performed to investigate the production of ozone, nitrogen dioxide, and nitric oxide in a GPCR device operated with air. Figure 3 plots the concentration of nitric oxide (30 amu), nitrogen dioxide (46 amu), and ozone (48 amu) versus power density at two flow rates. Concentrations were measured using a close-coupled quadrupole mass spectrometer.

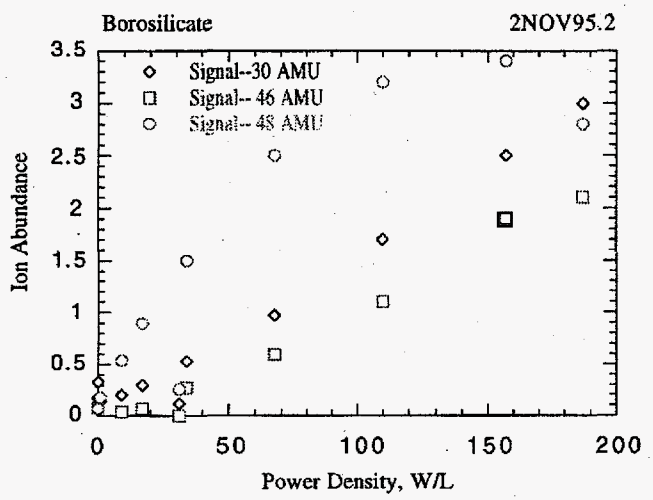

(a) Airflow at 1.5 L/min

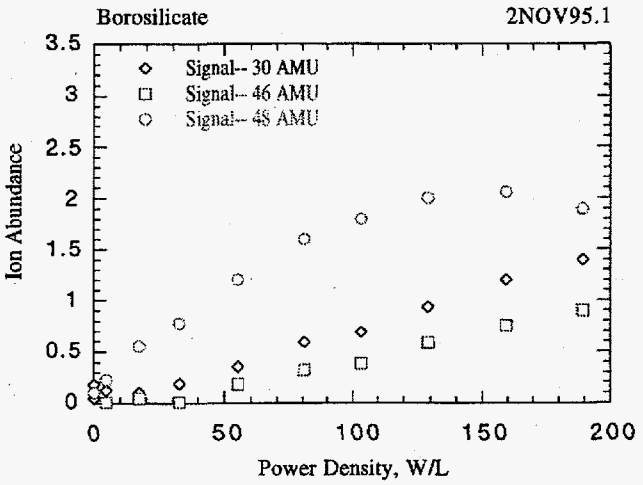

(b) Airflow at 3.0 L/min

Figure 3. Effect of power density on air byproducts.

At each flow rate, a maximum in ozone concentration (48 amu) appeared at a power density between 150 and 160 W/L. Evidently, the rates of ozone production and quenching reach an equilibrium that depends on power density since the airflows for each test (and thus the energy densities) differed by a factor of two. However, the concentrations of all species, including nitric oxide (30 amu) and nitrogen dioxide (46 amu), were inversely proportional with air flow rate as would be expected for production rates dependent on power.

Experiments were performed on four other packing materials as shown in Figure 4. Three of the packings, containing alumina (Figures 4a, b, and d), were discovered to produce significantly less ozone than produced on molybdenum oxide (Figure 4c) or borosilicate glass (Figure 3).

The two alumina catalysts containing surface-deposited noble metals (Figures 4b and d), produced essentially no NO_2 and trace levels of NO. The aluminosilicate packing (Figure 4a) appeared to produce trace levels of NO_2 and NO, however, in all cases, ion-abundance levels below 0.5 (corresponding to an ion current of 0.005 pA) are within the statistical noise of the mass spectrometer. As with ozone production, the molybdenum oxide packing produced NOx levels similar to borosilicate.

Our conclusion from these preliminary data is that packing materials containing alumina (and perhaps a noble metal) produce no measurable quantities of NOx and significantly less ozone than borosilicate or molybdenum oxide. As power densities were increased beyond 150 W/L, ozone production appeared to decline as noted by other researchers (Yamamoto et al. 1993). Energy requirements for trichloroethylene varied by nearly a factor of three among the packing materials tested, with alumina packings requiring less energy. Finally, we found that energy requirements vary logarithmically with humidity, approximately doubling as stream humidities increase from 0.1 to 100% RH.

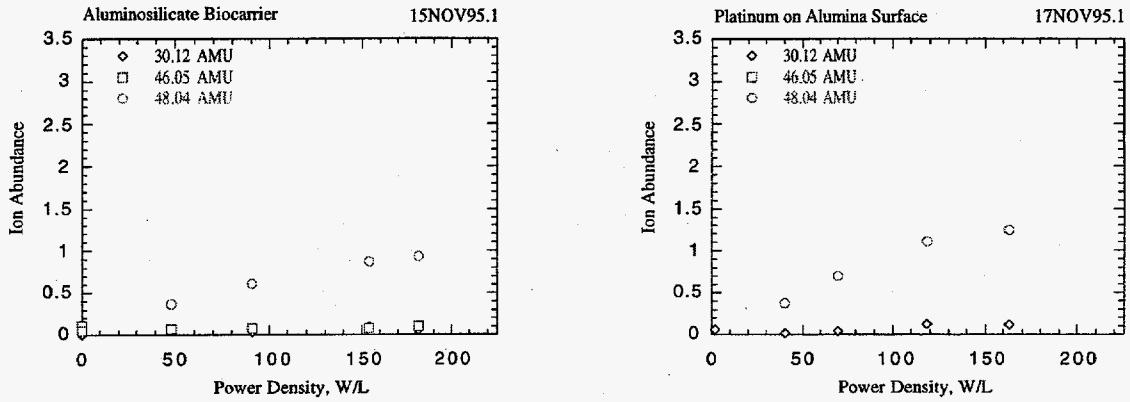

(a) Aluminosilicate

(b) Platinum on Alumina

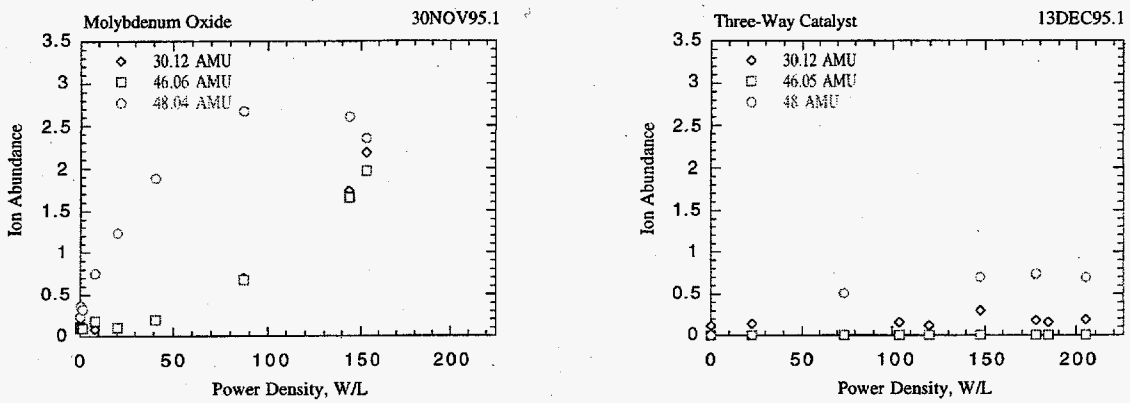

(c) Molybdenum Oxide

(d) Platinum and Palladium on Alumina

Figure 4. Effect of packing composition on air byproduct formation (airflow at 2.0 L/min).

References

B. Elliasson, and U. Kogelschatz. 1991. "Modelling and applications of silent discharge plasmas." IEEE Transactions on Plasma Science, Vol. 19, No. 2, pp. 309-323.

W.O Heath., J.W. Virden, R.L. Richardson, and T.M. Bergsman. 1993. *Method and Apparatus for Chemically Altering Fluids in Continuous Flow*. United States Patent 5,254,231.

O. Levenspiel. 1989. *The Chemical Reactor Omnibook*. Oregon State University, Corvallis, Oregon.

T. Yamamoto, P.A. Lawless, M.K. Owen, and D.S. Ensor. 1993. "Decomposition of volatile organic compounds by a packed-bed reactor and a pulsed-corona plasma reactor." *Nonthermal Plasma Techniques for Pollution Control*. Springer Verlag, Heidelberg.

Publication

R.G. Tonkyn, S.E. Barlow, and T.M. Orlando. 1996. "Destruction of carbon tetrachloride in a dielectric/ packed-bed corona reactor." *J. Appl. Phys.* 80 (8), 15.

Prediction of Physical Properties of Colloidal Gels

David R. Rector (Fluid Dynamics)

Project Description

A large fraction of the insoluble solids that exists in Hanford tank waste is in the form of submicron-sized particles. Under the high pH and salt concentration conditions that exist in the tanks, these colloidal particles tend to attract each other to form porous aggregates. Recent work related to tank waste processing indicates that the aggregation of these particles to form colloidal gels can have an enormous impact on tank waste processing. For example:

- The efficiency of solid-liquid separation through sedimentation depends on how effectively the particles in the final sediment pack. The formation of a colloidal gel can reduce or even eliminate the degree of settling that occurs during a pretreatment wash or leach procedure.

- The retrieval and transport of tank sludge depends on the viscosity of the suspension. The formation of a colloidal gel can change a low-viscosity Newtonian suspension into a high-viscosity shear-thinning fluid.

The objective of this work was to develop a computational tool for linking the interactions between colloidal particles to the physical properties of colloidal gels, such as those in Hanford tank waste, and perform a simulation to demonstrate this technology. The primary physical properties of interest are the compressive yield stress for sedimentation and rheological properties for transport.

Technical Accomplishments

The physical properties of a colloidal gel depend on the structure of the gel, the attractive potential between pairs of particles, and the resistance to bending for each chain of particles. A series of Brownian dynamics computer programs were developed to simulate the formation of colloidal gels and determine their physical properties.

In Brownian dynamics, the motion of individual particles is determined based on the random forces exerted by the surrounding fluid and particle-particle potential interactions. For solutions with a high salt concentration, such as those in tank waste, the repulsive electrostatic double-layer collapses resulting in a van der Waals attraction potential. The resistance to bending is modeled using a truncated harmonic potential with a reference angle for each group of three connected particles. The motions of the individual particles are integrated over time until the particles have aggregated to form a continuous network. Simulations of several thousand particles are typical.

Another Brownian dynamics algorithm has been developed which tracks individual particles until they contact another particle or cluster of particles. The new cluster is then treated like a rigid body with the appropriate Brownian and cluster-cluster interactions. This algorithm is useful for efficiently creating gels for diffusion-limited aggregation systems. The cluster size distribution as a function of time and the fractal dimension of the clusters compare favorably with values in the literature.

The physical properties of a colloidal gel are determined by applying forces to the simulated gel network and measuring the response. For example, the compressive yield stress is defined as the relative weight per unit area of sediment that can be supported by a colloidal gel as a function of solids volume fraction. This is simulated by forming a colloidal gel between two parallel walls, one which remains fixed and one which acts as a freely moving piston. A force is applied to the moving wall and the system is allowed to compress until it reaches a new equilibrium value. By repeating this procedure, the compressive yield stress versus solid fraction is determined. A series of simulations were performed for a simple model system which shows behavior consistent with the functional forms found in the literature.

Structure/Function Analysis

Timothy L. Hubler, Richard T. Hallen (Process Technology)

Project Description

The objective of this project was to provide an understanding of the fundamental structure/function relationships for organic phenolic ion-exchange materials through synthesis and characterization of resorcinol-formaldehyde resins "templated" with different alkali metal ions. The resins were characterized using solid-state ^{13}C nuclear magnetic resonance correlated with batch distribution coefficients to gain information on how templating affects the selectivity of resorcinol-formaldehyde resin for cesium ion. Resorcinol-formaldehyde resin is a regenerable ion-exchange material that may have application for removal of radioactive cesium from alkaline waste tank supernates.

The approach used for the templating study was to synthesize resorcinol-formaldehyde resin using the full range of alkali metal hydroxides. The resulting resins were then analyzed by solid-state nuclear magnetic resonance and K_ds. Two different stoichiometries were used for the resin preparations (1 MOH: 1 resorcinol and 2 MOH: 1 resorcinol) to assess the templating effect that occurs when one or both of the resorcinol ring hydroxyl groups are deprotonated during synthesis. Each of the ionic forms of the resin was converted to its acid form, which was also characterized.

Technical Accomplishments

The ionic forms of the resorcinol-formaldehyde resin contained more water than the acid forms, and there was a steady decrease in the amount of water that the resins absorbed in going from lithium to cesium. Overall, the resins prepared in a 1:2 stoichiometry of MOH:resorcinol absorbed the most water.

The K_ds for the ionic forms show a steady decrease in the K_d value in going from the sodium ion to the cesium ion, for both stoichiometries. This trend was expected based on the likely mechanism of selectivity, which is directly related to the swelling of the resin. Swelling equilibrium is achieved by exchange of an alkali metal ion in the resin that has a larger hydrated ionic radius (e.g., sodium) with one possessing a smaller hydrated ionic radius from the external solution (e.g., cesium). When exchange occurs, the resin is able to contract (energy minimization), due in this case to the smaller effective volume of the hydrated cesium ion. The effect is most pronounced for resins where there is high strain or cross-linking.

The acid forms for all the resins had a fairly constant water content (less than the ionic forms), and the resins prepared in the 2:1 stoichiometry (MOH:resorcinol) showed reduced K_d values compared to the 1:1 stoichiometries. Resin oxidation may be accelerated by the higher ionic content causing more strain as the polymer swells, which causes the resin to be more susceptible to air oxidation. Overall, there was a leveling effect in the K_ds, and any template effects appear to be minimal. However, the resins prepared with the cesium template ion have the lowest K_d in all cases while those prepared with sodium ion have the highest K_d in all but one case.

The solid-state ^{13}C CP-MAS NMR spectra for the resorcinol-formaldehyde resins had a typical appearance. For the acid forms, the resolution of the resorcinol ring carbon resonances around 120 ppm was enhanced relative to the ionic forms, in accordance with previous observations. There were very slight differences in the amount of oxidation that could be discerned by nuclear magnetic resonance characterization of the different stoichiometric preparations; for the lithium templated resins, there was clearly more oxidation and these resins also had smaller magnitude K_ds. The particular reason for the greater oxidation of the lithium templated resins is not yet known, however, the greater polymer strain that the highly hydrated lithium ion may impart to the resin may be part of the reason for the lowered performance.

For the alkali metal forms, the carbon and alkali metal elemental analyses were generally low, while hydrogen was high, suggesting that there was more water and oxygen in the resins than accounted for by the theoretical model. In the case of the cesium materials, the carbon analyses were high, while the cesium levels matched theory, and the additional carbon may have been present from additional methylene cross-linking groups. For the acid forms, all the carbon analyses were low again, but hydrogen analyses nearly matched the theoretical. There was modest incorporation of nitrogen, probably in the form of nitro groups on the aromatic rings, which amounts to around 1% or less nitrogen and there was about 1% residual sodium from

activation of these resins with sodium hydroxide during conversion to the acid form. The results from the acid forms indicate that there was more oxidation of the resin than seems to be accounted for, even in nuclear magnetic resonance spectra (which do indicate some oxidation).

There is no clear indication that potassium or any of the alkali metals other than cesium may be templating ion-exchange sites in resorcinol-formaldehyde resin. The template effect occurring with cesium ion, if it is efficacious, would be undesirable for a resin to be selective for cesium, while resins prepared using sodium ion have performance levels as high or higher than those prepared with potassium. These observations are all consistent with the probable mechanism of cesium selectivity for phenolic resins.

Publications and Presentations

T.L. Hubler, J.A. Franz, W.J. Shaw, M.O. Hogan, R.T. Hallen, G.N. Brown, and J.C. Linehan. 1996. *Structure/function studies of resorcinol-formaldehyde (R-F) and phenol-formaldehyde (P-F) copolymer ion-exchange, resins.* PNNL-11347, Pacific Northwest National Laboratory, Richland, Washington.

T.L. Hubler, J.A. Franz, W.J. Shaw, T.R. Hart, G.N. Brown, and J.C. Linehan. 1996. *Chemical derivatization to enhance the chemical/oxidative stability of resorcinol-formaldehyde (R-F) resin.* PNNL-11327, Pacific Northwest National Laboratory, Richland, Washington.

T.L. Hubler, W.J. Shaw, J.A. Franz, S.A. Bryan, R.T. Hallen, G.N. Brown, L.A. Bray, and J.C. Linehan. "Synthesis, structural characterization, and comparative performance evaluation of cesium-selective phenolic resins." *Macromolecules* (submitted).

T.L. Hubler and J.A. Franz. 1996. "Chemical derivatization of resorcinol-formaldehyde resin leading to enhanced chemical/oxidative stability of the resin." 211th ACS National Meeting, New Orleans, Louisiana, March.

T.L. Hubler. 1996. "Chemical derivatization to enhance chemical/oxidative stability of resorcinol-formaldehyde (R-F) resin." Efficient Separations and Processing Crosscutting Program (ESP) Annual Technical Exchange Meeting, Gaithersburg, Maryland, January.

Supercritical Fluids Separations

Clement R. Yonker (Chemical Sciences)

Project Description

This project develops capabilities to study the effects of pressure and temperature on the kinetics and thermodynamics of organometallic chemistries in supercritical fluids. The project specifically focuses on investigations using supercritical carbon dioxide, which shows promise as a "green" solvent of the future. The resulting developed capabilities and investigations will provide a fundamental background for the development of new separation and extraction technologies based upon supercritical fluids.

Technical Accomplishments

The separations and extraction of metal ions and radionuclides is important in the environmental remediation of hazardous waste sites throughout the nation and DOE's complex. The need to accomplish these extractions in a cost-effective, environmentally benign manner has driven the investigation of novel complexation agents and new solvents. Using supercritical fluids as a novel solvent, one can continuously vary density, dielectric constant, viscosity, and mass transport properties between that of a gas and liquid by manipulating pressure. The compressibility of a supercritical fluid is large just above its critical point, where small changes in pressure result in large changes in the solvent strength of the fluid. As a consequence, molecular interactions can be varied over a considerable range. As pressure is increased, the solubility of a metal complex will often increase by many orders of magnitude. These increased intermolecular interactions between the fluid and the metal complex will affect the kinetics and thermodynamics of complex formation and their chemistries which can be used to advantage in extraction schemes.

In FY 1994, the first year of the project, studies were undertaken investigating the solution dynamics of pure supercritical fluids as a function of pressure and temperature. Thermal ligand displacement reactions using supercritical fluid solvents were also investigated, in which the fluid solvent reversibly displaced a complex's organic ligand over time. This was the first instance of this behavior being observed using high pressure nuclear magnetic resonance.

In FY 1995, continuing high pressure nuclear magnetic resonance investigations built upon the previous year's effort and extended the project into structure/function determination of organic ligands using the thermodynamic variables of pressure and temperature. Systems investigated were acetylacetonate, trifluoroacetylacetonate, and hexafluoroacetylacetonate. These organic ligands are becoming important in metal extractions using supercritical CO_2. They have the capacity to undergo a keto/enol tautomeric equilibria which will affect their ability to complex with a metal ion. These studies demonstrated that fluorination enhanced ligand solubility in supercritical CO_2 for the metal complex and temperature plays a dominate role in the ligand tautomer equilibria.

During FY 1996, investigations were extended to organometallic photochemistry in supercritical fluids using on-line, in situ photolysis with high pressure nuclear magnetic resonance detection of the photoproducts. Fundamental investigations of the photocatalysized organometallic substitution reactions in supercritical ethylene and binary mixtures of CO_2/ethylene and CO_2/H_2 contributed to the understanding of solution dynamics in these systems. These efforts were the first demonstration of on-line detection of photolysis products using high pressure nuclear magnetic resonance. The molecular level information obtained through this technique related to molecular structure demonstrates the direct attachment of ethylene to the organometallic complex through a ligand substitution reaction.

Publications and Presentations

C.R. Yonker, and S.L. Wallen. 1996. "High-pressure on-line photolysis with NMR detection." *Appl. Spectrocs.*, 50, 781-784.

J.C. Linehan, S.L. Wallen, C.R. Yonker, J.T. Bays, and T.E. Bitterwolf. 1996. "Photolysis of organometallic complexes in supercritical solvents." Presented at the 211th ACS National Meeting, March 24-28, New Orleans.

Synthesis Reaction in a High Energy Corona

Gary B. Josephson (Process Technology)

Project Description

This project focused on converting methane to higher valued products, specifically C_2 hydrocarbons, ethane, ethylene, and acetylene. Methane is an attractive feed stock because of its natural abundance. However, current processes to convert methane are inefficient and energy intensive. A common difficulty is to convert methane to C_2s without further reaction to coke.

In this project, high energy corona was shown to be able to convert methane to C_2 hydrocarbons with conversion rates up to 23.8%. The reactor operated at about 100°C which is significantly below the 700°C to 900°C temperatures used commercially. The lower operating temperatures open up the opportunity to employ a wider variety of catalysts to improve upon the conversion efficiency and energy requirements. The lower temperature also offers promise that progressive reaction toward carbon can be minimized.

Technical Accomplishments

The formation of higher order hydrocarbons from methane occurs through a coupling reaction that initially forms ethane and hydrogen. The ethane can further dehydrogenate to form ethylene and then acetylene with concomitant formation of additional hydrogen. The most common hypothesis is that the initial active species for the forward reaction is the methyl radical and hydrogen radical from methane. As hydrogen is formed, the hydrogen can be a source of hydrogen radicals that can react with C_2 products progressively going back to methane. It is expected that removal of hydrogen product from this reaction is critical to achieving high yields of C_2s from methane.

Industry contacts have indicated that an economic target for this reaction is 30% conversion of methane to C_2s. The highest conversion to C_2s demonstrated during this project was 23.8%. The yield to C_2s was found to be proportional to the square root of the energy density. (See Figure 1.) Much of the initial work done in this project was conducted on the nonflammable mixture of methane and argon. Later work was conducted using pure methane and did not achieve conversions that were as high at the same reactor power. For a reaction system involving argon, it was determined that the appropriate parameter is energy per reactant rather than energy per total feed volume (which includes argon). When compared on this basis, the experiments with pure methane had a significantly lower energy input per mole of methane. The methane conversion achieved with pure methane was consistent with an argon methane system at a proportionately lower power. (See Figure 2.)

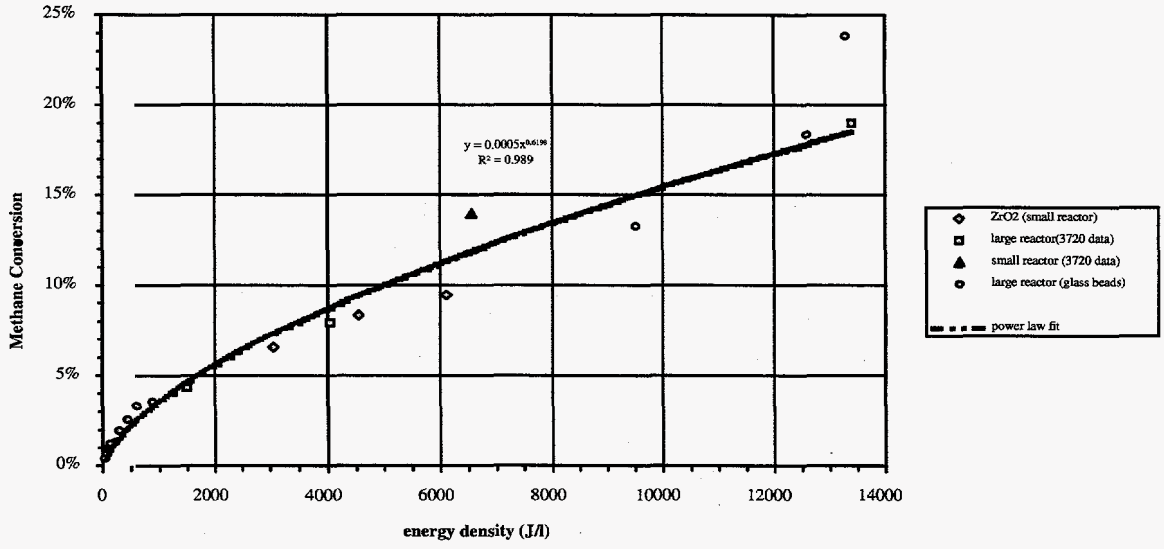

Figure 1. Energy density vs. conversion.

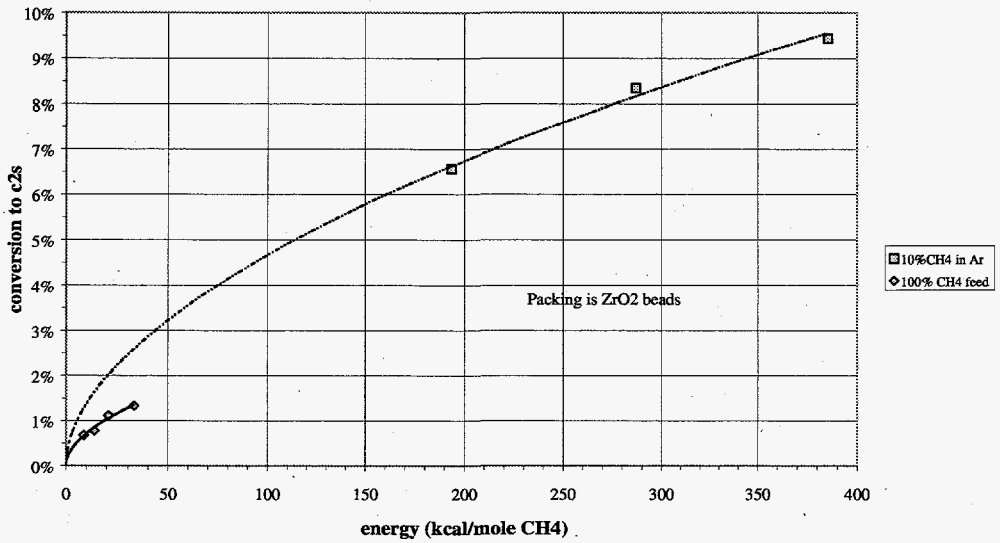

Figure 2. Energy density vs. conversion effect of CH4 concentration.

A gas-phase corona reactor (GPCR) with the plasma off can be electrically modeled as a pair of capacitors in series. The glass barrier is one capacitor, and the gas between the electrode which contains the packing and the gas is a second capacitor. When the plasma is "on," the gas and packing are modeled as a resistor. The system is then a capacitor (the glass barrier) and a resistor. When the reactor is powered with alternating current, the plasma goes "on" and "off" twice per cycle. A Lissajous diagram of the model system would be a parallelogram with nice sharp corners indicating plasma going on and going off. The slope of the voltage versus charge accumulation would represent the capacitance of the glass barrier with the plasma on and the capacitance of the barrier and packing with the plasma off. See Figure 3 for components in a Lissajous figure.

Figure 4 shows Lissajous diagrams from oscilloscope data of the voltage and current to the reactor. Two diagrams are shown that depict the performance of the two extremes of the packings tested. Each Lissajous plot represents approximately 16 watts of power to the reactor. Both diagrams show that two of the corners

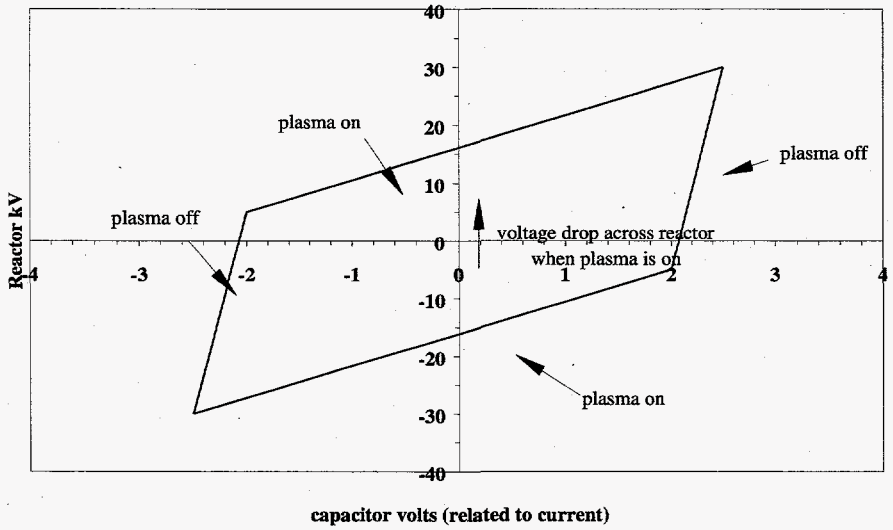

Figure 3. Lissajous plot of model plasma reactor.

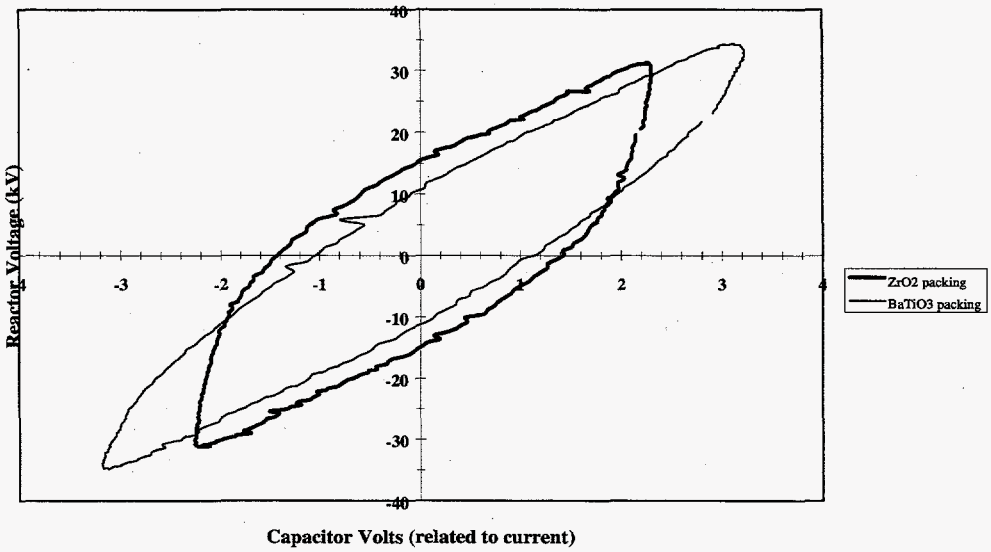

Figure 4. Lissajous plot of CH4 reactor with ZrO2 and BaTiO3 packings.

have significant rounding from the perfect parallelogram. This rounding shows greater charge transfer with lower voltage change than would occur with the perfect model. The root cause is accumulated space charge in the gas and/or surface charge on the packing which is "neutralized" when the voltage crosses zero before the next "on" period of the plasma. The quantitative aspects of this phenomenon are part of the plasma physics model pursued as a separate project.

After the initial studies with P-10 were completed, the reactor was disassembled and examined. The center electrode, which was stainless steel, showed very distinctive deposits of carbon at each contact point with the packing beads. More specifically, there was a small circle of carbon around a clear spot where the bead actually contacted the rod. There was a corresponding carbon deposit on the bead. However, there was no indication of any carbon on any of the beads which did *not* touch the metal electrode.

Reactions with 100% methane again showed carbon deposits on the center electrode and also a general brown discoloration of the light colored packings. This would indicate a more universal formation of carbon which indicates that some overreaction occurred. The total mass of carbon could not even be weighed. Almost certainly it amounted to less than a milligram which would be less than 0.1% of the methane converted to C_2s during a 6 hour test run. Therefore, although there was certain evidence that the overreaction of methane was occurring, it was not a significant loss of efficiency.

Conclusions

This report is an interim report of a continuing investigation into synthesis reactions with high energy corona. From this work to date we conclude:

- Plasma can be used to initiate reactions of methane and form significant yields of C_2s at low temperature.
- The energy requirements for formation of C_2s from methane would be too high to be practical for a commercial process unless significant improvements can be made.

This phase of the project demonstrated that GPCR can be used to synthesize materials (C_2s from methane) and demonstrated that energy density, dielectric properties, and surface reactions can affect the efficiency of the conversions. Most questions as to why are still to be resolved. The prime direction that is a ripe field for investigation is to identify and control the aspects which can bring about desirable surface reactions.

Ultra High Rate Sputter Deposition of Highly Reflective Metal Films

John D. Affinito (Materials Sciences)

Project Description

The objective of this study is to develop improved magnetron sputtering cathodes and processes that are capable of rates high enough to run simultaneously, in-line in a vacuum web coating process, with the polymer multi-layer (PML) flash evaporation process. Many multilayer film applications of interest require metal, oxide, nitride, and other types of layers deposited sequentially, one atop the other. We have developed a process for vacuum deposition of polymer layers, the PML process, that, in a roll-to-roll web coater, can deposit polymer layers at line speeds up to 600 m/min. In many instances the PML layer can replace an oxide or nitride in a traditional application. Often the PML layer can replace a polymer layer that, traditionally, is deposited in a separte atmospheric step which requires moving the substrate in and out of vacuum multiple times. In still other instances, new applications are under development that use PML layers along with oxides, metals, or both in a multilayer structure. In all of these cases, the production costs are determined by the overall deposition rate which is determined by the slowest of the deposition processes involved. Traditionally, metals have been faster than oxides or nitrides, while polymers require the substrate to be shuttled between air and vacuum, which is very slow. The PML process not only makes the polymer layer vacuum compatible, it makes it the fastest of the processes. To maximize the manufacturing benefit of the ultrahigh rate of the PML process, when it is used with sputtered metal and/or oxide layers, we are working to increase the rate of the metal and oxide processes by increasing the magnetron sputtering rate.

Technical Accomplishments

The Sputtering Process

Figure 1 depicts the basic sputtering processes in a schematic form (Affinito and Parsons 1984). A target material, which is to be sputtered to produce a thin film, is placed in a vacuum chamber. After the base pressure is reached, with the pumps still operating, a steady flow of gas, usually Ar, is allowed into the chamber and an equilibrium Ar partial pressure is reached. A negative

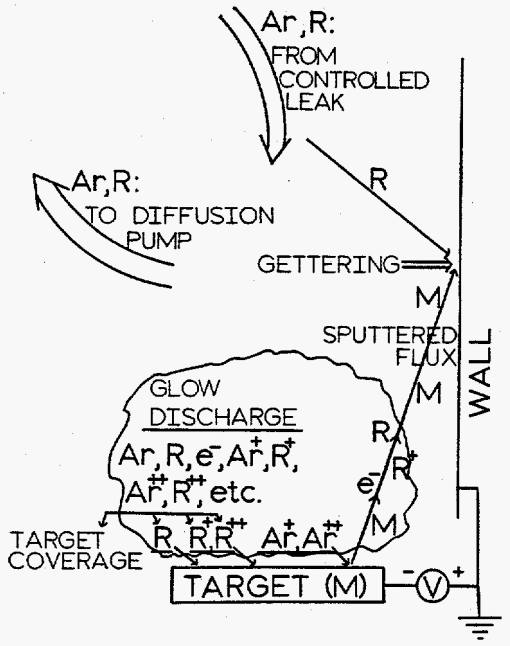

Figure 1. Schematic representation of the various processes that occur during the operation of a basic diode sputtering cathode. (Ar=Argon atom, R=reactive gas atom/molecule, e=electron, M=target material atom).

voltage is applied to the target and, if the Ar partial pressure is appropriate, a glow discharge is produced with the target acting as the cathode. Positive Ar ions in the glow are accelerated toward, and strike, the cathode. When the Ar^+ ions strike the cathode/target, electrons and target atoms are ejected through momentum and energy transfer mechanisms. The ejected electrons help to sustain the glow discharge by causing further ionization of the Ar, and the ejected atoms land on surfaces and form films. If reactive gas atoms (R) are mixed in with the Ar, then they may combine with the target material atoms (M) to form compounds (M_xR_y). This latter process is called reactive sputtering.

The basic diode sputtering process has the drawback of extremely low deposition rates per unit of power input to the glow discharge. This inefficiency is largely due to the diffuse nature of the glow discharge. The ions in the glow discharge plasma form a very diffuse cloud

with many of the Ar^+ species being produced so far from the target that they cannot contribute to the sputtering process. Therefore, several strategies have been developed to confine the plasma near the target surface in order to increase the sputtering efficiency.

Magnetron Sputtering

One strategy used to improve the sputtering efficiency is to place magnets behind the target so that the plasma is confined by the magnetic fields. This technique is called magnetron sputtering and the top portion of Figure 2 is a schematic representation of a conventional magnetron cathode. Magnetron cathodes show dramatic improvement in sputtering rate over diode cathodes. The two biggest drawbacks to the magnetron are that the target erosion is highly nonuniform due to the plasma distribution and that the technique is not very effective for magnetic target materials. This latter problem arises because the field from the magnets is shunted through the magnetic target material, which acts like a pole piece for the magnet, and there is not sufficient field in front of the target to confine the plasma. For efficient plasma confinement, the magnetic field strength above, and parallel to, the target surface must be at least 100 gauss, and 300 to 500 gauss is preferable.

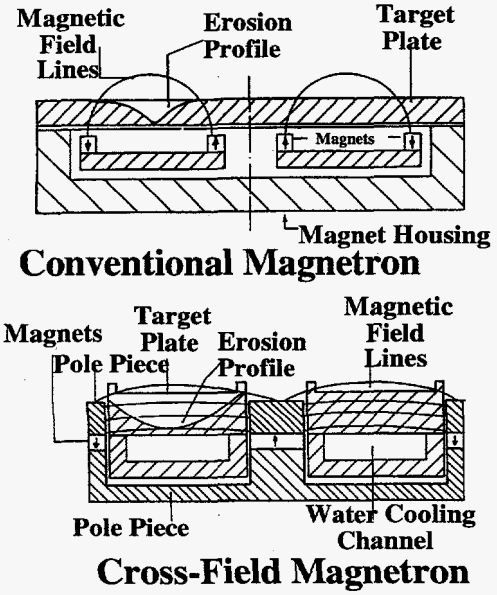

Figure 2. Comparison of magnet and target geometry for a conventional and a cross-field magnetron sputtering cathode.

Cross-Field Magnetron Cathodes

To get sufficient magnetic confinement, with highly magnetic target materials, the geometry shown in the bottom portion of Figure 2 was developed (Kukla et al.). This geometry, called the cross-field magnetron geometry, brings the magnet pole pieces up through the center of the target and up along the sides of the target. Thus, the pole pieces direct the field across the target surface. In this geometry, some field is still shunted into the magnetic target material, however, sufficient field remains above the target to provide efficient plasma confinement. The small vertical walls extending from the top of the target, illustrated in Figure 2, serve to provide a degree of electrostatic plasma confinement in addition to the magnetic field confinement.

This geometry affords two other advantages in addition to enabling magnetron sputtering of highly magnetic materials. First, as the field lines tend to be more uniform across the target surface than for a conventional magnetron, the target erosion is more uniform. This permits higher utilization of the target material. Second, the sputtering rate is much higher for nonmagnetic materials, as well as for magnetic materials, again for two reasons. First the higher magnetic field strengths provide better confinement and, thus, permit operation at higher power densities. Second, because the field is more uniform, sputtering occurs over a larger area of the target surface. Rates, for Cu, have been reported as high as 2000 Å/s above cross-field magnetrons (Kukla et al.). These rates are 5 to 10 times higher than for conventional magnetrons. With this type of cathode, the secondary electron emission, sputter rate, and plasma confinement efficiency can even be high enough to permit the target to sputter without any sputtering gas. This is called self-sputtering since it is ionized target atoms being turned around in the plasma and impinging on the target again that produce the sputtering effect.

Sputter Cathode Development at PNNL

Figure 3 depicts the vacuum web coater at PNNL. This system is set up to allow multiple vacuum deposition processes to be employed simultaneously, during a single pass of the substrate material through the system. Currently there are two cross-field sputtering stations, two PML flash evaporation (with e-beam and ultraviolet cure) stations, one monomer extrusion die (with e-beam and ultraviolet cure) station, one e-beam (or thermal) evaporation station, and two parallel plate glow discharge stations that can serve either for substrate pretreatment or for plasma enhanced chemical vapor deposition.

We have developed a new variation on the cross-field magnetron design as part of a program to raise sputter deposition rates high enough so as to take better advantage of simultaneous operation with the PML process. For instance, with conventional magnetrons, a

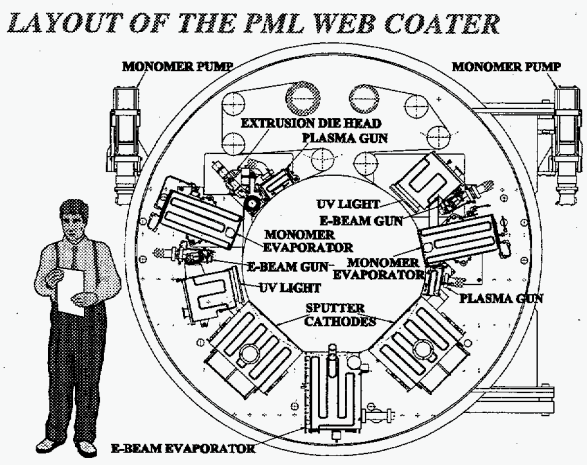

Figure 3. The modular design of the PML web coater permits many, and varied, deposition processes to be carried out simultaneously.

PML/Ag (1000 Å)/PML solar reflector might run at 5 to 10 m/min, gated by the Ag sputter deposition rate. Note that, while Ag has the highest sputter rate of any material, the PML process may deposit any thickness, from 0-to-several μm, at any speed from about 1 to 600 m/min. Also note that sputter deposition line speeds are not speed independent as is the PML process. Sputter line speeds are inversely proportional to the desired thickness for a given power. All other conventional, vacuum deposition processes have this same speed-thickness-power limitation. If we use cross-field magnetrons, we can push this rate to 25 to 50 m/min.

Figure 4 shows the type of modifications we have implemented on the target plate of a cross-field magnetron constructed at PNNL. The bottom portion

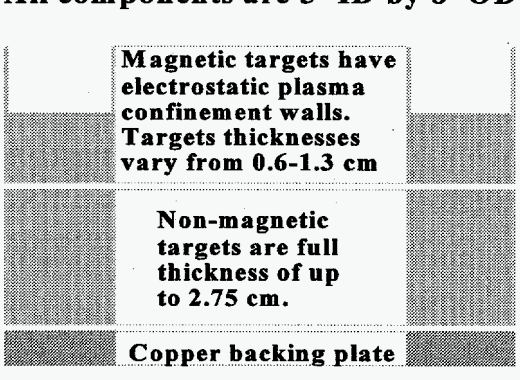

Figure 4. View of target backing plate, full size target, and electrostatic confinement target for magnetic materials. Target geometries, with our cross-field magnet configuration, support 40 kW of power and have been shown to enter self-sputtering mode for Ag and Cu targets.

of Figure 4 shows the copper backing plate, which is in direct contact with the water cooling. The target plate, shown in the center portion of Figure 4, is usually bonded to the backing plate. For reasonably machineable and inexpensive materials, the target and backing plate are machined from a single piece of metal. For nonmagnetic materials, the magnetic field in our design is high enough that targets up to 2.75 cm thick may be sputtered.

For highly magnetic materials, the target thickness must be reduced to counter the shunting of the field into the target material. In order to keep the same magnet assembly/cathode housing/form factor in our machine, we have employed the strategy depicted in the top portion of Figure 4. We machine the target plate surface down to a thickness at which it will sputter. However, we do not machine the entire surface down but, instead, leave thin walls ($\sim$0.1 cm thick) standing around the inner and outer diameter of the target plate. As these walls are perpendicular to the magnetic field lines, they contribute minimal shunting. The top and sides of the walls are the surfaces in closest proximity to the ground shield and the target wall-to-ground shield spacing (the dark space) must remain relatively constant. The walls do provide electrostatic confinement for the plasma, thus permitting the thickness of the magnetic target plate to remain greater than if the walls were not present. A much greater advantage, in regards to ease of operation and maintenance, is afforded by these walls however. Varying the wall-to-bulk target height allows all of the other cathode assembly/ground shield components to remain the same while still permitting sputtering of materials with all levels of permeability and coercivity.

In some cases the copper backing plate and walls are machined as a single, solid piece out of a copper block and a annular disk of the magnetic target material is bonded in the cavity. During the sputtering process, both the horizontal target plate and the vertical walls are sputtered. However, the rate of deposition of the material from the horizontal surface onto the vertical walls is greater than the rate at which it is re-sputtered from the vertical surface. Therefore, there is no contamination of the deposited film due to sputtering of the copper walls.

With these cathodes we have successfully sputtered the nonmagnetic metals Ag, Al, Cu, Mo, Ta, Zr, and Zn. We have also reactively sputtered AlN, Al_2O_3, Ta_2O_5, and ZnO. The nonmagnetic target material utilization is about 50%. The magnetic materials we have attempted are Fe, Ni, and several permalloy (NiFe) compositions. All sputtered well with target thicknesses of about 1 cm. Target utilization for the magnetic materials is in the 20% to 30% range.

Our initial work utilized a 10 kW, Advanced Energy MDX10, power supply. With this source, we could supply an average power of about 50 w/cm^2 to the target surface. This provided sufficient power to self-sputter Ag—at about 45 w/cm^2 Ag will sputter without gas. Recently, we had our existing MDX10 modified, and have obtained three additional, modified, MDX10 supplies. These modified supplies can operate as independent 10 kW supplies or they can be assembled in parallel to act as 20 kW, 30 kW, or 40 kW supplies. With the 40 kW combination we can now apply greater than 200 w/cm^2 to our cathodes. At 15 kW (~85 w/cm^2) we have self-sputtered Cu. Ag, Al, and Cu targets have each been sputtered at the 40 kW level.

To compare with the Leybold work for Cu (Kukla et al.), we deposited Ag at 38 kw of cathode power and the sample height above the target was set at 2 inches. The weight gain of the sample after deposition was measured in order to determine the Ag deposition rate. For Cu, at 200 w/cm^2 and 2-inch distance, Leybold obtained a rate of 2010 Å/sec. With our cathode, for Ag at 215 w/cm^2 and 2-inch distance, we obtained a little over 11,000 Å/sec.

Conclusions

The use of a variable wall height, as an electrostatic plasma confinement tool, built into a cross-field magnetron target plate has been successfully demonstrated. This design permits a single cathode/magnet/ground shield assembly to sputter the entire range of magnetic and nonmagnetic target materials at very high rates. Power densities in excess of 215 watts/cm^2 were achieved with this geometry. As well, these cathodes permit self-sputtering of Ag and Cu at power densities above 45 watts/cm^2 and 85 watts/cm^2, respectively.

References

J.D. Affinito and R. R. Parsons. 1984. "Mechanisms of voltage controlled, reactive, planar magnetron sputtering of Al in Ar/O2 and Ar/N2 atmospheres. *J. Vac. Sci. Technol.*, A2, p. 1275.

R. Kukla, T. Krug, R. Ludwig, and K. Wilmes. "A highest rate self sputtering magnetron source." A.G. Leybold, West Germany, Internal Report 12-562.02.

Publication

J.D. Affinito, P.M. Martin, M.E. Gross, C.A. Coronado, and E.N. Greenwell. "Vacuum deposited polymer/metal films for optical applications." *Thin Solid Films* (in press).

Vacuum Extruded Polymer Films

John D. Affinito (Materials Sciences)

Project Description

The objective of this project was to develop a new vacuum deposition technology capable of depositing polymer, polymer electrolyte, and polymer composite films at very high rate. A research and development prototype production vacuum roll coater designed for multilayer thin film deposition onto flexible substrates in a roll-to-roll configuration was adapted for use in this work. The machine is capable of simultaneous deposition of polymer, metal, semiconductor, oxide, nitride, or carbide thin film multilayer structures. To date, all single layers for battery and electrochromic devices have been deposited. A full, five-layer, electrochromic stack was deposited in the roll-to-roll configuration but failed to switch properly.

Technical Accomplishments

Monomer Extrusion Process

The method under investigation involves the vacuum coating of a substrate with a reactive liquid that is subsequently polymerized by exposure to a source of cross-linking radiation (usually ultraviolet or electron). The reactive liquid can be an organic monomer or mixture of monomers, a monomer/salt solution, or a monomer slurried with organic or inorganic particles. These particles could be compound or elemental powders (like oxides, metals, graphite powders, or other carbons) or high molecular weight polymer powders.

Our process starts with degassing the reactive liquid (stirring it while pumping the vapor away) before depositing it on the substrate and the deposition occurs in a vacuum environment. Once the degassed liquid layer has been deposited onto the substrate, the substrate is moved past a source of cross-linking radiation. The vacuum roll coater employs either ultraviolet or electron beam cross-linking sources.

To date, we have tested two methods for depositing the liquid layer in a vacuum environment. The web coater employs a slotted die extrusion nozzle to deposit the reactive liquid layer on the substrate. This method was chosen to reduce the total exposed area of liquid in the vacuum in order to reduce the contamination ofconcurrent processes to as low a level as possible. The flow of reactive liquid into the die head is controlled with a precision metering/degas pump. Using the same metering pump/degas arrangement, an ultrasonic atomizer has also been used to vacuum deposit reactive monomers and monomer/powder slurries.

Vacuum Extrusion Deposition Systems

Figure 1 is a schematic of the vacuum web coater. This modular system can simultaneously deposit as many as seven different layers in a single, roll-to-roll pass of the substrate through the system. In the work reported here, the extrusion die head is the primary deposition source being used.

Some system specifications for the chamber in Figure 1 follow: 0 to 500 feet/min web speed; bi-directional operation; deposition source enclosures isolate process atmospheres; roll-to-roll, closed loop, and drum only operation; and system is fully automated. The chamber in Figure 1 is set up in a modular fashion that permits multiple process enclosures to be mounted in any order for fabrication of multilayer structures. One of the closed-loop web paths has nothing in contact with the front surface. The current process capability includes

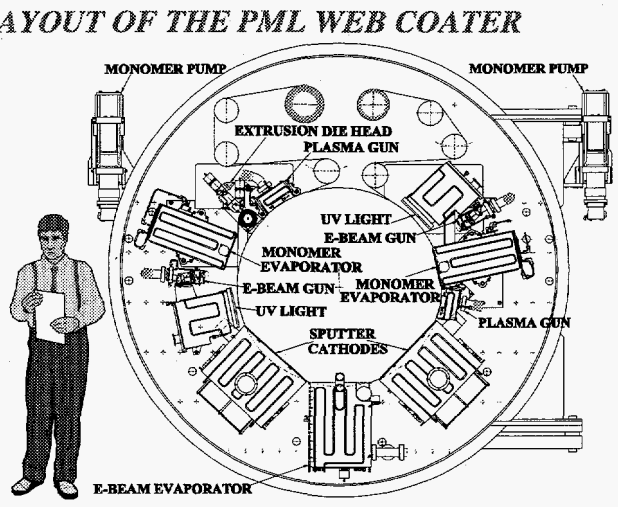

Figure 1. The modular design of the PML web coater permits many, and varied, deposition processes to be carried out simultaneously.

polymer multilayer flash evaporation, with e-beam or ultraviolet cure; sputtering, reactive or nonreactive; crucible or rod fed e-beam evaporation, reactive or nonreactive; thermal evaporation, reactive or nonreactive; plasma enhanced chemical vapor deposition; and monomer extrusion, with e-beam or ultraviolet cure.

Further, the entire drum can be biased with radio frequency or direct current electric fields, any deposition source enclosure may contain radio frequency or direct current bias electrodes, and any combination of deposition zones can be biased with fixed or rotating magnetic fields. Also, radio frequency glow discharge cleaning can be applied to the substrate before, or after, any deposition zone via small modular enclosures.

Results

Interdigitated, large area metal/polymer electrolyte/metal structures were vacuum fabricated by several variations involving PML, flash evaporated, electrolyte material or LML, extruded, electrolyte material. In all cases, a flexible web substrate was used and deposition was on a moving web in a roll-to-roll geometry. Variations of the web substrate that we employed included nickel foil, polyester, or polyester with aluminum foil patches taped to the surface. Bottom electrode variations included the nickel foil web, the aluminum foil patch, or sputtered aluminum. Top electrodes were aluminum deposited by either sputtering or e-beam evaporation. The electrolyte layers were deposited by both PML flash evaporation of monomer electrolyte mixtures followed by either e-beam or ultraviolet curing or by LML vacuum extrusion of monomer electrolyte mixtures that were ultraviolet cured. The lateral position of the deposition zones for each electrode were controlled by positioning the apertures of each source to form the desired interdigitated structure. The structures were sometimes deposited in a single, roll-to-roll pass through the system and sometimes in multiple passes. As part of the in-line processing, the substrate was always pretreated with an O_2 plasma prior to electrolyte deposition. The plasma pretreatment improved both wetting by the monomer electrolyte and adhesion of the cured polymer electrolyte.

Three different types of electrolyte mixtures were employed. One was a proprietary formulation supplied by a small company. The other two consisted of a salt mixed in a mixture of poly[ethelyene glycol] diacrylate (PEGDA, at 55% by volume), poly[ethelyene glycol] methyl ether (PEGME, 35% by volume), acrylic acid (5% by volume), and Darocure 4265 (5% by volume). The acrylic acid is added to promote adhesion to the substrates and the metal layers while Darocure 4265 is a commercial photoinitiator (a trimethylbenzophenone blend) supplied by Ciba Geigy. The salts used were lithium trifluoromethanesulfonate ($LiCF_3SO_3$) and lithium hexafluorophosphate ($LiPF_6$) at concentrations ranging from 0.1 m/L through 0.33 m/L. These two electrolyte mixtures were chosen for baseline tests of the process since Morita et al. (1990) published conductivity measurements for very similar materials when they were mixed and cured under atmospheric conditions in a beaker. In this way the results of the vacuum deposition process could be compared to those obtained when fabricating the same materials in air.

As mentioned earlier, two of the electrolyte formulations were selected specifically to attempt to relate the conductivity obtained by these vacuum deposition techniques to what is obtained when the material is mixed and polymerized in air. Morita made alternating current impedance measurements at 10 kHz with four salts ($LiCF_3SO_3$ and $LiPF_6$ among them) at several concentrations, with six variations of monomer-to-ether volume ratio. At 30°C, for all but the $LiCF_3SO_3$ salt, Morita found conductivities in the 10^{-4}-to-10^{-5} S/cm range. The conductivities for $LiCF_3SO_3$ mixtures were found to be about a decade lower. At 10 kHz, we found substantially the same results with measurements at 22°C as Morita et al. found at 30°C. To examine effects of the organic constituents independently of the salt, we used the proprietary electrolyte mixture but substituted $LiCF_3SO_3$ instead of their standard salt. Figure 2 shows conductivity measurements for three extruded, and one flash evaporated, monomer electrolytes containing $LiCF_3SO_3$. All four of these formulations were identical, though one was flash evaporated and the other three were extruded under identical process conditions. For the three extruded formulations, the conductivity variations are due to experimental process control fluctuations and measurement uncertainties. Also shown is a representative measurement of another formulation (Sample 4) with $LiCF_3SO_3$ as the salt. This material was measured only at 1 kHz.

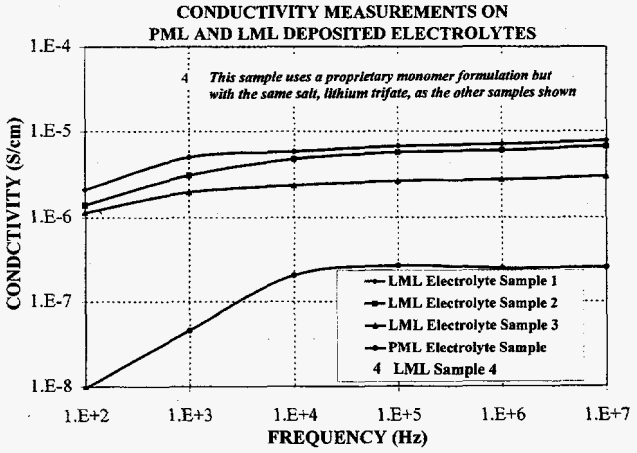

Figure 2. Either the LML (extruded) or PML (flash evaporated) process can be used to vacuum deposit polymer electrolytes.

Like Morita et al., we measured roughly a decade higher conductivity for the $LiPF_6$ mixtures compared to the $LiCF_3SO_3$ mixtures. However, the depth of cure was poor for these $LiPF_6$ mixtures. This gave rise to uncured interfaces at the bottom electrode when $LiPF_6$ salts were used. Future work will examine the $LiPF_6$ mixtures with

different photoinitiators and higher ultraviolet exposures. It is common to need different line speeds and photoinitiators to optimize cure for different monomer formulations in atmospheric roll coating. Therefore, this result is not surprising and is likely not indicative of any inherent inadequacy of $LiPF_6$ as a salt for use in these processes.

Note that the PML, flash evaporated electrolyte has conductivity about a decade lower than for the same monomer electrolyte solution deposited by the LML process. This is because not all of the salt gets carried over with the flash evaporated monomer. At the temperature of 245°C, at which we were operating the evaporator, the $LiCF_3SO_3$ would not be expected to evaporate at all on its own. We suspect that the Li^+ and $CF_3SO_3^-$ ions may be carried over as part of an evaporated complex of monomer and ether solvating the ions. The main advantages of being able to deposit the electrolytes with the PML process, as opposed to the LML process, would be better thickness uniformity (down to $\pm 1\%$ or less compared to a few percent) and much thinner films (100 Å compared with 10 μm). Whether or not these benefits offset the disadvantage of conductivities that are lower by more than a factor of ten will need to be determined for each individual application.

All of the polymer electrolytes deposited in this work were completely transparent in the visible range of the spectrum. This makes them viable for the electrolyte layer in electrochromic, switchable windows and mirrors. At PNNL, several years ago, we fabricated 35 cm X 35 cm electrochromic windows by sputter deposition of the electrochromic layer on glass, followed by an atmospheric application of a polymer electrolyte, with a further vacuum deposition of the counter electrode. We had hoped to demonstrate single pumpdown, in-line, deposition of a complete five-layer electrochromic device on a flexible substrate this year by carrying over our electrochromic batch coating technology. However, our batch coating process used sputtered W(Mo) tri-oxide and Nb_2O_5 as the electrochromic/counter electrode pair and we had problems obtaining sputtering targets this year and were forced to e-beam evaporate the oxides. The e-beam evaporated oxides failed to switch. We hope to continue this electrochromic work when we can obtain sputtering targets, as such an integrated process would eliminate the need for the three-step, vacuum-air-vacuum manufacturing technique required without the LML or PML technology.

Conclusions

The LML and PML processes have been demonstrated to produce polymer electrolyte layers in a vacuum deposition process that is compatible with simultaneous, in-line vacuum deposition by sputtering and e-beam evaporation. Based on our results, the conductivity to be expected from the LML process should be close to what one would measure if the same starting monomer electrolyte/salt mixture is polymerized in air. The conductivity for the PML flash evaporated electrolytes will be dependent upon the degree to which the salt, or solvated cation/anion complex, is carried over in the flash evaporation process. Thus, conductivities for PML deposited polymer electrolyte layers will need to be determined experimentally on a case-by-case basis. The ability to integrate these two polymer processes, with or without the added salts, into a single-step, multilayer vacuum deposition process with conventional vacuum deposition sources opens the way for lower cost production of a variety of products currently fabricated in multiple steps. Wide area electrochromic devices and lithium polymer batteries are the immediate target applications of this work.

Reference

M. Morita, T. Fukumasa, M. Motoda, H. Tsutsumi, and Y. Matsuda. 1990. *J. Electrochem. Soc.*, Vol. 137, No. 11.

Publications and Presentations

J.D. Affinito, P.M. Martin, M.E. Gross, C.A. Coronado, and E.N. Greenwell. "Vacuum deposited polymer/metal films for optical applications." *Thin Solid Films* (in press).

J.D. Affinito, M.E. Gross, P.M. Martin, C.A. Coronado, and G.C. Dunham. 1995. "High rate vacuum deposition of polymer electrolytes." In *Proceedings of 42nd Annual National Symposium of the American Vacuum Society*.

J.D. Affinito, M.E. Gross, C.A. Coronado, and P.M. Martin. 1995. "Vacuum deposition of polymer electrolytes on flexible substrates." Plenary talk given at the Ninth International Conference on Vacuum Web Coating, Tucson, Arizona, November.

Vegetable Oil-Pilot Scale Test: Transport Analysis

Glendon W. Gee, Gary P. Streile, Ashokkumar Chilakapati (Water and Land Resources)

Project Description

The objective of the LDRD project is to evaluate the feasibility of a pilot-scale field demonstration of the vegetable-oil-enhanced nitrate remediation methodology applied at an extraction well. Building on data from previous proof-of-principle tests, specific project objectives are to: 1) develop and test a modeling-based strategy for designing field tests and applications, 2) ascertain the suitability of previously obtained laboratory data for designing the field tests, and 3) identify potential field sites for the pilot-scale tests and use the design strategy to estimate the engineering parameters required to run the tests at those sites.

Technical Accomplishments

We reviewed the literature on the use of innocuous oil as a carbon/energy source for biodegradation enhancement, and we are currently collaborating with the USDA Agricultural Research Service (ARS) staff at Ft. Collins, Colorado, who have conducted a series of tests using vegetable (soy bean) oil as a carbon/energy source for denitrifying bacteria (Hunter and Follett 1995; Hunter et al. 1996). Batch reactor and column tests run by the ARS (designed as small-scale proof-of-principle tests for the overall concept) provided us with preliminary information regarding rates of nitrate removal, oil consumption, and microbial growth. We reviewed and analyzed data from these tests (Hunter and Follett 1995; Hunter et al. 1996; other unpublished data) for the purpose of a) determining appropriate mathematical forms for nitrate, oil, and microbial biomass rate laws; b) estimating the values of characteristic parameters contained in those rate laws; and c) determining the need for and design of supplementary experiments (to be conducted by PNNL and ARS) to improve quantification of the rate law parameters.

Based on our work with the ARS data, we have developed a strategy for designing the pilot-scale field test based on laboratory data and computer simulation. Two computer codes, RAFT (Chilakapati 1995) and STOMP (White and Oostrom 1996; Nichols et al. 1996), developed by PNNL, are being used as part of this design strategy. The refined strategy is as follows.

We use batch reactor and column data to determine appropriate conceptual and mathematical models for the overall denitrification process (i.e., the mathematical forms of rate laws for microbial growth, nitrate removal, and oil consumption that will be accommodated in the RAFT computer code for reactive solute transport). We then use the laboratory data (preferably batch reactor data) to estimate values for as many of the rate law parameters as possible. We also calculate theoretical values for as many of the rate law parameters as possible for comparison with the experimental values. We use the parameter estimation algorithms in the RAFT code to test goodness-of-fit of the model to the data and adjust the rate law parameters (within reasonable limits) if warranted. We performed one-dimensional RAFT simulations of the conditions of one or more column experiments to see if we can validate our reaction rate models and parameter values by generally reproducing the breakthrough results of these experiments. Further RAFT runs (fitting column data) are then done to estimate additional parameters in the transport equations. Once we are comfortable with the appropriateness of the reaction model and transport parameter values, we do RAFT simulations of an idealized field scenario consisting of steady one-dimensional water flow (at a rate representative of the expected rate of flow to an extraction well) containing nitrate (at a concentration representative of the expected concentration in the field) through a system with an initially uniform distribution of immobile oil throughout a given length. These simulations produce a rough estimate of what oil saturations and oil zone thicknesses would be needed to ensure that 1) the nitrate concentration in the groundwater would be reduced below the regulatory limit by the time the water is extracted from the well, and 2) the process would be effective for a specified length of time.

Next, once we know estimates of the required oil saturations and oil zone thicknesses, we conduct simulations with the STOMP computer code (for multiphase flow) to determine the oil injection protocols needed to establish such a zone around a well. These simulations are three-dimensional, in radial coordinates. Then, once we have determined how to establish an oil zone with the desired characteristics, we use the results from the STOMP simulations (i.e., the oil saturation distribution and the water flow velocity distribution) as inputs to additional RAFT simulations. These RAFT simulations indicate if the denitrification process will produce the desired concentration lowering in the extracted water for the desired length of time in the

pilot-scale field experiment scenario. Iterations between STOMP and RAFT simulations may be necessary to determine the ultimate design for the field test.

We tested the design strategy and the computer tools. The batch reactor and column data from the ARS proof-of-principle experiments led us to choose a dual-Monod model for the three rate laws describing the time-rate of change of microbe, oil, and nitrate concentration. This set of expressions contains five characteristic parameters: the maximum rate of microbial growth, the yield coefficient (for microbial biomass produced per amount of oil), the stoichiometric coefficient (for the amount of nitrate utilized per amount of oil), and the half-saturation constants for oil and nitrate. Theoretical values for the yield coefficient and the stoichiometric coefficient were calculated. Batch reactor and column data were used to calculate experimental estimates of the yield coefficient, stoichiometric coefficient, and maximum microbial growth rate. Because the batch data set available for use in the rate-law validation exercise corresponded to nitrate concentrations above the nitrate-limitation regime, the half-saturation constant for nitrate was fixed at zero, thus simplifying the goodness-of-fit calculations. Several RAFT simulations were run where different parameters were fixed at estimated values while allowing others (especially the half-saturation constant for oil) to be fitted by the code. A set of parameters was ultimately determined by this procedure that balanced goodness-of-fit to the batch data with consistency with the theoretical and experimental estimates of these parameters. In addition, experience gained in this exercise allowed us to develop a detailed plan for conducting future laboratory experiments specifically designed to determine all quantitative rate-law parameters needed for the field-design process.

Based on the estimates of rate law parameters, we then used RAFT to simulate the ARS column experiments. Estimates of additional parameters (beyond the rate law parameters) in the transport equations were first obtained from theory or from the experimental data. A series of RAFT simulations (using fixed parameter values) was conducted until the simulation generally reproduced the column effluent data. Experience gained in this exercise also led to the development of a plan for conducting future experiments specifically designed to determine values of some of the additional transport parameters (e.g., oil solubility and dissolution rate constant).

We also tested the use of the STOMP code for determining appropriate oil injection protocols. A desired oil zone thickness and saturation level was chosen, and STOMP simulations were conducted to determine the best way to achieve this oil distribution. The engineering variables investigated in the STOMP runs (both non-hysteretic and hysteretic simulations) were length of the well screen used for injection, location of the well screen with respect to the water table and a lower impermeable boundary, oil and water injection pressures, and the durations of different phases of the injection protocol. It was determined that, in order to establish an oil zone around the well that was composed of entrapped oil, there should be an oil injection phase, an oil redistribution phase, and a water injection phase. The simulations showed that oil injection with entrapment was feasible and produced estimates for engineering parameters required to achieve the desired distribution.

A few potential field sites for the pilot-scale demonstration were identified. However, at this time, we have not yet obtained site-specific data (e.g., groundwater velocities, hydraulic properties, nitrate levels) needed to conduct actual design simulations for the sites. However, based on work to date, we are satisfied that the strategy and available computer codes are adequate to assist in the engineering design of a pilot-scale test to remove elevated nitrates in situ.

References

A. Chilakapati. 1995. *RAFT: A simulator for ReActive Flow and Transport of groundwater contaminants.* PNL-10636. Pacific Northwest Laboratory, Richland, Washington.

W.J. Hunter, and R.F. Follett. 1995. "Use of vegetable oil to bioremediate high nitrate well water." pp 79-82. In *Clean Water - Clean Environment - 21st Century Conference Proceedings, Vol. II: Nutrients.* pp. 79-82. American Soc. Agr. Engrs., St. Joseph, Michigan.

W.J. Hunter, R.F. Follett, and J.W. Cary. 1996. "Use of vegetable oil to remove nitrate from flowing groundwater." *Trans. Am. Soc. Ag. Eng.* (submitted).

W.E. Nichols, N.J. Aimo, M. Oostrom, and M.D. White. 1996. *STOMP: Subsurface Transport Over Multiple Phases: Application Guide.* PNNL-11216, Pacific Northwest National Laboratory, Richland, Washington (in press).

M.D. White, and M. Oostrom. 1996. *STOMP: Subsurface Transport Over Multiple Phases: Theory Guide.* PNNL-11217, Pacific Northwest National Laboratory, Richland, Washington.

Publication

G.P. Streile, A.L. Ward, G.W. Gee, A. Chilakapati, M.D. White, and M. Oostrom. *Modeling the Use of Vegetable Oil for Enhanced Bioremediation of Nitrate Contamination.* Pacific Northwest National Laboratory, Richland, Washington (in preparation).

Risk and Safety Analysis

Data Quality Analysis for Risk and Environmental Assessment

John W. Buck (Strategic Environmental Management)

Project Description

In the current world of environmental modeling computer codes and high-speed computers, substantial volumes of environmental and risk information can be produced very rapidly. However, decision makers often express concerns over the quality assurance of the data input and significance of the results from these computer codes. There are sensitivity/uncertainty codes that provide information on how sensitive the results are to key input parameters and the relative uncertainty of the results to the input parameters. However, there are no codes that provide users and decision makers with information/ understanding of the input parameter values in relation to other parameters and typical environmental conditions. Users would like to see an audit trail of the input parameter values and how each parameter value relates to other values as a consistency check. This type of information can allow users to understand more fully their input information and conceptual site model before a run and compare the parameter values with typical environmental ranges of the parameter. This type of audit program should be built to fit different types of environmental and risk assessment codes. The proof of principle of this audit program will be applied to PNNL's Multimedia Environmental Pollutant Assessment System (MEPAS) to demonstrate technical and economic viability.

Technical Accomplishments

The objective of this effort was to develop an audit program that will:

- develop site conceptual models based on risk questions to be answered and site description
- define possible release scenarios and prioritize them based on site characterization data
- compare input parameter values with typical environmental ranges
- check for consistency of values between related parameters
- provide defensibility and traceability of results by creating an audit trail
- report the percentage of typical (provided by code) and user-defined (site-specific) values used in the analysis.

A prototype software package, Audit Code, was developed that links with MEPAS (Figure 1). Audit Code allows the user to develop the conceptual site model based on the environmental/risk question to be answered and available site data. Once the conceptual site model matches the question and data, Audit Code checks data consistencies and boundaries to ensure a viable model run.

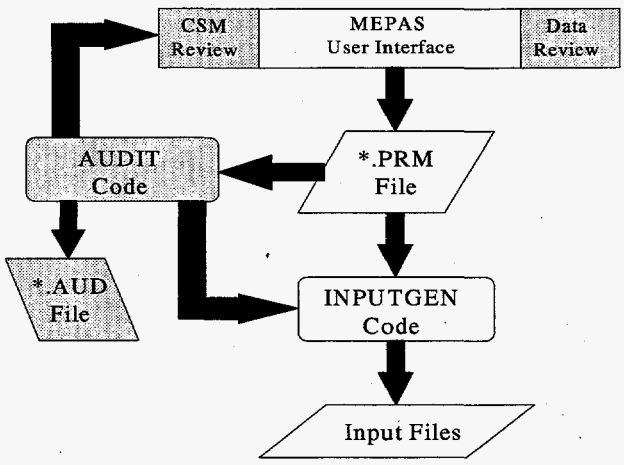

Figure 1. Audit Code linked with MEPAS. Shaded areas indicate new or modified software during this effort.

After the input data for the model (i.e., MEPAS) has been entered, Audit Code provides an audit report that the user can use to check the information or an independent auditor can use to understand the problem and question being modeled. Possible release scenarios based on the conceptual site model and available site data are defined by the software and prioritized to provide the user with information on how to model the problem.

This output file from Audit Code provides defensibility and traceability of the results, including references for the data and key assumptions. A comparison site-specific input data to "representative" input data allows the reviewer to understand the specificity of the results to the site problem.

Risk-Based Hydropower Refurbishment Methodology

Truong V. Vo (Decision, Safety and Risk Management)

Project Description

The objective of this project was to develop a reliability and risk-based method and application that could be used in support of rehabilitation and maintenance programs for power industries. The goal of the project was to develop a risk-based methodology adapted to the hydropower industry that could be used to evaluate requests for major rehabilitation funding.

This methodology must use formal risk assessment techniques to estimate and prioritize the safety and economic risks of failures of aging equipment. This will allow comparison of the risks of in-service failure against the risks and costs of refurbishment/replacement activities.

Technical Accomplishments

This methodology was developed using information provided in the Corps of Engineers Major Rehabilitation Program Guidance, and is consistent with current risk- and reliability-based programs used by other power industries.

The risk-based rehabilitation and maintenance process captures all necessary technical elements including engineering reliability analysis, benefits analysis, and environmental and economic models as they relate to hydroelectric power rehabilitation and maintenance projects. This risk-based process and application has been developed so that it would be easy to implement and lends itself to software application. This risk-based process is applicable to all power industries. A block diagram representing the methodology is shown in Figure 1.

As a result of the development, the U.S. Army Corps of Engineers subsequently requested PNNL to perform a study relating to the Corps of Engineers' major rehabilitation program for reliability and efficiency improvements at hydroelectric power stations in the United States. This developed rehabilitation and maintenance methodology was used as a foundation for information review to determine what information currently exists to support the methodology, and to determine what information needs to be developed to support the methodology.

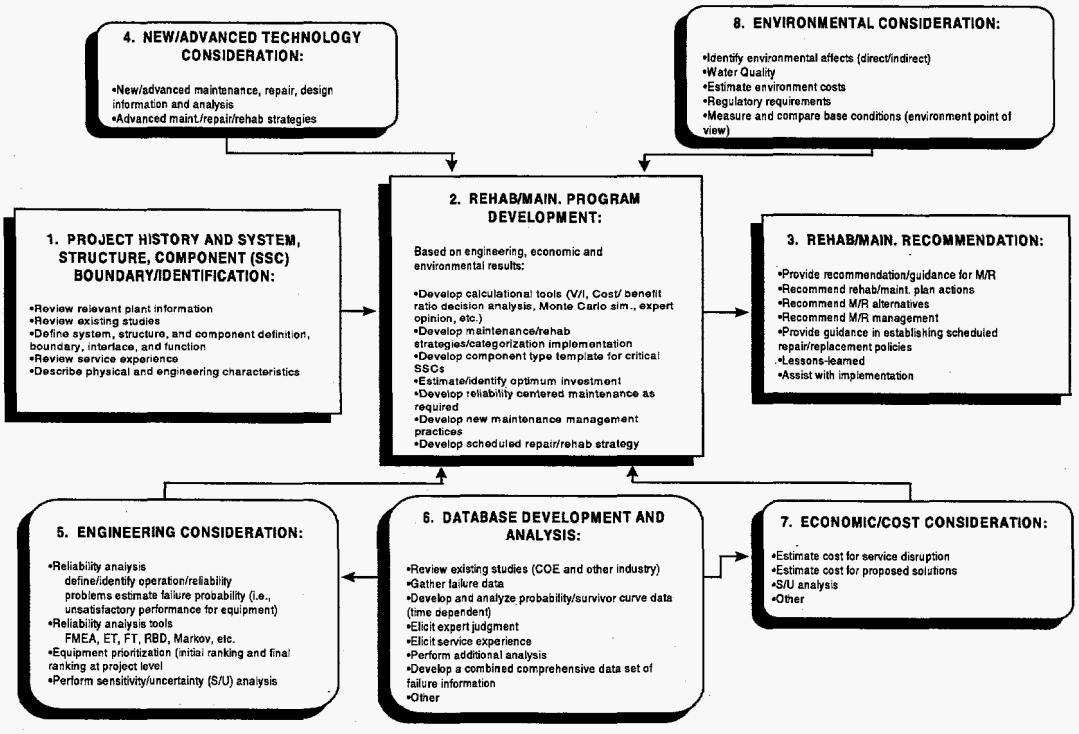

Figure 1. Risk-based rehabilitation and maintenance proposed methodology.

The results of document review show that there is a wealth of information available regarding reliability and risk analysis and economic analysis that would be useful in support of the Corps of Engineers' rehabilitation and maintenance program. Probabilistic risk assessment and reliability-centered maintenance for hydroelectric power have been developed by PNNL and the Electric Power Research Institute (EPRI). The results of the probabilistic risk assessment have been synthesized with environmental and economic consequence analyses to produce results in terms of economic risk. Reliability studies have been performed by the Corps of Engineers and EPRI on various hydroelectric power components and structures, reliability study guidance has been provided by the Corps of Engineers, and reliability data for hydroelectric power equipment are available from various data sources such as from the GADS data base, IEEE, COE, EPRI, and PNNL studies. Economic analysis guidance has been provided by the Corps of Engineers, and several excellent studies have been performed by the Corps of Engineers and its contractors. The methodologies used in these economic studies have been used in support of the Corps of Engineers' rehabilitation and maintenance program. Additionally, there has been a substantial amount of research done by other power industries that would be very useful for the development of the rehabilitation program.

The results of this study also show that there are some areas that could be improved for application to rehabilitation and maintenance and/or nonroutine maintenance programs. In some cases the methodologies could be altered to make the project relate more closely to rehabilitation and maintenance work, in other cases more data need to be collected to reduce the uncertainties in the results. The most significant data collection effort that should be performed in the future is to develop time-dependent reliability data for key hydropower components. The process would involve collecting and combining multiple data sources using Bayesian updating techniques. This data development effort can further be used for verifying and validating ongoing/existing studies.

At present the Corps of Engineers has many good tools for determining individual inputs to overall project cost (e.g., power replacement, construction, environmental, and interest), however the methods for combining these factors and accounting for uncertainties do not appear to be well defined for nonroutine maintenance programs. Based on these observations, PNNL has recommended several follow-on efforts to the Corps of Engineers. The Corps of Engineers has accepted these recommendations and has subsequently tasked PNNL with developing reliability data for several hydroelectric station components.

In summary, PNNL has developed a risk-based methodology for use in rehabilitation and maintenance decisions. PNNL also performed a document review to determine what follow-on work is required to implement the proposed methodology, and made these recommendations to the Corps of Engineers. The Corps of Engineers has accepted the recommendations and asked PNNL to further assist in the development of the data necessary to implement the proposed methodology.

Publication

T. V. Vo, T. R. Blackburn, L. O. Casazza, T. M. Mitts, and H. K. Phan. 1996. "Summary of studies, research, and reports in support of Corps of Engineers' rehabilitation and Maintenance Programs." Pacific Northwest National Laboratory, Richland, Washington.

Socio-Technical Systems Analysis

An Integrated Model of Organizations and Information Technology in the 21st Century

Mary D. Zalesny, Larry O. Levine, Peter A. O'Mara (Medical Technology)
David D. Hostetler (Information Technology)

Project Description

The objectives of this project were to integrate research and thought on organizational design and functioning and information technology and to define critical information technology and organizational issues that will confront organizations early in the 21st century. Analysis of the information gathered from research literature and experts will help DOE and its national laboratories focus research and technology to support anticipated needs of current and potential stakeholders and clients.

Technical Accomplishments

Political, economic, societal, and technological transformations during the 20th century have expanded our horizons while shrinking our world. Globally, political, organizational, and economic boundaries have fallen, creating new alliances and partnerships that have changed the economic playing fields. "International" is no longer a subarea of business; it defines business. Social and political change have altered the face of the work force. Technological innovations have narrowed geographical distances, widened socioeconomic gaps, and have unalterably changed how we live and work and what we value. In the face of increasingly rapid change, understanding where we have come is essential for planning where we will go.

Our approach was two-pronged: 1) review the scientific and popular literature in information technology and organizational science for evidence of integration between the disciplines, and 2) interview experts in both disciplines about the state of each field and their integration. The literature review led to some early observations. Overall, the two disciplines remain relatively unintegrated. Additionally, much of the information technology literature:

- is primarily technically oriented and descriptive of hardware and software
- describes successes and failures in application or implementation
- tends to be integrated with organizational science only in the area of management of information systems
- suffers from publication delays
- can be outdated very quickly.

Similarly, the organizational science literature

- focuses on a lot of things other than information technology
- examines impacts of information technology on organizational processes and ignores the features of information technology
- lags behind emerging organizational issues
- suffers from publication delays.

Because of the limited usefulness of the published literature, expert interviews became our primary source of information for this project. Twenty-eight organizational science and information science experts from academe and information technology users in business organizations were interviewed during July and September. Academicians were asked the following questions:

1. What major innovations, events, changes, or theories over the past 25 years have had the greatest impact on work and/or organizations?
2. What models/theories about work, organizations, or information technology have withstood the test of time—being relevant today and for the future?
3. What is the role of information technology in work and organizations? How has this role evolved over time? What changes would lead to a significant increase in work and organizational effectiveness?
4. What one thing would you recommend organizations do to prepare for the future?

Business experts were asked questions 1, 3, and 4 above and were also asked:

a) What business practices or management philosophies have withstood the test of time—being more than fads and relevant for organizations today?

b) What are the biggest mistakes organizations make with (or in using) information technology?

A content analysis was performed on the experts' responses to these questions. A brief summary follows.

Question 1. Political and economic events dominated the responses concerning the major impactful events of the past 25 years, including the end of the Cold War, the emergence of the economies affected by WWII, and the emergence of new organizational forms. Not surprisingly, the biggest innovations were the microprocessor and the personal computer. Major changes included the internationalization of life and demographic and socioeconomic changes in first and third world country populations. Cognition, cybernetics, genetics, social constructionism, and motivation theories dominated the major theories of the past 25 years.

Question 2. Enduring theories and business practices mirrored each other, with the business practices generally representing the application of the theories the academicians cited. Included among the academic theories were motivation, human relations, contingency, and systems. Enduring business practices included employee empowerment, total quality management, customer orientation, and balancing of stakeholder interests.

Question 3. Almost all of the responses to this question could be summarized by information technology playing a role as a resource or as an intervention into human activity. One obvious example of these roles is the rapid and widespread communication enabled by information technology that has changed work and the speed with which many tasks are completed. Information technology was also seen as playing a potentially dangerous role in creating illusions about information data bases and undermining the legitimacy of intuition and wisdom. Biggest mistakes that organizations made, as seen by business user experts, reflected the perceived dangers of information technology (above), and a lack of understanding of the purposes for which information technology is desired.

Question 4. Recommendations for what organizations could do to prepare for the future were very wide-ranging. They could be broadly categorized as those related to internal organizational processes, the organization's interaction with its external environment, technology use, and general issues related to strategic planning.

Conclusions

Information technology and organizational science experts generally made political, economic, and technological attributions for the major impacts on work and organizations when viewing the last 25 years. Although the experts' perspectives were clearly geocentric, their insights and observations underscore the importance of a very broadly bounded/defined external environment in shaping the work done, the characteristics of the people who do it, and the organizations that still provide a basis for it to be done. Their recommendations suggest that organizations revisit the "basics" of organizing and operating their enterprises. Preparation for the future means a reexamination and rethinking of an organization's mission, management philosophy, strategy, markets, systems and technologies, work force, and environment—all of the environment. The reexamination should be from the perspective of understanding whether the characteristics of the above areas are still relevant for the organization and for the environment which currently exists and will likely exist at least for the near future.

Implications

We see two major implications for DOE and its laboratories from this project. First, from an organizational standpoint, DOE must contend with the same issues and changes that experts describe as impacting all organizations. In addition to its usual approach to strategic and tactical planning, DOE should carefully consider the recommendations proposed by the information technology and organizational science experts.

Second, the changes occurring globally in work, organizations, and societies have consequences for DOE's strategic focus in all of its mission areas. Most evident in the experts' observations were implications for DOE's energy mission. Changes in where people work and what work they do will have energy consequences related to commuting and transportation patterns. This may influence the magnitude and location of demands for fossil and other fuels. It may also impact the acceptance of alternative "fuels" (e.g., the electric car). Air and water pollution may continue at present levels or increase, but the greater change may be in where they occur. All of the above are potential scenarios from an aging population and the potential for widespread "virtual" work and organizations.

Future Considerations

This project provided some insights into the future and into the integration of information technology and organizations that will be relevant to support organizations when the future arrives.

Ethical, Legal and Social Issues Surrounding Microbial Biotechnologies

Gordon R. Bilyard (Environmental Policy and Planning)

Project Description

This project studied legal and social concerns that are relevant to the research, development, and deployment of microbial biotechnologies for environmental remediation.

Technical Accomplishments

Legal and regulatory issues associated with microbial biotechnology arise from three sources. First, the United States has no coherent policy that defines its national biotechnology goals. Because Congress has not set national goals, government agencies and private industry face difficult decisions about investing in the research and developing of new biotechnology products. Very little information exists regarding the possible threat genetically altered or exotic organisms pose when introduced into native ecosystems, and technology developers may face uncertain liability and public opposition. Citizens aware of the damage caused by exotic species worry that underregulation of field releases of genetically altered organisms may result in similarly severe and unforeseeable problems.

Second, the United States has no coherent set of statutes related to bioremediation, but instead regulates bioremediation largely within the scope of existing statutes drafted for the regulation of other activities (e.g., protection of surface waters from contamination; regulation and permitting of chemicals for industrial, commercial, and private use). These statutes may overlap or impose conflicting requirements and inappropriate performance standards. Cleanup projects must often operate under overlapping agency oversight of remediation activities.

Third, the U.S. Environmental Protection Agency and certain state governments are now moving toward the adoption of risk-based policies and approaches to regulatory compliance. These policies and approaches are being adopted and implemented within the framework of the existing "command and control" statutes and regulations, often necessitating the development of new, unique approaches to regulatory compliance.

PNNL and BSRC staff prepared a report (Bilyard et al. 1996) that synthesizes legal and social concerns relevant to microbial biotechnologies at Hanford, and sets those issues within the larger national context of ethical, legal, and social issues related to bioremediation. This report identifies specific issues related to bioremediation technologies, including those involving the use of plants; native, naturally occurring microbes; non-native, naturally occurring microbes; genetically engineered organisms; and microbial products (e.g., enzymes, surfactants, chelating compounds). Issues fall within the following general categories:

1. U.S. biotechnology policy and the regulation of field releases of organisms
2. U.S. environmental laws and waste cleanup regulations
3. intellectual property and patenting issues
4. technology transfer procedures for commercializing technology developed through government-funded research
5. stakeholder concerns about bioremediation proposals
6. methods for ensuring public involvement in technology development and deployment.

Reference

G.R. Bilyard, G.H. McCabe, K.A. White, S.W. Gajewski, T.F. Grant, P.L. Hendrickson, J.A. Jaksch, H.A. Kirwan-Taylor, M.D. McKinney, F.B. Metting, F.A. Morris, M. Skumanich, and L.A. Stevenson. 1996. *Legal and Social Concerns to the Development of Bioremediation Technologies.* PNNL-11301. Pacific Northwest National Laboratory, Richland, Washington.

Statistics and Applied Mathematics

Environmental Statistical Sampling Design Framework Tool

Nancy L. Hassig, Brent A. Pulsipher, Richard O. Gilbert, Rick J. Bates, Robert F. O'Brien, Dennis R. Weier (Environmental Statistics)

Project Description

Several software tools exist at various stages for developing a statistical sampling design when characterizing a site with spatially heterogeneous potential contamination. Each of the tools is applicable for specific sampling objectives, decision criteria, and/or underlying statistical assumptions. Practitioners are confused about which tool is appropriate for their particular application and very little guidance is available to non-statisticians on which tool, if any, may meet their needs. This project will develop a decision framework that is capable of leading an environmental remediation practitioner through the process of determining which tool should be selected for determining sampling requirements and defining an optimal sample design. The framework will have a secondary benefit to the principal investigators. It will help them identify holes in the current offerings where new sampling design tools should be developed. The framework will also permit the developers to sell the concept of an overarching design tool that is capable of pulling together existing plus newly developed sampling design software tools.

Technical Accomplishments

The resulting product from this project was a Web site that contains the sampling design framework.

The site contains a decision tree for a standard sampling design problem, as well as links to textual descriptions of alternative sampling designs referenced in the decision tree. The problem addressed in the example decision tree currently on the Web site is to select a sampling design when sampling a single population to estimate a mean, percentile, or spatial pattern. In a sequence of screens presented to visitors to the Web site, a series of yes/no questions are asked about the sampling goals and the nature of the site to be sampled. Based on the responses to these questions, the user is told which class of design would best achieve the sampling goals given the conditions at the site. Hypertext links are interspersed throughout the decision tree that point the user to additional information on a topic and tools which could be used to implement the selected design. We eventually will provide links to downloadable software that can be used to implement the selected design.

In order to develop the final product for this LDRD project, the project team completed the following tasks:

- A matrix of key questions and potential responses to the questions that experienced statisticians would ask to understand the sampling problem and the site conditions. In fact, several matrices were developed that reflect the different perspectives of members of the project team and how they would approach design problems.

- A logic diagram for a hypothetical problem. The hypothetical problem selected was the following: design a sampling plan for finding buried drums in a field.

- A matrix of standard sampling designs and their strengths/weaknesses. Again, multiple matrices were developed that reflected the experiences and expert knowledge of the project team members.

- An inventory of available tools, primarily software tools, for calculating sample size, strata size, power calculations, and other sampling design components.

These tasks were reviewed by the project team members and consensus was reached on issues where there were differences. The team members identified a generic sampling design problem as the focus for the decision tree that is currently on the Web site. In the future, we will add additional decision trees that deal with other sampling design goals and site conditions. Eventually, the framework will be comprehensive in that it can match the most common problem/sampling goal combinations to the appropriate sampling designs.

Thermal and Energy Systems

Advanced Numerics and Visualization for Power Systems

Donald J. Hammerstrom, Jeffery E. Dagle (Analytic Sciences and Engineering)

Project Description

The progress that some electrical utilities have made in developing more comprehensive access to power system operating data has outstripped their means for extracting and distributing the imbedded information. Thus, system control centers are progressively inundated by data that they are not yet able to use effectively. Utility restructuring and other factors promise to sharply increase the need for measurement-based information, while contracting the time frame in which it must be produced and incorporated into decision processes. These factors also dictate that cost recovery for the requisite technology investments be prompt and low risk.

The primary focus of this activity is to develop and demonstrate the application of visualization tools to represent power system analysis and simulation results, with the overall objective of improving effectiveness of these tools with improved interpretation of data using scientific visualization techniques. In addition, advanced numerics play an important role in communicating complex data in a manner that can be easily comprehended, augmenting man-machine interfaces for power system analysis tools. These technologies are also applicable to other areas of power system operations related to the DOE initiative in real-time power system control.

The application of wavelet transform methods to the identification, compression, and recognition of anomalous electrical power system events was the numerical method of greatest project interest in 1996.

Background

The application of PNNL scientific visualization expertise to power systems has been demonstrated for a variety of applications. Visualization can increase comprehension and insight of complex and intricate processes valuable for conveying information in operational, planning, or public relation arenas. Recent breakthroughs in scientific visualization technology, including both hardware and software, have led to imaginative and effective ways of conveying information for a variety of applications, leading to better ways of envisioning information.

The major advantage of visualization is that it directly engages the powerful pattern recognition capabilities of the human eye-brain system. An effective visual representation helps humans generate immediate insights from data, replacing a large part of the processing with computers. Visualization also permits the presentation of much more data to the user. Utilizing human pattern recognition skills, and by communicating the global organization of the results, as well as the results themselves, visualization permits a rapid grasp of the results and their meaning. Natural encoding of the information is important, as it represents data that ties into an existing mental pattern common to most users and produces a meaning which is intuitively apparent.

PNNL has extensive expertise in scientific visualization technology, developed for a variety of applications. This project is intended to build upon this capability to extend our visualization competency into power system applications, complementing advances in visualization techniques which are being developed by the utility industry for use in both operational and planning environments. As a natural extension of investigating advanced visualization methods, the goals of this project also include investigating advanced numerical methods associated with power system planning software.

Technical Accomplishments

The first year of the project (FY 1994) was primarily a scoping period to evaluate visualization tools and compare issues associated with the various tools available.

Several activities were completed during 1995 including: 1) a visualization package for eigenvalue analysis software was demonstrated, 2) an interactive interface for the portable dynamic analysis and design system was developed, 3) methods for ambient mode analysis were investigated, 4) the possibility of combining fast/slow dynamics in time-domain simulation analysis tools was evaluated, and 5) an automatic generator control simulation software was appraised.

Activities in FY 1996 included the following areas which are described in detail below:

- continue investigation of ambient mode estimation by supporting an Associated Western Universities summer fellow

- gather both orthogonal and nonorthogonal wavelet and wavelet packet software tools

- gather real-wide-area electrical power system data appropriate for training real-time recognition tools

- develop wavelet compression software suitable for compression of electrical power system event data.

Research on signal analysis methods to identify the electric power system dynamic characteristics from measured ambient data was performed. One of the approaches studied uses a high order finite impulse response whitening filter on ambient data where models can be identified as the dominant polynomial roots in the frequency band of interest. Results of this research indicate that system identification using ambient data can approach the accuracy of perturbed system-response identification as would be performed with Prony analysis software tools. Ambient data analysis could become part of a suite of real-time analysis tools for observing ambient electrical power system data and reacting to avoid risky operating modes.

The majority of 1996 activity focused on bringing wavelet and wavelet packet transform methods, understanding, and software into the power system arena. Wavelets can be considered transform bases that bridge the gap between time domain data representations, consisting of a series of time impulses, and Fourier bases, which are simple translated and compressed sinusoids. An impulse in the time domain requires only one time domain coefficient but requires many Fourier coefficients. Conversely, a perfect sinusoidal oscillation may require only one Fourier basis but requires many time coefficients. Signals that are banded in both time and frequency are more efficiently represented by wavelets.

Wavelets were investigated for three attributes of importance to electrical power system operation: 1) wavelets might readily identify the onset of disturbances because the onset of many disturbances is marked by sudden activity at small wavelet basis scales; 2) wavelets serve as good prefilters for recognition tools because the wise choice of a wavelet places most of a signal's interesting and recognizable features in relatively few wavelet bases and coefficients; 3) wavelets and wavelet packets can be very effective at compressing data for archival purposes. This last point is particularly important for the electrical power industry due to the great number of system recorders and the high data collection rate needed to observe electrical power signals.

These three attributes are part of our vision for an archive walker, a software tool that scans wide area power system data either off- or on-line to identify, recognize, and compress power system events. The tool might eventually notify operators of anomalous events and initiate a remedial action. The archive walker would relieve operators from the task of scanning enormous data sets and choosing what might be saved or discarded.

Many wavelet software tools are now available on the Internet for noncommercial purposes. The MathWorks MatLab Wavelet Toolbox was beta tested through this project, and the software was purchased when it became available later in the year.

Bonneville Power Administration assisted us by compiling and sharing wide area monitor data collected for more than 30 power system events. More than 90 data channels were available for each event, and each event spanned approximately 2 minutes. The categories of power system events included generator trips, AC line outages, DC intertie events, LADWP Adelanto fault tests, Chief Joseph brake insertions, and miscellaneous. Wavelet packets in conjunction with the recognition tool CART were able to readily distinguish Chief Joseph brake insertions, generator trips, and the miscellaneous categories. Many of the data sets displayed more than one event characteristic due to cascading power system responses, and these multiple events confounded attempts to accurately train the categorization tool.

Wavelet methods proved very effective for event data compression. Software was coded to successively choose the best wavelet dictionary from a basis library and choose the best basis set from that dictionary. The number of bases needed for a signal representation was chosen by minimum description length as described in N. Saito's 1994 Yale University dissertation. Consistently 5% to 10% of the original number of coefficients were necessary to accurately represent the real power system data signals. This compression rate is of great interest for storage needs of large power system data archives.

Artificial Intelligence for Power System Control

Robert G. Pratt (Engineering and Analytic Science)

Project Description

We are developing two new analysis tools targeted toward advanced electric distribution system planning and operation. The primary analysis tools currently envisioned are:

1. a distributed utility least-cost resource screening tool designed to analyze gensets, storage, and customer-side alternatives to traditional system capacity upgrades

2. short-term distribution load forecasting incorporating a group-typing methodology that clusters metered customer load shapes and maps the clusters to customer characteristics, providing a means of estimating load shapes for customers without metered time-series loads.

The tools being constructed, the data needed, and the benefits for the utility are outlined in more detail below.

Technical Accomplishments

Distributed Utility Least-Cost Resource Screening Tool

This tool will envelop a distribution load flow tool with data and a framework for 1) estimating customer-induced loads at any and all points in the system; 2) sizing and siting distributed utility resources such as gensets, fuel cells, storage, and customer efficiency and load control; 3) simulating system utilization over time; and 4) comparing the net life-cycle cost of alternative distributed utility options to traditional capacity upgrades. We are seeking to develop an open-architecture software system as a family of stand-alone but interacting programs. These will make up a toolkit whose elements can be rearranged to conduct other analyses such as development and testing of dynamic reconfiguration control algorithms, long-range distributed utility resource planning and potential studies, load test beds for technology development and penetration studies, etc.

Three types of data are required to drive this tool:

1. capitalize distribution system configuration data for a planning area encompassing that served by a substation, including the properties and capacities of all equipment and conductors and the physical layout of the system, including customer locations. This may be in the form of "one-line" data; GIS formats are not required.

2. customer billing data for each customer in the planning area for the prior 12 months, with identification of customer class membership (see next item).

3. customer class load research data (sometimes referred to as "PURPA data") in the form of metered 15- or 30-minute interval kilowatt loads for 1 year for each class of customer represented in the planning area, including identification of any specific customers in the planning area who are part of the metered sample.

We constructed and tested the dynamic load estimation process and linked it with a load flow tool that performs an engineering analysis of the distribution system. We added identifiers to the system configuration data that map customers to the billing data and customer class load research data used to estimate loads. This mapping, termed here group-typing (see discussion of Distribution Load Forecasting, below) is then used to drive load estimates for any time of day and year (historically) or for any weather condition (in a forecasting mode) for each customer served by any portion of the distribution system being analyzed. The load estimates are dynamically added to the configuration data so that the load flow tool can then base its analysis on them. We have added functions that allow arbitrary patterns of load growth or load reduction (through customer efficiency measures, load control, real-time pricing, etc.) to be applied to each customer on an hourly basis. These capabilities support analysis of any (or all) critical hours of each year through the investment horizon to compare alternative investments with traditional upgrades.

The software supporting these capabilities consists of a set of independent, modular programs that communicate through input and output files. They are written in the *perl* script language that runs in both the UNIX and Windows operating systems. When utilities have digitized their configuration data, it is generally in a form compatible with the specific load flow tool they use, so we have anticipated and planned for the need to "plug in" the tool favored in place of the one we used in development.

In addition to this load estimation process, we have begun development of an economic engine that will allow detailed, engineering-based optimizations of alternative distribution investments to be driven automatically from a data base of technologies. We have gathered extensive transmission and distribution cost data and distributed

utility technology costs and performance metrics for this system. We have also developed a methodology for conducting these complex nonlinear optimizations, which can include variations in technology, siting, sizing, and incremental versus lumped investments, by a highly parallel process that allows scenarios to diverge at key decision points and continue computing operating costs and savings until proven not cost-effective against a competing scenario.

Short-Term Distribution Load Forecasting

General Forecasting Methodology. We have previously demonstrated a method for automatically characterizing and forecasting loads for customers whose loads are time-series metered. This method involves fitting a neural network to the loads on the basis of time-of-day, time-of-week, outdoor temperature, and recent load history. We have also developed a non-linear non-parametric statistical method (multi-dimensional lowess response surfaces) that is analogous to a neural network, and shown that it also can accurately forecast loads. These methods appear generalizable to prediction of loads from a broad population of buildings.

However, it will take some time before such data is readily and universally available in usable form for all customers. Until then, the major technical challenge will be to develop an analogous forecasting capability for customers that are not time-series metered. The best available information on which to estimate loads for these customers is described in the previous section. It is only as good, however, as the mapping (or group-typing) scheme that is used to find another customer that is metered proxy. Our efforts to improve group typing are discussed below.

Group-Typing Methodology. When estimates of customer loads are needed for distribution system planning or control purposes, and when metered time-series loads are not available for a given customer, then the loads must be estimated from available information. Currently, this entails 1) billing data which provides monthly energy consumption and possibly peak demand, and 2) the customer class of which the customer is a member. Typically, load estimates are then based on the average load shape for the customer class, scaled to match the energy consumption of the specific customer. The implicit assumption in this process is that the load shapes of all customers in a given class are reasonably similar.

In this effort, we are attempting to improve this process by replacing this assumption with a statistical grouping of customers with similar load shapes. We have developed techniques that create these groups (group-types) by looking at the actual metered loads and then identifying characteristics that determine which group-types customers should be assigned to minimize the variance in each group. Thus, we are further segmenting or modifying the customer class assignments to better explain loads and improve the precision of the load estimating process for customers that are not metered. Whereas traditional customer segments are used for system load forecasting and demand-side management potential assessments, much more accurate group-types are needed for designing distributed utility alternatives for small groups of customers in the distribution system and forecasting loads for its control.

The data required to drive this tool include:

1. all available individual customer metered time-series (15-, 30-, or 60-minute interval) kilowatt loads used by a utility for class load estimates for a period of 1 year so that they can be statistically processed

2. the current customer class membership of each of these load series

3. a set of as many uniform characteristics data on these customers as possible.

We also intend to identify the types of characteristics data a utility has, is planning to get, or could reasonably obtain on *all* customers so that we can bound the upper limit of detail used to classify group-type membership and quantify the value of obtaining additional key variables.

Status of Development. We have developed and tested three group-typing methods using a population of 150 commercial buildings. The best of these methods promises substantial improvements beyond the base case load research data sample frame in the ability to predict load shapes as a function of customer characteristics. What is needed now is a test using an actual set of class load research data, to quantify these improvements and establish the absolute overall accuracy achievable.

We have also developed and demonstrated a web-based customer load forecaster for a building utilizing the lowess response surface model. The forecast is developed by obtaining and processing the weather forecast from the Internet and posting the results on a web page. Also posted are yesterday's predictions compared with the actual metered loads, along with a second "forecast" based on the actual weather data (metered on-site) to differentiate the error associated with the weather and the load forecasts.

Expected Results. The results of this analysis when applied for a utility are: 1) a refined set of customer load shape segments (group-types), 2) quantification of the reduction in variance of these group-types compared to the current customer class approach, and 3) models of customer group-type membership based on readily available and future customer characteristics data.

Distributed Power System Dynamic Controller

Jeffery E. Dagle (Energy)

Project Description

The deployment of distributed load control devices, such as smart controls for end-use equipment, could enhance the dynamic stability of the western U.S. power grid. The potential value of distributed versus centralized grid modulation has been examined by simulating the western power grid under extreme loading conditions. In these simulations, a scenario in which active grid stabilization enables power imports into the southern California region to be increased several hundred megawatts beyond present limitations is analyzed. Modeling results show distributed load control is up to 30% more effective than traditional centralized control schemes in achieving grid stability.

Technical Accomplishments

A novel approach has been conceived by PNNL to combine the objectives of flexible AC transmission systems (FACTS) and the technologies inherent in demand-side management (DSM) to provide a distributed power system dynamic controller. This technology has the potential to dramatically offset major investments in FACTS devices by using direct load control to achieve dynamic stability objectives. A primary distinction between the end-use load control for stability enhancement and conventional demand-side management is that for stability enhancement, the load would only need to be turned on and off for a second or two several times over a few minutes. If deployed properly, such control action would be transparent to the consumer, and could provide significant benefit to wide-area dynamics. It is envisioned that several classes of end-use load could be similarly controlled using this technology. A schematic of this concept, and how it contrasts with the conventional approach, is given in Figure 1.

The end-use load controller was modeled in the Extended Transient/Midterm Stability Package (ETMSP), developed by the Electric Power Research Institute. Consistent with standard transmission planning practices applied by the utility industry, the simulation and analysis in this study uses a full model representation of the western North American power system. Developed by WSCC member utilities, it represents heavy loading conditions and infrastructure projected to be in place near the turn of the century. Based on the results of these planning studies, stability constraints that limit the amount of power which can be safely imported into southern California are determined.

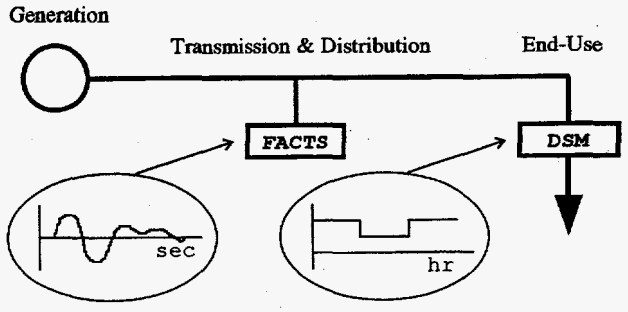

(a) Conventional approach

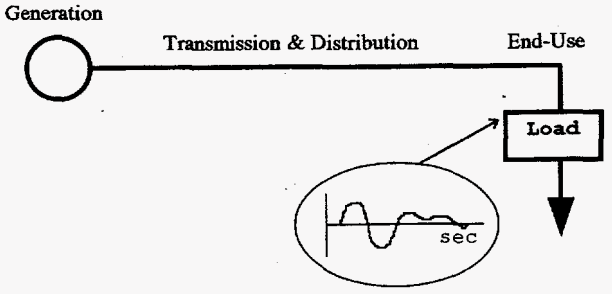

(b) End-use control for dynamic controller implementation schematic

Figure 1. Distributed dynamic controller implementation schematic.

A case was developed in which 10 modulation devices were deployed at key sites throughout southern California. The sites were selected to distribute the overall control power throughout the region at individual sites which have sufficient transmission capacity to the bulk power system. Therefore, most sites had multiple high voltage lines (230 kV or equivalent) connecting them to other sites, and were usually close to 500 kV bulk power substations.

Following the methodology described above, appropriate feedback signals were chosen and the controller was tuned. Tuning the controller requires several steps and involves the use of modal analysis tools and classical feedback-control design techniques. After an initial controller is designed, several simulations are performed to optimize its performance (selecting sufficient gain, for instance, which is difficult to predict when simulating highly complex, nonlinear dynamics). When the properly tuned and optimized controller has been tested, a suite of simulations are performed with progressively smaller limits to determine the minimum modulation power needed to result in a marginally stable response to the critical contingency.

It was shown that the case with 10 devices providing 43 MW of modulating power (positive swings only) was sufficient to provide a stable result. With an aggregate combined capacity of 430 MW, this is a 30% improvement over the 600 MW needed for the single modulating device. Another set of simulations with 100 control points yielded similar results.

A series of simulations were performed to compare centralized and distributed feedback modulation control. The results of these simulations indicate that both approaches require similar controller deployment to achieve the same transmission capacity enhancement.

If the total cost of the distributed control system for increasing southern California transmission capacity by 400 MW is less than $50 million, it is competitive with alternate conventional methods of achieving the same result. Because this analysis indicates 430 MW of distributed load control is needed to achieve this goal, the target break-even cost is therefore about $116/kW.

A detailed assessment of end-use control potential in southern and northern California was performed. Based on this analysis, for example, household refrigerators contribute about 1250 MW to the southern California regional peak load; each one contributing 0.17 kW on average (taking into account demand and diversity factors). Therefore, in order to achieve the 430 MW of distributed load control described previously using only residential refrigerators, about 34% of all refrigerators would need to be equipped with control hardware. If the per-unit cost were less than about $20, this control implementation would be cost-competitive.

Another example is residential central air conditioning, which contributes 3752 MW to the regional southern California 3:00 to 5:00 p.m. peak demand, each unit contributing 2 kW on average. In this example, the distributed load control target can be achieved with only 11.5% penetration, and each individual controller can cost $230 and meet the break-even target.

The distributed end-use load control concept was tested experimentally in a laboratory setting at PNNL. An unmodified household refrigerator was chosen as the subject appliance. The refrigerator was fitted with a relay switch to facilitate the cycling of the distributed controller. In this experimental setup, the power to the entire appliance was switched. The voltage and current supplied to the refrigerator were then instrumented and monitored. The appliance was run through a series of tests aimed at determining the response characteristics of the load as it applies to power system dynamics. A residential-type air conditioner was obtained and configured for testing.

This study evaluated end-use load control as a means of increasing power transfer on selected transmission paths in the southwestern United States power system. Power modulation to stabilize electromechanical power swings is shown to provide increased transmission capability, enabling increased power imports into southern California. In addition to stability enhancement, end-use load control can be used to augment remedial action schemes, and is well suited to provide other benefits such as load leveling, automatic generator control, spinning reserve, and voltage support. The results of this study indicate that highly-leveraged multiple benefits possible with this approach provide a strong overall encouragement that cost-effective applications exist using end-use load control to enhance power transmission in southern California.

Flat Residential/Commercial Light Architecture

Donald J. Hammerstrom (Thermal and Electric Systems Development and Analysis)
Joseph G. Birmingham (Process Technology)

Project Description

The purpose of this project was to develop a flat architecture for residential and commercial lighting. The lighting fixtures would fuse the function of conventional room lighting and architectural structure. The distribution of light source over flat structures should greatly increase light quality and eliminate shadows. Less total light and light power are needed if one places lights exactly where they are needed and distributes the light source evenly. The flat light architecture might eventually serve the function of ceiling and floor panels, desk tops, and moveable picture frame light panels. Flexible flat light structures might be molded around computer screen cabinets and safety equipment like children's bicycle helmets.

In FY 1996, funding was requested to determine the feasibility of a proposed technical avenue for achieving the flat light architecture—the flat fluorescent panel light. Preliminary proof-of-concept tests conducted in 1995 suggested that plasmas of the type needed for phosphor excitation could be maintained in narrow, flat cavities.

While light efficiency was and still is considered the most challenging aspect of this research avenue, we quickly found that multiple innovations resulted from the area of study. Many offshoot innovations do not require as great an achievable efficiency. For example, a laser concept resulting from this research would be successful with as little as 2% electrical to light efficiency.

Background

Primary lighting for residences and commercial buildings is generally considered challenging because the existing technology, the fluorescent tube, has proven itself cheap, effective, and relatively long-lived. However, there are several areas in which the fluorescent primary lighting is still vulnerable. First, fluorescent tubes have improved to a lighting efficacy that corresponds to about 30% efficiency. This is respectable, but it leaves room for revolutionary improvements that will probably not be realized by following the low-pressure fluorescent tube technical pathway. Second, the standard T-12 fluorescent tube contains enough mercury that it is treated as a flow stream of toxic waste. Competitors who reduce or eliminate mercury from their designs stand to make market inroads. Third, the standard fluorescent tube physics is such that one cannot deviate greatly from the shape of the well-known 40 W fluorescent tube without suffering unacceptable efficiency decreases. The existing low pressure fluorescent light plasma system contains many competing optical and chemical interactions that create a clear optimum geometry and pressure for efficient operation. Therefore, the low pressure fluorescent tube is geometrically limited. The ballasts of conventional fluorescent lighting are also a cause of poor power quality, a growing concern for industry and electrical utilities. Finally, human engineering has become critical from the lighting perspective. Every light structure on the market is vulnerable to criticism about its light rendering, glare, and other qualities related to eye strain or lost work. Modular work stations are now being developed to pre-plan all ergonomics of the office environment including primary lighting.

The fact that many consumers still use inefficient incandescent lighting where fluorescent lights would be a cheaper life cycle alternative means that many of the concerns listed in the previous paragraph will not be of vital concern to consumers. A flat structure would enable a new blending of structure and light with which standard fluorescent fixtures could not compete. Therefore, the flat primary lighting architecture is the overriding vision of this line of inquiry.

Silent discharge plasmas were chosen as the flat light architecture technical path to investigate in 1996. In a silent discharge, both electrodes are covered with a dielectric barrier and the system can be affected only by alternating current electrical excitation. If the plasma region is filled with noble gas, the silent discharge system results in formation and relaxation of dimers of the noble gas, called excimers. The relaxation of the excimers is accompanied by energetic ultraviolet emission. Since the excimer has no stable ground state, it does not compete for and absorb the same photons emitted by its neighbors. The silent discharge plasma is stable at high pressures from less than 10 kPa to about 300 kPa.

Technical Accomplishments

Several flat and annular silent discharge plasma test articles were designed, built, and tested in 1996. Both flat and annular geometries supported noble gas plasmas equally well. Flat plasma regions of depth about 3 mm were the narrowest tested. High voltages tend to create arcs from exposed edges of electrodes around the dielectric barrier. Typical excitation voltages were 1 kV,

and alternating current frequencies from 60 Hz to tens of kHz were successfully used.

Several excimer gas combinations were observed to emit ultraviolet near the important ultraviolet emission lines of mercury. This observation raised the hope that mercury might be eliminated by this technical path. Indeed, coupling of the ultraviolet emission to a GE Daylight phosphor was observed both visually and with a scanning monochrometer. However, the efficiently of exchange of electrical to light energy in our test apparatus has not yet exceeded 1%. Narrow excimer emission peaks in the VUV range (below the wavelengths that couple to daylight phosphors) account for some of the system inefficiency.

Low Cost Microchannel Heat Exchangers

Peter M. Martin, Dean W. Matson, Wendy D. Bennett, Carolyn E. McDonald, Donald C. Stewart (Materials and Chemical Sciences)

Project Description

Microscale components have significant potential uses in energy and chemical applications, including heating and cooling, chemical separations, combustors, micropumps and valves, pollution control and prevention, plasma reactors, and fuel cells. However, widespread use of microscale components for miniaturization of energy and chemical systems will not be realized unless the manufacturing processes and materials are efficient and cost-effective. A flexible manufacturing process is needed to fabricate a wide variety of microscale components. High-precision microcomponents will always have niche applications (defense, sensors, etc.), however, low-cost, low-precision microcomponents will also find applications in a broad range of consumer-based products suitable for widespread use. Low-precision components also have their own unique applications such as sheet architecture heat pumps and heat exchangers.

The objectives of this project were to evaluate low-cost materials and manufacturing processes for microscale components being developed at PNNL, and to demonstrate low-cost fabrication processes for low-tolerance microchannel heat exchangers. These processes have extensions to microchannel plasma reactors, chemical reactors, and combustors. Eight fabrication processes were evaluated for their viability to manufacture low-cost microscale components: stamping, electrodischarge machining, electrochemical machining, rolling, slitting and milling, molding and electrodeposition, laser micromachining, and photochemical milling followed by lamination. The potential for batch processing is an important consideration for low-cost fabrication. Materials such as metals and ceramics should be readily available and low cost.

Technical Accomplishments

The photochemical milling with lamination process was found to have the best potential for low-cost batch processing and manufacturing of low-cost microchannel heat exchangers.

Photochemical milling, or etching, is amenable for mass production:

- low cost and production line efficiency can be readily achieved
- thousands of parts at a time can be fabricated, (both large and small parts with microchannels can be fabricated)
- photochemically etched parts are clean and burr free.

A sheet architecture array of heat exchangers was fabricated by photochemical milling. Microphoto, Inc. of Roseville, Michigan, performed this work. An array of 49 microchannel heat exchangers was fabricated in a 12-inch square piece of copper, 0.125 inch thick. The microchannels were well formed and very clean. It cost $2000 to fabricate this matrix of heat exchangers; about $40/heat exchanger. This process shows promise for fabrication of sheet architecture designs.

Photochemical Milling of Horizontal Lamination

Using this process, a microchannel heat exchanger is constructed by horizontally laminating thin copper sheets. The design consisted of a top plate, channel plates, header plates, and inlet and outlet plates. The aspect ratio could be increased by adding more channel plates. Either single or sheet architecture heat exchangers could be fabricated. This process used low-cost materials such as copper and aluminum. The photochemical milling was used to cut all lamination plates which were then to be diffusion bonded.

This process was found to be unacceptable for production of microchannel heat exchangers. Parts were cut by photochemical milling in 100 μm thick copper. Because the fin regions between channels were so thin, they were not supported, lost shape, and deformed. They could not be laminated together to form continuous channels.

If this technique had been successful, the cost for four microchannel heat exchangers was $4000, or $1000 per part.

Photochemical Milling and Vertical Lamination

This process was the most successful and produced five successful test articles. The microchannel heat exchanger consists of a number of microchannels, in this case 100, formed in a thermally conductive substrate. The channel widths typically range from 50 to 200 μm. The channels can be between 100 and 500 μm (0.004 inch to 0.020 inch) deep. Fin regions separate the channels, and typically have comparable width as the channels.

Headers are machined at each end of the channels for inlet and outlet of coolant fluid or gas. The working (cooling) fluid is introduced and removed through outlet fittings.

Photochemical milling was used to form the laminations, but other processes such as stamping and laser machining could be used. The laminated strips must not have burrs.

This process can be used to fabricate complex patterns. A laminated two-level microchannel heat exchanger for use in transferring heat from one fluid to another can also be fabricated using this concept. Another unique aspect of this design is that non-planar geometries can be fabricated. For example, a heat exchanger with a curved bottom surface and curved channels can be fabricated.

The fabrication process for this heat exchanger has the potential to be very cost-effective, compared to present fabrication techniques (silicon micromachining, LIGA, physical machining). The sections that are laminated can be manufactured in very large quantities by high-volume low-cost processes. Materials are readily available, durable, and easily machined. The sections can be stamped using a die. This involves the initial investment of making a die, but millions of parts can be fabricated from one die. The photochemical etching process can be used, and is well established and readily amenable for fabricating large quantities of the laminated strips. This process can be computer automated for large batches. The advantages of this design and fabrication process are:

- low-cost readily available materials are used
- high-aspect ratio channels can be achieved
- high-volume/low-cost production amenable
- multilayered/multicomponent systems can be fabricated
- heat exchangers with curved surfaces can be easily fabricated
- very uniform microchannels can be produced.

The cost for four microchannel heat exchangers was $1300, or $325 per part. This was the lowest cost of any fabrication technique evaluated. If millions of laminations could be made on a production line basis, it is conceivable that this cost could be cut by an order of magnitude.

Microcompressor Development

Michele Friedrich, M. Kevin Drost (Thermal and Electric Systems)

Project Description

This project focused on resolving issues related to microcompressor design and performance. The ultimate objective was the demonstration of one microcompressor concept with suitable performance characteristics. FY 1994 activities focused on screening potential compressor concepts and on the demonstration of an oscillating liquid metal piston which could ultimately be used as a compressor. FY 1995 activities involved investigations of key phenomena associated with electromagnetic pumping of liquid metals. Our concept for an electromagnetic liquid metal compressor is fundamentally a liquid metal pump and the development of an efficient electromagnetic pump would advance the compressor concept, in addition to developing an important standalone product. Though the liquid metal electromagnetic microcompressor continues to appear to be technically feasible, it was clear that many other issues remain to be resolved and an early demonstration of a complete liquid metal microcompressor was unlikely.

Other FY 1995 work suggested an alternative path. The sheet architecture task successfully demonstrated a microscale absorber and showed that the heat generation rate in the absorber could approach the very high heat transfer rates attainable in our microscale heat exchangers. Based on these results and cycle simulations, it appears that a heat actuated thermochemical microcompressor (an absorption cycle heat pump) could be demonstrated in the relatively near term. Therefore, the scope of work for the 1996 microcompressor task was directed toward fabricating and demonstrating a microscale thermochemical compressor.

Heat actuated heat pumps are attractive options for energy systems miniaturization because this class of heat pump relies primarily on heat and mass transport to provide compression, avoiding the need for a mechanical compressor. We are currently focusing on demonstrating a lithium bromide/water absorption cycle heat pump.

Previous research at PNNL has demonstrated all of the components of a microchannel absorption cycle heat pump with the exception of the compressor. We have demonstrated that evaporators and condensers will have heat transfer coefficients that exceed 3.0 W/cm^2-K. In addition, we have tested a range of conceptual designs of the microchannel absorber, with the results confirming the high absorption rates predicted through microscale mass transport enhancement. Using ammonia absorption in water, we have demonstrated the ability to absorb ammonia at a rate that generates 10 W/cm^2 of heating. We believe that we can ultimately reach a heat generation rate of 30 W/cm^2.

The objectives of the FY 1996 thermochemical compressor development project were to:

- complete a detailed design and fabrication plan for a microscale, thermochemical compressor which can be integrated into the microscale sheet architecture heat pump
- fabricate and demonstrate the microscale sheet architecture thermochemical compressor.

Technical Accomplishments

FY 1996 microscale thermochemical compressor development focused on four activities:

1. *Cycle Simulation*. The ABSIM computer code developed at ORNL was used to simulate the performance of compact lithium bromide/water and ammonia/water absorption cycle heat pumps. The results of this task were used to size components and to select the chemical compressor design. Simulation was also used to support the design of the desorber and the test apparatus.

2. *Microscale Desorber (generator) and Recuperative Heat Exchanger Design and Fabrication*. Designs were developed for the desorber test bed and the regenerative heat exchanger. The desorber test bed was a flexible design, allowing performance characterization for a number of desorber geometries. The original design was to be heated by hot water, but the design was modified to include electrical resistance heating because of the higher degree of control available from resistance heating.

   The regenerative heat exchanger used microchannels for both the low and high temperature sides of the heat exchanger. The device was fabricated out of copper using conventional fabrication techniques.

3. *Design and Assembly of the Desorber Test Apparatus.* The desorber test apparatus was designed to allow performance characterization of a range of desorber designs. Strong solution, with a known concentration of H_2O was supplied to the desorber where it was heated, driving off H_2O vapor. The mass flow rate of vapor and the concentration of H_2O in the weak solution was measured, as was the carry over of lithium bromide in the water vapor stream. The test apparatus was assembled and used to conduct the tests described below.

4. *Desorber and Recuperative Heat Exchanger Proof-of-Principle Demonstration.* A number of desorber designs were tested and the results showed that heat fluxes up to 4.5 W/cm^2 could be supplied to the desorber and still maintain stable desorption. At this heating rate, the desorber for a portable cooling system would have a size of 70 cm^2. We believe that simple design modifications will ultimately allow us to reach heat fluxes of 10 W/cm^2.

Results of the FY 1996 LDRD funded microcompressor task successfully demonstrated the technical feasibility of the microtechnology-based desorber. With the successful demonstration of the desorber, all of the components of a microtechnology-based $LiBr/H_2O$ absorption cycle heat pump have been demonstrated. With this development, the demonstration of a complete chemical compressor and ultimately the complete desorber should be straightforward. Future work will focus on the continued evaluation of alternative desorber designs, completion of the thermochemical compressor demonstration, and the development of an advanced ammonia/water absorption cycle heat pump.

Publications and Presentations

M.K. Drost, R.S. Wegeng, and D.A. King. 1996. "Distributed space conditioning for residential applications." Presented at 1996 American Council for an Energy Efficient Economy Conference, August 25 to 31.

T.A. Ameel, R.O. Warrington, R.S. Wegeng, and M.K. Drost. 1996. "Miniaturization technologies applied to energy systems." *Journal of Energy Conversion and Management* (accepted).

R.S. Wegeng, M.K. Drost, T.A. Ameel, and R.O. Warrington. 1995. "Energy systems miniaturization technologies, devices, and systems." *Proceedings of the International Symposium on Advanced Energy Conversion System and Related Technologies*, RAN95, The Society of Chemical Engineers, Najoya, Japan, pp. 607-614, December.

R.S. Wegeng, C.J. Call, and M.K. Drost. 1996. "Micro thermal and chemical systems." Presented at Government Microcircuit Applications Conference, March.

T.A. Ameel, R.O. Warrington, R.S. Wegeng, and M.K. Drost. 1996. "Miniaturization technologies applied to energy systems." Presented at the 3rd Biennial Joint Conference on Engineering Systems Design & Analysis, Montpelier, France, July.

Micro Heat Exchanger Development

M. Kevin Drost (Thermal and Electric Systems)

Project Description

In FY 1996, the objective of testing in the microchannel test loop was to obtain data comparing the performance of different microchannel designs in single-phase and boiling heat transfer. Tests were conducted in the microchannel heat exchanger test loop using two test article designs. The first of these was the "first generation" design, which consisted of 54 microchannels (125 μm wide by 1000 μm deep) cut in a copper-substrate using a slitting saw. The "second generation" design used a new fabrication technique, in which layers of thin ($\sim$125 microns thick) laminate are stacked in alternating layers of fins and spacers to build up an array of microchannels. The headers and the channel openings in the spacers were made by chemical etching, and were nominally 254 μm deep.

For each microchannel test section design, tests were run over a range of flow rates and power input to obtain data for single-phase and two-phase flow. The working fluid was R124, and the conditions tested were from approximately 25 mL/min up to 300 mL/min at 70 to 80 psia, with inlet subcooling from 10°C to 15°C.

Technical Accomplishments

Single-Phase Test Results

A total of 85 single-phase test points was obtained in the six geometries tested. The data is presented graphically in plots of pressure drop versus Reynolds number, and average heat transfer coefficient versus Reynolds number. Figure 1 shows a plot of pressure drop versus Reynolds number for all geometries tested. There is a very marked difference in performance between the "first generation" Cu-substrate test articles in which the microchannels were cut with a slitting saw, and the "second generation" laminated test articles. In general, the Cu-substrate test articles show significantly lower pressure drops and achieve much higher Reynolds numbers than the laminated test articles.

Figure 2 shows a plot of the calculated average heat transfer coefficient versus Reynolds number for all three of the Cu-substrate geometries tested, and also includes the results obtained in the small laminated test articles. The blank test articles (i.e., the one with no microchannels) has a much lower heat transfer coefficient at all Reynolds numbers. The heat transfer coefficient

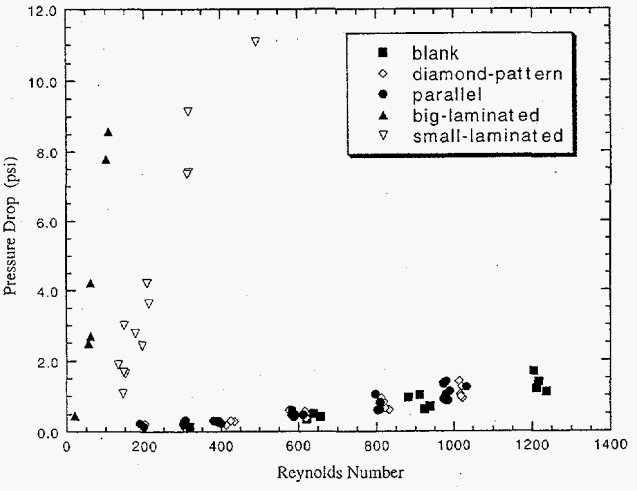

Figure 1. Pressure drop versus Reynolds number for single-phase tests in all geometries.

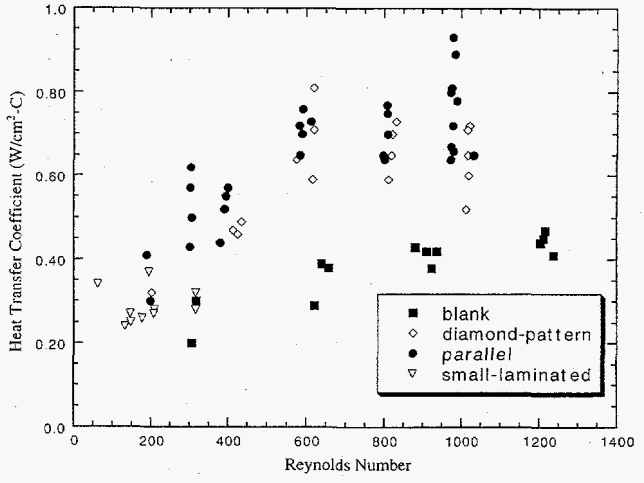

Figure 2. Single-phase heat transfer coefficient versus Reynolds number in all geometries.

values obtained in the laminated test articles are slightly lower than those obtained in the parallel-channel and diamond-pattern Cu-substrate test articles at low Reynolds numbers. The parallel-channel configuration appears to perform slightly better than the diamond-pattern configuration, but the two data sets overlap at least in part. In general, the heat transfer coefficients obtained in the diamond-pattern and the parallel-channel test articles are two to three times those obtained in the blank test article, at essentially the same pressure drop and Reynolds number.

In general, the results of the single-phase testing show that the Cu-substrate microchannels perform significantly better than the laminated test articles in terms of pressure drop as a function of flow rate. This result might be expected for the small laminated test articles, since the individual microchannel flow area is an order of magnitude smaller than in the Cu-substrate devices. But the total flow area is the same order of magnitude, and for the large laminated test article, both the individual microchannel areas and the total flow area are larger than those of the Cu-substrate test articles. Without more information on the flow and heat transfer behavior within the microchannels, it is not possible to explain the cause of these differences with any confidence. However, one obvious speculation suggestion itself immediately from the design of the laminated test articles.

The most significant difference between the two designs, apart from the microchannel geometries, is the design of the inlet and outlet headers. In the Cu-substrate devices, the headers are huge in comparison to the microchannels, and the fluid enters/exits from the center of the header. In the laminated devices, each header is essentially a microchannel; or more properly, a micro-manifold, since the header is oriented perpendicular to the microchannels. The proper design of manifolds is a somewhat arcane art, and it is not possible to predict precisely how this design should be expected to perform using conventional models. However, a cardinal rule of manifold design is to make the feeder pipe significantly larger than the distribution pipes, if it is desirable to see uniform flow in all the branches. The design of the laminated test articles violates this rule rather egregiously. It may be the case that there is a significant decrease in the volume of flow in the microchannels near the end of the header. Such a flow maldistribution would force a large percentage of the flow to go through only a few microchannels, resulting in a much higher pressure drop that would be obtained if all channels had an approximately equal volume of flow for the same overall flow rate.

Two-Phase Test Results

The total number of tests with boiling flow in this series was 87, with 72 in the Cu-substrate test articles, and 15 in the laminated test articles. Only a small number of two-phase data points were obtained in the laminated test articles because of the high pressure drops encountered. In boiling flow, it proved impossible to obtain flow rates above approximately 100 mL/min in the laminated test articles. (In contrast, flow rates of 250 to 300 mL/min were obtained in the Cu-substrate test articles in boiling flow).

The somewhat confusing jumble of data can be resolved into lines of constant flow rate, as shown in Figure 3. In general, at a given flow rate the pressure drop increases with increasing quality. The blank test article tends to

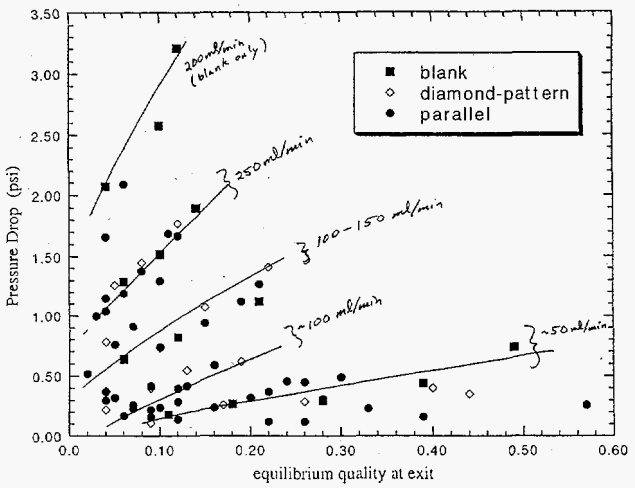

Figure 3. Pressure drop versus exit equilibrium quality in Cu-substrate geometries, with lines of constant flow rate.

have a higher pressure drop for the same quality (at a given flow rate) than is observed in either the parallel-channel or the diamond-pattern device. It is interesting to note that the higher the flow rate, the steeper the increase in pressure drop with increasing exit quality. This looks suspiciously like increasing phase slip with increasing flow velocity, but until the two-phase flow behavior can be observed in flow visualization studies, this is no more than speculation.

Figure 4 shows the pressure drop results for the laminated test articles only. As with the Cu-substrate data, it is helpful to group the data by constant flow rate, where possible. In general, the same pattern of increasing pressure drop with increasing quality at a given flow rate is observed in these results, too. The pressure drop values, however, are very high even at low quality, for what are for the most part extremely low flow rates.

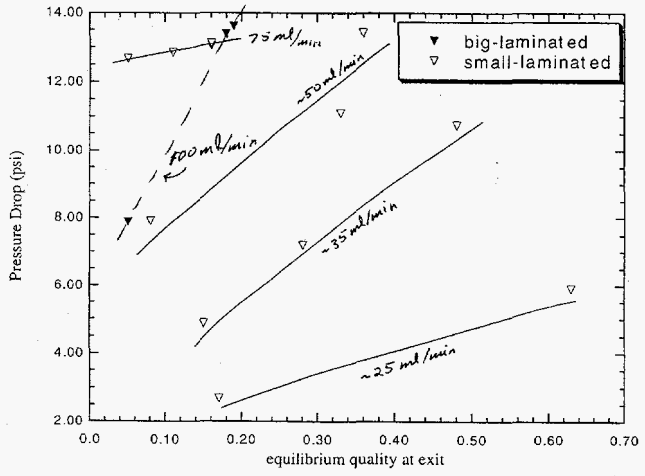

Figure 4. Pressure drop versus exit equilibrium quality in laminated geometries, with lines of constant flow rate.

The two-phase heat transfer performance of all tested geometries is presented in the plot in Figure 5, which shows the heat transfer coefficient as a function of flow rate. The shot-gun scatter of points resolves to a very tight distribution with flow rate for each test section. For the parallel-channel Cu-substrate device, the heat transfer coefficient appears strongly dependent on exit quality at low flow rates (i.e., 75 mL/min and below), but at higher flow rates is essentially constant, and may even be decreasing slightly. In the diamond-pattern and in the blank test articles, the heat transfer coefficient seems relatively independent of either exit quality or flow rate. The heat transfer coefficient appears to be essentially constant with increasing exit quality in the laminated test articles. The data obtained in these devices does not span a wide range of flow rates, but at the low flow rates, where the parallel-channel Cu-substrate device appears to give superior performance, the laminated test articles are no better than the blank test article (which has no microchannels at all).

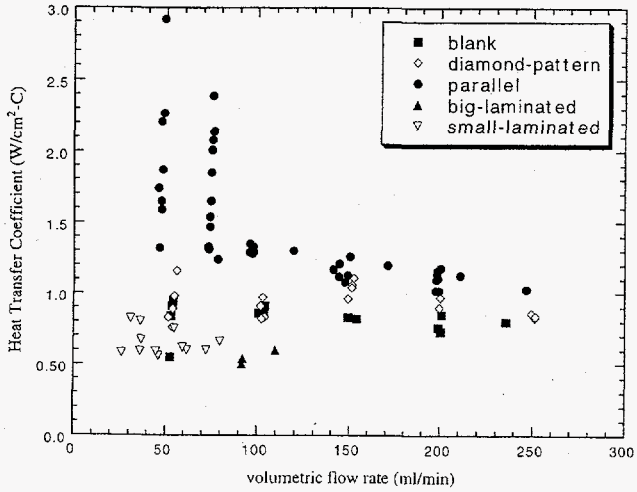

Figure 5. Two-phase heat transfer coefficient versus flow rate, in all geometries.

Presentations

J.M. Cuta, W.D. Bennett, C.E. McDonald, and T.S. Ravigururajan. 1995. *Fabrication and Testing of Micro-Channel Heat Exchangers*, presented at SPIE MicroMachining and Microfabrication '95 Conference, Austin, Texas, October 23-24.

M.K. Drost, C.J. Call, J.M. Cuta, and R.S. Wegeng. 1996. *Microchannel Integrated Evaporator/Combustor Thermal Processes*, Presented at 2nd U.S.-Japan Seminar in Molecular and Microscale Transport Phenomena, Santa Barbara, California, August 8-10.

Acronyms and Abbreviations

Acronyms and Abbreviations

2D-PAGE	two-dimensional polyacrylamide gel electrophoresis
ANN	artificial neural network
BDCA	bromodichloroacetate
BNCT	boron neutron capture therapy
CORE	collaboratory research environment
CP	cross polarized
CREB	cAMP response element binding
DCA	dichloroacetate
DGPS	differential global postioning system
DMSO	dimethyl sulfoxide
DNAPL	dense nonaqueous phase liquids
EDTA	ethylenediaminetetraacetic acid
EMSL	Environmental Molecular Sciences Laboratory
EPR	electron paramagnetic resonance
ESI	electrospray ionization
ESI-MS	electrospray ionization mass spectrometry
ESD	electron-stimulated desorption
FDTD	finite-difference time-domain
FNR	ferredoxin-NADPH-reductose
FTICR	Fourier transform ion cyclotron resonance
GC/MS	gas chromatography/mass spectrometry
GNP	glycine nitrate process
GPCR	gas-phase corona reactor
GSTs	glutathione S-transferases
HEPA	high efficienty particulate air
HERMES	Health and Ecological Risk Management and Evaluation System
HTLC	hydrotalcite-like compounds
IVE	immersive virtual environmental
LCAO	linear combinations of atomic orbitals
LEED	low energy electron diffraction
LLW	low-level waste
MALDI	matrix-assisted laser desorption ionization
MAPK	mitogen-activated protein kinase
MAS	magic angle spinning
MASS	magic angle sample spinning
MEC	microelectrochemical cell
MOs	molecular orbitals
MPI	Message-Passing Interface
MPR	micromachined plasma reactor
MS	mass spectrometry
NAPL	nonaqueous phase liquids
NASA	National Aeronatics and Space Administration
NIST	National Institute for Science and Technology

NMR	nuclear magnetic resonance
NNSF	near net shape forming
NOM	natural organic matter
NTA	nitrilotriacetate
PBPK	physiologically based pharmacokinetic
PCB	polychlorinated biphenyls
PCE	perchloroethylene
PKA	protein kinase A
PKC	protein kinase C
PMF	potential of mean force
PNC-CAT	Pacific Northwest Consortium Collaborative Access Team
PROD	pentoxy resorufin-O-deethylase
RCM	regional climate model
RTDS	Rapid Thermal Decomposition of precursors in Solution
RTUIS	real-time ultrasonic imaging system
SAMMS	self-assembled monolayers on mesoporous supports
SEM	scanning electron microscope
SID	System for Information Discovery
SPC/E	extended simple point change
STM	scanning tunneling microscope
TAGA	Trace Atmospheric Gas Analyzer
TBP	TATA-box binding protein
TCA	trichloroacetate
TCE	trichloroethylene
TeCH-RD	tetrahydroquinone reductive dehalogenase (aka) tetrachloro-*p*-hydroquinone
TEM	transmission electron microscopy
TEOS	tetraethyl orthosilicate
TNT	trinitrotoluene
TRAPDOR	transfer of populations in double resonance
VOAG	vibrating orifice aerosol generator
WWW	World Wide Web
XAFS	x-ray absorption fine structure
XPAC	xeroderma pigmentosum A complementing
XPS	x-ray photoelectron spectroscopy
XRD	x-ray diffraction